Kinetics of the Reversible Insertion of Cations in Positive Electrode Materials Under Dynamic Conditions

Vom Fachbereich Produktionstechnik

der

UNIVERSITÄT BREMEN

zur Erlangung des Grades
Doktor-Ingenieur
genehmigte

Dissertation

von

M.Sc. Collins Erinmwingbovo

Gutachter:

Prof. Fabio La Mantia

Prof. Dr. Ir. Annick Hubin (Vrije Universiteit Brussel)

Tag der mündlichen Prüfung: 29.05.2020

Dedication

To Courtins Erinmwingbovo († June 2017)

with whom I shared an amazing childhood,

to me you never died.

Declaration

The work presented in this thesis were carried out during my doctoral work from 01.10.2016 to 30.11.2019 in the Energy Storage and Conversion Systems' Group of the University of Bremen, chaired by Professor Fabio La Mantia. Here I confirm that

- The work was carried out without any unauthorized third party assistance,
- No other sources or aids than the ones specified have been used,
- Works/text passages which have been included word by word or by content accordingly from other sources have been indicated.

Date: 30.11.2019

Collins Erinmwingbovo

Abstract

The need for cost-effective energy storage systems to integrate more renewable energy has increased over the years, as we strive to reduce carbon emissions arising from the use of fossil fuels. Aqueous rechargeable batteries (ARBs) have been reported as promising energy storage system for stationary applications due to their cost-effectiveness, safety, high round trip efficiency and environmental friendliness. To optimize ARBs for enhanced electrochemical performance and to model the power-energy relation of ARBs under different working conditions, a deep understanding of the kinetics of reversible insertion process in-operando is required. To achieve this, dynamic impedance spectroscopy (DEIS) acquired using dynamic multi-frequency analysis (DMFA) was used to investigate the kinetics of the reversible insertion process in various electrode materials under working conditions.

To extract quantitative and qualitative mechanistic information that are physical correlated to the system been investigated, a model for the impedance response of (de)insertion of cations in cathode materials was developed. Using nickel hexacyanoferrate (NiHCF) films, which are unstable in their oxidized form, the advantages of using DMFA in kinetic investigation of unstable electrochemical systems was illustrated. The rate determining step of the reversible insertion process of univalent cations in NiHCF nanoparticles, a promising electrode material for ARBs was observed to depend on the state of charge. Quantitative kinetic information such as transfer coefficients and activation energies, which are useful in modelling the reversible insertion process was also extracted for the reversible insertion process of univalent cations (Na^+ and K^+) in NiHCF nanoparticles. The effect of film thickness on the kinetics of the reversible insertion of Li^+ in $LiMn_2O_4$ films made by multi-layer pulse laser deposition was also investigated in this work. The result indicates that processes such as (de)solvation process were independent on film thickness, while interfacial and bulk properties (charge transfer and mass transport) depended on the film thickness.

Kurzfassung

Der Bedarf an kostengünstigen Energiespeichersystemen zur Integration von noch mehr erneuerbaren Energien ist im Laufe der Jahre gestiegen, da wir bestrebt sind die Kohlenstoffemissionen zu reduzieren, die durch den Einsatz fossiler Kraftstoffe verursacht werden. Wässrige wiederaufladbare Batterien gelten aufgrund ihrer Wirtschaftlichkeit, Sicherheit und hohen Umlaufeffizienz und Umweltfreundlichkeit als vielversprechende Energiespeichersysteme für stationäre Anwendungen. Um die wässrigen wieder aufladbaren Batterien für eine verbesserte elektrochemische Leistung zu optimieren und um deren Relation von Leistung und Energie unter verschiedenen Arbeitsbedingungen zu modellieren, ist ein tiefes Verständnis der Kintetik des reversiblen Einlagerungsvorgangs in operando erforderlich. Um das zu erreichen wird die dynamische Impedanzspektroskopie (DIES) unter Anwendung von dynamischer Multifrequenzanalyse (DMFA) verwendet, um die Kinetik des reversiblen Einlagerungsprozesses in unterschiedlichen Elektrodenmaterialien im Betrieb zu untersuchen.

Um quantitative und qualitative mechanistische Informationen zu extrahieren, die eine direkte physikalische Bedeutung für das untersuchte System haben, wurde ein Modell für die Impedanz Reaktion der (De-)Insertion von Kationen entwickelt. Durch Verwendung von Nickel hexacyanoferrat (NiHCF) Filmen, die in oxidierter Form instabil sind, wurden die Vorteile der Verwendung von DMFA bei der kinetischen Untersuchung instabiler elektrochemischer Verbindungen dargestellt. Es wurde beobachtet, dass der geschwindigkeitsbestimmende Schritt des reversiblen Einlagerungsprozesses von univalenten Kationen in NiHCF-Nanopartikeln - ein vielversprechendes Elektrodenmaterial für ARBs-, abhängig vom Ladezustand ist. Quantitative kinetische Informationen wie z.B. Übertragungskoeffizienten und Aktivierungsenergie, die für die Modellierung des reversiblen Einlagerungsprozesses nützlich sind, wurden ebenso für den reversiblen Einlagerungsprozess von univalenten Kationen (Na^+ und K^+) in NiHCF Nanopartikeln extrahiert. Der Effekt der Filmdicke auf die Kinetik der reversiblen Einlagerung von Li^+ in $LiMn_2O_4$ wurde ebenso in dieser Arbeit untersucht. Das Ergebnis zeigt, dass Prozesse wie z.B. (De-)Solvatisierungsprozess unabhängig von Filmdicke waren, während Grenzflächen- und Bulkeigenschaften (Ladungstransfer und Massentransport) von der Filmdicke abhängig waren.

Acknowledgment

My profound gratitude goes to my doctoral advisor Prof. Fabio La Mantia for the opportunity to conduct my doctoral research in an exciting and innovating group. I would like to thank Prof. Fabio La Mantia, who over the years has become a mentor and a friend for his support, contributions and scientific discussions. I am also grateful to Prof. Dr. Ir. Annick Hubin for her interest in the topic and accepting to review this thesis. Special thanks to Prof. Dr.-Ing. Maren Petersen, who chaired my doctoral colloquium for her support and encouragement.

I would also like to acknowledge Dr. Doriano Brogioli for his support, robust scientific discussions and the coffee capsules during the last months of writing this thesis. I am grateful to my collaborators from the Catalonia institute for energy research (IREC), Dr. Rafael Trocoli, Dr. Alex Morata and Valerie Siller for providing the $LiMn_2O_4$ films used in this work. I would also like to express my gratitude to Dr. Giorgia Zampardi and Dr. Aleksandar Zeradjanin for their advise and support. Special thanks to my former colleagues, Dr. Anastasia Duschina, Dr. Amir Bani Hashemi, Dr. Ghoncheh Kasiri, Dr. Maria Sofia Palagonia and Dr. Dominique Koster for their support. I am grateful to my colleagues Michela, Kurt, Caroline, Sasha and Tom for their support. At this point, I would like to express my sincere gratitude to Miriam Gutjahr for assisting me with the bureaucratic processes and her patience for allowing me practice my never improving German with her, danke schön Miriam. I gratefully acknowledge Dr. Jens Glenneberg for taking the SEM images. My profound gratitude goes to the members of the advanced energy systems (AES), innovative sensor and functional materials (ISFM) group and the Fraunhofer institute for manufacturing technology and advanced materials (IFAM) for the scientific meetings and discussions.

Furthermore, I would like to thank my friends, Dr. David Aromokeye, Oladunni, Seun and Chukwuma for the fun times especially during holiday seasons. With them, I had a feel of home ca. 5000 km from the motherland. I would like to express gratitude to my angel mother, all that I am and hope to be, I owe to you my angel mother. Special thanks to my siblings, Jennifer and Osaro for their support and encouragement. Lastly, I would like to thank my partner Jenni for her encouragement and support.

Contents

List of Figures

List of Tables

Acronyms

ARABs	Aqueous rechargeable alkali-ion batteries
ARBs	Aqueous rechargeable batteries
CAES	Compressed air energy storage
CB	Capacitive bridge
CE	Counter electrode
CES	Chemical energy storage
CuHCF	Copper hexacyanoferrate
CV	Cyclic voltammetry
DEIS	Dynamic electrochemical impedance spectroscopy
DFT	Discrete Fourier transform
DL	Diffuse layer
DMFA	Dynamic multi-frequency analysis
EDX	Energy-dispersive X-ray spectroscopy
EIS	Electrochemical impedance spectroscopy
ESS	Energy storage systems
EVs	Electric vehicles
FFT	Fast Fourier transform
FFT-EIS	Fast Fourier transform electrochemical impedance spectroscopy
FT	Fourier transform
FWs	Flywheels
GCE	Glassy carbon electrode
GITT	Galvanostatic intermittent titration technique

HCF	Hexacyanoferrate
IFT	Inverse Fourier transform
IHP	Inner Helmolthz plane
KIBs	Potassium-ion batteries
LIBs	Lithium-ion batteries
LMO	$LiMn_2O_4$
LTO	Lithium titanate
MHCFs	Transition metal hexacyanoferrate
NiHCF	Nickel hexacyanoferrate
NMP	N-methyl-2-pyrrolidone
OHP	Outter Helmolthz plane
PBAs	Prussian blue analogues
PHES	Pumped hydro energy storage
PHS	Pumped hydro storage
PLD	Pulse laser deposition
PVDF	Polyvinylidene fluoride
QCV	Quasi-cyclic voltammetry
QTW	Quasi-triangular waveform
RE	Reference electrode
RPM	Rotation per minute
SEI	Solid electrolyte interphase
SEM	Scanning electron microscopy
SHE	Standard hydrogen electrode

SIBs	Sodium-ion batteries
SMES	Superconducting magnetic energy storage
STFT	Short time Fourier transform
TLM	Transmission line model
WE	Working electrode
XRD	X-ray diffraction

List of symbols

Symbol	Description	Unit
A_p	Cross sectional area of the pore	cm^2
bw	Bandwidth	Hz
C_1	Capacitance of the outer Helmolthz plane	F cm^{-2}
C_2	Capacitance of the inner Helmolthz plane	F cm^{-2}
C_{Ox}	Concentration of oxidized species	mol cm^{-3}
C_{Red}	Concentration of reduced species	mol cm^{-3}
C_{st}	Stray Capacitance	F
C_{ad}	Capacitance due to adsorption	F cm^{-2}
C_{A_ε}	Concentration of the cations in the electrolyte	mol cm^{-3}
C_{dl}	Double layer capacitance	F cm^{-2}
C_{int}	Capacitance due to insertion reaction	F cm^{-2}
C_0	Reference concentration	mol cm^{-3}
C_T	Maximum concentration of the cations in the solid host	mol cm^{-3}
D_{A_ε}	Diffusion coefficient of the cation in solution	cm^2 s^{-1}
D_θ	Diffusion coefficient of the cation in the solid	cm^2 s^{-1}
d	Distance between frequencies in the mutlisine	–
$\bar{E}$	(de)insertion potential	V
E	Electrode potential	V
$\tilde{\mu}$	Electrochemical potential	J mol^{-1}
$\tilde{G}$	Electrochemical free energy	J mol^{-1}
E_a^1	Activation energy of the (de)solvation process	eV
E_a^2	Activation energy of the (de)insertion process	eV
E_a^3	Activation energy of the mass transport in the electrolyte	eV
f_b	base frequency of the multisine	Hz
F	Faraday constant	C mol^{-1}
G	Chemical free energy	J mol^{-1}

Symbol	Description	Unit
i_s	Steady state current	A
i	Current	A
I	Fourier transform of current	A
i_1	Current due to (de)solvation process	A
i_2	Current due to (de)insertion process	A
I_m	Measured current in Fig. 5.3	A
I_s	Current flowing through Z_s in Fig. 5.3	A
I_{st}	Current flowing through C_{st} in Fig. 5.3	A
$i_{0,1}$	Exchange current of the (de)solvation step	A
$i_{0,2}$	Exchange current of the (de)insertion step	A
i_1	Current due to the (de)solvation step	A
i_2	Current due to the (de)insertion step	A
i_c	Capacitive current	A
i_f	Faradaic current	A
j	Imaginary unit	–
i_T	Total current flowing through the system	A
k_1^0	Standard rate constant of the (de)solvation process	cm s^{-1}
k_2^0	Standard rate constant of the (de)insertion step process	cm s^{-1}
N_{ad}	Maximum number of adsorption site	mol cm^{-3}
P	Pressure	Pa
r_1	Reaction rate of the (de)solvation process	mol cm^{-3} s^{-1}
r_2	Reaction rate of the (de)inseriton process	mol cm^{-3} s^{-1}
R	Universal gas constant	J mol^{-1} K^{-1}
R_m	Current measuring resistor in I/E converter	-
R_{ad}	Adsorption resistance	Ω cm^2
R_{ct}	Charge transfer resistance	Ω cm^2
R_p	Resistance of the pores	Ω cm^2
R_s	Resistance of the electrolyte	Ω
R_u	Uncompensated cell resistance	Ω
t	Time	s
T	Absolute temperature	K
u_s	Steady state voltage	V
u	Voltage	V

Symbol	Description	Unit
U	Fourier transform of voltage	V
V_2	Voltage drop across Z_s in Fig. 5.3	V
V_1	Voltage drop across R_m in Fig. 5.3	V
Z	Impedance of reacting sites	Ω cm^2
Z_T	Total impedance of the electrode	Ω cm^2
Z_m	Measured impedance	Ω
Z_s	Impedance of the system	Ω
Z_{V2}	Impedance of V_2 in Fig. 5.3	Ω
Z_{V1}	Impedance of V_1 in Fig. 5.3	Ω
Z_{tr}	Transimpedance of potentiostat described in page 74	-
Z_{Wad}	Warburg impedance in the electrolyte	Ω cm^2
Z_{Wct}	Warburg impedance in the solid	Ω cm^2
α_1	Transfer coefficient of the (de)solvation process	-
α_2	Transfer coefficient of the (de)insertion process	-
β	Molar fraction of the adsorption site	-
ΔE_p	Cathodic and anodic peak separation	V
ΔG^0	Gibbs free energy of insertion	J·mol^{-1}
ΔG	Gibbs free energy	J·mol^{-1}
ΔU_{ac}	Amplitdue of the multisine	mV
η	Overpotential	V
μ	Chemical potential	J mol^{-1}
$\tilde{\omega}$	characteristic diffusion frequency	rad s^{-1}
ω	Angular frequency	rad s^{-1}
ϕ_1	Potential drop due to the (de)solvation step	V
ϕ_2	Potential drop due to the reversible insertion step	V
ϕ_T	Total potential drop across the electrode/electrolyte interface	V
φ	Phase lag (see equation 2.34)	–
σ_{ad}	Warburg coefficient of the cation in the electrolyte	Ω s$^{-0.5}$
σ_{ct}	Warburg coefficient of the cation in the solid	Ω s$^{-0.5}$
$\sigma_{\bar{x}}$	Absolute standard error of the parameters obtained from the formal covariance matrix of χ^2 minimization	-
τ	Diffusion time constant	s

Symbol	Description	Unit
θ	Molar fraction of the intercalaction site	-

Chapter 1

Introduction

The need to address global environmental concerns caused by the use of fossil and nuclear fuels has resulted in increasing demand for integrating renewable energy into the grid. The utilization of renewable energy involves three aspects, namely: harvesting/conversion, energy storage and efficient energy usage. The growth of renewable energy capacity around the globe has doubled from 2010 to 2016 and is expected to increase by 43% from 2017 to 2022 as shown in Fig. 1.1 [1]. This is expected as we strive towards a carbon neutral society and keep the global average temperature increase below 2°C pre-industrial levels as stipulated in the Paris agreement [1]. Since these renewable energy sources are intermittent in nature and their availability largely depends on the weather, season and location, this constrains their use in society where the demand for electrical energy is relatively constant [2]. Energy storage systems (ESS) are then required to harness renewable energy sources in our society to reduce or eliminate the use of fossil fuels [2].

Energy storage systems are also playing a leading role in the decarbonization of road-based transportation. Carbon (IV) oxide (CO_2) from road transportation has increased from 22.7 billion metric tons in 1990 to 35.27 billion metric tons in 2013 resulting in low air quality especially in large urban centers [3]. As a result of this, there is an urgent need for more efficient transportation systems taking into consideration that the number of cars will increase as world population increases [3]. This has resulted in the research and development of methods to reduce carbon emissions arising from road-based transportation. One of the most promising method to achieve this goal, is the use of electric vehicles (EVs) [3]. The number of electric vehicles sales globally increased from less than 10,000 in 2010 to 774,000 in 2016 [4]. EVs utilize batteries, fuel cells and ultra-capacitors with the main source of electricity been renewable sources resulting in a plug in charged storage system. EES has also been widely used in portable electronic devices, which are integral parts of our daily lives such as mobile phones, laptops, e-book readers and cameras [5, 6].

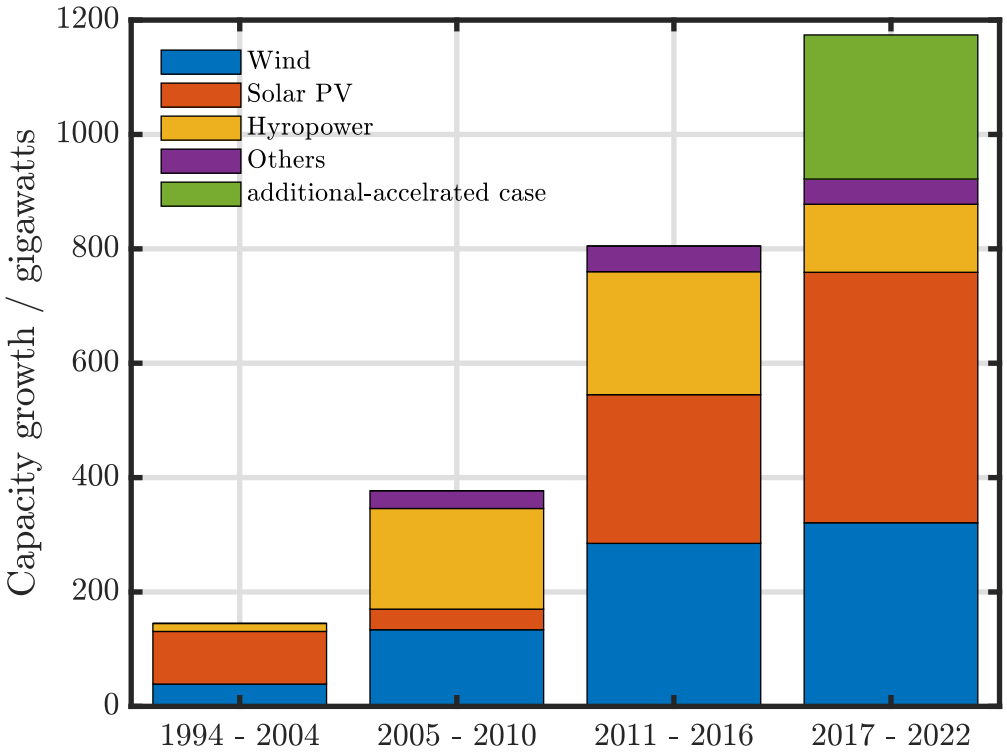

Figure 1.1: Capacity growth of renewable energy from 1994 to 2022. Adapted from [1].

1.1 Energy Storage Systems

The essential criteria for electrical energy storage systems include cost-effectiveness, safety, efficiency, durability, reliability and environmental friendliness [7–9]. ESS can be classified with the use of energy in a specific form into mechanical, thermal, electrical and chemical energy storage systems [3, 10]. Mechanical energy storage systems such as pumped hydro storage (PHS), compressed air energy storage (CAES) are suitable for power management while flywheels (FWs) are suitable for high power-low energy applications and basically useful for power management. The limitation to this form of energy stems from scarcity of available sites as in the case of CAES and PHS, which are constrained by geology and topography respectively [10]. The large initial investment needed for this form of energy is also another limiting factor for the application of these technologies to single households [10]. Frictional losses in FWs renders them unattractive for long term energy storage applications [10].

Thermal energy storage has been reported as a promising form of ESS [11]. The working principle of this form of energy storage involves the transfer of heat. During the charging process, a thermal storage comprising of materials such as molten salts, solar heating systems or magnesium salts is heated or cooled, and during discharge the stored energy can then be used for cooling applications or power generation [12, 13]. The cost-effectiveness and better reliability

it offers makes it an attractive form of energy storage system [13, 14]. However, they are limited by standby losses as well as its relatively low efficiencies. Electrical Energy storage which includes capacitors/supercapacitors and superconducting magnetic energy storage (SMES) have also been reported as a promising technology for rapid exchange of electrical power with grid during small and large disturbances. It is also an interesting option for controlling output power of wind plant and improving the stability of power system [15]. This form of energy is relatively efficient and has high power capability as well as high cycle lifetime. Its low density and high cost per installed energy makes it less attractive compared to chemical energy storage such as batteries. Chemical energy storage (CES) systems operate by the reversible transformation of electrical energy to chemical energy. The energy is stored in the forms of chemical bonds in molecular compounds [1]. This form of energy storage system includes fuel cells, rechargeable batteries and flow batteries [1].

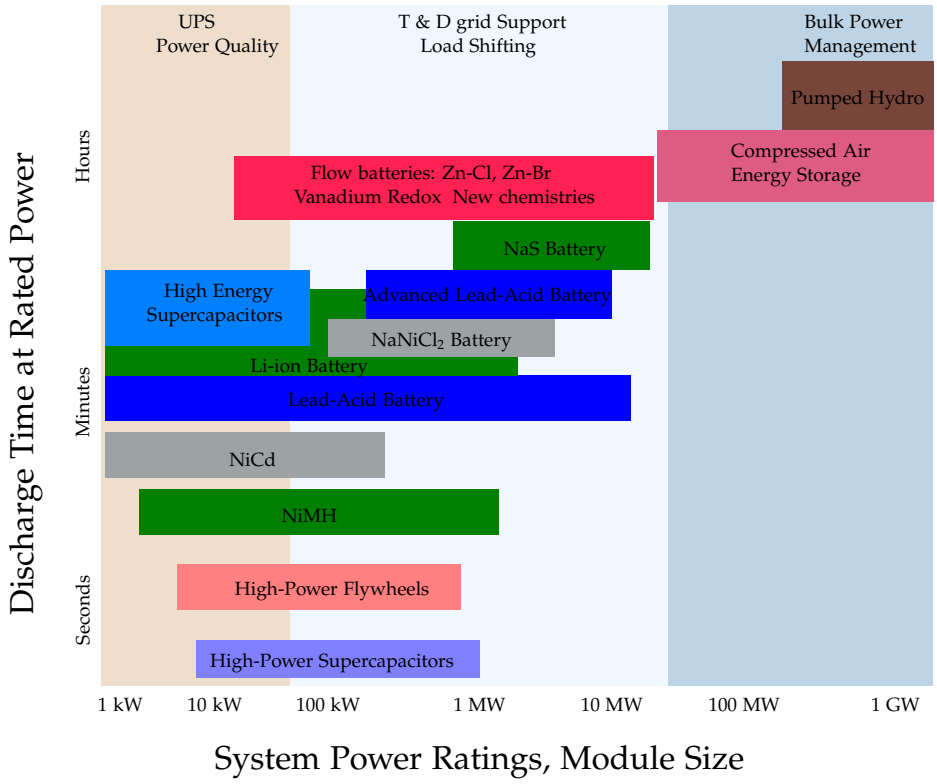

Figure 1.2: Classification of energy storage system based on system power ratings and discharge time for suitable generation. Adapted from [1].

Efficient usage of ESS involves the selection of the most appropriate form of energy storage to meet the requirements of the intended application. A comprehensive analysis of the technical specification, physical constrains and environmental impact assessment is therefore required for the efficient design and implementation of EES [1]. Based on the result of this analysis, the

appropriate EES for the intended application can be selected. The application of EES can be classified into generation, transmission/distribution and consumer level power system application using system power ratings and discharge time for suitable generation as shown in Fig 1.2 [1].

Of the various energy storage systems available for transmission/distribution and consumer level power system application, rechargeable batteries have been reported as one of the most promising technologies[1, 16, 17]. This is due to their economically viability, high specific energy, high power density and performance (long life cycle) [16]. Lead-acid batteries already in the use in automotive applications as starter for internal combustion engines has been proposed for load leveling in grid scale applications [17]. A lead-acid battery consists of lead (Pb) as the negative electrode and lead oxide (PbO_2) as the positive electrode with sulphuric acid as the electrolyte (H_2SO_4). During discharge, Pb and PbO_2 react with the electrolyte to form $PbSO_4$ and H_2O respectively and during charge the process is reversed. The overall reaction in lead-acid battery is shown in the equation below [17]:

$$Pb + PbO_2 + 2\,H_2SO_4 + 2e^-_{\alpha'} \rightleftharpoons 2\,PbSO_4 + 2\,H_2O + 2e^-_{\alpha} \tag{1.1}$$

where α' and α represents the phase of the electron. Lead-acid batteries suffer from setbacks ranging from degradation when high power is drawn to periodic water maintenance and environmental concern due to the usage of lead [11]. Nickel based batteries comprise of nickel hydroxide as the positive electrode and another element as the negative electrode. The classification of nickel-based batteries is done using the second element, for example when Fe is used as the negative electrode it is referred to as Ni-Fe and when cadmium is used, it is referred to as Ni-Cd. The electrolyte used in nickel-based batteries is potassium hydroxide solution (KOH). Using the Ni-Cd chemistry as an example, the charge/discharge process can be described with the equation below [17].

$$Cd + 2\,NiOOH + 2\,H_2O + 2e^-_{\alpha'} \rightleftharpoons 2\,Ni(OH)_2 + Cd(OH)_2 + 2e^-_{\alpha} \tag{1.2}$$

Nickel-based batteries have been the battery of choice for EVs due to their long cycle life, overcharge capability, high rates of charge/discharge and energy density [11]. However, the application of nickel based batteries is limited due to the high cost, high maintenance cost and memory effect [17]. The memory effect is a term used to describe a phenomenon where batteries lose their maximum capacity if they are repeatedly charged after partial discharge. Among rechargeable

batteries, Lithium-ion batteries (LIBs) are among the most widely used battery systems due to the advantages they offer. The next section will focus on the operating principle, advantages and limitations of LIBs.

1.2 Lithium-ion Batteries

Since their development in the 1970s and commercialization by Sony in the early 1990s, lithium-ion batteries (LIBs) have been used extensively for portable electronics due to their small size, durability, high specific energy, light weight and reasonably fast charge/discharge rates [17–19]. They are also used in the automotive industry in both hybrid and EVs, due to their volumetric and gravimetric power and low self-discharge [1, 20]. LIBs are also used in stationary and back-up power applications due to their high efficiency, fast response and long lifetime [1]. In LIBs, the number of lithium ions stored in the electrode material is determined by the chemistry and the structure of the electrode material itself. Electrodes with sufficient storing sites are thus needed to achieve high specific capacity [21]. The theoretical capacity of cathode materials (C_t) in mAh g^{-1} can be described as $C_t = nF/(3.6 \cdot M)$, where M is the molar weight of the materials in g/mol and n is the number of electrons involved in the (de)insertion process [21]. As C_t is inversely proportional to the molar weight and directly proportional to the number of electron transferred to the host, it implies electrode materials with smaller molecular weight that requires more electrons per formula unit results in higher capacity.

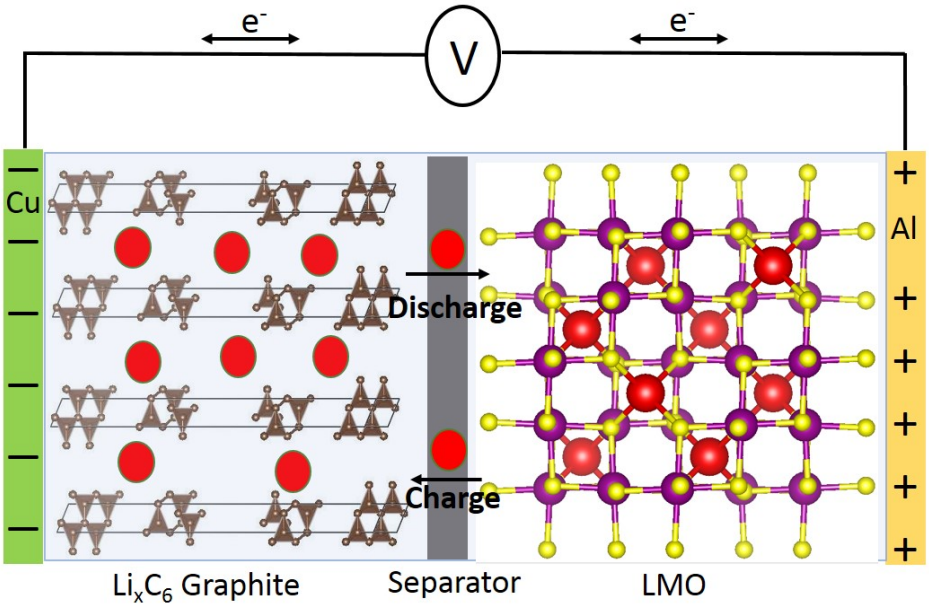

Figure 1.3: Schematics of a rocking chair type lithium-ion battery. Adapted from [22].

Fig. 1.3 shows the schematics of a rocking-chair type LIB with a lithium metal oxide ($LiMeO_2$) and graphite as the positive and negative electrodes respectively. The term 'rocking chair' was first used by Armand to describe batteries which involve the shuttling of ions in/out of the electrode materials during charge and discharge [23, 24]. The schematics indicates two electrodes immersed in an electrolyte separated by a separator. The electrodes are in contact with the current collector, which is connected to the external circuit. During charge, intercalated lithium ions (red spheres) move from the positive electrode through the electrolyte into the negative electrode. This process is reversed during discharge of the battery. Using $LiCoO_2$ as an example of the positive electrode and graphite as negative electrode, the electrochemical process occurring in rocking-chair type LIB shown in Fig. 1.3 can be represented as:

$$Li_{1-x}CoO_2 + Li_xC_6 + xe^-_{\alpha'} \rightleftharpoons LiCoO_2 + C_6 + xe^-_{\alpha} \tag{1.3}$$

The rocking-chair type LIB used for the illustration in Fig. 1.3 is just an example of one of the methods in which lithium can be stored. Other methods for hosting the lithium include alloying and conversion. In alloying, lithium is trapped by the formation of alloys formed between metals and lithium. Alloying electrodes are particularly interesting due to their high theoretical capacity [25]. For example, tin (Sn) an alloy electrode whose half cell reaction is depicted in eq. 1.4 could deliver high capacity of 993 mAh g^{-1} compared to graphite which is a commonly used insertion negative electrode with a theoretical capacity of 372 mAh g^{-1} [25]. Despite this high capacity, alloy electrodes are limited by the volume changes during alloying process resulting in pulverization. This leads to poor cycling stability [25].

$$xLi^+ + Sn + xe^- \rightleftharpoons Li_xSn \tag{1.4}$$

In conversion, electrode materials react during lithiation to form new products which are reversed during delithiation. The half cell reaction for conversion electrodes can be described as [26]:

$$M_aX_b + (b \times c)Li^+ + (b \times c)e^- \rightleftharpoons aTM + bLi_cX \tag{1.5}$$

where M denotes transition metal and X is anionic species such as oxides sulphides fluorides and phosphides [26]. Conversion electrodes like their alloying counterparts have high theoretical capacities (500 —1500 mAh g^{-1}) [25, 27]. However, the volumetric changes upon cycling which leads to capacity loss and the contact failure between the conversion electrode and the current collector

hinders the application of conversion electrode in practical applications [27]. Electrodes utilizing the (de)insertion mechanism are thus the materials of choice at the moment due to their stability. The energy density of LIBs is determined by the capacity and the potential of the electrochemical process. The capacity of the electrode material depends on the ability of the electrode materials to change their oxidation states, availability of storage sites for lithium and the reversibility of the (de)insertion process [21].

Several positive electrode materials utilizing the shuttling of lithium ions have been used in LIBs since its inception ranging from $LiCoO_2$, with a specific capacity of 140 mAh g^{-1} [3], to $LiMn_2O_4$, $LiNiO_2$ and $LiFePO_4$. On the negative electrode side, carbon in the form of graphite is widely used in LIBs due to its availability, low weight, low average voltage, low voltage hysteresis, low cost and high environmental friendliness [3, 28]. Other negative electrode materials include lithium alloyed metal, such as lithium aluminum ($Li-Al$) [7]. $Li-Al$ tends to undergo volumetric changes during the lithiation. Lithium titanate (LTO) $Li_4Ti_5O_{12}$ has also been used as negative electrode material as it does not undergo volumetric changes during the reversible insertion of lithium. However, it is limited to low energy density application due to its high potential window (1.0 —2.5 V vs Li/Li^+) compared to 0.005 —1.0 V vs Li/Li^+ for graphite [29].

Another key aspects of LIBs that influences their performance is the solid electrolyte interphase (SEI) which is a solid layer formed from the irreversible electrochemical decomposition of the electrolyte. The SEI is formed at the negative electrode due to the instability of electrolyte at the operating potential of the negative electrode during charge. The SEI prevents further solvent decomposition and allows for the transport of Li^+. The function of the SEI is vital for the chemical and electrochemical stability of the LIBs. However SEI formation and growth utilizes lithium and electrolyte and as such result to capacity fading, increasing the internal resistance of the battery and poor power density. Despite the importance of the SEI in performance of LIBs, the growth mechanism of the SEI is still not fully understood. At the moment, the SEI layer is being studied with the aim of understanding the formation of the layer and subsequently improving the performance of LIBs [30, 31].

LIBs have been optimized for currently used applications, however as the demand for energy storage for different applications increase, the need to tailor and develop technologies for emerging and future applications is increasing. LIBs powered EVs have been reported to have a driving range of 160 kilometres per single charge and the batteries amount to 65% of the total cost of EVs [20]. Thus, battery technologies offering more energy density at cheaper price are needed for EVs applications. In stationary applications, where cost and safety are prioritized, LIBs are limited due to their high cost arising from specialized cell design, cost of manufacturing process, which

requires an inert atmosphere and the high prices of battery materials such as electrodes, electrolytes [20]. Another drawback to the use of LIBs for stationary applications, is the flammability of the organic solvents used and the thermal runaway arising from unwanted reactions between the electrolyte and the electrode materials [20]. In the next paragraph, strategies employed in optimizing LIBs to meet some of the new demands will be addressed.

There has been an increase in the research and development of alternative positive and negative electrode materials for LIBs to improve the safety, power and energy density as well as the rate capability. This includes the research and development of layered nickel rich, lithium rich and manganese rich electrode materials as an alternative due to their safety and enhanced capacity [18]. These layered electrode materials have been reported to experience low capacity retention arising from structural and surface changes [18]. The use of transition metal doping, surface coating with AlF_3, Al_2O_3 $AlPO_4$ and TiO_2 has been reported as effective method in reducing the capacity fading arising from surface/structural changes [18, 32, 33]. $Li_{1.19}Mn_{0.54}Ni_{0.13}Co_{0.12}Ru_{0.01}O_2$ has also been used as a positive electrode material instead of $LiCoO_2$. Coupled with a graphite negative electrode an increase in energy density by 6.7% from 491 Wh l^{-1} to 524 Wh l^{-1} was reported indicating nickel rich based electrode material as a promising alternative to the currently used positive electrode materials for high energy density LIBs [18].

Silicon is a promising alternative to graphite due to its high theoretical capacity ($>$ 4000 mAh g^{-1}) and low operating voltage ($\sim$ 0.3 V vs Li/Li^+) [18]. Its drawback such as volumetric expansion during lithium extraction/insertion resulting in the breaking of the SEI layer which protects the electrode surface. The use of smart electrode structures and binder designs to avoid volume expansion as well as the selection of appropriate electrolyte for the formation of SEI layer on the silicon is currently being researched [18, 34, 35].

1.3 Emerging Alternatives to LIBs

In this section, emerging battery technologies which are under development in order to address some of the challenges associated with LIBs will be briefly discussed. The section includes strength of the emerging technologies, their limitations and strategies under development to overcome these challenges.

1.3.1 Lithium-Sulphur Batteries

Lithium-sulphur ($Li-S$) batteries are an emerging alternative to LIBs due to their use of sulphur which is naturally abundant, cost-effective and has a high theoretical capacity (1675 mAh g^{-1}) [18].

Li−S batteries also has a high energy density of 2500 Wh kg^{-1} compared to ca. 200 —250 Wh kg^{-1} for LIBs [18]. It consists of sulphur as the positive electrode material and Li metal as the negative electrode which undergoes plating and dissolution.

During discharge, the positive electrode material releases sulphur into the electrolyte forming long-chain polysulphides, which migrate through the electrolyte to the lithium metal where they are reduced to short chain polysulphides (Li_2S) which are insoluble and electrically insulating in nature. During charge the process is reversed as Li_2S, moves back to the sulphur positive electrode where it is oxidized [36]. The challenges associated with this process are related to the self-discharge, low coulombic efficiency, capacity loss on the positive electrode side and the aging of the lithium metal (use of lithium metal in side reactions) [36]. Despite the high specific capacity (3800 mAh g^{-1}) and low potential (-3.04 V vs SHE), metallic lithium as negative electrode material is limited due to safety concern and low cycling reversibility caused by lithium dendrites. The dendrites are formed due to irregular electrochemical plating resulting in spiky microstructures. This dendrites could lead to short circuit between the positive and negative electrode resulting in thermal runaway and possible combustion [36–38]. The use of 3D lithium structures has been reported as an alternative to lithium metal to circumvent this problem. These three-dimensional structures suppress the dendrite growth, accommodate volumetric change and protect lithium from parasitic side reactions. The use of carbon matrix at the positive electrode has also been reported to resolve the poor electronic conductivity associated with using sulphur. For Li−S batteries to be competitive with the current lithium-ion technology, further research is required to develop high density electrodes, to reduce or eliminate the polysulphides dissolution, to develop volatile electrolytes and reversible negative electrode materials as alternative to metallic lithium or three-dimensional lithium been currently used [18].

1.3.2 Metal-Air Batteries

Metal-air batteries such as lithium-air, zinc-air, magnesium-air and aluminum-air batteries have received a lot of attention due to their working principle using oxygen from air, which reduces the weight of the battery and improves its energy density [20]. In general, metal-air batteries consists of a metallic negative electrode, electrolyte and a porous positive electrode. Metals such as Li, Na, Fe and Zn can be used as negative electrode materials. During discharge, the reduction occurs in ambient air positive electrode and the metal negative electrode is oxidized and processes are reversed during the charge. Metal-air batteries can be grouped based on the electrolyte used as: aqueous metal batteries, which are not sensitive to moisture, non-aqueous metal air batteries which are sensitive to moisture, mixed/hybrid electrolyte and solid-state electrolyte [20]. Several

metal-air batteries based on different metals have been reported, such as lithium-air, zinc-air and aluminum-air. The electrochemical process occurring in lithium-air battery which has a theoretical energy density 5200 W h kg^{-1} can be described with the equation below [18]:

$$O_2 + 2\,Li + 2e^-_{\alpha'} \rightleftharpoons Li_2O_2 + 2e^-_{\alpha} \tag{1.6}$$

Problems associated with lithium-air batteries include irreversibility of discharge products resulting in clogging and the use of coated Li metal which fails to provide the long-term protection needed against dendrite formation and pH variation resulting in low rate performance. Non-aqueous systems tend to suffer also from the problem of the irreversibility of Li_2O_2 formed during discharge [18]. To solve these issues, several strategies with the aim of increasing the decomposition rate of the discharge products and of reducing the side reactions have been reported. These include the use of a non-carbonaceous electrode as the positive electrode and dimethyl sulfoxide (DMSO) as the electrolyte to improve the decomposition of Li_2O_2 resulting in a capacity retention of 95% after 100 cycles [39, 40]. The use of redox mediator which is dissolved in the electrolyte (soluble catalysts) has also been reported to increase the decomposition of Li_2O_2 [40]. Lim et al. reported 900 cycles with a charge overpotential of 0.25 V with a discharge depth of 1000 mAh g^{-1} at a current density of 2000 mA g^{-1} using a soluble catalyst [40].

Another common metal air battery is the zinc-air battery which is centuries old but has attracted a lot of interest recently due to its large storage capacity and estimated cost-effectiveness (ca. 10 \$ kW^{-1} h^{-1}) compared to LIBs (400 —800 \$ kW^{-1} h^{-1}) [41, 42]. Zinc-air batteries consists of Zn as the negative electrode, a positive air electrode in alkaline electrolyte and a membrane separator. During discharge, Zn is oxidized to zinc oxide (ZnO) which is soluble and as such the process is reversible [20]. However, during discharge a parasitic reaction between Zn and water occurs resulting in the formation of $Zn(OH)_2$ and in the evolution of hydrogen gas (H_2). This side reaction results to corrosion of the zinc metal, consumes the electrolyte and reduces the battery lifetime [43]. Other challenges with zinc-air batteries include the development of effective oxygen evolution reaction(OER) and oxygen reduction reaction (ORR) catalysts, and the prevention of carbonate formation [43]. Amalgamated zinc was used in the 1980s to reduce corrosion, but this process is not environmentally friendly [43]. Alloyed zinc coupled with additives, such as silicates, surfactants and polymers, have been reported to reduce hydrogen gas evolved in the side reaction [44–46]. Aprotic electrolytes especially ionic liquids also used for lithium-air batteries have been demonstrated to reduce the dendrite formation, hence improving the cyclability of the zinc electrodes [43, 47].

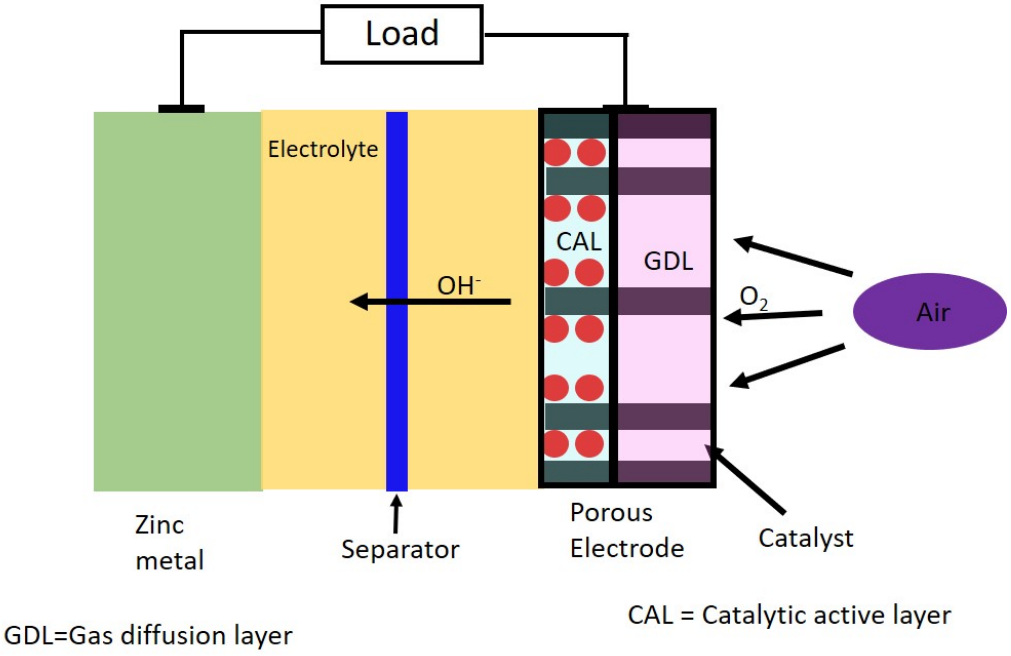

Figure 1.4: Schematic representation of zinc-air battery. Adapted from [48].

1.3.3 Non-Lithium Based Batteries

Due to constrains such as lithium resources limitations, high cost of lithium, potential safety issues and the uneven global distribution of lithium reserves, the research and development of batteries based on alternative metal ions has increased [49]. The emerging alternatives includes alkali metal (Na^+ and K^+) [50, 51], alkaline earth metals (Mg^{2+} and Ca^{2+}) [52], transition metals such as Zn^{2+} [53] and group 3A metals Al^{3+} based metal-ion batteries [54]. Sodium-ion batteries (SIBs) have been proposed as a promising alternative to LIBs due to the abundance of sodium, low cost and environmental friendliness. The operating principle of rocking chair type SIBs is similar to that of LIBs and it involves the reversible insertion of Na^+ in host structures though aqueous and non-aqueous media during charge/discharge. During discharge, Na^+ is extracted from a low voltage negative electrode material into the solution, and then inserted into a positive electrode material usually of high voltage. This process is reversed during charge.

Positive electrode materials for SIBs include layered transition-metal oxides, sodium polyanion compounds and Prussian blue analogues (PBAs) [55]. Layered materials have higher specific capacities but exhibit poor cycling rate capability, which has been attributed to their structural instability upon the reversible insertion of Na^+ [55]. Polyanion materials which are stable upon cycling exhibit poor specific capacities, due to their low electronic conductivity [55]. Prussian blue analogues (PBAs) have been reported as promising positive materials for SIBs. They are transition metal hexacyanometallates with an open framework crystal structure. The large interstitial sites

and large channels found in this class of materials allow for extraction/insertion of Na^+ [55]. PBAs exhibit good cycle life and rate performance both in non-aqueous and aqueous electrolytes. Nickel hexacyanoferrate (NiHCF), a Prussian blue analogue was shown to be a zero-strain insertion positive electrode material for SIB having a lattice variation less than 1% during cycling even after 200 cycles while exhibiting a specific capacity of 66 mAh g^{-1} [56]. Higher specific capacities have been reported for other Prussian blue analogues such as 209 mAh g^{-1} for $Na_2Mn^{II}[Mn^{II}(CN)_6]$ and 134 mAh g^{-1} for $Na_{1.71}Mn[Fe(CN)_6]$ [55, 57, 58]. Carbon in various form (soft carbon, hard carbon and reduced graphene oxide) and low transition-metal oxides and phosphates are currently used as negative electrode in SIBs [59]. Amongst the carbon based materials, hard carbon is particularly of interest due to its large interlayer distance and disordered structure which allows for the reversible insertion of Na^+ [59]. Sodium phosphide (Na_3P) with a specific capacity of 2595 mAh g^{-1} has been reported as a promising negative electrode material. It is often mixed with carbon to improve its conductivity and reduces the volumetric changes due to the reaction with sodium [59, 60].

Potassium-ion batteries (KIBs) are also among one of the emerging non-lithium battery systems. Like sodium, potassium is also an abundant element in the earth crust [61]. The operating principle of KIBs is similar to that of SIBs and LIBs. The use of cheaper aluminum current collectors and electrolyte solutions and salts reduces the cost of KIBs when compared to LIBs [61]. Graphite is a common negative electrode material for KIBs having a theoretical capacity of 279 mAh g^{-1} [62]. A specific capacity of 273 mAh g^{-1} was observed for K/graphite half cell when cycling at low C-rates (C/40) in 0.8 M KPF_6 in 50:50 ethylene carbonate (EC):diethylcarbonate(DEC) electrolyte [63]. However, at high C rate the capacity drops rapidly. The less stable K ion SEI layer formed on graphite compared to the SEI layer formed in LIBs has been speculated as the cause of this fast capacity fading [63]. Currently, the reversible insertion process of potassium in graphite is being studied with the aim of reducing the capacity fading and improving the efficiency in order to reach the commercialization standards [62–64]. Other carbon alternatives include soft-carbon electrode, hard carbon, carbon nanofibers and graphene [65–68]. Attempts to use metals and metal-oxides which rely on alloying or on reversible insertion of potassium as possible negative electrode materials for KIBs has also been reported [69, 70]. K_3Sb which utilizes alloying, has been reported to have a capacity of 110 mAh g^{-1} after 50 cycles with 98 % coulombic efficiency [70].

Layered compounds, polyanionic compounds and Prussian blue analogues are among some of the currently used positive electrode materials for KIBs [62]. Layered oxides show relatively low specific capacity and fast capacity fading due to changes in the lattice parameters as a result of

the reversible insertion of potassium which has a large ionic radius (1.38Å) [62, 71]. To this end, PBAs are used as positive electrode materials in KIBs due to their open channels which allows for the reversible insertion of K^+ [62]. Copper hexacyanoferrate, a PBA has been reported as positive electrode materials for KIBs in non-aqueous media with 88% capacity retention after 500 cycles [72].

Rechargeable batteries utilizing multivalent cations (Ca^{2+}, Mg^{2+}, Zn^{2+} and Al^{3+}) as charge carriers have been reported as promising candidates for the next generation battery concepts, due to their potentially higher energy density. The theoretical energy density of a hypothetical 4V calcium electrode is 450 Wh kg^{-1}, which is higher than the energy density of LIBs (260 Wh kg^{-1}) [73]. The natural availability of materials is also a major advantage of multi-valent batteries, as some of the cations employed are abundantly available in the earth crust. For example, aluminum, calcium and magnesium are the third, fifth and eighth most naturally occurring elements in the earth crust [73]. The operating principle of rocking chair type multivalent battery is similar to the already discussed working principle for LIBs, SIBs and KIBs. It involves the shuttling of these multivalent cations during charge/discharge. Currently studies are focused on the synthesis and optimization of electrode materials for multivalent cations, as well as the optimization of the electrolyte for these battery technologies [73–77].

1.4 Aqueous Rechargeable Batteries

Aqueous rechargeable batteries (ARBs) have been reported as promising candidates for stationary applications, as they resolve some of the challenges associated with LIBs, such as cost, safety issues and environmental concerns [16]. The ionic conductivity of aqueous electrolytes is two order of magnitudes higher than the ionic conductivity of non-aqueous electrolyte which results in higher round trip efficiency [16]. The use of aqueous electrolyte also makes ARBs more environmentally friendly than batteries utilizing organic solvents [16]. ARBs were first reported in 1994 by Dahn and co-workers using $LiMn_2O_4$ as the positive electrode and β—VO_2 as the negative electrode [78].

The ARBs reported by Dahn and co-workers had an average operating voltage of 1.5 V with an energy density of 75 Wh kg^{-1}, which is lower than the energy density of conventional LIBs (250—400 Wh kg^{-1}) [78]. This relatively low energy density can be attributed to the constrain of working with aqueous electrolytes which have a narrow stability window [78]. The components of an electrolyte including solvents (in this case water), salts and electrolyte additives determines the stability window of the electrolyte. To avoid parasitic side reactions which are detrimental to the battery efficiency, the charge/discharge process is conducted within a potential window

where the main redox process occurs excluding side reactions [78]. The stability window of water is 1.2 V. Exceeding the stability window results in the splitting of water with the gas evolution of O_2 and H_2. To overcome this challenge, the use of concentrated solutions (water in salts) increases the stability window up to 3.0 V on stainless steel electrodes [79]. This was reported to increase the energy density of ARBs to 100 Wh kg^{-1} [79].

An increase of the stability window to 3.1 V, and a subsequently increase in the energy density to 130 Wh kg^{-1} has been reported by using $Li(TSFI_{0.7}(BETI)_{0.3})\cdot H_2O$ in water [80, 81]. This electrolyte is obtained by mixing the organic lithium salts $LiN(SO_2CF_3)_2$|(LiTSFI) and $LiN(SO_2C_2F_5)_2$—LiBETI [80, 81]. The concentration of this hydrate melt electrolyte is 27.8 mol kg^{-1} while the concentration of water is 6.3 mol kg^{-1} [80, 81]. The water molecule is reduced to a minimal amount such that the exiting water molecules in the electrolyte takes part in the hydrating the lithium ions, in contrast to regular aqueous electrolyte with free water molecules [80, 81]. The conductivity of the hydrate melt was 3.0 mS cm^{-1}, despite its low viscosity as the transport of Li^+ [80]. An increase in oxidation potential of water was also observed using the hydrate melt due to strong coulombic bonding of the oxygen atom in water molecule by Li^+. This increases the anodic limit of the potential window of the electrolyte from 4.0 vs Li/Li^+ to 5 V vs Li/Li^+ [80]. The passivation of the negative electrode surface due to the formation of the interphase between the hydrate melt and the aluminum electrode also extends the electrolyte stability window to 1.75 V vs Li/Li^+ thereby increasing the potential window to 3.1 V [80, 81].

Another challenge associated with working with aqueous electrolytes is the stability of electrode materials in aqueous media. Several positive electrode materials used in LIBs can be utilized in aqueous systems, such as $LiCoO_2$, $LiMn_2O_4$, $LiFePO_4$, and PBAs. PBAs in particular have been reported as promising positive electrode materials for aqueous media involving univalent, divalent and trivalent cations [50, 52, 53, 82–86]. Wessels et al. reported copper hexacyanoferrate and nickel hexacyanoferrate as positive materials in aqueous electrolyte of potassium and sodium, with long cycle life, good rate capability and high round trip efficiency [87]. CuHCF exhibited a capacity retention of 83% after 40,000 deep discharge in aqueous potassium electrolyte while cycling at 17 C [87]. NiHCF another PBA, which is also an interesting positive material for ARBs as its electrochemical process occurs within the stability window of water [53, 88, 89] exhibited a good cycling behaviour with a negligible capacity loss after 5000 cycles while cycling in aqueous potassium and sodium electrolyte at 8.3 C [50].

Common negative electrodes used in LIBs such as carbon (graphite, soft and hard carbon), cannot be used in ARBs due to the instability of carbon in aqueous media [16]. The use of VO_2(B), spinel $Li_2Mn_2O_4$, layered LiV_3O_8, TiO_2, PBAs ($K_{0.11}Mn[Mn(CN)_6]_{0.83}\cdot 3.64\,H_2O$) polyanonic com-

pounds and metals as negative electrode materials has been reported [16]. The use of $LiTi_2(PO_4)_3$ coated with 25 nm carbon layer using chemical vapour deposition has been reported to have a capacity retention capacity of 80% after 200 cycles [90, 91]. Pasta et al. has reported the PBA $K_{0.11}Mn[Mn(CN)_6]_{0.83} \cdot 3.64\,H_2O$ as an negative electrode material with negligible capacity loss up to 1000 cycles with 99.8% coulombic efficiency at 10 C in 10 M $NaClO_4$ [92]. A battery of CuHCF as the positive electrode and $K_{0.11}Mn[Mn(CN)_6]_{0.83} \cdot 3.64\,H_2O$ as negative electrode in aqueous media was reported to have 96.7% round trip energy efficiency when cycling at 5 C with no measurable loss of capacity after 1000 deep-discharge cycles [92].

The properties of electrode materials are determined by their crystal structure, microstructure and electronic structure. The crystal structure which is an inherent property of the material determines to an extent the electrochemical performance of the electrode [21]. Despite crystal structure been an inherent property, crystal parameters can be tuned to meet specific needs [21]. The use of dopants is a common approach in electrode engineering to enhance the stability and the specific capacity of the materials [93]. Dopants also tend to affect the crystal field, thus affecting the electronic structure of the electrode materials. Microstructure of electrode materials has also been reported as an important aspect in electrode engineering. The use of nanomaterials as electrode materials reduce the transport path of the ions, changes site energy in the host structure which affects the electrochemical potential of the electrode material [21].

The stability of the host structure involves two aspects, namely the crystal structure and the reaction interface. The crystal structure which is the periodic arrangement of atoms, ions and molecules in a solid material is an important aspect in electrode materials [21]. It determines the diffusion channels and the interstitial sites, which are crucial parameters to consider when choosing electrode materials, as they determine which ions can be inserted/extracted [21]. In the next section, crystal structures of common positive electrode materials used in aqueous batteries will be discussed. The focus is on positive electrode materials in aqueous system as the electrode materials studied in this thesis were positive electrode materials utilized in aqueous media.

1.5 Crystal Structure of Some Positive Electrode Materials

Transition metal oxides are among the most commonly used positive electrode materials in batteries due to their low molecular weight and solid-state properties [21]. The first aqueous battery reported by Dahn and co-workers utilized the spinel $LiMn_2O_4$, which is an example of oxide materials [78]. Since then, numerous transition metal oxides have been reported in aqueous batteries, including layered $LiCoO_2$, manganese dioxide (MnO_2), vanadium-based positive electrode mate-

rial $Na_{1.6}V_3O_8$ and olivine structures ($LiFePO_4$). $LiMeO_2$ is a layered structured transition metal oxide where the oxygen anions plane is arranged in a ABCABC sequence. The lattice consists of MnO_6 octahedral sharing four edges with other MnO_6. For y number of anion (O) in a unit cell, $2y$ tetrahedral and y octahedral sites of anion is formed. The hexagonal structure of layered $LiCoO_2$ in ball and stick mode is shown in Fig. 1.5. It comprises of $-Li-O-Co-Li-O-$ arranged in the ABCABC sequence associated with $LiMO_2$ structure. In $LiCoO_2$, Li^+ is accommodated in layers between the octahedrons slabs created by cobalt and oxygen atoms, as shown in Fig.1.5. The two-dimensional interstitial space allows for fast reversible insertion of Li^+ [94]. The potential profile of layered structures is relatively more slopy than their spinel and olivine transition metal oxide counterparts, due to distortions which results in increase in site energy and sloping potential profile [95]. Due to the cost of $LiCoO_2$, its usage in ARBs whose concept is centred around cost effectiveness is limited [96].

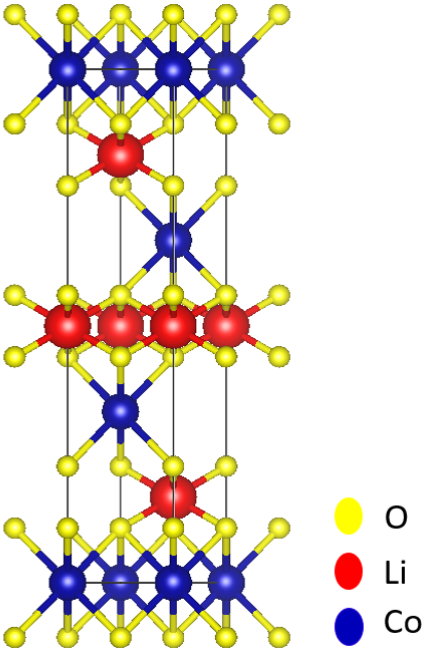

Figure 1.5: Crystal structure of layered $LiCoO_2$. Adapted from [97].

$LiMn_2O_4$ a spinel type compound has been reported as a relatively cost-effective positive electrode material for ARBs [96]. Spinel compounds have the general formula AB_2O_4 with the cations A and B occupying the tetrahedral (8a) and octahedral (16d) sites respectively, with the O anions in the spinel located in the 32e sites forming cubic structure with a space group of *Fd3m* [96]. Each unit cell in the spinel comprises of 64 tetrahedral sites, one-eighth of it occupied by A cations and 32 octahedral sites from which 16 is occupied by B cations [96]. Every empty tetrahedral or empty octahedral site in the unit cell shares at least two faces of A tetrahedral and B octahedra [96].

This prevents the simultaneous occupation of interstitial sites and A or B sites due to coulombic interactions between guest ions in interstitial sites and ions in the or B sites [96]. Fig. 1.6 shows the crystal structure of spinel $LiMn_2O_4$ (LMO). In $LiMn_2O_4$, Li occupies the 8a sites, Mn occupies the 16d sites and O occupies the 32e sites. The Mn and O forms the octahedra MnO_6 while Li occupies the tetrahedral sites. Each 8a sites in the spinel unit cell has an adjacent 16c sites which is empty as shown in Fig. 1.6. The Mn is octahedrally coordinated to the O forming a three-dimensional edge sharing MnO_6 resulting in a crystal structure with three-dimensional transport channels (*16c-8a-16c*) for the reversible insertion fo Li^+. This crystal structure offers LMO good crystal structural stability during the (de)insertion of Li^+ [96]. The reversible insertion process of Li^+ in $LiMn_2O_4$ occurs between 0.4 to 1.2 V vs Ag/AgCl (3M KCl) which is just within the stability window of the aqueous electrolyte.

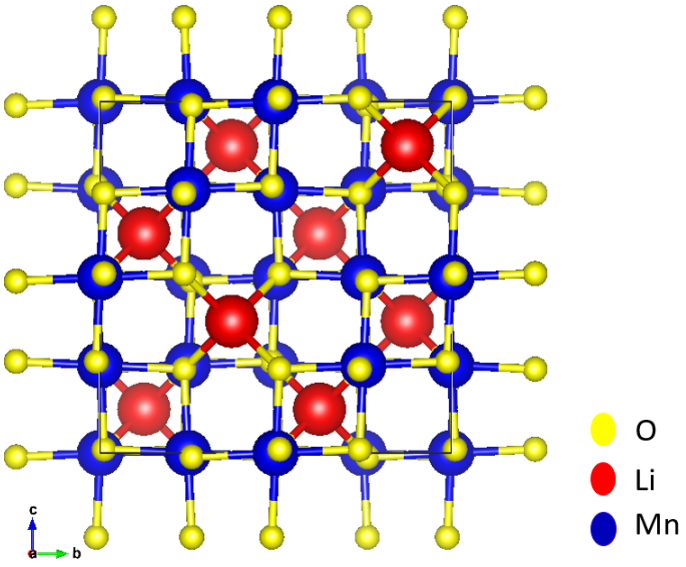

Figure 1.6: Crystal structure of spinel $LiMn_2O_4$. Adapted from [98].

Prussian blue analogues are interesting materials for aqueous batteries, as they allow for the reversible insertion of univalent, divalent and trivalent cations, and as such they can be used as positive electrode materials for alternative battery chemistry [50, 88, 89, 92, 99]. PBAs are cost-effective, relatively eco-friendly and relatively safe compared to other positive electrode materials used in aqueous batteries [50, 88]. Iron (II) hexacyanoferrate popularly known as Prussian blue is the most common and well known example of PBAs and has been used since the 17th century as a pigment for painters [100]. Prussian blue is a mixed valence polynuclear transition metal cyanide complex, often referred to as ferrocyanide. PBAs have a general formula $A_xM_y[M'(CN)_6]_{Z'} \cdot xH_2O$ where A is an alkali metal (Li, Na, K), M and M' are transition metals (Cr, Mn, Fe, Co, Ni and

Cu) [101]. When M′ is Fe, the term hexacyanoferrate (HCF) is used [101]. The transition metals (M and M′) may be the same in some materials as in the case of sodium iron hexacyanoferrate $Na_xFe[Fe(CN)_6]$. PBAs have perovskite-type structure in which the transition metals M and M′ coexist on alternate side of cubic structure with each unit cell comprising of eight sub cells. The transition metals are bridged by linear cyanide anions (M^{3+}—NC—M'^{II} or M^{2+}—NC—M'^{III}), forming an open cubic framework with large interstitial sites, also called A sites [101]. PBAs have been reported to contain two types of water molecules: coordinated water which is chemically bonded to M ions and zeolitic water which can be found in the large A sites [101]. The large diameter of the A sites and three-dimensional diffusion channels connecting the A sites in the 100 direction allow for the reversible insertion of various ions [99, 102, 103]. These ions can be monovalent (Na^+, Li^+, K^+ and NH_4^+), divalent (Mg^{2+}, Zn^{2+}, Ca^{2+}) and trivalent ions (Al^{3+}) [50, 52, 53, 82–86, 88, 99]. Fig. 1.7 shows the schematics of the crystal structure of nickel hexacyanoferrate, a PBA with a chemical formula of $ANiFe(CN)_6 \cdot xH_2O$ comprising of transition metals Fe and Ni linked by CN ligands forming a face centred cubic structure [50, 88, 104].

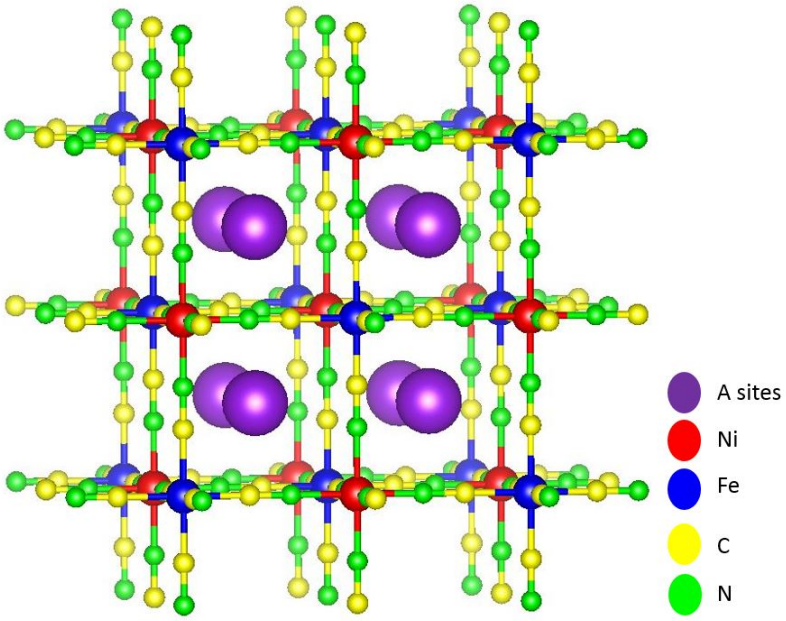

Figure 1.7: Crystal structure of nickel hexacyanoferrate. Adapted from [105].

1.6 Relationship between Energy and Power in Batteries

The electrical energy (W) and the instantaneous power (P) of the battery, which are important performance characteristics of a battery, are given by [106]:

$$W = -q_{max} \int_{Q_i}^{Q_f} [\Delta E_{eq}(Q)]\, dQ - \int_0^t i(t)\, \eta_b(Q, i) dt \tag{1.7}$$

$$P = -i(t)\, \Delta E_{eq}(t) - i(t)\, \eta_b(t) \tag{1.8}$$

where q_{max} is the maximum charge, i is the current, Q_i and Q_f are the initial and final charge of the battery respectively. ΔE_{eq} is the equilibrium voltage of the battery which is the difference between the equilibrium potential of the positive and negative electrode ($\Delta E_{eq} = E_{eq}^{+} - E_{eq}^{-}$) and η_b is the overvoltage of the battery which represents the energy losses in the system. The minus sign in front of the equation allows for the power and energy to be described according to the electrochemical convention i.e. for positive power, electrical energy is produced [106]. Equation 1.7 and 1.8 indicates that the electrical energy and power of the battery comprises of two contributions: thermodynamic contributions which is represented by the first term in eq. 1.7 and eq. 1.8 and losses in the systems which is represented with the second term in eq. 1.7 and eq. 1.8.

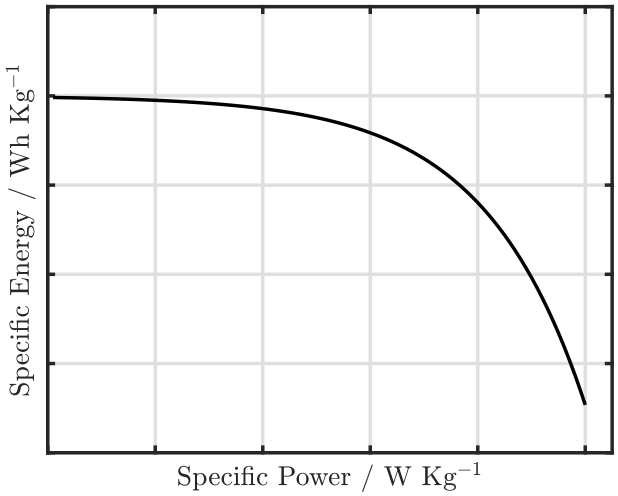

Figure 1.8: Plot of specific energy versus specific power.

The relationship between the average power and energy for a battery is given by [106]:

$$P_{avg} = \frac{1}{\Delta t} \int_0^t i(t)\, \Delta E(t)\, dt = \frac{W}{\Delta t} \tag{1.9}$$

Fig. 1.8 shows a plot of specific energy versus specific average power which is commonly referred to as the Ragone plot [106]. It is used for predicting the specific energy that can be stored/withdraw from a battery at specific power at different working conditions. The model to predict the power-energy relation requires information about the thermodynamic contribu-

tions which can be estimated from tables and the overvoltage under different working conditions, which has to be measured as they cannot be easily predicted. The potential of the electrode is related to the equilibrium potential and the summation of the overpotential of the (de)insertion process [107]:

$$E^{+/-} = E_{eq}^{+/-} + \sum \eta(i^{+/-}) \tag{1.10}$$

Using the ideal solution approximation, the equilibrium potential of the electrode depends on the specific insertion chemistry through the standard equilibrium potential (E^0), temperature (T), concentration of the cation (C_{A_ϵ}) and occupancy of the cation in the electrode (x) [104]:

$$E_{eq} = E^0 + \frac{RT}{nF} \ln \frac{C_{A_\epsilon}}{C_0} - \frac{RT}{nF} \ln \frac{x}{1-x} \tag{1.11}$$

where C_0 is the reference concentration (1 M) [104]. Fig. 1.9 shows the experimental potential profile of a positive electrode material in aqueous electrolyte versus occupation of ions in the host structure during a charge and a discharge cycle.

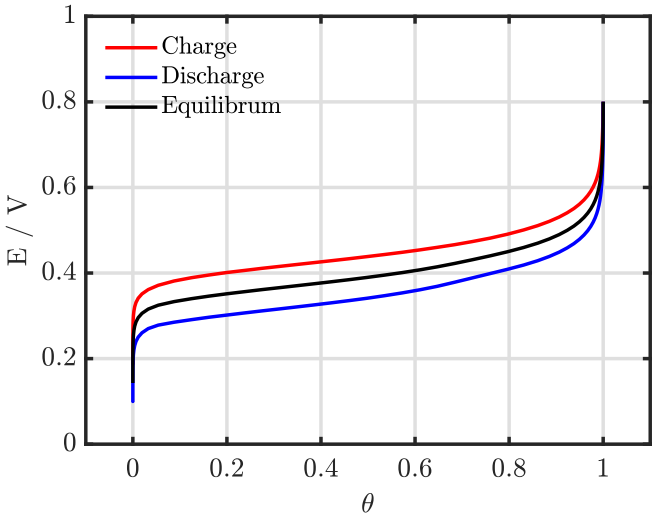

Figure 1.9: Experimental potential profile of a positive electrode material versus occupancy of the cation in the host in aqueous media showing the charge/discharge curve and the equilibrium curve.

The plot suggests the displacement of the charge potential (red curve) and discharge potential (blue curve) from the equilibrium potential (black curve) as predicted by eq. 1.10. This difference between the equilibrium potential and the charge/discharge potential profile is the overpotential. In other to successfully model the energy-power relation of this system at different working conditions, the overpotential of the system has to be measured. As the overpotential represents energy loss as explained earlier on, it reduces the electrochemical performance of the system [15]. The overpotential in rocking chair type battery consists of contributions from different phenomena

occurring during the reversible insertion process, such as charge transfer and mass transport. The charge transfer overpotential is related to the kinetics of the movement of the charge across the interface, while the mass transport overpotential also called concentration overpotential is due to the limitation of the mass transport [108]. Other possible sources of overpotential include electrolyte overpotential arising from electrolyte concentration gradient during the electrochemical reaction and the IR drop. The nucleation overpotential which can arise due to other phases nucleating is also another source of overpotential in an electrochemical system.

To reduce the energy/power loss and successfully model the energy-power relation of batteries, a deep understanding of the kinetics of the reversible insertion process is required. Thus far, the reversible insertion process has been portrayed as a single step process in the operating principle of batteries shown in the previous section. In reality it is more complex than this, since it comprises of several steps. As the kinetics and kinetic parameter depend on the occupancy of the ions in the host structure, it is also imperative that kinetic study be done in extensive conditions, including in-operando. This will allow for a better understanding of the reversible insertion process and also for the temporal evolution of the kinetic parameters under investigation.

Presently, electrochemical impedance spectroscopy is one of the most widely used techniques for qualitative and quantitative mechanistic studies of the reversible insertion process [109]. It relies on the perturbation of an electrochemical system with a sinusoidal wave and on the measurement of the current response. The acquired impedance is required to meet certain criteria for the spectra to be reliable such as stability (i.e. system does not undergo any change during the acquisition of impedance), linearity (i.e. response of the system obeys the principle of superimposition) and causality (i.e. the response of the system is due to applied perturbation) [109, 110]. As most electrochemical systems are not linear, a small amplitude voltage is used for the perturbation such that the system is in a quasi-linear state [110]. Impedance spectra using the classic form of EIS are acquired from high frequency to low frequency with a logarithmic spacing. The acquisition of low frequency data points requires longer time, which complicates the acquisition of impedance spectrum as some electrochemical systems are not stable. The amount of time required to acquire impedance at different state of charge is a drawback for employing EIS in kinetic studies even for stable electrode materials. In the absence of the time acquisition limitations, the use of classic EIS for studying the kinetics of the reversible insertion of cations in positive electrode materials neglects the temporal evolution of the kinetic parameters under dynamic conditions which is needed for a better understanding of the process. A better approach will be to perturb the electrochemical system under analysis with a combined wave comprising of multi-sine and quasi-triangular potential sweep. This allows for non-stationary impedance to be

acquired during the voltage sweep. This concept termed dynamic impedance spectroscopy was first introduced in the 1970s by Bond et.al and has been optimized by various researchers [111–116]. This idea proposed by Bond et al. is commonly referred to as fast Fourier transform EIS (FFT-EIS). Currently FFT-EIS employs the use of classic short time Fourier transform (STFT) and window function with bandwidth centered at the time t. This method is however limited by the bandwidth of the window function with respect to the temporal length resulting in errors in the low frequency data points [117].

Recently La Mantia and co-workers reported the dynamic multi-frequency analysis (DMFA) as a powerful method for extracting dynamic impedance spectra of electrochemical systems [117–119]. DMFA which utilizes digital filters, has an advantage of faster computational time, a more general description due to its usage of filters and better resolution of low frequency data points compared to FFT-EIS [117]. The concept of impedance spectroscopy and the various method of acquiring dynamic impedance spectroscopy will be discussed in details in chapter 2. DMFA has been applied for studying the kinetics of electrochemical systems such as redox couple, oscillatory electrodissolution of p-type silicon and hydrogen evolution reaction (HER) [118–121]. The technique (DMFA) thus offers the ability to study the kinetics of the reversible insertion process in positive electrode materials under dynamic conditions. This will allow for a better understanding of the (de)insertion process which is required for optimization of electrode engineering and tailoring of interface to achieve fast kinetics and better rate capability.

This PhD thesis will focus on the application of dynamic multi-frequency analysis on the investigation of the kinetics of reversible insertion of univalent cations (Li^+, Na^+ and K^+) in various cathode materials such as nickel hexacyanoferrate thin film, nickel hexacyanoferrate nanoparticle and thin films of $LiMn_2O_4$ in aqueous media. As discussed above, the understanding of the reversible insertion mechanism under dynamic conditions is a prerequisite in the optimization of ARBs which are promising alternatives to LIBs and modelling the power-energy relation of ARBs.

1.7 Aim of Study

As we strive towards a carbon neutral society, the need for efficient energy storage systems to fully utilize renewable energy sources increases. Aqueous rechargeable batteries are promising candidates for stationary applications due to their cost-effectiveness and safety. To improve the electrochemical performance of ARBs and model the power-energy relation of ARBs under different working conditions, it is important to understand the kinetics of the reversible insertion process occurring in electrode materials used in ARBs under working conditions. Currently, the kinetics of the reversible insertion process is often studied using the classic electrochemical impedance spectroscopy. However, due to the steady state requirement of this technique, it is unsuitable for investigating kinetics of the electrochemical system in non-stationary conditions and kinetics of unstable electrode materials. Using DMFA, which defines dynamic impedance based on quadrature filter, the steady state requirement of EIS is resolved allowing for the kinetics of electrochemical system to be investigated under dynamic conditions.

The aim of this thesis is to understand the kinetics of the reversible insertion process in positive electrode materials in-operando. To achieve this aim, the kinetics of the reversible insertion in selective and non-selective electrode materials under working conditions were investigated using DMFA. Using impedance models which are obtained from reaction sequences in the reversible insertion process, unique qualitative and quantitative mechanistic information, which have direct physical correlation to the system were extracted for NiHCF (non-selective electrode) and $LiMn_2O_4$ (selective electrode).

Chapter 2

Theoretical Background

In this chapter, the fundamentals of electrochemistry needed for this work will be introduced. This includes an introduction of the following topics: double layer theory, cell potential, electrochemical kinetics, electrochemical impedance spectroscopy (EIS), limitations of EIS, dynamic electrochemical impedance spectroscopy (DEIS), methods of acquiring DEIS and the introduction of modelling the impedance of electrochemical systems.

2.1 Introduction

Electrochemistry is the branch of physical chemistry that deals with the relationship between electrical and chemical energy, and the conversion of one to the other [122]. It plays a vital role in the fabrication and optimization of technologies in energy storage and conversion, materials/chemical processing, corrosion and protection as well as electrolysis. Electrochemical cells can be classified as galvanic or electrolytic cell. In galvanic cells, chemical energy is converted to electrical energy and the redox processes occurring in the cell are usually spontaneous. Examples of galvanic cells include batteries (primary and secondary) and fuel cells. On the other hand, electrolytic cells convert electrical energy to chemical energy thus requiring electrical energy to be supplied for reaction (non-spontaneous) to occur. Examples of electrolytic processes include electrolytic synthesis, electrorefining and electroplating. Fig. 2.1 shows the schematics of a simplified electrochemical cell.

The Galvani representation of the cell is shown below (Table 2.1) comprising of the metal wires as phase α and α' connecting the left and right electrode respectively. Phase β and β' is the left and right electrode (electronic conductor) respectively, while phase ε is the electrolyte (ionic conductor).

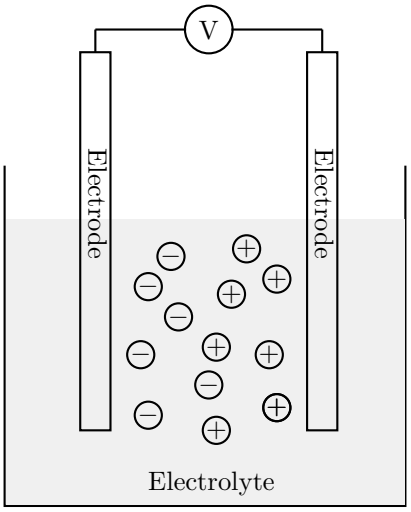

Figure 2.1: Schematics of a simple electrochemical cell.

α	β	ε	β'	α'
Cu	electrode	electrolyte	electrode	Cu

Table 2.1: Galvani representation of the simple electrochemical cell shown in Fig. 2.1. [110]

The electric potential of the phase α and α' can be different despite having same chemical state (same material), as they may not be at the same potential [110]. The electrochemical equilibrium at the interface between two phases that can exchange a species (electron or ion) can be written as the equality of the electrochemical potential of the species that is transported through the interface. For example, phase α and phase β can exchange an electron thus the electrochemical equilibrium is [122]:

$$\tilde{\mu}_{e^-}^{\alpha} = \tilde{\mu}_{e^-}^{\beta} \tag{2.1}$$

The electrochemical potential ($\tilde{\mu}$) for species i with a charge z_i can be described as [122]:

$$\tilde{\mu}_i = \mu_i + z_i F \phi \tag{2.2}$$

where μ_i is the chemical potential of species i. $\tilde{\mu}_i$ and μ_i can be described in terms of the electrochemical free energy ($\tilde{G}$) and chemical free energy (G) respectively as [122]:

$$\tilde{\mu}_i = \left(\frac{\partial \tilde{G}}{\partial n_i}\right)_{T,P,n_j \neq i} \tag{2.3}$$

$$\mu_i = \left(\frac{\partial G}{\partial n_i}\right)_{T,P,n_j \neq i} \tag{2.4}$$

where n_i is the number of moles of i, n_j is the number of moles of all species except i, T is the temperature and P is the pressure [122, 123].

2.2 Electric double layer

When an electrode comes in contact with an electrolyte, an interface that behaves like a capacitor is formed with a charge (q^M) on the electrode side and (q^S) on the electrolyte side. q^M represents the excess/deficiency of electrons in a thin layer at the electrode surface, while q^S represents the excess/deficiency of cations or anions on the electrolyte side, hence $q^M = -q^S$ [122]. This region of charged species and the associated oriented dipoles existing in the electrode/electrolyte interface is referred to as the electric double layer. The electric double layer can also be due to structural properties of the surface, such as surface active groups in ionizable media and orientation of permanent or induced dipoles [122]. The theories describing the electric double layer have evolved over the years, starting from the parallel plate condenser model proposed by Helmholtz. This theory describes the double layer analogous to electrostatic capacitor comprising of layers of charge with opposite sign separated by a fixed distance. A more advanced model is the triple layer model, which describes the double layer as comprising of three regions namely inner Helmholtz plane (IHP), outer Helmholtz plane (OHP) and diffuse layer (DL).

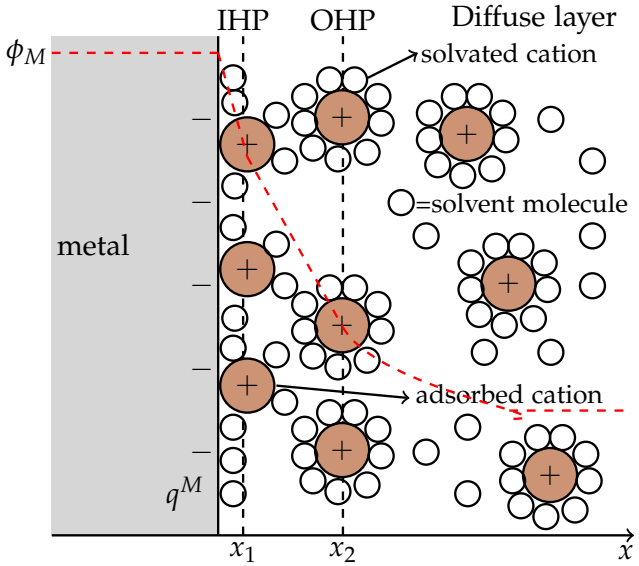

Figure 2.2: Schematics of the electric double layer according to the water-dipole model. Adapted from [122].

The IHP is described as the region between the electrode surface and the locus of centers of desolvated ions attached to the electrode surface while the OHP describes the region between the centers of desolvated ions to the locus of the nearest solvated cation [124]. The diffuse double layer consists of ions which are distributed in a region which starts from the OHP to the bulk of the solution. As most electrochemical systems utilizes solvents, the water-dipole model was proposed by Bokris, Devanathan and Muller [124]. This model also proposed occurrence of molecules attached to the electrode as well as the occurrence of partially desolvated molecules in the IHP due to strong interactions between the charged electrode and dipoles.

The description of the double layer in electrochemical systems is important as it affects the potential drop at the electrode/electrolyte interface. The potential experienced by an electroactive species in the double layer thus depends on its location in the double layer as seen in Fig. 2.2 [108]. The rate of the reaction depends on the potential drop at the interface as shown later in this work. In addition to this, the concentration of the electroactive species in the double layer may differ from the concentration of the species in the bulk, and this also affects the rate of the electrochemical process, which is a function of concentration of the electroactive species as well. The effect of the double layer is particularly interesting when the charging current is far more than the faradaic current as in the case of electrochemical systems utilizing electrolytes with low concentration [108]. For electrochemical systems with high amount of electroactive species the faradaic current is higher than the charging current, the effect of the double layer may be negligible.

2.3 Cell Potential

Using a simplified interface of a metal in contact with an electrolyte which contains a redox couple, the reaction can be described as:

$$\mathrm{Ox} + \mathrm{ne}^- \rightleftharpoons \mathrm{Red} \tag{2.5}$$

At equilibrium [110],

$$\tilde{\mu}^S_{Ox} + n\tilde{\mu}^M_e = \tilde{\mu}^S_{Red} \tag{2.6}$$

where the superscripts S and M denote the solution and electrode phase respectively. Expanding the electrochemical potential in terms of the chemical potential results to [125]:

$$\mu^{0,S}_{Ox} + RT\ln a_{Ox} + Z_{Ox}F\phi^S + n\mu^{0,M}_e + Z_{Red}F\phi^M = \mu^{0,S}_{Red} + RT\ln a_{Red} + nF\phi^S \tag{2.7}$$

$$\mu_{Ox}^{0,S} + n\mu_e^{0,M} - \mu_{Red}^{0,S} + RT \ln \frac{a_{Ox}}{a_{Red}} = nF(\phi^M - \phi^S) \tag{2.8}$$

Hence,

$$\phi^M - \phi^S = \frac{\mu_{Ox}^{0,S} + n\mu_e^{0,M} - \mu_{Red}^{0,S}}{nF} + \frac{RT}{nF} \ln \frac{a_{Ox}}{a_{Red}} \tag{2.9}$$

$\phi^M - \phi^S$ is the electric potential difference between the metal phase and solution phase. The electrode potential is measured with respect to the standard hydrogen electrode (SHE), with a constant potential, which is equal to zero. Under the assumption that the liquid junction is negligible, the equilibrium potential of the redox process versus SHE can be described as:

$$E_{eq} = (\phi^M - \phi^S) - (\phi_R^M - \phi_R^S) = E^0 + \frac{RT}{nF} \ln \frac{a_{Ox}}{a_{Red}} \tag{2.10}$$

$$E^0 = \frac{\mu_{Ox}^{0,S} - \mu_{Red}^{0,S}}{zF} \tag{2.11}$$

where the term ϕ_R^M and ϕ_R^S is the electric potential of the reference electrode and the electric potential of the solution at the reference electrode respectively, while E^0 is the standard electrode potential measured versus SHE. This equation (eq. 2.10) is the Nernst equation and relates the equilibrium potential to the activities of the electroactive species. Thus far, activities have been used in describing the redox couple. For ions and molecules in solution, the activity can be described as $a_i = \gamma_i C_i / C^0$ where C_i is the concentration of species, γ_i is activity coefficient and C^0 is the reference concentration in the bulk usually 1 M [122]. For an ideal or infinite dilute solution, γ_i tends to unity and equation 2.10 can be described in terms of the concentration of the species as:

$$E_{eq} = E^0 + \frac{RT}{nF} \ln \frac{C_{Ox}}{C_{Red}} \tag{2.12}$$

2.4 Introduction into Electrochemical Kinetics

The current flowing through an electrochemical system is [122]:

$$i = i_f + i_c \tag{2.13}$$

where i_f and i_c denotes the Faradaic current and the capacitive current respectively [122]:

$$i_f = -nFAr \tag{2.14}$$

$$i_c = C_{dl} \frac{\partial \phi}{\partial t} \tag{2.15}$$

where C_{dl} is the double layer capacitance, A is the surface area and r is the reaction rate, which for a simple redox couple in solution is [122]:

$$r = k_f C_{Ox}(0,t) - k_b C_{Red}(0,t) \tag{2.16}$$

where k_f and k_b are the forward and backward rate constants, $C_{Ox}(0,t)$ and $C_{Red}(0,t)$ are the concentration of the oxidized and reduced species at the electrode surface respectively. The forward and backward rate constants can be defined with the equations below [122]:

$$k_f = k'_f \exp\left(\frac{-\alpha n F \eta}{RT}\right) \tag{2.17}$$

$$k_b = k'_f \exp\left(\frac{(1-\alpha) n F \eta}{RT}\right) \tag{2.18}$$

where k'_f and k'_b are the cathodic and anodic kinetic constant when η = 0. Subsequently,

$$r = C_{Ox}(0,t) k'_f \exp\left(\frac{-\alpha n F \eta}{RT}\right) - C_{Red}(0,t) k'_b \exp\left(\frac{(1-\alpha) n F \eta}{RT}\right) \tag{2.19}$$

The faradaic current flowing through the system as a result of the intercalation process can then be described with the equation below [122]:

$$i_f = -nFA\left[C_{Ox}(0,t) k'_f \exp\left(\frac{-\alpha n F \eta}{RT}\right) - C_{Red}(0,t) k'_b exp\left(\frac{(1-\alpha) n F \eta}{RT}\right)\right] \tag{2.20}$$

At equilibrium, the rate of the forward is equal to the rate of the backward reaction and the net current flowing through the system is zero. The exchange current density is given by [122]:

$$i_0 = nFC_{Red} k'_b \exp\left(\frac{(1-\alpha) n F E_{eq}}{RT}\right) = nFC_{Ox} k'_f \exp\left(\frac{-\alpha n F E_{eq}}{RT}\right) \tag{2.21}$$

$$\exp\left(\frac{nFE_{eq}}{RT}\right) = \frac{k'_f}{k'_b}\frac{C_{Ox}}{C_{Red}} \tag{2.22}$$

$$E^0 = \frac{RT}{nF} \ln \frac{k'_f}{k'_b} \tag{2.23}$$

$$E_{eq} = E^0 + \frac{RT}{nF} \ln \frac{C_{Ox}}{C_{Red}} \tag{2.24}$$

This is the Nernst equation (eq. 2.12) which relates the equilibrium potential to the concentration of the electroactive species. Raising both side of eq. 2.22 by $-\alpha$ and substituting it into eq. 2.21

results to [122]:

$$i_0 = Fk^0[C_{Ox}]^{[1-\alpha]}[C_{Red}]^{\alpha} \tag{2.25}$$

where $k^0 = k_f'^{(1-\alpha)}k_b'^{(\alpha)}$. This equation indicates that the exchange current depends on the concentrations of the oxidized and reduced species as well as on the standard rate constant k^0. The current overpotential relationship is given by [122]:

$$i_f = Ai_0\left[\exp\left(\frac{-\alpha F\eta}{RT}\right) - \exp\left(\frac{(1-\alpha)F\eta}{RT}\right)\right] \tag{2.26}$$

Equation 2.26 is the Butler-Volmer equation which relates the current to the electrode potential.

2.5 Electrochemical Impedance Spectroscopy

Electrochemical impedance spectroscopy is one of the most commonly used technique in studying the kinetics and mechanisms of electrochemical processes [109, 126]. EIS allows for the investigation of various processes occurring in an electrochemical system with various timescales in a single experiment. As spectra are acquired over a wide range of frequencies (1 MHz to 1 mHz), this allows for various process such as mass transport in liquid/solid, ion-sorption, adsorption and charge transfer across interface to be investigated in a single experiment [109, 126]. EIS measurement involves the perturbation of an electrochemical system with a sinusoidal excitation and the measurement of the corresponding response [122, 126, 127].

The impedance of a system is defined as the ratio of the Fourier transform (FT) of the voltage perturbation (u) to the Fourier transform of the current response (i) [122, 126]:

$$Z(\omega) = \frac{\mathrm{FT}[u(t)](\omega)}{\mathrm{FT}[i(t)](\omega)} = \frac{U(\omega)}{I(\omega)} \tag{2.27}$$

where U and I are the Fourier transform of the voltage perturbation and current response respectively.

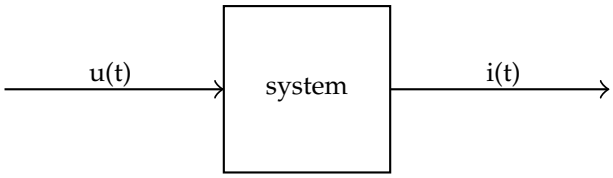

Figure 2.3: Illustration of the working principle of electrochemical impedance spectroscopy.

In the classic EIS, the system is commonly perturbed around its steady state with a frequency f with a small amplitude sinusoidal perturbation. As most electrochemical systems are nonlinear, the use of a small amplitude potential is used to achieve pseudo-linearity. The current response of the system is also a sinusoidal wave of same frequency but shifted in phase as shown in Fig. 2.4.

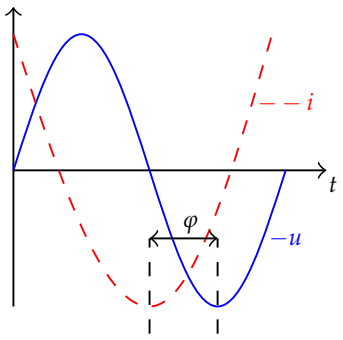

Figure 2.4: Schematic representation of the phase shift between a voltage perturbation and current response.

It is important to point out that other waveforms can be used. However, the use of sinusoidal waveforms results in the simplification of the measurement and data interpretation. The voltage perturbation and current response is given by:

$$u(t) = u_s + \mid u_i \mid \sin(\omega t) \tag{2.28}$$

$$i(t) = i_s + \mid i_i \mid \sin(\omega t - \varphi) \tag{2.29}$$

where the terms u_s and i_s represents the steady state voltage and current of the system while $\mid u_i \mid$ and $\mid i_i \mid$ represents the amplitude of the oscillating voltage and current. ω is the angular frequency ($\omega = 2\pi f$) and while t is the time [108, 110]. φ represents the phase lag between the voltage perturbation and the current response of the system (Fig. 2.4) which is usually measured with respect to the voltage perturbation [108, 110]. The Fourier transform of a function g(t) is given by:

$$\mathrm{FT}(\omega)[g(t)] = \int_{-\infty}^{+\infty} g(t) \cdot e^{-j\omega t} dt \tag{2.30}$$

Since the impedance is not acquired between $-\infty$ and ∞, the limits in eq. 2.30 is replace with 0 and T (total time of the measurement). Using eq. 2.30, the impedance of the system is:

$$Z(\omega) = \frac{\mathrm{FT}[u(t)](\omega)}{\mathrm{FT}[i(t)](\omega)} = \mid Z \mid \; e^{j\varphi} \tag{2.31}$$

where $\mid Z \mid$ is the magnitude of the impedance. Equation 2.31 indicates that impedance is a complex conjugate. Using the Euler's relationship $e^{(jx)} = \cos(x) + j\sin(x)$, the impedance can be rewritten as [110, 122, 126]:

$$Z(\omega) = \mid Z \mid \cos(\varphi) + \mid Z \mid j\sin(\varphi) \tag{2.32}$$

where the first term $|Z| \cdot \cos(\varphi)$ corresponds to the real part of the impedance (Z_{Re}) and $|Z| \cdot \sin(\varphi)$ is the imaginary part of the impedance (Z_{Im}). The real part represents the resistance of the movement of the charged species, while the imaginary part represents the reactance of the charged species in the system i.e. the opposition of the charged species to be separated in the system [126]. The impedance can thus be represented as:

$$Z(\omega) = Z_{Re} + jZ_{Im} \tag{2.33}$$

Equation 2.33 can be represented in the complex plane diagram shown in Fig 2.5 where the phase lag (φ) and the amplitude of the impedance ($|Z|$) is described as [110]:

$$\varphi = \tan^{-1}\left(\frac{Z_{Im}}{Z_{Re}}\right) \tag{2.34}$$

$$\mid Z(\omega) \mid = \sqrt{{Z_{Re}}^2 + {Z_{Im}}^2} \tag{2.35}$$

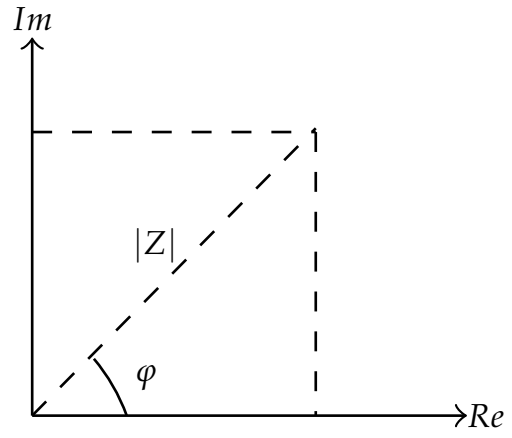

Figure 2.5: Schematic of the complex plane of impedance. Adapted from [110].

One of the advantages of working with electrochemical impedance is the ability to model

properties of electrochemical systems using passive electrical circuit elements. This is due to the fact that the impedance is a transfer function and it can be applied in general to different systems [110, 122]. The resistor is a passive element where the current potential relationship is described using the Ohm's law i.e. $V(t) = I(t)R$. The impedance of the resistor is equal to its resistance and has a phase shift equal to zero i.e. $Z = R$. The impedance of a capacitor is given by $Z_c = (j\omega C)^{-1}$ while the impedance of an inductor is described as $Z_L = j\omega L$. For passive elements in series and parallel combination shown in Fig 2.6, the impedance of the system can be described as [110]:

$$Z = Z_1 + Z_2$$
$$Z = \left[\frac{1}{Z_1} + \frac{1}{Z_2}\right]^{-1} \tag{2.36}$$

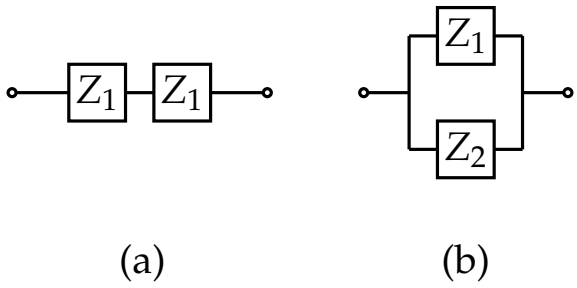

Figure 2.6: Schematic representation of (a) series combination of passive elements with impedance Z_1 and Z_2 (b) parallel combination of passive elements with impedance Z_1 and Z_2. Adapted from [110].

Impedance is usually visualized graphically using either Nyquist plots or Bode plots depending on the data and the aim of the author. In the Bode plot, $|Z|$ and φ are plotted versus frequency as shown in Fig 2.7. This type of data representation has the advantage of showing the necessary information explicitly displaying the frequency, the magnitude of the impedance and the phase of the impedance. Impedance is also visualized using Nyquist plot where $-Z_{Im}$ is plotted against Z_{Re} in equal scale, as shown in Fig. 2.8. The Nyquist plot has the advantage of allowing the easy prediction of the circuit elements from the shape of the impedance spectra. This representation also allows for the estimation of physical constants from the impedance data using graphical methods [126]. Information about the frequency is however lost using the Nyquist plot. A modified Nyquist plot where the frequency is plotted in the x-axis of a 3D plot with the y and z-axis as the real and imaginary part of the impedance respectively can be used to display the frequencies of the impedance spectra if needed. In this work, the impedance is represented either in Nyquist

or Bode plot depending on the data being represented.

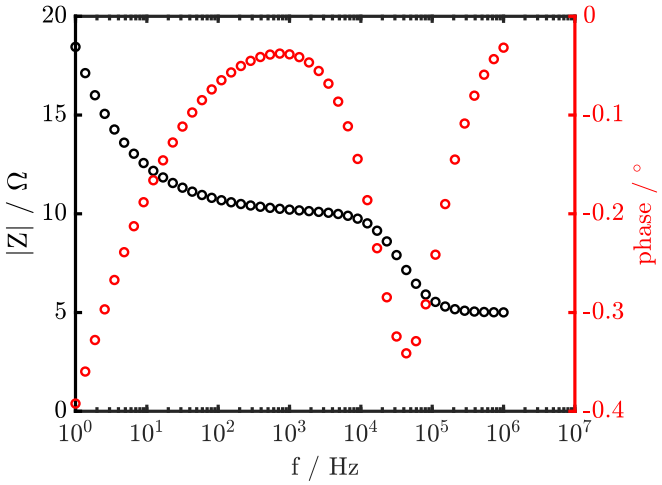

Figure 2.7: Bode plot of a simulated impedance spectrum with uncompensated cell resistance of 5 Ω, capacitance of the double layer 1 μF, charge transfer resistance of 5 Ω and Warburg coefficient of 20 Ω $s^{-0.5}$.

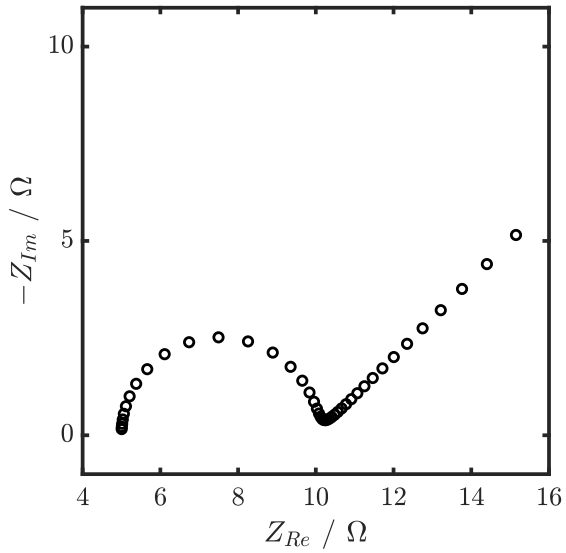

Figure 2.8: Nyquist plot of a simulated impedance spectrum with uncompensated cell resistance of 5 Ω, capacitance of the double layer 1 μF, charge transfer resistance of 5 Ω and Warburg coefficient of 20 Ω $s^{-0.5}$.

To reduce uncertainty in the interpretation of the impedance spectra, a proper cell is required for the measurement of impedance [110]. For a two-electrode cell configuration, the measured impedance (Z_m) is a combination of the impedance of positive electrode ($Z_+(\omega)$) and negative electrode ($Z_-(\omega)$) as well as the resistance of the electrolyte (R_s).

$$Z_m(\omega) = Z_+(\omega) + Z_-(\omega) + R_s \tag{2.37}$$

This configuration is useful if the impedance of the whole cell is to be measured [110, 128]. If the impedance of a single electrode is to be measured, a three-electrode cell configuration has to be used where the electrode of interest is the working electrode. The measured impedance in a three-electrode cell can described as [128]:

$$Z_m(\omega) = Z_{WE}(\omega) + R_u \tag{2.38}$$

where R_u is the uncompensated cell resistance. In this configuration, no current flows through the reference electrode (RE), so that the potential of the RE remains stable during measurement. The potential difference is then the difference between the working electrode potential and reference electrode potential. To ensure that no current is flowing through the reference electrode, a potentiostat of high input impedance is recommended and widely used [110, 128]. In general, a counter electrode and reference electrode with a low impedance is recommended for a three-electrode cell configuration to avoid distortions which may arise from the position of the working electrode. More details about these distortions can be found in literature [110, 128, 129].

The description of impedance spectroscopy requires the system to be in steady state. The spectra are acquired from predetermined start frequency to a stop frequency with each frequency applied separately. The common practice is to acquire the spectra from the high frequency to the low frequency.

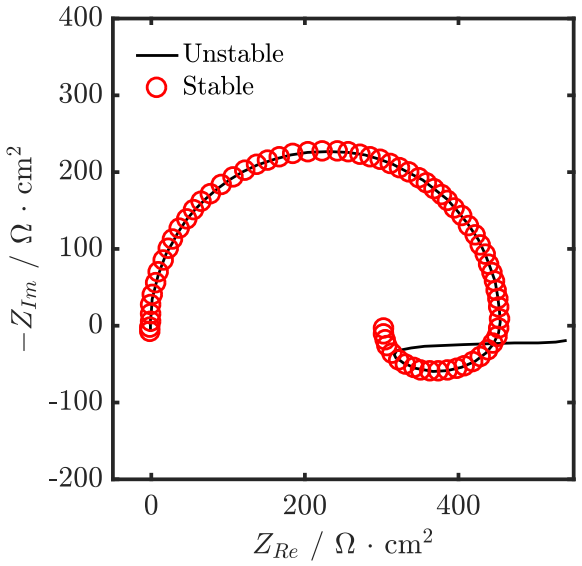

Figure 2.9: Nyquist plot of impedance spectra for dissolution of one adsorbed intermediate species following Langmuir isotherm for stable and unstable system. Adapted from [130].

The implication of this is that a relatively longer time is required to acquire the low frequency data points compared to the high frequency data point. For unstable electrochemical system,

irreversible changes and/or degradation may occur during the acquisition of the low frequency data points. This may lead to distortions in the acquired impedance spectra and results in error in the estimated kinetic parameters and/or incorrect interpretation of reaction mechanisms [130, 131]. Fig. 2.9 shows the impedance acquired for a dissolution reaction involving one adsorbed intermediate species following Langmuir isotherm under stable and unstable conditions [130]. The result indicates that the shape of the spectra for the stable system was remarkably different from the shape of the spectra acquired for the unstable system. The unstable system was observed to exhibit a low frequency loop which the authors attributed to instability of the system [130]. The analysis of data acquired from an unstable system will lead to either error in estimated kinetic parameters or an incorrect interpretation of the dissolution mechanism. For such systems (unstable electrochemical systems), EIS in its classic form is not a suitable method for the acquisition of impedance spectra. Another limitation of the steady state requirement for the classic impedance spectroscopy, is the quest to extract kinetic parameters during non-stationary processes such as charge/discharge or natural oscillating systems. The ability to follow the temporal evolution of kinetic parameters during this non-stationary processes will provide more insights into the reaction mechanism of the electrochemical system. To resolve this steady state limitation of the classic impedance spectroscopy, several methods of acquiring non-stationary impedance have been reported. Dynamic impedance spectroscopy extends the concept of impedance spectroscopy which in its classic form is defined for a system in steady state to time dependent systems under certain conditions. Several methods have been reported for the acquisition of dynamic impedance spectra, ranging from the widely used Fast Fourier transform EIS (FFT-EIS) [111, 114, 132, 133] to potentiodynamic electrochemical impedance spectroscopy [134]. Other methods includes the use of odd random phase multisine electrochemical impedance spectroscopy based on polynomial fitting of frequency signals [135–137] to the recently developed dynamic multi-frequency analysis (DMFA) which utilizes quadrature digital filters for defining dynamic impedance spectroscopy [117–119]. A brief description on FFT-EIS and DMFA is given in the next sections.

2.6 Fast Fourier Transform EIS

The concept of dynamic impedance spectroscopy was reported in the 1970s by Bond and coworkers who extended the concept of stationary impedance to non-stationary processes [111, 132, 133]. It involved the superimposition of multi-sine wave onto a ramped voltage sweep or staircase potential variation. It is generally referred to as fast Fourier transform electrochemical impedance spectroscopy (FFT-EIS) [111, 132, 133]. The acquired data is then split into smaller sections and

analyzed using fast Fourier transform (FFT). This method of acquiring dynamic impedance was further developed by Haze et al. in the 1990s following the advancement in information technology which allowed for the development of microcomputer based instrumentation [113]. The use of microcomputers enabled the impedance to be extracted over a wide range of frequencies using high quality Fourier transform [113]. However, this method had a setback that the accuracy of the FT was low due to the time variation of the system during the measurement. To this end, a numerical method which allowed for the estimation of the errors arising from the time delay of the system was proposed by Stoynov et al. [112]. Over the years, several methods have been reported with the aim to address the shortcoming of FFT-EIS which is widely used in the acquisition of non-stationary impedance, such as the optimization of the design of the multi-sine, the use of short time Fourier transform with window function and a baseline correction to decrease spectral leakage [114, 115, 138]. Dynamic impedance spectroscopy using FFT-EIS can be described as [114, 117, 119]:

$$Z'(\omega, t) = \frac{\mathrm{STFT}[u](\omega, t)}{\mathrm{STFT}[i](\omega, t)} \tag{2.39}$$

where STFT denotes short time Fourier transform. The STFT of a signal $x(t')$ can be described as [119]:

$$\mathrm{STFT}[x](\omega, t) = \mathrm{FT}[x(t') \cdot w(t' - t)](\omega) = (X \circledast [W \cdot e^{-j\omega t}])(\omega) \tag{2.40}$$

where $\circledast$ is the convolution symbol, $w(t')$ is the general window function with a Fourier transform $W(\omega')$ and $X(\omega')$ is the FT of $x(t')$ [119]. The convoluted term $(X \circledast [W \cdot e^{-j\omega t}])(\omega)$ is expressed as [119]:

$$(X \circledast [W \cdot e^{-j\omega t}])(\omega) = \int_{-\infty}^{+\infty} X(\omega')W(\omega - \omega')e^{(-j(\omega-\omega')t)}d\omega' \tag{2.41}$$

$$(X \circledast [W \cdot e^{-j\omega t}])(\omega) = e^{-j\omega t} \int_{-\infty}^{+\infty} X(\omega') \cdot W(\omega - \omega') \cdot e^{(-j\omega' t)}d\omega' \tag{2.42}$$

Equation 2.42 can be rewritten as the equation below by taking the inverse Fourier transform (iFT) of the last term in eq. 2.42:

$$\mathrm{STFT}[x](\omega, t) = e^{-j\omega' t}\mathrm{iFT}[X(\omega')W(\omega - \omega')] \tag{2.43}$$

Applying this treatment for the voltage perturbation and current response results to [119]:

$$\mathrm{STFT}[U](\omega,t) = e^{-j\omega' t}\mathrm{iFT}[U(\omega')W(\omega-\omega')(t)] \tag{2.44}$$

$$\mathrm{STFT}[I](\omega,t) = e^{-j\omega' t}\mathrm{iFT}[I(\omega')W(\omega-\omega')(t)] \tag{2.45}$$

Equation 2.39 can then be rewritten as [119]:

$$Z'(\omega,t) = \frac{\mathrm{STFT}[u](\omega,t)}{\mathrm{STFT}[i](\omega,t)} = \frac{\mathrm{iFT}[U](\omega)\ W(\omega-\omega')(t)}{\mathrm{iFT}[I](\omega)\ W(\omega-\omega')(t)} \tag{2.46}$$

The common window function used in FFT-EIS is the Blackmann-Harris periodic window function [117]:

$$w(t'-t,bw) = a_0 + a_1\cdot\cos\big(2\cdot\pi\cdot bw\cdot(t'-t)\big) + a_2\cdot\cos\big(4\cdot\pi\cdot bw\cdot(t'-t)\big) + a_3\cdot\cos\big(6\cdot\pi\cdot bw\cdot(t'-t)\big) \tag{2.47}$$

Although the FFT-EIS offers the possibility to acquire dynamic impedance in a non-stationary system using windows function. The precision of the low frequency data points of the dynamic impedance obtained using FFT-EIS was observed to be low due to the bandwidth of the window function [114, 117].

2.7 Dynamic Multi-frequency Analysis

Recently, La Mantia and co-workers reported the acquisition of dynamic impedance spectroscopy using a technique called dynamic multi-frequency analysis (DMFA) [117–119]. This technique differs from the already described FFT-EIS in using quadrature filters, which are more general in the time domain than the windows function used in FFT-EIS. This implies that DMFA has a more general definition than FFT-EIS [117, 119]. Dynamic impedance using DMFA can be described as [117, 119]:

$$Z'(\omega,t) = \frac{\mathrm{iFT}[U(\omega')\cdot g(\omega'-\omega,bw)}{\mathrm{iFT}[I(\omega')\cdot g(\omega'-\omega,bw)]} \tag{2.48}$$

where g is the quadrature filter and bw is the bandwidth of the filter function. The filter function has been reported as a L^1 function while the term g/bw is a nascent delta function described as [119]:

$$\lim_{bw\to 0}\frac{g(\omega'-\omega,bw)}{bw} = \delta(\omega'-\omega) \tag{2.49}$$

The Dirac function is a tempered distribution, thus it has a well-defined Fourier transform which is defined as [139]:

$$\int_{-\infty}^{+\infty} f(t)\delta(t-a)dt = f(a) \tag{2.50}$$

Applying this method to eq. 2.49 results to [119]:

$$\lim_{bw\to 0} \int_{-\infty}^{+\infty} \left[\frac{g(\omega'-\omega, bw)}{bw} k(\omega')\right] d\omega' = k(\omega) \tag{2.51}$$

Subsequently, iFT of the FT of variable and the filter function can be described as [119]:

$$\text{iFT}[X(\omega')\ g(\omega'-\omega, bw)] = \int_{-\infty}^{+\infty} X(\omega')\ g(\omega'-\omega, bw)\ e^{j\omega' t} d\omega' \tag{2.52}$$

When the bandwidth tends to zero one obtains [119]:

$$\lim_{bw\to 0} \frac{1}{bw}\ \text{iFT}[X(\omega')\ g(\omega'-\omega, bw)] = X(\omega)\ e^{j\omega t} \tag{2.53}$$

The voltage perturbation and current response can then be described as [119]:

$$\lim_{bw\to 0} \text{iFT}[U(\omega')\ g(\omega'-\omega, bw)] = U(\omega)\ e^{j\omega t} \tag{2.54}$$

$$\lim_{bw\to 0} \text{iFT}[I(\omega')\ g(\omega'-\omega, bw)] = I(\omega)\ e^{j\omega t} \tag{2.55}$$

Subsequently,

$$Z'(\omega, t) = \frac{\text{iFT}[U(\omega')\cdot g(\omega'-\omega, bw)]}{\text{iFT}[I(\omega')\cdot g(\omega'-\omega, bw)]} = \frac{U(\omega)}{I(\omega)} \tag{2.56}$$

When $bw \to 0$ eq. 2.48 collapse to the eq. 2.27 describing the classic stationary impedance as shown in eq.2.27, and also similar to the equation describing dynamic impedance using FFT-EIS (eq. 2.46) if $g(\omega'-\omega, bw) = W(\omega-\omega')$. In this work, a quadrature filter with a rectangular or quasi-rectangular shape was used, which is obtained by multiplying two Fermi-Dirac functions and normalizing it to one at the central frequency [117, 119]:

$$g(\omega'-\omega, bw) = \frac{1+\exp(-n)]^2}{\left[1+\exp\left(-n\cdot\frac{\omega'-\omega+bw}{bw}\right)\right]\cdot\left[1+\left(\exp -n\cdot\frac{\omega'-\omega+bw}{bw}\right)\right]} \tag{2.57}$$

The shape of the filter is determined by the term n in eq. 2.57. n used in this thesis is equal to 8 resulting in g having a shape similar to a flat-top filter [117, 119, 140]. By selecting an appropriate filter, the impedance as a function of time and frequency can be optimally resolved. The advantage of using a quadrature filter over the window method employed in FFT-EIS has been demonstrated

in [117]. The use of digital filters with a bandwidth that can be determined from the design of the multisine in DMFA allows for all data sets to be evaluated at once with filters with sharp bandwidths, eliminating the problem associated with windowing methods [117]. In addition to this, DMFA also has an advantage of reduced computational cost [117]. The computational time for 2000 spectra from 5 million samples using FFT-EIS is hundreds of times more than the time taken to extract same impedance using DMFA, indicating faster computational time with respect to FFT-EIS [117]. One drawback of DMFA, is the distortion at the beginning and at the end of the dynamic impedance associated with the analysis of non-periodic data sets. This distortion are caused by the increase in the dc skirts and overlaps with the signal of the multisine [117]. The use of mirroring of the data sets around its last point (doubling length of data set) before DMFA analysis has been demonstrated to fast dropping of the dc skirts [117]. More details about the comparison and comparative advantages of DMFA and FFT-EIS can be found in [117].

DMFA as used in this thesis involves the superimposition of a multi-sine signal to a triangular waveform. The combined waveform is then used to perturb the electrochemical system under investigation. Using the voltage perturbation and the current response, the dynamic impedance is then calculated using eq. 2.48 with filter. To extract accurate and high-quality dynamic impedance spectra using DMFA requires the adaptation and optimization of waveforms and parameters used in DMFA. Koster et al. investigated the effect of the shape of the triangular waveform, the effect of the distance between frequencies and the effect of the amplitude of the multi-sine on dynamic impedance spectra acquired in a solution containing redox couple [119]. The result obtained from the study indicates that the quasi-triangular waveform (QTW) is preferred to the classic triangular waveform due to the advantages it offers in the fast dropping of the skirt of the potential and current response as shown in Fig. 2.10 [119]. This fast dropping skirts were attributed to the shape of applied potential [119]. The quasi-triangular waveform is described as [119]:

$$QT(t) = \begin{cases} 4 \cdot t & (0 \leq t \leq 0.2) & \text{(2.58a)} \\ 0.8 + \dfrac{0.4}{\pi} \cdot \sin\left[\dfrac{(t-0.2)}{0.1} \cdot \pi\right] & (0.2 < t < 0.3) & \text{(2.58b)} \\ 2 - 4 \cdot t & (0.3 \leq t \leq 0.7) & \text{(2.58c)} \\ -0.8 + \dfrac{0.4}{\pi} \cdot \sin\left[\dfrac{(t-0.8)}{0.1} \cdot \pi\right] & (0.7 < t < 0.8) & \text{(2.58d)} \\ -4 + 4 \cdot t & (0.8 \leq t \leq 1) & \text{(2.58e)} \end{cases}$$

where t is the normalized time which has a value between 0 and 1 [119]. The use of quasi-triangular waveform allows for the acquisition of low frequency data points when using high scan rates in the voltage sweep, due to the fact that the lowest frequency in the multisine can be placed at a distance where it does not interfere with the harmonics of the DC component, as their

skirts drop faster [119].

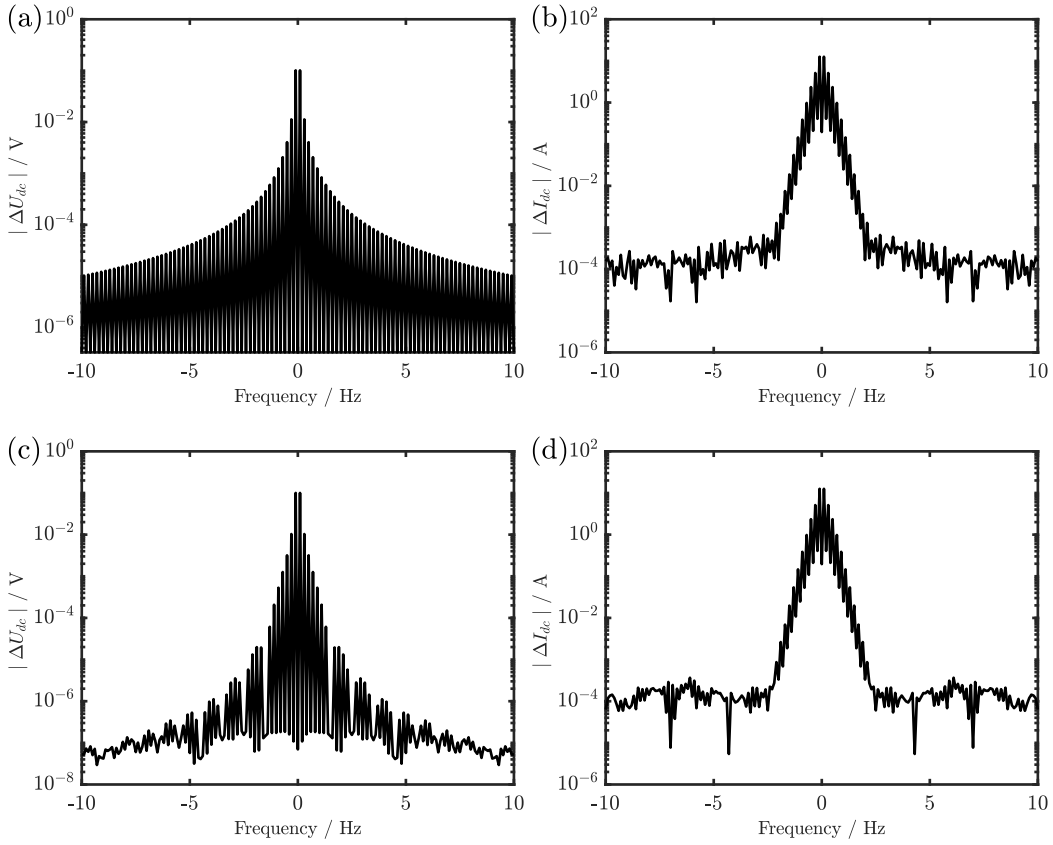

Figure 2.10: Discrete Fourier transform of the (a) voltage perturbation for the classic triangular waveform (b) current response for the classic triangular waveform. (c) voltage perturbation for the quasi-triangular waveform (b) current response for the quasi-triangular waveform [119]. Adapted from Ref [119].

The lowest frequency of the multisine is selected such that it does not interfere with the skirts of the dc component. An ideal method for this is to check the discrete Fourier transform (DFT) of the perturbation and response of the system and to choose the lowest frequency of the multisine base on the dropping of the skirts. In order to obtain high quality impedance spectra, the design of the multisine wave is done to avoid interference of frequencies with each other and/or with the sum or difference of frequencies with the fundamental frequency. To achieve this, a series of algorithms were proposed by Koster et al., which is summarized as [119]:

- The constant of proportionality (m_k) between the base frequency (f_b) and each frequency (f_k) which is a multiple of the base frequency is expressed as $m_k = f_k/f_b$. Values of m_k is chosen in quasi-logarithmic distribution covering a predefined set of decades [119].

- The minimum distance (d) between frequencies in the multi-sine must fulfil the criterion $|m_k - m_i| > d$; $|m_k - m_i \pm m_j| > d$ with the subscript k different from the subscript i and j.

When the sign $\pm$ is reduced to negative sign i can be equal to j [119].

Frequencies which do not conform to the above listed criteria are removed from the multi-sine and as such the parameter d determines the number of frequencies in the multi-sine. Each frequency in the multisine is amplified using [119]:

$$A_k = A_0 \cdot \left(1 + \frac{70[\mathrm{Hz}^{0.5}]}{\sqrt{f_k}}\right) \tag{2.59}$$

where A_0 is the initial amplitude of the signal [119]. This amplification increase the signal to noise ratio of the low frequency data points. To have a more homogeneous waveform, the phase shift of the fundamental harmonics is chosen in such a way that an optimal crest factor is obtained. The crest factor (C_r) used in DMFA and in this work is described as [119]:

$$C_r = \frac{max[abs(u_{ac})]}{\sqrt{\frac{1}{T}\int_0^T u_{ac}^2(t)dt}} \tag{2.60}$$

where u_{ac} is the multisine signal. The crest factor has been reported to improve by 20% to 30% for ca. 1000 iterations using the optimization algorithm "fminimax" of MATLAB compared to the non-optimized wave [119]. The distance between each frequency (d) also determines the choice of the bandwidth (bw) of the filter whose maximum value can be expressed as [119]:

$$bw_{max} = 2\pi f_b \left[\frac{d+1}{2}\right] \tag{2.61}$$

Higher values of d which translates to large distance between frequencies in the multi-sine allows for different values of bandwidth to be used as against limited choice if the distance between successive frequencies is used. For $d = 7$, Koster et al. reported a bandwidth between 1 Hz to 4 Hz compared to the bw of 1 which can be used for wave designed with $d = 1$. The large distance between the frequencies of in the multi-sine also ensures that the voltage perturbation and current response do not contain unwanted signals, resulting in high quality spectra. Spectra acquired far from the formal potential of the redox couple ($[Fe(CN)_6]^{3-/4-}$) were observed to be more sensitive to the distortions. The signal-to-noise ratio of the impedance spectra acquired around the formal potential using a multisine with d = 7 were higher than those acquired using a multisine with d = 1 [119]. The role of the intensity of the multisine is also an important parameter in dynamic multi-frequency analysis as it affects the nonlinear components of the electrochemical system under study. Electrochemical systems are usually linear within a range of intensity and may become nonlinear outside this region. Nonlinear response of system can generate noise thus reducing

the quality of the acquired impedance spectra. The second order harmonic influences the fundamental frequency of the quasi-triangular waveform while the third order harmonic influences the frequency f_k in the multi-sine. The signal-to-noise ratio due to the nonlinear component of the k-th frequency R_k is described as [119]:

$$R_k = \frac{1}{\Delta U_{ac}^2} \cdot \sum_j \frac{\mid A'(\omega_k, \omega_j) \mid}{\mid Z(\omega_k \mid A_j^2} \tag{2.62}$$

where A_j is the intensity of the fundamental harmonics of the frequency f_j. ΔU_{ac} denotes the amplitude of the multisine signal and the term $A'(\omega_k, \omega_j)$ is the third order response of the frequency f_j and f_j. Equation 2.62 implies that by reducing the amplitude of the multisine, the signal-to-noise ratio increased quadratically [119]. As the signal-to-noise ratio may be difficult to detect optically, the value of χ^2 from fitting the impedance may serve as an indicative tool [119]. Koster et.al reported an increase in χ^2 value from $3.9{\cdot}10^{-5}$ to $3.7{\cdot}10^{-4}$ for an increase in ΔU_{ac} from 10 mV to 50 mV, indicating a decrease in the quality of the spectra. The shape of the quasi-voltammogram has exhibits negligible distortions if the intensity of the multisine used is in the region where the electrochemical system is linear [119].

2.8 Introduction to Modelling Impedance of Electrochemical Systems

To extract kinetic parameters and obtain mechanistic information of electrochemical system studied using impedance spectroscopy, the measured impedance is fitted with a model describing the physicochemical process occurring in the electrochemical system. In this section, an introduction to the development of models for fitting measured impedance will be given. The fitting of measured impedance with models based on reaction mechanism is a better approach to the use of arbitrary circuit comprising of different passive elements. This approach provides information about the physicochemical processes occurring in the electrochemical system. Using a simple redox couple, a brief discussion about the modelling of an electrochemical system will be discussed in this section. The electrochemical reaction occurring in the electrode surface in a solution containing a redox couple is:

$$\mathrm{Ox} + \mathrm{ne}^- \rightleftharpoons \mathrm{Red} \tag{2.63}$$

The admittance (inverse of the impedance) is expressed as:

$$\frac{1}{Z(\omega)} = \frac{\mathrm{FT}[i(t)](\omega)}{\mathrm{FT}[u(t)](\omega)} \tag{2.64}$$

In EIS the electrochemical system is perturbed with small amplitude sinusoidal voltage such that the condition of quasi-linearity holds (eq. 2.28). This results in the rate determining variables, in this case (simple redox couple) C_{Ox}, C_{Red} and ϕ described as the sum of dc and oscillating component: $C_{Ox} = C_{Ox,\mathrm{dc}} + \widetilde{C_{Ox}}$; $C_{Red} = C_{Red,\mathrm{dc}} + \widetilde{C_{Red}}$. $\widetilde{}$denotes the oscillating variable which is given by $\widetilde{C_{Red}} = \Delta C_{Red}\ e^{j\omega t} + \Delta C^{*}_{Red}\ e^{-j\omega t}$ and $\widetilde{C_{Ox}} = \Delta C_{Ox}\ e^{j\omega t} + \Delta C^{*}_{Ox}\ e^{-j\omega t}$, where Δ denotes the Fourier transform and $*$ represents the complex conjugate [118]. The current response of the perturbation and the impedance can be described as:

$$\widetilde{i} = -nF\left[\frac{\partial r}{\partial \phi}\widetilde{\phi} + \frac{\partial r}{\partial C_{Ox}}\widetilde{C_{Ox}} + \frac{\partial r}{\partial C_{Red}}\widetilde{C_{Red}}\right] + C_{dl}\frac{\partial \widetilde{\phi}}{\partial t} \tag{2.65}$$

$$\frac{1}{Z(\omega)} = -nF\frac{\Delta r}{\Delta \phi} + C_{dl}\frac{\partial \Delta\phi}{\partial t} \tag{2.66}$$

The Fourier transform of a derivative ($\partial x(t)/\partial t$) is [126]:

$$\mathrm{FT}(\omega)\left[\frac{\partial x(t)}{\partial t}\right] = j\omega X(\omega) \tag{2.67}$$

where X is the FT of x. Equation. 2.66 can then be expressed as:

$$\frac{1}{Z(\omega)} = -nF\left[\frac{\partial r}{\partial \phi} + \frac{\partial r}{\partial \Delta C_{Ox}}\frac{\Delta C_{Ox}}{\Delta \phi} + \frac{\partial r}{\partial \Delta C_{Red}}\frac{\Delta C_{Red}}{\Delta \phi}\right] + j\omega C_{dl} \tag{2.68}$$

The mass balance of the reacting species can be described using the appropriate boundary conditions with the equations below [127]:

$$\frac{\partial \Delta C_{Ox}}{\partial t} = D_{Ox}\frac{\partial^2 \Delta C_{Ox}}{\partial x^2} \tag{2.69}$$

$$\frac{\partial \Delta C_{Red}}{\partial t} = D_{Red}\frac{\partial^2 \Delta C_{Red}}{\partial x^2} \tag{2.70}$$

At the electrode/electrolyte interface, the reaction rate can be described as [127]:

$$D_{C_{Ox}}\frac{\partial \Delta C_{Ox}}{\partial x}\bigg|_0 = \Delta r_1 \tag{2.71}$$

$$D_{C_{Red}}\frac{\partial \Delta C_{Red}}{\partial x}\bigg|_0 = -\Delta r_1 \tag{2.72}$$

$$\frac{\Delta r}{\Delta \phi} = -\frac{\Delta C_{Ox}}{\Delta \phi}\sqrt{j\omega D_{Ox}} \tag{2.73}$$

Equation 2.68 can thus be rewritten as:

$$\frac{1}{Z(\omega)} = nF\left[\frac{\Delta C_{Ox}}{\Delta \phi}\sqrt{j\omega D_{Ox}}\right] + j\omega C_{dl} \tag{2.74}$$

Solving for $\Delta C_{Ox}/\Delta\phi$ results to:

$$-\frac{\Delta C_{Ox}}{\Delta \phi}\sqrt{j\omega D_{Ox}} = \frac{\partial r}{\partial \Delta \phi} + \frac{\partial r}{\partial \Delta C_{Ox}}\frac{\Delta C_{Ox}}{\Delta \phi} + \frac{\partial r}{\partial \Delta C_{Red}}\frac{\Delta C_{Red}}{\Delta \phi} \tag{2.75}$$

$$\frac{\Delta C_{Red}}{\Delta \phi} = -\frac{\Delta C_{Ox}}{\Delta \phi}\sqrt{\frac{D_{Ox}}{D_{Red}}} \tag{2.76}$$

$$\frac{\Delta C_{Ox}}{\Delta \phi} = \frac{\dfrac{\partial r}{\partial \Delta \phi}}{\left[-\sqrt{j\omega D_{Ox}} - \dfrac{\partial r}{\partial \Delta C_{Ox}} + \dfrac{\partial r}{\partial \Delta C_{Red}}\sqrt{\dfrac{D_{Ox}}{D_{Red}}}\right]} \tag{2.77}$$

Substituting eq. 2.77 into eq. 2.74 leads to:

$$\frac{1}{Z(\omega)} = \frac{-nF\dfrac{\partial r}{\partial \Delta \phi}}{1 + \dfrac{1}{\sqrt{j\omega}}\left[\dfrac{\partial r}{\partial \Delta C_{Ox}}\dfrac{1}{\sqrt{D_O x}} - \dfrac{\partial r}{\partial \Delta C_{Red}}\sqrt{\dfrac{1}{D_{Red}}}\right]} + j\omega C_{dl} \tag{2.78}$$

The derivatives in the equation describing the impedance can be related to physical phenomena occurring in the electrochemical system such as charge transfer and the mass transport of the redox couple. The charge transfer resistance (R_{ct}) which describes the kinetic limitation of the charge transfer process and the Warburg impedance which describes the mass transport resistance of the redox species (Z_W) can be defined as:

$$R_{ct} = \left[-nF\frac{\partial r}{\partial \Delta \phi}\right]^{-1} \tag{2.79}$$

$$Z_W = \left[-nF\frac{\partial r}{\partial \Delta \phi}\right]^{-1}\frac{1}{\sqrt{j\omega}}\left[\frac{\partial r}{\partial \Delta C_{Ox}}\frac{1}{\sqrt{D_O x}} - \frac{\partial r}{\partial \Delta C_{Red}}\sqrt{\frac{1}{D_{Red}}}\right] \tag{2.80}$$

$$Z_C = [j\omega C]^{-1} \tag{2.81}$$

The impedance can then be rewritten as:

$$\frac{1}{Z(\omega)} = \frac{1}{R_{ct} + Z_W} + \frac{1}{Z_C} \tag{2.82}$$

The graphical representation of the impedance obtained from modelling a redox couple (eq. 2.78) is shown in Fig. 2.11.

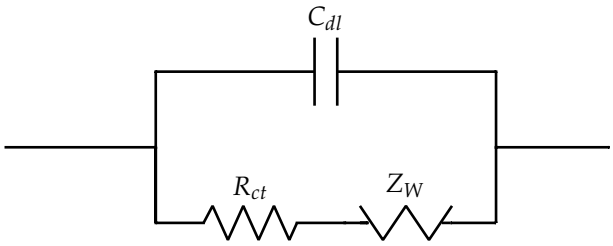

Figure 2.11: Graphical representation of the impedance obtained from modelling a redox couple.

If the impedance is measured in a three-electrode cell, the measured impedance is described with eq. 2.38, comprising of the uncompensated cell resistance (R_u) and the impedance of the redox couple (Fig. 2.11). The measured impedance can then be represented graphically as Fig. 2.12 which is commonly referred to as the Randles circuit.

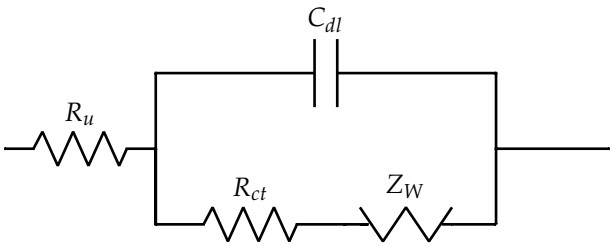

Figure 2.12: Graphical representation of the impedance obtained from modelling a redox couple assuming a three-electrode configuration.

2.9 Fitting Algorithm

In order to extract mechanistic information and kinetic parameters from the electrochemical system under investigation, the measured impedance is usually fitted with a model. This model as shown in the previous section should describe the physicochemical processes occurring at the interface. The model may be represented graphically with an equivalent circuit derived from the mathematical description of the system. The passive circuit elements in the equivalent circuit represents the physicochemical process occurring in the system. For example, the resistor (R_{ct}) in Fig. 2.12 represents the kinetic limitation of the transport of electrons between the redox couple in solution and the electrode. A common method of fitting impedance data is the complex nonlinear least squares (CNLS) regression technique. This is an extension of nonlinear least squares (NLS) as it offers the advantage of estimating a common set of parameters using the regression of the model to both real and imaginary data [127]. In the general form, the sum of squares can be

described as [127, 128]:

$$S_k = \sum_{m=1}^{N_{f,k}} \left\{ W'_m \left[Z'_{k,m}(\omega_m) - Z'_k(\omega_m, \bar{P}) \right]^2 + W''_m \left[Z''_{k,m}(\omega_m) - Z''_k(\omega_m, \bar{P}) \right]^2 \right\} \tag{2.83}$$

where $\bar{P}$ is the vector of the parameters and $N_{f,k}$ is the number of frequencies of the k-th impedance. $Z'_{k,m}$ and $Z''_{k,m}$ are the real and imaginary part of the measured impedance, while Z'_k and Z''_k are the real and imaginary part of the model. W'_m and W''_m represents statistical weighting factor for the real and imaginary part of the data [127]. Due to the fact that the absolute values of impedance changes in order of magnitude, the absolute values of the impedance is used as weighting factor. Thus, eq. 2.83 can be described as [127, 128]:

$$\chi^2_k = \frac{1}{N_{f,k}} \sum_{m=1}^{N_{f,k}} \frac{\left\{ [Z'_{k,m} - Z'_k(\omega_m, \bar{P})]^2 + [Z''_{k,m} - Z''_k(\omega_m, \bar{P})]^2 \right\}}{[Z'_{k,m}]^2 + [Z''_{k,m}]^2} \tag{2.84}$$

This objective function is suitable for fitting single impedance spectra. To fit impedance data obtained using DMFA (acquired during non-stationary process) an objective function which takes into account the time variation of the system was reported by Battistel et al. [129]:

$$\chi^2 = \sum_{k=1}^{N} \chi^2_k + \sum_{n=1}^{N_p} W_n^2 \sum_{k=1}^{N} \left[\frac{\partial^2 \bar{P}}{\partial t^2} \bigg|_{tk} \right]^2 \tag{2.85}$$

where W_n is the weighting factor, which allows for the variation of parameters to be controlled [118, 121]. for $W_n = 0$, the parameters are allowed to develop freely and for $W_n =$ infinity, the parameters are fixed. The term $\partial^2 \bar{P} / \partial t^2$ allows for the minimization of the smoothing parameter, resulting in the variation of the parameters to change smoothly [121].

Chapter 3

Experiment and Method

In this section of the thesis, the experiments and method used in this work will be described in details. It includes: the electrodeposition of nickel hexacyanoferrate thin film, synthesis for nickel hexacyanoferrate nanoparticles, brief introduction into the operating principle of the structural characterization method (X-ray diffraction and scanning electron microscopy), the electrochemical setup, electrochemical characterization, data acquisition method and data analysis.

3.1 Electrodeposition of Nickel Hexacyanoferrate Thin Film

Thin films of nickel hexacyanoferrate were electrodeposited using the cathodic deposition technique reported by Bacskai et al. on a 1 mm diameter glassy carbon electrode (GCE) [141]. Prior to the electrodeposition, the electrodes were polished using 0.250 μm and 0.1 μm polishing pads (Struers) with the corresponding diamond suspension (Struers) on a polishing machine with 300 rpm. The electrodes were then sonicated in water to remove any diamond suspension left on the electrode surface and electrochemical cleaning was done by sweeping of the 1 mm GCE in a 1 M H_2SO_4 from 1.5 V to -0.250 V vs Ag/AgCl using a scan rate of 25 mVs^{-1}. The cleaned 1 mm GCE was then cycled in a freshly prepared solution containing 2 mM $K_3Fe(CN)_6$ (Sigma-Aldrich), 2 mM $NiSO_4$ (Sigma-Aldrich) and 0.5 M K_2SO_4 (Sigma-Aldrich) until a stable voltammogram was obtained.

3.2 Synthesis of Nickel Hexacyanoferrate

Nickel hexacyanoferrate nanoparticles were synthesized using the co-precipitation method reported by Trócoli et al. [53]. The synthetic procedure involves the simultaneous addition of 120 ml of 50 mM of $K_3Fe(CN)_6$ and 120 ml of 100 mM of $Ni(NO_3)_2$ using a flow-rate of 1 ml per minute to 60 ml of distilled water held at 70°C in water bath while stirring constantly [53]. The resultant solution was sonicated for 30 minutes at 70°C and left overnight to precipitate. The precipitates

were washed with distilled water and dried for 12 hours at 60°C . The resulting material was then pulverized using laboratory mortal and stored in desiccator.

3.3 Preparation of Slurries

Slurries were prepared using a weight ratio of 80:10:10 of the synthesized NiHCF, carbon C65 (Timcal, Bodio Switzerland) which serve as a conductive additive and polyvinylidene fluoride (PVDF) solution in N-methyl-2-pyrrolidone (NMP) (Solef S5130, Solvay) which acts as a binder. The slurries were stirred with an ultra Turrax mixer (IKA) for 30 minutes using a 10 minutes stirring and a 10 minutes rest period sequence.

3.4 Electrode Preparation

The NiHCF nanoparticles electrode used for the electrochemical characterizations were prepared by doctor blading NiHCF slurries with a 200 μm doctor blade on a 3 mm Glassy carbon electrode (GCE). The electrodes were dried at 60°C for 12 hours. Before doctor blading, the electrode was polished using a 2000 grit sandpaper using a polishing machine at 400 rpm. The electrodes were dried at 60°C for 12 hours.The electrode was further polished using 0.250 μm and 0.1 μm polishing pads (Struers) with the corresponding diamond suspension (Struers) on a polishing machine with 300 rpm. The electrode was rinsed with distilled water and then sonicated to remove any diamond suspension left on the electrode surface.

3.5 Structural and Morphological Characterization

3.5.1 X-ray Diffraction

X-ray diffraction (XRD) was used for structural characterization of the synthesized materials studied in this work. It is a non-destructive technique based on the constructive interference of monochromatic X-rays and a crystalline sample. Crystalline materials consists of atoms with an interatomic spacings in the order of a 100 pm or 1 Å [142]. The technique involves the bombardment of the sample with accelerated X-rays with wavelengths in the same order of magnitude as the spacings of the atoms which are produced by the application of a high voltage. Constructive interference is produced when Bragg's law is fulfilled ($n\lambda = 2dsin(\vartheta)$) [142]. X-ray diffractometer works by generating accelerating electrons from x-rays with sufficient energy which are produced by heating a metal filament. The electrons are accelerated by an applied voltage to bombard the

target sample which in turn generates characteristic X-ray spectra with peaks of various intensity. The detector in the XRD diffractometer records and converts the output X-ray signals into a count rate which can be printed.

3.5.2 Scanning Electron Microscopy

Scanning electron microscopy (SEM) was employed for the morphological characterization of the studied cathode materials. The working principle of SEM can be summarized as the scanning of the sample with a beam of electrons generated by an electron source.

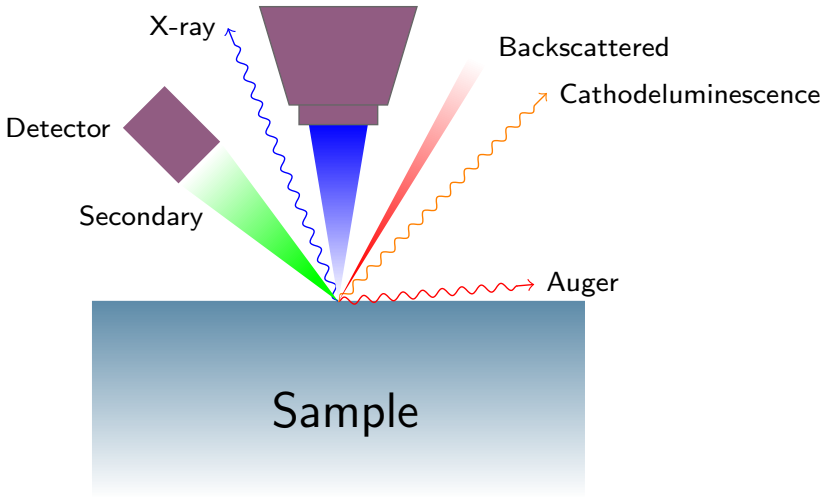

Figure 3.1: Simple schematics of scanning electron microscopy (SEM) set-up illustrating the working principle. Adapted from [143].

The electron sources accelerates the electrons through a high accelerating voltage in the range of 1—30 keV. The beam of electrons then passes through a series of lenses (condenser and objective lenses), which focuses the beam to produce a thin beam of electrons. This thin beam of electrons is used by scanning coils for scanning the surface of the sample which is held in vacuum (10^{-4} Pa). The resultant electrons (scattered primary electrons, secondary electrons and X-rays) from the sample are then collected by their respective detectors [144–146]. Scattered primary electrons are generated by the scattering of the incident electron beam through the sample at an angle of 90° to 180° and secondary electrons are created by primary electron-matter interactions between the negative primary electrons and the atomic nuclei of the sample. X-rays with specific energies were generated by interaction of source X-rays with the sample due to the changes in the energy states of the constituent atoms of the sample [144]. The emitted X-rays with specific energies are then measured by energy-dispersive spectrometer. The elemental composition of the sample can then

be analyzed as energies of X-rays are characteristics of the emitting element. The SEM image with the sample shape (surface topography) and the sample composition is created from the scattered primary electrons and the secondary electrons [144, 147].

3.6 Electrochemical Setup

The electrochemical characterization of the cathode materials studied in this work were carried out in an optimized three-electrode cell configurations for impedance spectroscopy reported by Battistel et al. [129].

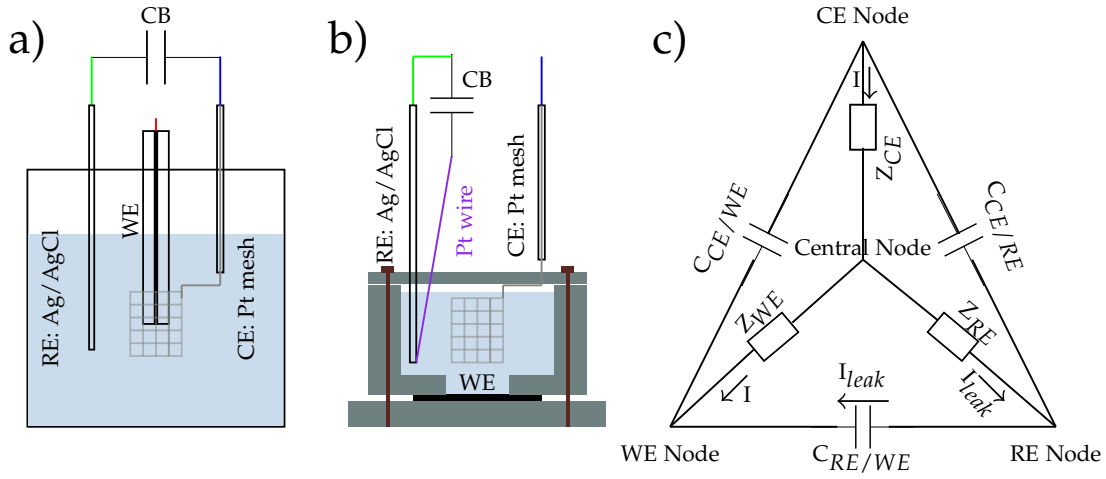

Figure 3.2: Schematics of the electrochemical set-up used for the characterization of (a) NiHCF thin films and NiHCF nanoparticles (b) $LiMn_2O_4$ thin films, (c) Circuit of the electrochemical setup. Adapted from [129].

The configurations consists of the working electrode (WE), a platinum mesh (Labor Platina) which serves as the counter electrode (CE) and a home-made Ag/AgCl (3M KCl) as the reference electrode (RE). As previously reported, these configurations minimize artefacts arising cell geometry which is a common problem when working with impedance spectroscopy [129]. The advantages of these configurations include reduced electrolyte IR drop, reproducible impedance, minimization of the current density distribution [129]. The cell geometry depicted in Fig 3.2a was used in the electrodeposition and characterization of NiHCF thin films and the characterization of NiHCF nanoparticles, while the geometry in Fig 3.2b was used in studying the $LiMn_2O_4$ thin films. Artefacts which manifest as a high frequency arc, was circumvented by using a 100 nF capacitive bridge (CB) as depicted in Fig. 3.2. This high frequency arc has been reported to occur in the presence of WE — RE stray capacitance when the impedance of the RE is non-negligible [129]. This stray capacitance is due to voltage drop in the Z_{RE} when there is a leaking current flow-

ing into the RE node toward the WE node as depicted in the electrochemical cell schematics in Fig. 3.2c [129]. The use of a capacitive bridge between the CE and WE increases the capacitive coupling between these nodes resulting in current from the CE node balancing the leaking current in the RE node. For the electrochemical characterization of $LiMn_2O_4$, a capacitively-coupled low-impedance Ag/AgCl (3M KCl) reference electrode was used to circumvent high frequency artefacts arising from series resistance of the RE. In this case the series resistance of the Ag/AgCl (3M KCl) was ca. 1.2 kΩ. By using the capacitively-coupled low-impedance RE fabricated by coiling 0.1 mm platinum wire around the tip of the reference electrode and connecting it through a 100 nF capacitor to the Ag/AgCl (3M KCl), the resistance of the RE was reduced to 20 Ω eliminating possible artefacts.

3.7 Measurement of Stray Capacitance and Transimpedance of Potentiostat

The instrumental artefacts caused by the non-ideal behaviour of the components of potentiostat (operational amplifiers, I/E converter and stray capacitance) were investigated in this work. To measure the stray capacitance and the transimpedance of the potentiostat, high precision resistors were used in a two-electrode cell configuration. The impedance of the resistors were measured using a multisine wave with a base frequency of 1 Hz covering five decades corresponding to the impedance been measured between 1 MHz to 8 Hz. The amplitude of the multisine was scaled with the resistors been measured to avoid errors due to current-voltage amplification. An amplitude of 100 mVpp was used for the equivalent resistor (R_m) of the current range and the amplitude used for other resistors was scaled by the ratio of the resistor to R_m of the current range. The bandwidth of the I/E converter of the potentiostat was measured by measuring the resistor scaled to the R_m of the current range i.e. for the 100 mA current range, a 10 Ω was used and for 1 μA current range, a 1 MΩ was used.

3.8 Electrochemical Characterization

Electrochemical characterizations in this thesis were done in a two or three-electrode setup using Bio-Logic SP300 potentiostat. To measure dynamic impedance using DMFA the potentiostat was connected to a 33512b waveform generator (Keysight) and dual channel oscilloscope. Fig. 3.3 shows a simplified schematics of the instrumental setup used in the acquisition of dynamic impedance using DMFA in this thesis. The WE is held at a predetermined potential (E_h)

and then polarized with a combination of the quasi triangular wave and the multisine wave. The multisine wave comprises of frequencies selected with the criteria reported in section 2.7. The quasi-triangular wave is used due to its fast dropping of the voltage perturbation skirts compared to the classic triangular wave as shown in section 2.7.

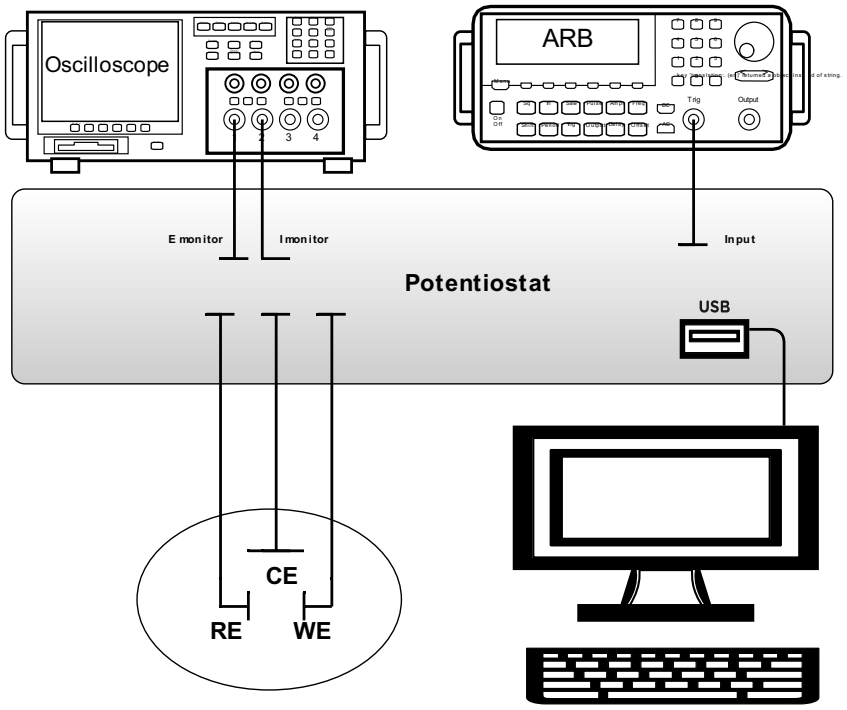

Figure 3.3: Schematics of the instrumental set up for dynamic multi-frequency analysis as used in this thesis.

The frequency of the quasi-triangular wave (f_{dc}) and its amplitude (ΔU_{dc}) were selected depending on the potential window under study and the intended scan rate. The lowest frequency of the multisine was chosen to avoid interference of the skirts of the dc component with the lowest frequencies of the multisine. This was done by looking at the discrete Fourier transform of the the voltage perturbation and the current response of the system and selecting the lowest frequency of the multisine in a way that it does interfere with the skirt of the dc component. The amplitude of the multisine (ΔU_{ac}) used depended on the system been characterized and was selected to enable the acquisition of high quality impedance spectra, while maintaining the linearity of the electrochemical system. Summary of the parameters used for each cathode material studied in this work is shown in table 3.1.

Parameters	NiHCF thin film	NiHCF nanoparti-cles	$LiMn_2O_4$	redox couple
E_h (V)	0.1	0.0*	0.4	0.25
f_{dc} (mHz)	125	5	10	50
ΔU_{dc} (mVpp)	400	400	400	250
f_{ac} (Hz)	1.25	0.35	0.5	1
ΔU_{ac} (mVpp)	175	50	100	50
No of sample ($\cdot 10^6$)	10	400	400	200
sample rate (μs)	1	1	0.5	0.2
current range (mA)	1	100**	100	1***
bw (Hz)	5	1	0.175	2

* The holding potential (E_h) was 0.0 V for Na^+ and 0.1 V for K^+ .

** The current range for NiHCF powder depended on the concentration of the electrolyte. 100 mA was used for 500 mM and 250 mM solutions while 10 mA was used for 100 mM and 50 mM solution.

*** 10 mA current range was also used to investigate the effect of choosing the current range as a compromise between the d.c signal and impedance been acquired. For more details see section 5.7.2.

Table 3.1: Table of the parameters used in the dynamic multi-frequency analysis of different cathode materials studied in this work.

3.9 Effect of the Intensity of the Multisine

The role of the nonlinear response on the noise level of the impedance spectra was investigated. The current response contains in addition to the fundamental harmonics, the nonlinear harmonics related to the fundamental harmonics. The dc component is influenced by the first order harmon-

ics while the fundamental harmonic is influenced by the second order harmonics [119]. The signal-to-noise ratio relative to the nonlinear component (R_k) of the response of the fundamental frequency can be described as [119]:

$$R_k = \frac{1}{\Delta U_{ac}^2} \frac{C_k}{\mid Z(\omega_k) \mid} \tag{3.1}$$

$$C_k = \sum_j \frac{\mid A'(\omega_k, \omega_j) \mid}{A_j^2} \tag{3.2}$$

where ΔU_{ac} denotes the amplitude of the multisine signal, A' is the second order harmonic response and A_j is the intensity of the fundamental harmonics at frequency f_j. ω_k and ω_j are the k-th and j-th frequency of the multisine signal [119]. Equation 3.1 can be rewritten as:

$$\frac{1}{Z(\omega_k)} = \Delta U_{ac}^2 \frac{R_k}{C_k} \tag{3.3}$$

Equation 3.3 allows for R_k to be estimated from the slope of admittance ($1/Z(\omega_k)$) acquired at different intensity versus ΔU_{ac}^2. The error due to the nonlinear component at the intensity used in the acquisition of the impedance can then be described as:

$$Error = \frac{R_k}{Y_0} \Delta U_{ac}^2 \tag{3.4}$$

where Y_0 is the intercept of the plot $1/Z(\omega_k)$ versus ΔU_{ac}^2. The result obtained for dynamic impedance of the redox couple using a multisine intensity of 50 mVpp and for NiHCF nanoparticles using a multisine intensity of 50 mVpp is shown in Fig. 3.4.

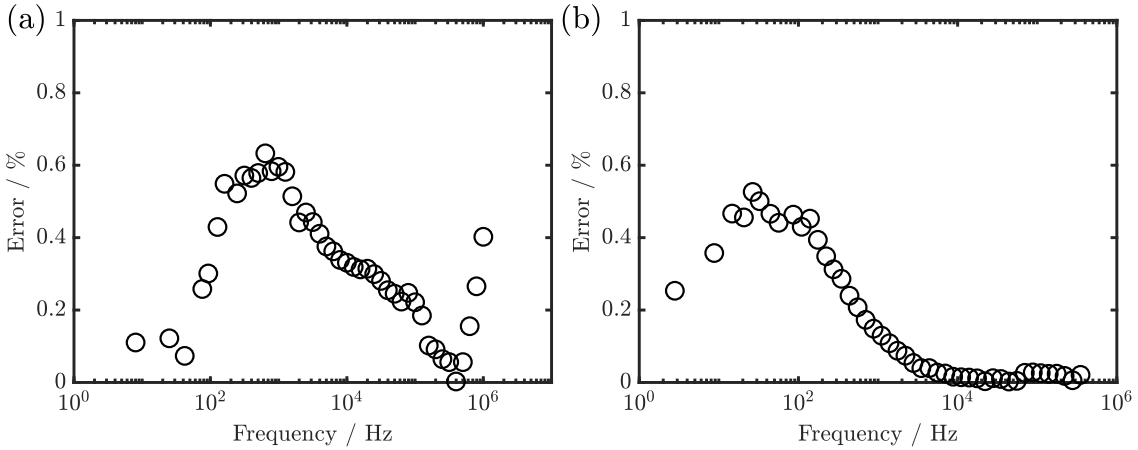

Figure 3.4: Plot of the estimated error due to the nonlinear component of the fundamental frequencies of dynamic impedance acquired using a multisine intensity of 50 mVpp in (a) $[Fe(CN)_6]^{3-/4-}$ redox couple (b) nickel hexacyanoferrate nanoparticles.

The result indicates that the error introduced by the nonlinear components at the intensity of the multisine used in acquiring the dynamic impedance in both cases were less than 1%. This suggests no significant changes in the measured impedance due to nonlinear components are present. In both cases, a multi-sine intensity of 50 mVpp is a good trade off between signal intensity and error arising from the nonlinear components. For NiHCF thin film and $LiMn_2O_4$ film a different approach was employed in checking the influence of the nonlinear components. The approach involves checking for the nonlinear components in the discrete Fourier transform of the current response of the system.

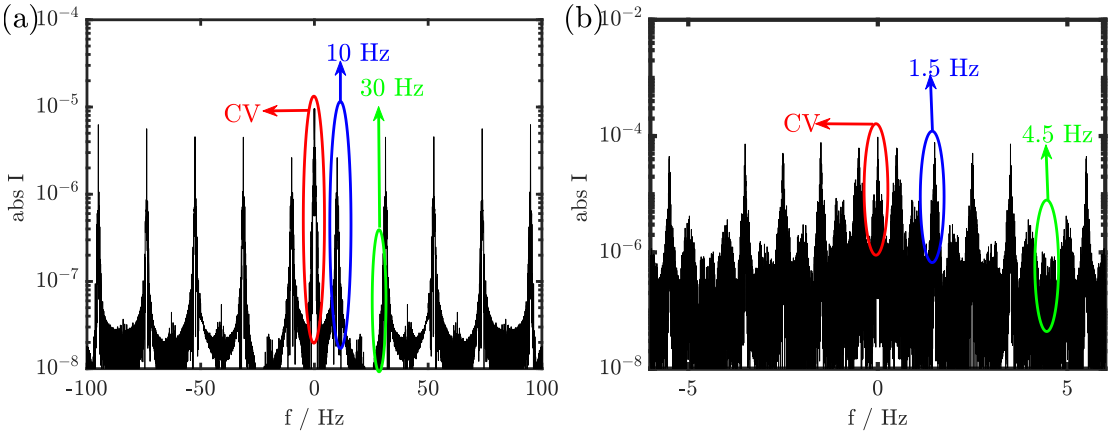

Figure 3.5: Discrete Fourier transform of (a) current response of NiHCF film highlighting the first frequency of the multisine at 10 Hz and the negligible second order harmonics at 30 Hz indicating that the system is linear with the a multisine amplitude of 175 mVpp (b) current response of 200 nm $LiMn_2O_4$ thin film highlighting the first frequency of the multisine at 1.5 Hz and the negligible second order harmonics at 4.5 Hz indicating that the system is linear with a multisine amplitude of 100 mVpp.

The DFT of the current response indicates that the system is linear within the intensity of the multisine used due to the negligible intensity of the second order harmonic (green eclipse) in the DFT of the current response shown in Fig. 3.5

3.10 Data Analysis

The acquired data were analyzed using a home-made MATLAB script. For non-periodic data set (NiHCF thin film), the mirroring method explained in section 2.7 was used to avoid the distortions associated with non-periodic data set in DMFA. Using the quadrature filter function described in eq. 2.57 with *bw* (see table 3.1) the dc and ac component were extracted and the dynamic impedance was calculated using eq. 2.48 with a home-made MATLAB script. For easy handling of the data, the amount of impedance was reduced to 4000 spectra by increasing the sampling interval during the data analysis. Artefacts which can arise from instrumental set-up occurring at

high frequencies were corrected using the method proposed in chapter 5. 100 spectra for cathodic and 100 spectra for the anodic scan were then fitted using the corresponding model of the system with the modified nonlinear square method described in section 2.9.

3.11 Statistical Analysis

To avoid over parametrization of the model (equivalent circuit) with physicochemical processes which are negligible or processes which occur outside the frequency range used in the acquisition of measured impedance, the results obtained from fitting was subjected to statistical analysis using student *t*-test. The *t*-value is described as [121]:

$$t = \frac{\hat{x}}{\sigma_{\bar{x}}} \tag{3.5}$$

where $\hat{x}$ is the estimated parameters from the fit of the measured impedance and the model and $\sigma_{\bar{x}}$ is the absolute standard error of the parameters obtained from the formal covariance matrix of χ^2 minimization [121]. The *t*-values was compared to cumulative t-distribution for n-1 degrees of freedom with a confidence level of 95% [121]. When one or more parameters are below the confidence level, the one with the least t value is removed from the circuit. The removal of the parameter is then connected to a physical assumption. The new model (equivalent circuit) obtained without the parameter is used to fit the measured impedance and the result is again subjected to the t-test. This process is repeated until all the remaining parameters in the model (equivalent circuit) are above the confidence level.

Chapter 4

Modelling Impedance of the Reversible Insertion Process

Electrochemical impedance spectroscopy has been reported as a powerful technique in extraction of kinetic parameters and transport properties of electrode materials [82, 148–152]. It is also widely used in studying the aging mechanism of electrode materials [153–155]. Impedance is often interpreted using equivalent circuits, where electrochemical phenomena are represented by passive circuit elements such resistors, capacitors and inductors. The use of arbitrary equivalent circuits in the interpretation of impedance of an electrochemical system results in the extraction of kinetic parameters with no direct physical meaning. Equivalent circuit with same number of time constants tend to have same frequency response. Thus, a spectra can be fitted with multiple equivalent circuits with similar time constants [156]. A good fit (low χ^2) obtained using the complex linear regression analysis does not necessarily validate an arbitrary model as this may arise from over-parametrization [156, 157]. A better approach to the arbitrary selection of equivalent circuit, is the development of models for the impedance response [156, 157]. These models are obtained starting from reaction sequences detailing the physicochemical phenomena in each sequence. In this chapter, impedance model describing the kinetics of reversible insertion of cations in solid host structure is presented.

4.1 Development of Impedance Model

The reversible insertion of cations in aqueous media has been reported as a two step process with the first step as (de)solvation step which is followed by the (de)insertion step [158, 159]:

$$A_e^+ \rightleftharpoons A_i^+ \tag{4.1}$$

$$A_i^+ + [\ ] + e^- \rightleftharpoons [A] \tag{4.2}$$

where the subscript letters ε and i denotes the electrolyte phase and the adsorbed phase respectively. [ ] represents the empty intercalation sites and $[A]$ represents the occupied intercalation sites . The potential drop across the interface can be described using the equations below:

$$\phi_1 = \phi_i - \phi_\varepsilon \tag{4.3}$$

$$\phi_2 = \phi_T - \phi_1 \tag{4.4}$$

where ϕ_1, ϕ_2, and ϕ_T represents the potential drop due to the (de)solvation step, potential drop due to the (de)insertion step and total potential drop across the electrode/electrolyte interface respectively. The current-potential relation can be described as:

$$i_T = -Fr_1 + C_1\frac{\partial\phi_1}{\partial t} = -Fr_2 + C_2\frac{\partial\phi_2}{\partial t} \tag{4.5}$$

where r_1 and r_2 represents the rate of reaction for the (de)solvation step and (de)insertion step respectively while C_1 and C_2 denotes the capacitance of the outer and inner Helmholtz plane respectively. The rate of the formation of the ad-ion can be described as the difference between the two reaction rates:

$$N_{ad}\frac{\partial\beta}{\partial t} = r_1 - r_2 \tag{4.6}$$

where N_{ad} is the maximum number of adsorption site, and β represents the molar fraction of the adsorption sites. The effect of the ad-ion on ϕ_1 is given by:

$$\phi_1 = \frac{F\beta N_{ad}}{C_1 + C_2} + \frac{C_2}{C_1 + C_2}\phi_T \tag{4.7}$$

The current-potential relation can then be rewritten as:

$$i_T = -F\frac{C_2}{C_1 + C_2}r_1 - F\frac{C_1}{C_1 + C_2}r_2 + \frac{C_1 \cdot C_2}{C_1 + C_2}\frac{\partial\phi_T}{\partial t} \tag{4.8}$$

$$\gamma = \frac{C_1}{C_1 + C_2} \tag{4.9}$$

$$C_{dl} = \frac{C_1 \cdot C_2}{C_1 + C_2} \tag{4.10}$$

$$i_T = -F(1-\gamma)r_1 - F\gamma r_2 + C_{dl}\frac{\partial\phi_T}{\partial t} \tag{4.11}$$

Using the treatment introduced in section 2.8, the impedance can be described in terms of the Fourier transform of the oscillating variables denoted with Δ as:

$$\frac{1}{Z(\omega)} = \frac{\Delta i_T}{\Delta \phi_T} = -F(1-\gamma)\frac{\Delta r_1}{\Delta \phi_T} - F\gamma\frac{\Delta r_2}{\Delta \phi_T} + j\omega C_{dl} \tag{4.12}$$

The mass balance of the reacting species can be described using the appropriate boundary conditions with the equations below:

$$\frac{\partial \Delta C_{A_\varepsilon}}{\partial t} = D_{A_\varepsilon}\frac{\partial^2 \Delta C_{A_\varepsilon}}{\partial x^2} \tag{4.13}$$

$$-D_{A_\varepsilon}\frac{\partial \Delta C_{A_\varepsilon}}{\partial x}\bigg|_0 = -\Delta r_1 \tag{4.14}$$

$$\frac{\partial \Delta \theta}{\partial t} = D_\theta\frac{\partial^2 \Delta \theta}{\partial x^2} \tag{4.15}$$

$$-D_\theta\frac{\partial \Delta \theta}{\partial x}\bigg|_0 = \Delta r_2 \tag{4.16}$$

where D_{A_ε} and D_θ is the diffusion coefficient of the cation in solution and in the solid respectively. Solving the Fick's diffusion for ΔC_{A_ε} and $\Delta\theta$ using semi-infinite and finite length diffusion with a reflective boundary respectively leads to [127]:

$$\frac{\Delta r_1}{\Delta \phi_T} = -\frac{\Delta C_{A_\varepsilon}}{\Delta \phi_T}\sqrt{j\omega D_{A_\varepsilon}} \tag{4.17}$$

$$\frac{\Delta r_2}{\Delta \phi_T} = \frac{\Delta \theta}{\Delta \phi_T}\sqrt{j\omega D_\theta}\tanh\left(\sqrt{j\omega\tau}\right) \tag{4.18}$$

where τ is the diffusion time constant. The reaction rates for the (de)solvation and (de)insertion step can then be described as:

$$\frac{\Delta r_1}{\Delta \phi_T} = -\frac{\partial r_1}{\partial \Delta \phi_1}[1-\gamma] + \left[\frac{\partial r_1}{\partial \beta} - \frac{\partial r_1}{\partial \Delta \phi_1}\cdot\frac{N_{ad}}{C_1+C_2}\right]\frac{\Delta \beta}{\Delta \phi_T} + \frac{\partial r_1}{\partial C_{A_\varepsilon}}\frac{\Delta C_{A_\varepsilon}}{\Delta \phi_T} \tag{4.19}$$

$$\frac{\Delta r_2}{\Delta \phi_T} = -\frac{\partial r_2}{\partial \Delta \phi_2}\gamma + \left[\frac{\partial r_2}{\partial \beta} + \frac{\partial r_2}{\partial \Delta \phi_2}\cdot\frac{N_{ad}}{C_1+C_2}\right]\frac{\Delta \beta}{\Delta \phi_T} + \frac{\partial r_2}{\partial \theta}\frac{\Delta \theta}{\Delta \phi_T} \tag{4.20}$$

The adsorption resistance R_{ad} which describes the kinetic limitation of the (de)solvation of the cations can be defined as $(-F\cdot\partial r_1/\partial\phi_1)^{-1}$ and the charge transfer resistance (R_{ct}) which describes the kinetic limitation due to the further (de)solvation of the ad-ion and transfer of the desolvated ion across the interface can be described as $(-F\cdot\partial r_2/\partial\phi_2)^{-1}$, therefore allowing equation 4.19 and 4.20 to be expressed as:

$$\frac{\Delta r_1}{\Delta \phi_T} = -\frac{[1-\gamma]}{FR_{ad}} + \frac{\partial r_1}{\partial C_{A_\varepsilon}}\frac{\Delta C_{A_\varepsilon}}{\Delta \phi_T} + \left[\frac{\partial r_1}{\partial \beta} - \frac{1}{R_{ad}}\cdot\frac{N_{ad}}{C_1+C_2}\right]\frac{\Delta \beta}{\Delta \phi_T} \tag{4.21}$$

$$\frac{\Delta r_2}{\Delta \phi_T} = -\frac{\gamma}{FR_{ct}} + \frac{\partial r_2}{\partial \theta}\frac{\Delta \theta}{\Delta \phi_T} + \left[\frac{\partial r_2}{\partial \beta} + \frac{1}{R_{ct}}\cdot\frac{N_{ad}}{C_1+C_2}\right]\frac{\Delta \beta}{\Delta \phi_T} \tag{4.22}$$

Substituting equation 4.17 and 4.18 into equation 4.21 and 4.22 results to

$$\sqrt{j\omega D_{A_\varepsilon}}\frac{\Delta C_{A_\varepsilon}}{\Delta\phi_T} = \frac{[1-\gamma]}{FR_{ad}} - \frac{\partial r_1}{\partial C_{A_\varepsilon}}\frac{\Delta C_{A_\varepsilon}}{\Delta\phi_T} - \left[\frac{\partial r_1}{\partial\beta} - \frac{1}{R_{ad}}\cdot\frac{N_{ad}}{C_1+C_2}\right]\frac{\Delta\beta}{\Delta\phi_T} \tag{4.23}$$

$$\sqrt{j\omega D_\theta}\tanh\left(\sqrt{j\omega\tau}\right)\frac{\Delta\theta}{\Delta\phi_T} = -\frac{\gamma}{FR_{ct}} + \frac{\partial r_2}{\partial\theta}\frac{\Delta\theta}{\Delta\phi_T} + \left[\frac{1}{R_{ct}}\cdot\frac{N_{ad}}{C_1+C_2} + \frac{\partial r_2}{\partial\beta}\right]\frac{\Delta\beta}{\Delta\phi_T} \tag{4.24}$$

The derivatives of the reaction rates were related to physical phenomena through the equations below:

$$Z_{Wad} = \left[-F\frac{\partial r_1}{\partial\phi_1}\right]^{-1}\frac{\partial r_1}{\partial C_{A_\varepsilon}}\frac{1}{\sqrt{j\omega D_{A_\varepsilon}}} \tag{4.25}$$

$$\frac{1}{C_{ad}} = \left[F\frac{\partial r_1}{\partial\phi_1}\right]^{-1}\frac{\partial r_1}{\partial\beta}\frac{1}{N_{ad}} \tag{4.26}$$

$$Z_{Wct} = \left[F\frac{\partial r_2}{\partial\phi_2}\right]^{-1}\frac{\partial r_2}{\partial\theta}\frac{1}{\sqrt{j\omega D_\theta}\tanh\left(\sqrt{j\omega\tau}\right)} \tag{4.27}$$

$$\frac{1}{C_{int}} = \left[-F\frac{\partial r_2}{\partial\phi_2}\right]^{-1}\frac{\partial r_2}{\partial\beta}\frac{1}{N_{ad}} \tag{4.28}$$

where Z_{Wad} denotes the Warburg impedance of the cation in the electrolyte which describes the mass transport limitation of the cation in the electrolyte phase and C_{ad} is the capacitance of the adsorbed layer. Z_{Wct} is Warburg impedance of the cation in the solid which describes the mass transport in the solid and (C_{int}) capacitance of the double layer due to the insertion reaction. Using the above descriptions equation 4.23 and equation 4.24 can be rewritten as:

$$\sqrt{j\omega D_{A_\varepsilon}}\frac{\Delta C_{A_\varepsilon}}{\Delta\phi_T} = \frac{\frac{[1-\gamma]}{F} - \left(\frac{1}{C_{ad}} + \frac{1}{C_1+C_2}\right)\sqrt{\frac{D_\theta}{j\omega}}\tanh\left(\sqrt{j\omega\tau}\right)\frac{\Delta\theta}{\Delta\phi_T}}{\left[R_{ad} + Z_{Wad} + \frac{1}{j\omega C_{ad}} + \frac{1}{C_1+C_2}\frac{1}{j\omega}\right]} \tag{4.29}$$

$$\frac{\Delta\beta}{\Delta\phi_T} = \frac{-\frac{1}{N_{ad}}\frac{1}{j\omega}\frac{[1-\gamma]}{F} - \frac{1}{N_{ad}}\sqrt{\frac{D_\theta}{j\omega}}\tanh\left(\sqrt{j\omega\tau}\right)[R_{ad}+Z_{Wad}]\frac{\Delta\theta}{\Delta\phi_T}}{\left[R_{ad} + Z_{Wad} + \frac{1}{j\omega C_{ad}} + \frac{1}{C_1+C_2}\frac{1}{j\omega}\right]} \tag{4.30}$$

$$\begin{aligned}\sqrt{j\omega D_\theta}\tanh\left(\sqrt{j\omega\tau}\right)\frac{\Delta\theta}{\Delta\phi_T} &= \\ &= \frac{-\frac{\gamma}{F}\left[R_{ad} + Z_{Wad} + \frac{1}{j\omega C_{ad}} + \frac{1}{C_1+C_2}\frac{1}{j\omega}\right] - \frac{[1-\gamma]}{F}\left(\frac{1}{C_{int}}\frac{1}{j\omega} + \frac{1}{C_1+C_2}\frac{1}{j\omega}\right)}{(R_{ct}+Z_{Wct})(R_{ad}+Z_{Wad}) + \left(\frac{R_{ct}+Z_{Wct}}{C_{ad}} + \frac{R_{ad}+Z_{Wad}}{C_{int}}\right)\frac{1}{j\omega} + \left(\frac{R_{ct}+Z_{Wct}+R_{ad}+Z_{Wad}}{C_1+C_2}\right)\frac{1}{j\omega}}\end{aligned} \tag{4.31}$$

$$\sqrt{j\omega D_{A_\varepsilon}}\frac{\Delta C_{A_\varepsilon}}{\Delta\phi_T} = \\ = \frac{\frac{(1-\gamma)}{F}\left[R_{ct}+Z_{Wct}+\frac{1}{j\omega C_{int}}+\frac{1}{C_1+C_2}\frac{1}{j\omega}\right]+\frac{1}{j\omega}\left(\frac{1}{C_{ad}}+\frac{1}{C_1+C_2}\right)\frac{\gamma}{F}}{(R_{ct}+Z_{Wct})(R_{ad}+Z_{Wad})+\left(\frac{R_{ct}+Z_{Wct}}{C_{ad}}+\frac{R_{ad}+Z_{Wad}}{C_{int}}\right)\frac{1}{j\omega}+\left(\frac{R_{ct}+Z_{Wct}+R_{ad}+Z_{Wad}}{C_1+C_2}\right)\frac{1}{j\omega}} \quad (4.32)$$

The impedance of the system can thus be defined as:

$$\frac{1}{Z(\omega)} = \frac{\gamma^2(R_{ad}+Z_{Wad})+(1-\gamma)^2(R_{ct}+Z_{Wct})+\left(\frac{\gamma}{C_{ad}}+\frac{(1-\gamma)}{C_{int}}\right)\frac{1}{j\omega}+\left(\frac{1}{C_1+C_2}\right)\frac{1}{j\omega}}{(R_{ct}+Z_{Wct})(R_{ad}+Z_{Wad})+\left(\frac{R_{ct}+Z_{Wct}}{C_{ad}}+\frac{R_{ad}+Z_{Wad}}{C_{int}}\right)\frac{1}{j\omega}+\left(\frac{R_{ct}+Z_{Wct}+R_{ad}+Z_{Wad}}{C_1+C_2}\right)\frac{1}{j\omega}}+j\omega C_{dl} \quad (4.33)$$

At equilibrium, $C_{ad} \approx C_{int}$ (see section A.1 in appendix), the impedance of the system can then be rewritten as:

$$\frac{1}{Z(\omega)} \approx \frac{\gamma^2(R_{ad}+Z_{Wad})+(1-\gamma)^2(R_{ct}+Z_{Wct})+\left(\frac{1}{j\omega C_{ad}}+\frac{\gamma(1-\gamma)}{j\omega C_{dl}}\right)}{(R_{ct}+Z_{Wct})(R_{ad}+Z_{Wad})+(R_{ct}+Z_{Wct}+R_{ad}+Z_{Wad})\left(\frac{1}{j\omega C_{ad}}+\frac{\gamma(1-\gamma)}{j\omega C_{dl}}\right)}+j\omega C_{dl} \quad (4.34)$$

Fig. 4.2 represents the equivalent circuit obtained from equation 4.34 using the nodal method.

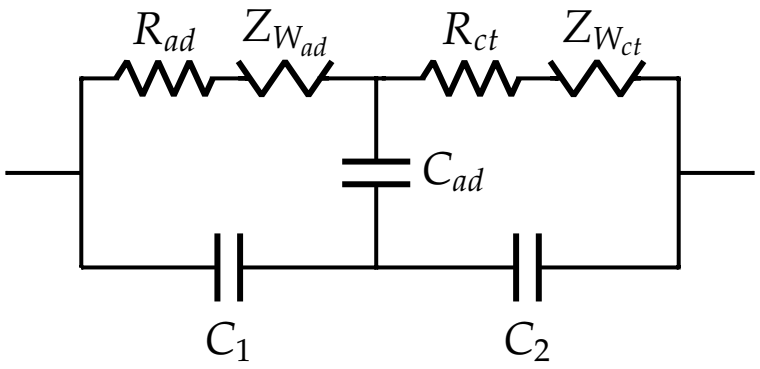

Figure 4.1: Schematic representation of the equivalent circuit obtained from modelling the reversible insertion process as a two-step process.

As the electrode materials studied in this work were all porous, the simplified transmission line model (TLM) for describing cylindrical pores was used in this work [157]. Using the TLM model, the impedance of the working electrode $Z_{WE}(\omega)$:

$$Z_{WE}(\omega) = R_p\left[\frac{\coth(\kappa d)}{\kappa d}\right] \quad (4.35)$$

where R_p is the resistance of the pores, κd corresponds to the impedance of single reacting sites (Z) described as [157]:

$$\kappa d = \sqrt{\frac{R_p}{Z}} \quad (4.36)$$

The graphical representation of the impedance of the TLM model including the circuit obtained from modelling the reversible insertion process as a two-step process is shown in Fig. 4.2.

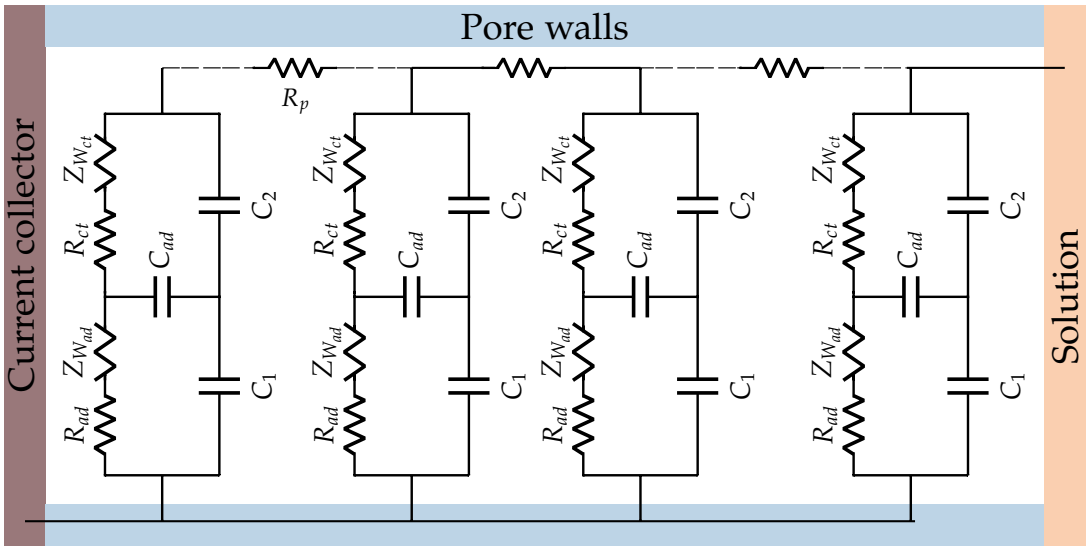

Figure 4.2: Equivalent circuit of the porous electrode, including the impedance describing the reaction at the surface.

4.2 Theoretical Description of Adsorption Resistance and Charge Transfer Resistance

The rate of the (de)solvation and (de)insertion step can be described as:

$$r_1 = k_{f,1} C_{A_\varepsilon} [1 - \beta] - k_{b,1} \beta \tag{4.37}$$

$$r_2 = k_{f,2} C_T [1 - \theta] \beta - k_{b,1} [1 - \beta] C_T \theta \tag{4.38}$$

where C_{A_ε} represents the concentration of the species in the electrolyte phase, C_T is the maximum concentration of the cations in the solid host, β is the molar fraction of the adsorbed species while θ represents the molar fraction of the inserted cation in the host structure. k_f and k_b are the rate constants for the cathodic and anodic reaction with subscript 1 and 2 denoting the (de)solvation and (de)insertion step respectively and can be described as:

$$k_{f,1} = k'_{f,1} \exp\left(\frac{-\alpha_1 F \phi_1}{RT}\right) \tag{4.39}$$

$$k_{b,1} = k'_{b,1} \exp\left(\frac{(1 - \alpha_1) F \phi_1}{RT}\right) \tag{4.40}$$

$$k_{f,2} = k'_{f,2} \exp\left(\frac{-\alpha_2 F\phi_2}{RT}\right) \tag{4.41}$$

$$k_{f,2} = k'_{b,2} \exp\left(\frac{(1-\alpha_2) F\phi_2}{RT}\right) \tag{4.42}$$

with k'_f and k'_b representing the kinetic constant when the ϕ_1 or ϕ_2 is equal to zero with subscript 1 and 2 denoting the (de)solvation and (de)insertion step respectively. α represents the transfer coefficient with subscript 1 and 2 specifying the (de)solvation and (de)insertion step respectively. Equations 4.37 and 4.38 can then be rewritten as:

$$r_1 = k'_{f,1} \frac{C_{A_\varepsilon}}{C_0}[1-\beta] \exp\left(\frac{-\alpha_1 F\phi_1}{RT}\right) - k'_{b,1}\beta \exp\left(\frac{(1-\alpha_1) F\phi_1}{RT}\right) \tag{4.43}$$

$$r_2 = C_T[1-\theta]\beta k'_{f,2} \exp\left(\frac{-\alpha_2 F\phi_2}{RT}\right) - [1-\beta] C_T \theta k'_{b,2} \exp\left(\frac{(1-\alpha_2) F\phi_2}{RT}\right) \tag{4.44}$$

The current-potential relationship for the individual step is expressed as:

$$i_1 = -nFAk_1^0 \left[\frac{C_{A_\varepsilon}}{C_0}[1-\beta] \exp\left(\frac{-\alpha_1 F\phi_1}{RT}\right) - \beta \exp\left(\frac{(1-\alpha_1) F\phi_1}{RT}\right)\right] \tag{4.45}$$

$$i_2 = -nFAC_T k_2^0 \left[[1-\theta]\beta \exp\left(\frac{-\alpha_2 F\phi_2}{RT}\right) - [1-\beta]\theta \exp\left(\frac{(1-\alpha_2) F\phi_2}{RT}\right)\right] \tag{4.46}$$

where i_1 and i_2 are the current due to the (de)solvation and (de)insertion step respectively while k_1^0 and k_2^0 are the standard rate constant of the (de)solvation and (de)insertion step respectively. At equilibrium, the current flowing in the (de)solvation and (de)insertion step is zero thus,

$$\exp\left(\frac{F\phi_1}{RT}\right) = \frac{C_{A_\varepsilon}}{C_0} \frac{1-\beta}{\beta} \tag{4.47}$$

$$\exp\left(\frac{F\phi_2}{RT}\right) = \frac{1-\theta}{\theta} \frac{\beta}{1-\beta} \tag{4.48}$$

$$\exp\left(\frac{F\phi_T}{RT}\right) = \frac{C_{A_\varepsilon}}{C_0} \frac{1-\theta}{\theta} \tag{4.49}$$

The exchange current density (i_0) for each of the reaction steps can then be expressed with the equations below and the current can then be described as a function of the exchange current density:

$$i_{0,1} = nFk_1^0 \left[\frac{C_{A_\varepsilon}}{C_0}\right]^{1-\alpha_1} [1-\beta]^{1-\alpha_1} \beta^{\alpha_1} \tag{4.50}$$

$$i_{0,2} = nFC_T k_2^0 [1-\theta]^{1-\alpha_2} \beta^{1-\alpha_2} [1-\beta]^{\alpha_2} \theta^{\alpha_2} \tag{4.51}$$

$$i_1 = -i_{0,1} A \left[\exp\left(\frac{-\alpha_1 F\phi_1}{RT}\right) - \exp\left(\frac{(1-\alpha_1) F\phi_1}{RT}\right)\right] \tag{4.52}$$

$$i_2 = -i_{0,2}A\left[\exp\left(\frac{-\alpha_2 F\phi_2}{RT}\right) - \exp\left(\frac{(1-\alpha_2)F\phi_2}{RT}\right)\right] \tag{4.53}$$

Under the assumption that the perturbed electrochemical system is linear, $e^x \approx 1 + x$ and equation 4.52 and 4.53 can be rewritten as:

$$i_1 = -i_{0,1}\frac{F}{RT}\phi_1 \tag{4.54}$$

$$i_2 = -i_{0,2}\frac{F}{RT}\phi_2 \tag{4.55}$$

The resistance can be described with respect to the current in the two-step intercalation model as $R_{ad} = (-\partial i_1/\partial\phi_1)^{-1}$ and $R_{ct} = (-\partial i_2/\partial\phi_2)^{-1}$ allowing for R_{ad} and R_{ct} to be described with the equation below:

$$R_{ad} = \frac{RT}{F^2 k_1^0 \left[\frac{C_{A_\varepsilon}}{C_0}\right]^{1-\alpha_1}[1-\beta]^{1-\alpha_1}\beta^{\alpha_1}} \tag{4.56}$$

$$R_{ct} = \frac{RT}{F^2 C_T k_2^0 [1-\theta]^{1-\alpha_2}\beta^{1-\alpha_2}[1-\beta]^{\alpha_2}\theta^{\alpha_2}} \tag{4.57}$$

The expression for R_{ad} (equation 4.56) is observed to give a dependence of the adsorption resistance on the molar fraction of the adsorption sites (β). However, the concentration of the adsorption sites could not be quantified with the techniques used in this work. The adsorption sites can be estimated from the electrode potential using the equation below which is obtained from the substitution of equation 4.7 into equation 4.47.

$$\exp\left(\frac{F(1-\gamma)\phi_T}{RT} + \frac{F^2 N_{ad}}{RTC_1 + C_2}\beta\right) = \frac{C_{A_\varepsilon}}{C_0}\frac{1-\beta}{\beta} \tag{4.58}$$

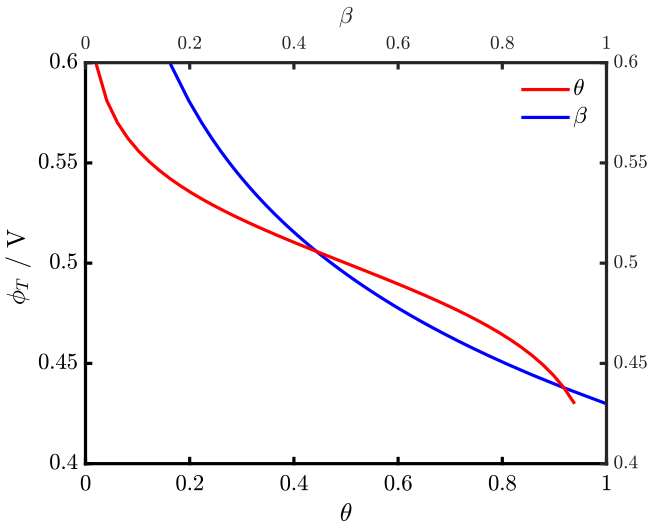

Figure 4.3: Dependence of electrode potential (ϕ_T) on molar fraction of adsorption sites (β) evaluated from equation 4.58 and molar fraction of cations in the solid (θ).

The electrode potential is obtained from the molar fraction of the cation in the solid which can be estimated from the charge flowing through the system and β can be obtained from the numerical solution of equation 4.58. Using a fractional coverage for the cations in the solid, the result obtained indicates that the dependence of β on ϕ_T is similar to the dependence of θ on ϕ_T as shown in Fig. 4.3 [140]. This treatment is valid for host structure where the reversible insertion process occurs in a single solid solution and the chemical potential of the (de)inserted cation in the host structure does not change during the (de)insertion process. This is not the case of $LiMn_2O_4$ where the reversible insertion of Li^+ has been reported to be proceed via multi-step process in two separate solid solutions, with the chemical potential of Li^+ differing in each of the separate solid solutions [160–162]. The reversible insertion step in the two solid solution can thus be described as:

$$A_i^+ + [\ ]_1 + e^- \rightleftharpoons [A]_1 \tag{4.59}$$

$$A_i^+ + [\ ]_2 + e^- \rightleftharpoons [A]_2 \tag{4.60}$$

where the empty site is represented as $[\ ]$ while $[A]$ is the occupied site in the solid solutions with subscript 1 and 2 denoting the different solid solutions. The equilibrium potential can thus be described as:

$$E_1 = E_1^0 + \frac{RT}{F}\ln\frac{C_{A_\varepsilon^+}}{C_0} + \frac{RT}{F}\ln\frac{(1-\theta_1)}{\theta_1} \tag{4.61}$$

$$E_2 = E_2^0 + \frac{RT}{F}\ln\frac{C_{A_\varepsilon^+}}{C_0} + \frac{RT}{F}\ln\frac{(1-\theta_2)}{\theta_2} \tag{4.62}$$

where E^0 the standard equilibrium potential with subscript 1 and 2 specifying the solid solutions and θ_1 and θ_2 represents the molar fraction of A^+ in the solid solutions. The total molar fraction (θ_T) in such system is estimated as $\theta_T = (\theta_1 + \theta_2)/2$ [163]. For each solid solution, a corresponding adsorption site was estimated using eq. 4.58. The decision to describe a separate adsorption site for each solid solution is based on the fact that the atomic arrangements of the surface structure in $LiMn_2O_4$ changes during the reversible insertion process [164, 165]. Fig. 4.4 shows the curve of ϕ_T versus β_T is similar to the curve of ϕ_T versus θ_T, suggesting that the adsorption sites assume a fractional coverage similar to the intercalation sites. The expression for R_{ad} and R_{ct} can thus be rewritten to reflect the different solid solution as:

$$R_{ad} = \frac{RT}{F^2 k_1^0 \left[\frac{C_{A_\varepsilon}}{C_0}\right]^{1-\alpha_1} [1-\beta_i]^{1-\alpha_1}\beta_i^{\alpha_1}} \tag{4.63}$$

$$R_{ct} = \frac{RT}{F^2 C_T k_2^0 [1-\theta_i]^{1-\alpha_2} \beta_i^{1-\alpha_2} [1-\beta_i]^{\alpha_2} \theta_i^{\alpha_2}} \tag{4.64}$$

where the subscript i denotes the different solid solution.

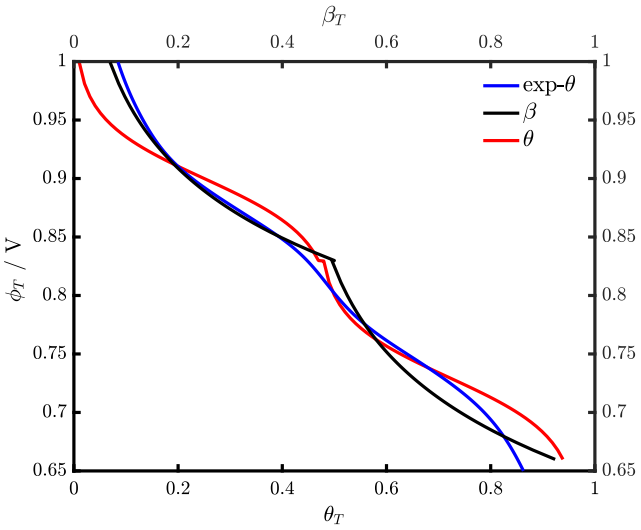

Figure 4.4: Dependence of electrode potential (ϕ_T) on total molar fraction of adsorption sites (β_T) evaluated and total molar fraction of cations in the solid (θ_T) for $LiMn_2O_4$.

4.3 Description of the Mass Transport in the Liquid and in the Solid Host

The mass transport resistance of the cation in the liquid in the model has been described as:

$$Z_{Wad} = \left[-F\frac{\partial r_1}{\partial \phi_1}\right]^{-1} \frac{\partial r_1}{\partial C_{A_\varepsilon}} \frac{1}{\sqrt{j\omega D_{A_\varepsilon}}} \tag{4.65}$$

The derivatives of the reaction rate can be described as:

$$-\frac{\partial r_1}{\partial \phi_1} = \frac{F}{RT}\left[\alpha_1(1-\beta)C_{A_\varepsilon}k_{f,1} + (1-\alpha_1)\beta k_{b,1}\right] \tag{4.66}$$

$$\frac{\partial r_1}{\partial C_{A_\varepsilon}} = k_{f,1}(1-\beta) \tag{4.67}$$

$$Z_{Wad} = \frac{RT}{F^2}\frac{k_{f,1}(1-\beta)}{\alpha_1(1-\beta)C_{A_\varepsilon}k_{f,1} + (1-\alpha_1)\beta k_{b,1}} \frac{1}{\sqrt{j\omega D_{A_\varepsilon}}} \tag{4.68}$$

Under the assumption that the system is in equilibrium, the ratio of the rate constant can be described as:

$$\frac{k_{b,1}}{k_{f,1}} = \frac{C_{A_\varepsilon}(1-\beta)}{\beta} \tag{4.69}$$

$$Z_{Wad} = \frac{RT}{F^2}\frac{1}{\sqrt{j\omega D_{A_\varepsilon}}}\frac{1}{C_{A_\varepsilon}} \tag{4.70}$$

$$\sigma_{ad} = \frac{RT}{F^2}\frac{1}{\sqrt{D_{A_\varepsilon}}}\frac{1}{C_{A_\varepsilon}} \tag{4.71}$$

where σ_{ad} is the Warburg coefficient in the liquid. Subsequently, the Warburg impedance in the liquid can be rewritten as:

$$Z_{Wad} = \frac{\sigma_{ad}}{\sqrt{j\omega}} \tag{4.72}$$

A similar treatment to the mass transport in the solid which has been described in the model as:

$$Z_{Wct} = \left[F\frac{\partial r_2}{\partial \phi_2}\right]^{-1}\frac{\partial r_2}{\partial \theta}\frac{1}{\sqrt{j\omega D_\theta}\tanh\left(\sqrt{j\omega\tau}\right)} \tag{4.73}$$

The derivatives for the rate constant is given by:

$$\frac{\partial r_2}{\partial \phi_2} = -\frac{F}{RT}\left[\alpha_2\beta C_T(1-\theta)k_{f,2} + (1-\alpha_2)(1-\beta)C_T\theta k_{b,2}\right] \tag{4.74}$$

$$\frac{\partial r_2}{\partial \theta} = -[k_{f,2}\beta + k_{b,2}(1-\beta)] \tag{4.75}$$

$$Z_{Wct} = \frac{RT}{F^2}\frac{k_{f,2}\beta + k_{b,2}(1-\beta)}{\alpha_2\beta C_T(1-\theta)k_{f,2} + (1-\alpha_2)(1-\beta)C_T\theta k_{b,2}}\frac{1}{\sqrt{j\omega D_\theta}\tanh\left(\sqrt{j\omega\tau}\right)} \tag{4.76}$$

Assuming the system is in equilibrium,

$$k_{f,2}\beta = k_{b,2}(1-\beta)\frac{\theta}{(1-\theta)} \tag{4.77}$$

$$Z_{Wct} = \frac{RT}{F^2}\frac{1}{C_T}\frac{1}{(1-\theta)\theta}\frac{1}{\sqrt{j\omega D_\theta}\tanh\left(\sqrt{j\omega\tau}\right)} \tag{4.78}$$

$$\sigma_{ct} = \frac{RT}{F^2}\frac{1}{\sqrt{D_\theta}}\frac{1}{C_T}\frac{1}{(1-\theta)\theta} \tag{4.79}$$

where σ_{ct} is the Warburg coefficient of the cation in the solid. Subsequently, the Warburg impedance in the solid can be rewritten as:

$$Z_{Wct} = \frac{\sigma_{ct}}{\sqrt{j\omega}}\coth\left(\sqrt{j\omega\tau}\right) \tag{4.80}$$

Chapter 5

Estimation and Correction of Instrumental Artefacts in Impedance Spectroscopy

In this chapter, the problems associated with artefacts arising from the instrumental setup used in measuring impedance will be discussed. Using resistors, $[Fe(CN)_6]^{3-/4-}$ redox couple, and a cathode material (nickel hexacyanoferrate nanoparticles), the effect of this instrumental artefacts on measured impedance and a method for the correcting these artefacts will presented.

5.1 Introduction

Electrochemical impedance spectroscopy is a highly sensitive technique used for studying various electrochemical systems, where it is employed in the elucidation of reaction mechanisms and determination of kinetic parameters [110, 122, 126]. This procedure relies on the correct interpretation of the impedance data [110]. To achieve this, high quality impedance data free from artefacts must be acquired over a wide range of frequencies [126]. Electrode setup and instrumental setup are some of the major sources of artefacts in electrochemical impedance spectroscopy [129, 166, 167].

Several methods for identifying artefacts arising from electrode setup and procedures for avoiding and/or correcting these artefacts have been reported in literature [129, 166, 168–172]. Following the works of Fletcher [170] and Sadkowski et al. [172], Battistel and co-workers proposed solutions to circumvent the artefacts occurring in a three-electrode cell setup. It comprises of using the three-electrode cell in a coaxial geometry which offers advantages, such as reduction in electrolyte ohmic drop, insensitivity to the position of the reference electrode and the reproducibility of the current line distribution [129]. It also involves the use of capacitive bridge to circumvent WE— RE stray capacitance and the use of low impedance electrode for circumventing large CE— RE coupling [129]. The use of an instrument with a high input impedance or a reference electrode with zero impedance has also been reported to eliminate distortions arising from

artefacts associated with voltage amplifier [110, 173]. Tran et al. with the help of simulations explained the use of low impedance RE fabricated by connecting a platinum wire to the RE through a capacitor, which has been used for a long time in circumventing high frequency artefacts [174, 175]. A zero-gap cell combined with by-pass modified and sensing electrodes was proposed by Stojadinovic and co-workers to minimize distortions arising from artefacts in a four-electrode cell setup [176] and a four-probe setup to measure high impedance values (up to 10 GΩ) has also been reported by Fafilek et al. to circumvent artefacts arising from four electrode cell setup [166, 177].

The aforementioned methods reduce and/or eliminate artefacts arising from electrode setups/configurations, but they do not address artefacts arising from the instrumental setup. The instrumental setup used for the data acquisition often contains parts (cables, operational amplifiers and current/voltage converters) which deviate from ideal behaviour [129]. The focus of this chapter is the estimation and correction of the artefacts arising from the instrumental setup. To this end, a specifically developed methodology will be shown and discussed in this chapter. Using resistors, redox couple ($[Fe(CN)_6]^{3-/4-}$) and NiHCF nanoparticles, the effect of artefacts occurring at the high frequencies due to non-ideal behaviour of the potentiostat on measured impedance will be investigated. The correction of these artefacts using a method that will be proposed in this chapter will also be illustrated using the various system studied.

5.2 Sources of Instrumental Artefacts

The potentiostat is a common instrument used in laboratories as it allows for potentiostatic control of electrochemical systems. In addition to the building blocks of a potentiostat (operational amplifiers, I/E converter, scaler/inverter and integrators), modern potentiostats also consists of auxiliary ports and outputs which allows for the potentiostat to be interfaced with other devices such as temperature probes, pressure gauges, waveform generators and oscilloscopes. Potentiostats used for impedance measurements are equipped with voltage adders, which sums the dc potential and the ac potential delivered by the function generator. A simplified schematics of the measurement principle of a potentiostat in a three-electrode cell configuration is shown in Fig. 5.1 [110]. The output potential is measured as the voltage difference between voltage of the WE, which is grounded and the potential of the RE [110]. The cell voltage is controlled by an appropriate amount of current delivered to the counter electrode from the op-amp as shown in Fig. 5.1 [110]. The operational amplifier (op-amp) ideally has a infinite input impedance and zero input current needed to maintain a stable potential of the RE branch.

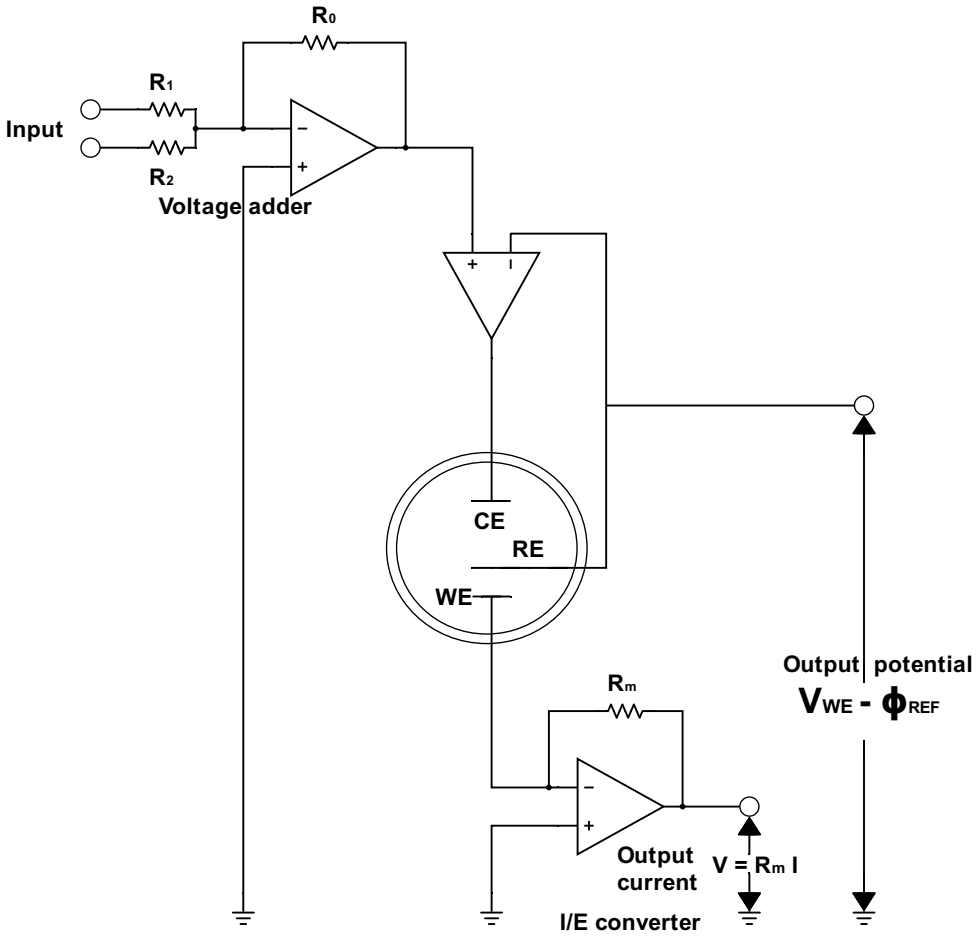

Figure 5.1: Simplified schematic diagram of a potentiostat used for electrochemical impedance spectroscopy. Adapted from [110].

The current in the potentiostat is measured using the current follower also called I/E converter. It measures the current as a voltage drop in the current measurement resistor (R_m) shown in Fig 5.1. Switchable resistors of different magnitude are used in a potentiostat thus allowing for measurement of high precision current [178]. The resistors are switched by selecting the appropriate current range in the potentiostat. This selection depends on the maximum readable voltage per full current range of the I/E converter, which in our case is 1 V. This translates to R_m of 1 kΩ at a current range of 1 mA. In impedance measurements, the current range is selected so that the uncompensated cell resistance of the measured cell is higher than R_m of the I/E converter. The components of a potentiostat often deviates from ideal behaviour at high frequencies in AC

mode. The signal applied to the cell at high frequency by the control loop in the potentiostat may be shifted in phase due to its response bandwidth [177]. The use of larger inputs and monitoring of the feedback signal to the cell has been suggested for circumventing this problem [177].

Possible sources of distortions in the potentiostat at high frequency region includes I/E converter, op-amp and stray capacitance in the potentiostat. The achievable gain of the I/E converter depends on current source input impedance (measured impedance), bandwidth of the I/E converter and the transimpedance of the I/E converter. The bandwidth of the I/E converter depends on the gain such that the greater the gain (lower current range), the lower the bandwidth of the I/E converter. This could result in measuring impedance different from the impedance of the system. Therefore, it is important to measure the bandwidth of the I/E converter at different current ranges and use this as a guide in selecting maximum frequency for impedance measurements. In addition to the bandwidth, the transimpedance of the I/E converter is also frequency dependent and as such at high frequency the voltage drop in I/E converter may differ from the real voltage.

Another source of artefacts in impedance measurements is stray capacitance arising from inputs of the potentiostat [179]. Fig 5.2 shows the main sources of stray capacitance in a three-electrode cell configuration [179]. It indicates stray capacitance between CE — RE, RE — ground, RE — WE and WE — ground [179]. To remove these stray capacitance and increase the accuracy of the potentiostat, calibration at the factory is done by the manufacturers and a contour plot of the result is usually added to the manual. This contour plot shows the specified accuracy of the potentiostat. However, the electrochemical system and its surrounding has been reported to affect the accuracy of the contour plot, in most cases reducing the accuracy [179]. Thus, it is important to measure the stray capacitance of the potentiostat at different current ranges. In the next section, a mathematical description of the potentiostat will be presented.

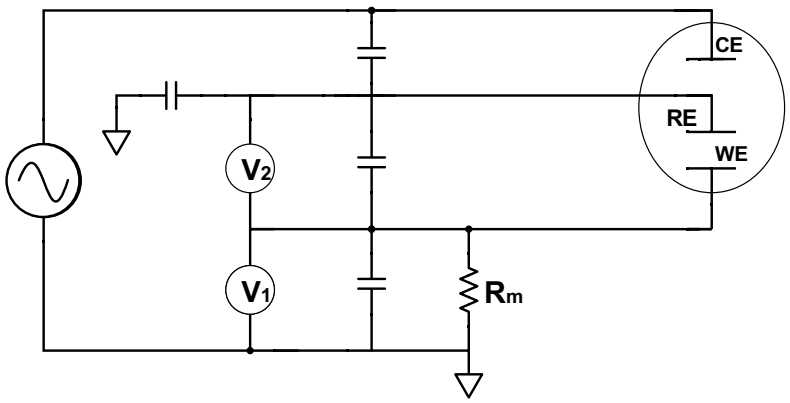

Figure 5.2: Simplified schematic diagram of a potentiostat in a three-electrode configuration showing the main sources of stray capacitance. Adapted from [179].

5.3 Theoretical description of the potentiostat

Fig 5.3 shows the electric circuit of a potentiostat in a two-electrode cell configuration used for measuring the transimpedance and stray capacitance of the potentiostat.

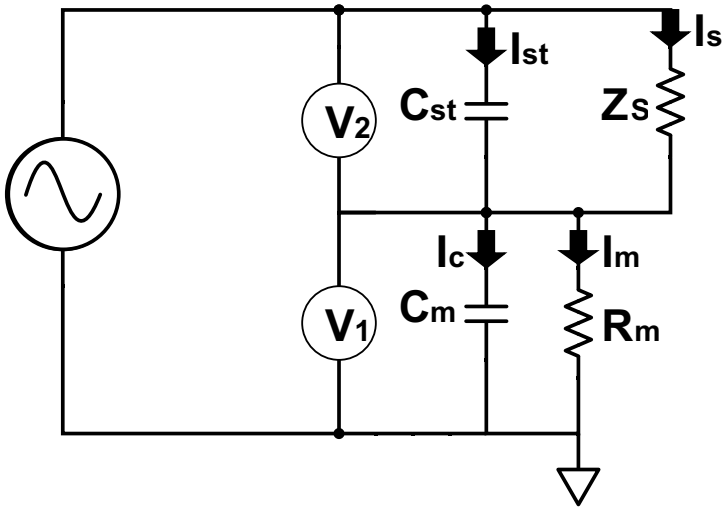

Figure 5.3: Simplified schematic diagram of a potentiostat in a two-electrode cell setup used for measuring the transimpedance and stray capacitance of the potentiostat used in this work.

Z_s in Fig. 5.3 is the impedance of the system being measured while C_{st} is the stray capacitance between the WE — RE/CE. This is the stray capacitance of interest as the other stray capacitances in the potentiostat (stray capacitance from RE — ground and from RE — CE) becomes negligible when a low impedance reference electrode is used [179]. The measured impedance can be described as [179]:

$$Z_m = \frac{V_2}{I_m} = \frac{V_2}{V_1} R_m \tag{5.1}$$

where V_2 is the voltage drop across Z_s and C_{st} while I_m is the measured current. V_2 can be described as:

$$V_2 = I_s Z_s Z_{V_2} = \frac{I_{st}}{j\omega C_{st}} Z_{V_2} \tag{5.2}$$

where I_s and I_{st} are the current flowing through Z_s and C_{st} respectively and their sum is equal to the measured current ($I_m = I_{st} + I_s$). Z_{V_2} is the impedance of the electrometer (V_2) which is unknown. V_1 which measures the current as a voltage drop across R_m is given by:

$$V_1 = I_m Z_{V_1} R_m = I_{Cm} \frac{1}{j\omega C_m} Z_{V_1} \tag{5.3}$$

where Z_{V_1} is the impedance of V_1 and I_{Cm} is the current flowing through C_m which is described as $I_{Cm} = j\omega C_m R_m I_m$. Equation 5.1 can then be rewritten as:

$$Z_m = \frac{I_s Z_s Z_{V_2}}{I_m Z_{V_1}} \tag{5.4}$$

The total measured current (I_{m_T}) is given by $I_{m_T} = I_s + I_{st} = I_m + I_{Cm}$, subsequently $I_{m_T} = I_m(1 + j\omega C_m R_m)$. Defining $Z'_{V_1} = Z_{V_1}/(1 + j\omega C_m R_m)$, eq. 5.4 can be rewritten as:

$$Z_m = \frac{I_s Z_s Z_{V_2}}{I_{m_T} Z'_{V_1}} \tag{5.5}$$

$$Z_m = \frac{I_s Z_s Z_{V_2}}{(I_{st} + I_s) Z'_{V_1}} \tag{5.6}$$

$$\frac{1}{Z_m} = \frac{Z'_{V_1}}{Z_{V_2} Z_s} + \frac{I_{st} Z'_{V_1}}{I_s Z_s Z_{V_2}} \tag{5.7}$$

$$\frac{Z_s}{Z_m} = \frac{Z'_{V_1}}{Z_{V_2}} + \frac{I_{st} Z'_{V_1}}{I_s Z_{V_2}} \tag{5.8}$$

Redefining I_s and I_{st} from equation 5.2 will lead to $I_s = V_2/Z_{V_2} Z_s$ and $I_{st} = V_2 j\omega C_{st}/Z_{V_2}$. Substituting the term I_{st}/I_s in equation 5.8 with $j\omega C_{st} Z_s$ leads to:

$$\frac{Z_s}{Z_m} = \frac{Z'_{V_1}}{Z_{V_2}} + \frac{j\omega C_{st} Z_s Z'_{V_1}}{Z_{V_2}} \tag{5.9}$$

The transimpedance of the potentiostat Z_{tr} can be defined as $Z_{tr} = Z'_{V_1}/Z_{V_2}$. Subsequently, equation 5.9 can be rewritten as:

$$\frac{Z_s}{Z_m} = Z_{tr} + Z_{tr} j\omega C_{st} Z_s \tag{5.10}$$

Equation 5.10 indicates a linear relationship between the relative admittance of the system being measured (Z_s/Z_m) and Z_s with a slope which corresponds to $Z_{tr} j\omega C_{st}$ and an intercept which is equal to Z_{tr}.

5.4 Bandwidth of the I/E converter

The bandwidth of the I/E converter at different current range measured using the method described in section 3.7 is shown in Fig 5.4a. Ideally, the normalized impedance should be unitary with a phase shift of zero at all frequencies. The result indicates that the cut off frequency defined herein as the frequency where the modulus of the impedance deviates from the ideal unitary with -30% decreases with increasing gain (decreasing current range). The cut off frequency was

observed to decrease from 794 kHz in 1 mA current range to 251 kHz in 100 μA and further decreases to 8 kHz in the 1 μA range.

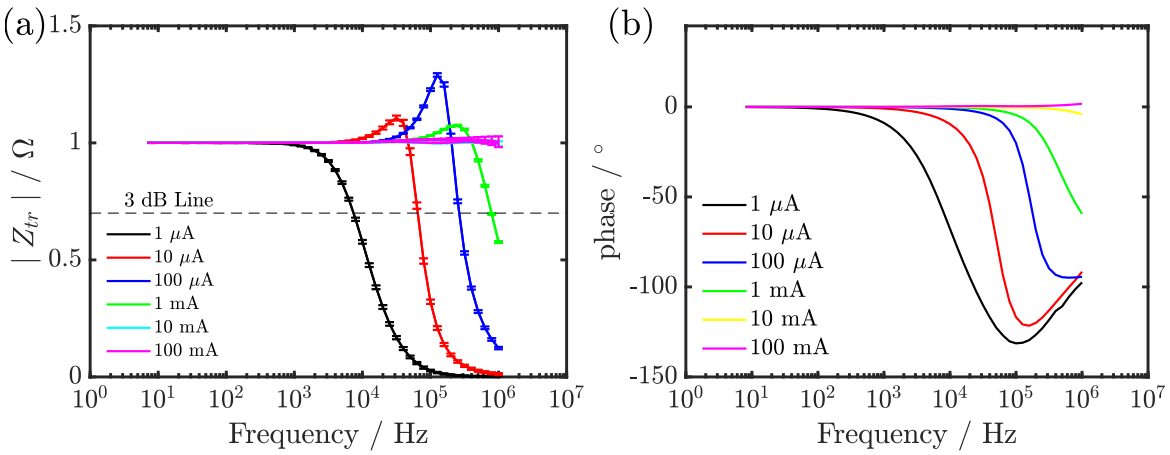

Figure 5.4: (a) Plot of the transimpedance of the potentiostat at different current range versus frequency. (b) Plot of phase of transimpedance of the potentiostat at different current range versus frequency.

The result is in line with the predictions that cut off frequency has an inverse proportionality with the gain of the system. For the phase, it was also observed that the onset of deviation decreases as the gain increases as seen in Fig. 5.4b. For the 10 mA and 100 mA where the deviation in the modulus of the transimpedance is negligible, a phase shift of 1.4° and -3° at 1 MHz respectively was observed. The result indicates that for the 1 mA current range the phase is delayed by -59.5° with onset frequency of 158 kHz, -94.37° with onset frequency of 63 kHz for the 100 μA and -131° onset frequency of 1 kHz for the 1 μA current range.

5.5 Deviation of Measured Impedance

The deviation of the measured impedance was investigated to evaluate the frequency limit where the various impedance using different current range can be measured without distortions. The permissible limit set in this work is 1% for magnitude of the impedance and 1° for phase. The deviation of the magnitude of the impedance and phase between the Z_m and Z_s are shown in Fig. 5.5 for various resistance in the 100 mA to 1 mA current range. The result suggests that the deviation in magnitude and phase were below the limit for all frequencies up to 1 MHz indicating that impedance can be acquired up to 1 MHz for these current ranges (100 mA to 1 mA). For 100 μA current range (Fig. 5.6a and Fig. 5.6b), the result indicates that the deviation of the measured impedance is below the 1% limit in magnitude and 1° in phase with the exception of 100 kΩ which exceeds the limit in magnitude at 39 kHz.

Using 10 μA current range this frequency limit for 100 kΩ can be extended to 100 kHz as shown in Fig. 5.6c and Fig. 5.6d. The measured impedance using the 10 μA current range were observed to deviate above the 1° phase limit at 100 kHz as shown in Fig. 5.6d even when the magnitude is within the limit (Fig. 5.6c). The high frequency limit, which the real impedance can be measured without exceeding the limit was observed to decrease as the impedance increase for the 1 μA as shown in Fig. 5.6e. The result obtained in this section shows the frequency limit which the impedance of the system can be measured using different current range without distortions arising from artefacts. In the next sections, the possibility of extending the frequency limit which the impedance of the system can be acquired without distortions will be illustrated.

5.6 Extracting the Transimpedance and Stray Capacitance

The transimpedance and stray capacitance of the potentiostat were extracted from the intercept and slope of the first order polynomial fit of the relative admittance (Z_s/Z_m) versus Z_s according to equation 5.10. Z_s was extracted from the low frequency data points of the measured impedance where distortions arising from instrumental artefacts is negligible. The stray capacitance is obtained from the slope of the plot of the high frequency data point of $j\omega C_{st}$ versus ω. Once the stray capacitance (C_{st}) and the transimpedance (Z_{tr}) has been extracted, the true impedance of the system devoid of the instrumental artefacts (C_{st} and Z_{tr}) for all frequencies can be estimated from the measured impedance using an extension of equation 5.11 described below:

$$Z_s = \frac{Z_{tr}Z_m}{1 - j\omega C_{st}Z_m Z_{tr}} \tag{5.11}$$

5.7 Extracting Impedance of the System From Measured Impedance

The impedance of the various electrochemical systems (resistors at different current ranges, a $[Fe(CN)_6]^{3-/4-}$ redox couple and an intercalation electrode (nickel hexacyanoferrate)) were extracted from the measured impedance using the equation 5.11.

5.7.1 Resistor

The use of eq. 5.11 to obtain the real impedance from the measured impedance of various resistors is illustrated in this section. The magnitude and phase of the impedance of 50 Ω resistor measured in 100 mA current range is shown in Fig 5.7a. The result suggests that the correction of the

magnitude of the impedance measured at this current range was not necessary as the magnitude did not show any distortion up to 1 MHz with negligible deviation in the phase ($\leq 1°$).

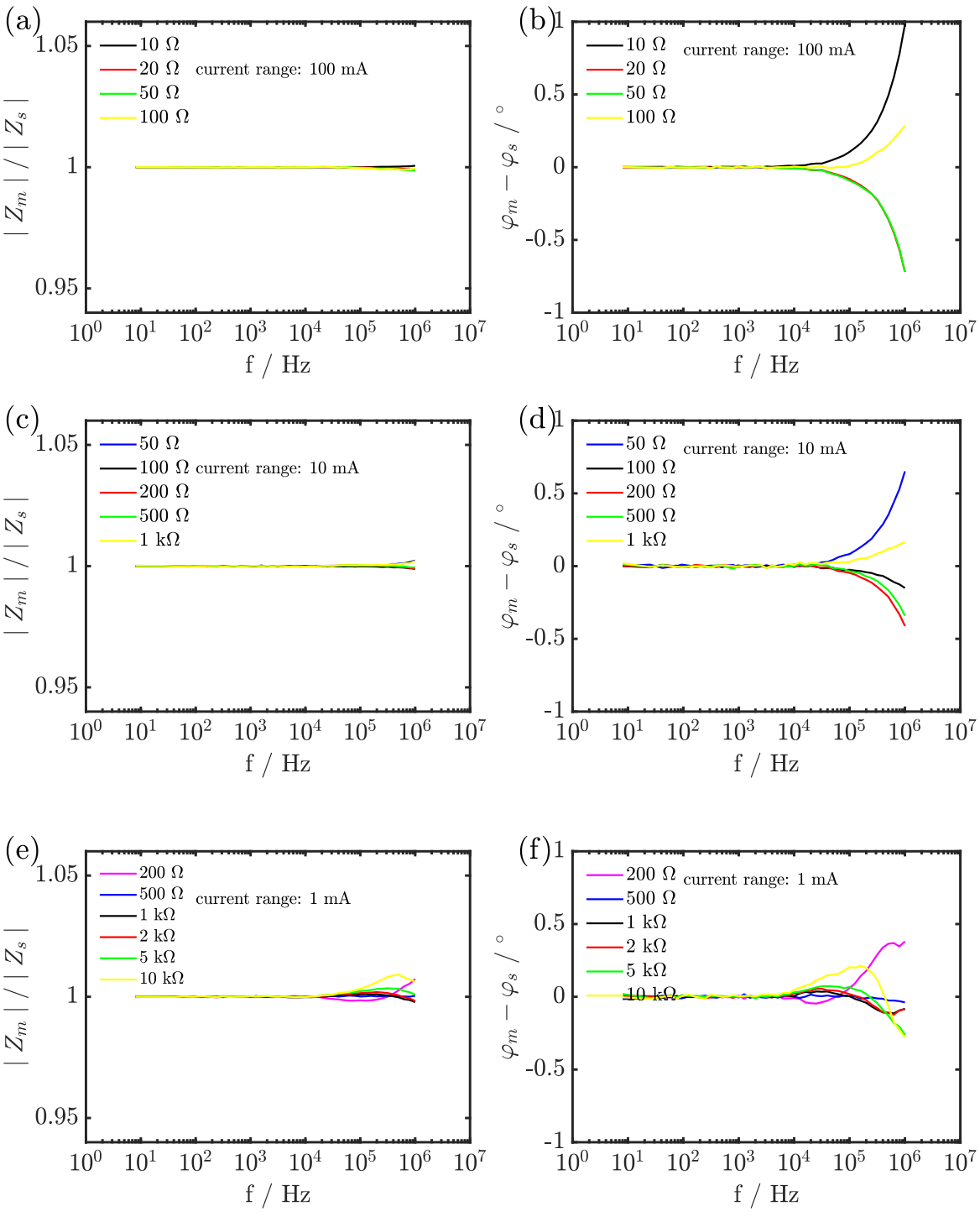

Figure 5.5: Plot showing the estimated error of the magnitude and phase of the impedance of the resistors at different current range from 100 mA to 1 mA.

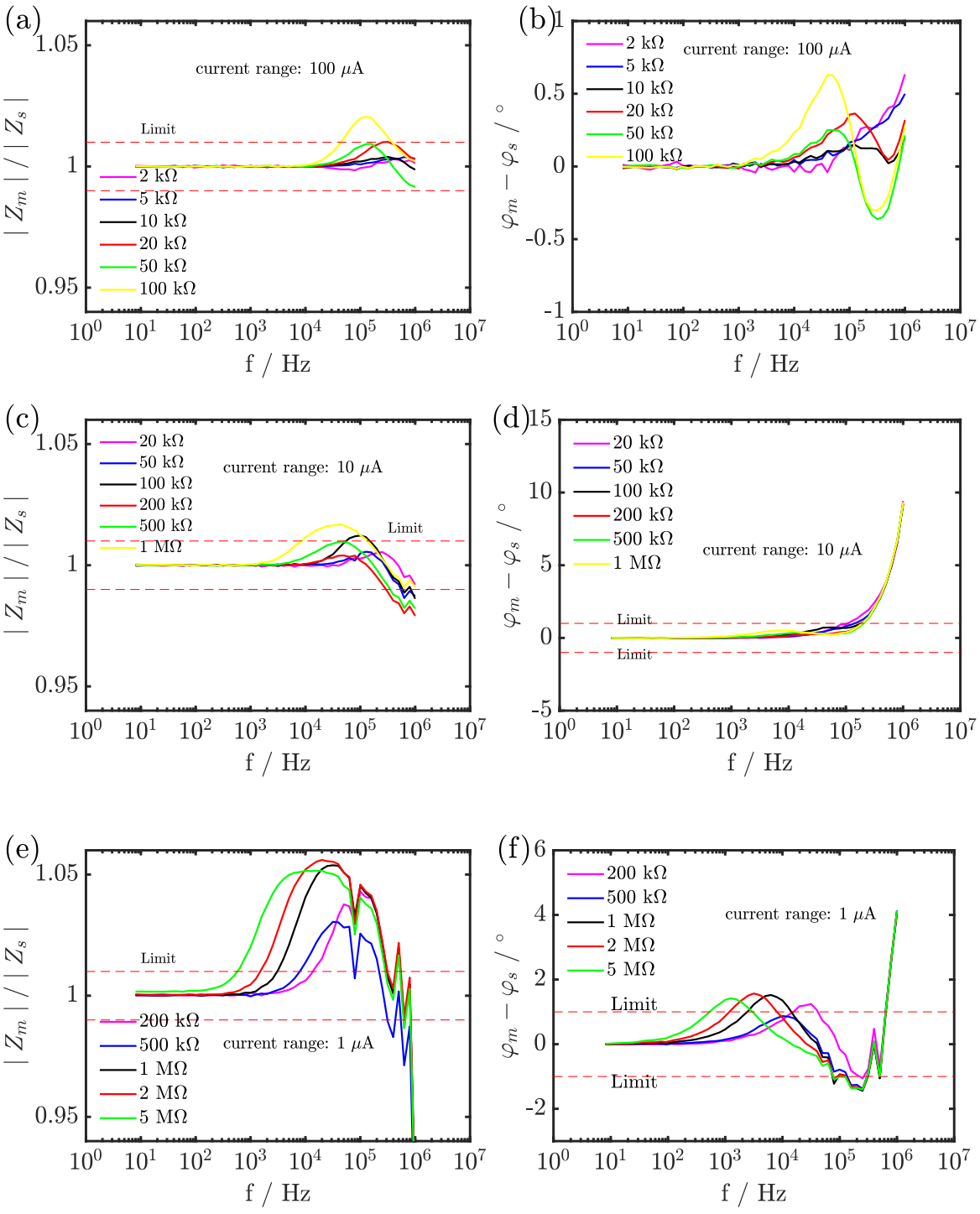

Figure 5.6: Plot showing the estimated error of the magnitude and phase of the impedance of the resistors at different current range from 100 μA to 1 μA.

The result obtained for 500 Ω measured at 10 mA is shown in Fig. 5.7b indicating that the correction of the magnitude was also not necessary but the phase shift for the 500 kΩ at 1 MHz was -1.5°, which was reduced to -0.3° using the correction method. The correction method allowed

for the true impedance of the 5 kΩ resistor to be extracted from the measured impedance at 1 mA despite the distortions between 100 kHz to 1 MHz as shown in Fig. 5.7c.

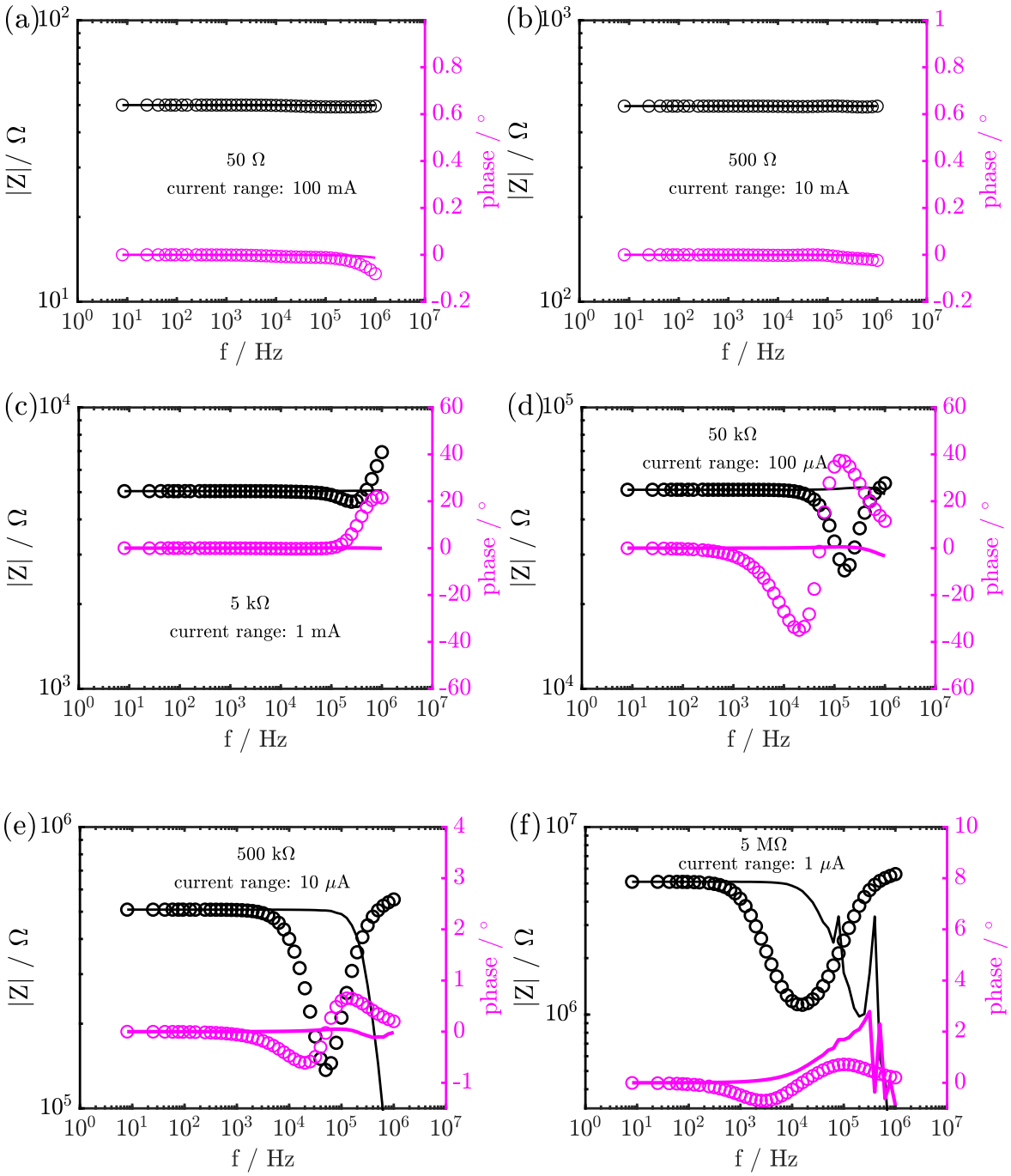

Figure 5.7: Correction method applied to various impedance measured at different current range. ◯ represents the measured impedance, while — represents the corrected impedance using the proposed method.

The correction of the impedance at the μA range was particularly of interest in this study as the cut off frequency is expected to be lower than those of the mA current range. Fig. 5.7d

shows that the proposed method allows for the measurement of the true impedance for 50 kΩ in 100 μA for frequencies up to 1 MHz despite the early onset distortions at 10 kHz. The usage of the proposed correction method at even lower current range was observed to extend the frequency limit which the impedance of the system can be extracted from 1 kHz to 100 kHz for the 10 μA current range for a 500 kΩ resistor. In the 1 μA current range, the measurement limit for 5 MΩ was extended from 2 kHz to 20 kHz using the correction. The result obtained indicates that the proposed correction method allows for the extension of the frequency limit which the impedance of the system can be measured especially in the μA current range where there is an early onset of distortions caused by instrumental artefacts.

5.7.2 Redox Couple

The effect of instrumental artefacts and application of the proposed correction method was also investigated using a $[Fe(CN)_6]^{3-/4-}$ redox couple on a 250 μm Pt electrode in a three-electrode (Fig 3.2). The uncompensated cell resistance of the cell was 275 Ω and a current range of 10 mA ought to be used for measuring the impedance. Ideally, the current range for measuring impedance is chosen in a way that the resistance of the system been measured is higher than R_m of the I/E converter used.

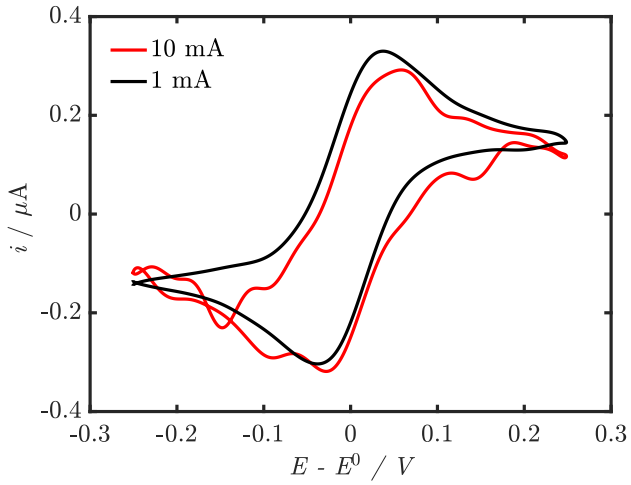

Figure 5.8: Quasi Voltammogram obtained at different current range for 250 μm Pt electrode in 5 mM $K_3[Fe(CN)_6]$ solution with 1 M KCl as supporting electrolyte.

However, the use of 10 mA current range was observed to reduce the data quality of the voltammogram obtained as shown in Fig. 5.8. The precision of measured current is determined by the current range selected in the potentiostat. The current range is chosen to be as close as possible to the measured current range to achieve high precision. To increase the precision, 1 mA current range was used which corresponds to an increase in precision by one order of

magnitude. The result indicates an increase in the signal to noise ratio of the voltammogram as seen in Fig. 5.8 (black curve). The dynamic impedance obtained using 1 mA current range (R_m = 1 kΩ) was observed to exhibit an inductive behaviour in the high frequency region (316 kHz to 1 MHz) as shown in Fig. 5.9b. This inductive behaviour of the impedance is clearly an instrumental artefacts as the impedance measured using the 10 mA current did not exhibit it and the equivalent circuit obtained from modelling a simple redox couple (Fig. 2.12 in chapter 2) does not include an inductor. This artefact can be attributed to the use of R_m (1 kΩ) higher than that of R_u of the cell (275 Ω). Using the proposed correction method, the real impedance without this artefact can be extracted from the measured impedance, as shown in Fig. 5.9c and Fig. 5.9d.

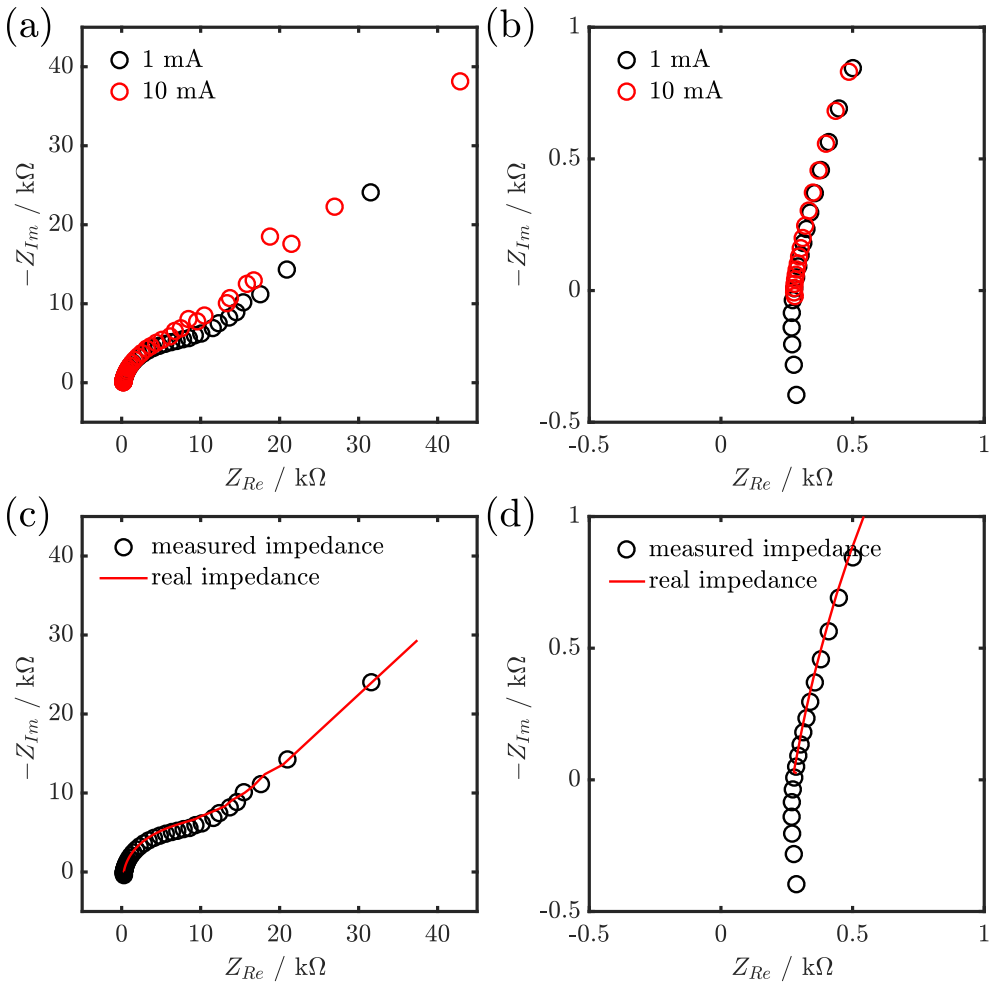

Figure 5.9: (a) Nyquist plot of impedance spectra obtained for 250 μm Pt electrode in 5 mM $K_3[Fe(CN)_6]$ solution with 1 M KCl as supporting electrolyte using 1 mA and 10 mA current range, (b) High frequency region of Nyquist plot of Fig. 5.9a (c) Nyquist plot of impedance spectra obtained for 250 μm Pt electrode in 5 mM $K_3[Fe(CN)_6]$ solution with 1 M KCl as supporting electrolyte (d) High frequency region of Nyquist plot of Fig. 5.9c.

The result suggests that the proposed correction method allows for an appropriate current range to be chosen as a compromise between the precision of the DC measurement (quasi CV)

and ac measurement (dynamic impedance) when acquiring dynamic impedance spectroscopy during voltage sweep.

5.7.3 Nickel Hexacyanoferrate Nanoparticles

The correction of artefacts arising from instrumental setup in measured impedance for electrochemical systems involving the (de)insertion of cations is illustrated in this section. The system of choice is nickel hexacyanoferrate (NIHCF) nanoparticles which has been reported as a promising cathode material for aqueous and non-aqueous battery system [50, 88, 89, 92, 99]. For insertion materials such as NiHCF nanoparticles, the impedance is normally acquired over a wide range of frequencies as it allows for the study of the various physicochemical processes occurring during the intercalation process such as (de)solvation, interfacial charge transfer and mass transport in the solid. Thus, it is imperative that artefact free impedance is acquired. The impedance measured in the frequency range from 350 kHz to 2.8 Hz shows two RC time constants terminated by a straight line attributed to mass transport in the solid as seen in Fig. 5.10.

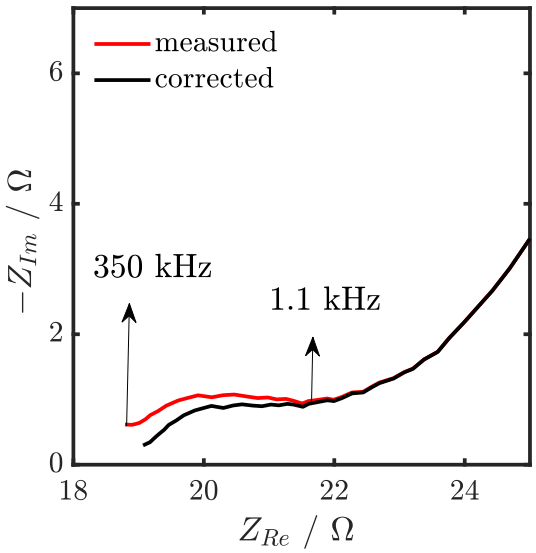

Figure 5.10: Nyquist plot of NiHCF in 0.5 M K_2SO_4 within the frequency range of 350 Hz to 2.8 kHz at 0.50 V during cathodic scan.

A comparison between the measured and true impedance indicates that the measured impedance is shifted towards the left from the true impedance between 350 kHz and 1.1 kHz as shown in Fig. 5.10. This can be attributed to the artefacts occurring at the high frequency region. Although the measured impedance can still be fitted using the same equivalent circuit, the extracted kinetic parameters will be different due to the artefacts. This shows that in order to quantify kinetic parameters, the measured impedance has to be corrected.

5.8 Conclusion

The result obtained in this chapter indicates that the artefacts arising from transimpedance and stray capacitance of the potentiostat can be corrected using the proposed correction method. It was observed that the onset frequency of the distortions decrease as the current range decreases, which can be attributed to decreasing bandwidth of the potentiostat. The possibility to estimate the true impedance from the measured impedance up to a certain limit, which depends on the current range and the value of the impedance was illustrated using various resistors. The results indicate that it is possible to acquire impedance up to 1 MHz for the mA current range using the proposed correction method. For the μA current ranges, the result shows that it is possible to extend the frequency limit for obtaining the real impedance up to two orders of magnitude (500 kΩ resistor from 1 kHz to 100 kHz in the current range of 1 μA). Using the proposed correction method, the artefacts (inductive behaviour) observed in the measured impedance of a redox couple acquired using a current range of 1 mA were properly corrected. This highlights that the proposed correction method allows for the selection of current range for high signal-to-noise voltammogram and artefact free impedance. The need to correct measured impedance especially those acquired at high frequencies was illustrated using a NiHCF nanoparticles.

Chapter 6

Dynamic Impedance Spectroscopy of Nickel Hexacyanoferrate Thin Films

In this chapter, the kinetics of the reversible insertion of univalent cations (Na^+ and K^+) in nickel hexacyanoferrate (NiHCF) thin films made by cathodic electrodeposition is studied using DMFA during cyclic voltammetry. For such system, stationary impedance spectroscopy is not suitable due to the instability of the oxidized form of NiHCF films. Electrochemical systems that are unstable tend to undergo drift during the acquisition of low frequency data points using the conventional electrochemical impedance spectroscopy. In this chapter, the advantage of using DMFA coupled with an optimized electrochemical cell in studying the kinetics of unstable electrochemical systems over the classic EIS will be illustrated.

6.1 Introduction

Thin films of nickel hexacyanoferrate have attracted a lot of interest over the years due to their use in various applications such as batteries [180], ion exchange applications [181–184] and ion sensing [185, 186]. The use of NiHCF thin films in these applications is connected to their large ion-exchange capacities [187], fast charge and discharge rates [188, 189], cost effectiveness and relatively low toxicity [190]. NiHCF is a Prussian blue analogue and shares the open framework with other metal hexacyanometallates which allows for the non-selective reversible insertion of various cations or zeolitic water [104, 141, 181, 191–196]. Thin films of NiHCF can be prepared basically by two methods: anodic derivatization and cathodic electrodeposition [141, 197] . The cathodically deposited NiHCF thin film exhibits better electrochemical performance due to large ion-exchange capacitance, hence its usage in most applications [187, 198]. In anodic derivatization, thin films of NiHCF are formed as precipitates when metallic nickel is oxidized in the presence of divalent nickel ions while the cathodic deposition involves the reduction of ferricyanide on an inert surface in the presence of divalent nickel. It has been reported that cathodically deposited

thin films of NiHCF are unstable; losing 40 % of its initial charge after 500 cycles while cycling at 10 mVs^{-1} [199]. This instability makes the conventional EIS unsuitable for studying the kinetics of the reversible insertion of cations in NiHCF thin films made by cathodic deposition. For such systems the acquisition of low frequency data points may lead to shapes in the spectra that are not related to the reaction mechanism itself. This could be the reason for the shape of the impedance obtained by Bandarenka and co-workers, who reported a low frequency inductive loop for thin films of NiHCF made by cathodic electrodeposition and other Prussian blue analogue in aqueous and non-aqueous media [200–202]. Another plausible reason for this inductive loop could be the artefacts arising from the use of a relatively high impedance reference electrode [129, 174].

For unstable electrochemical systems like NiHCF, which may undergo degradation during the acquisition of low frequency impedance data, the acquisition of all frequencies at each potential during a voltage sweep would be a better approach. In this chapter, I demonstrate that dynamic multi-frequency analysis coupled with an optimized electrochemical set-up is a better method for studying the kinetics of the reversible insertion of univalent cations in thin films of NiHCF made by cathodic electrodeposition.

6.2 Nickel Hexacyanoferrate Thin Films

Fig. 6.1 shows the cyclic voltammogram obtained during the electrodeposition of NiHCF films using the procedure described in section 3.1 . Steady film growth is observed during the potential cycling as the cathodic and anodic peak current increases as shown in Fig. 6.1. NiHCF film growth occurs during the reductive scan of the voltage sweep when $[Fe(CN)_6]^{4-}$ which is obtained from the reduction of $[Fe(CN)_6]^{3-}$ reacts instantaneously with Ni^{2+} and K^+ present in the solution to form sparingly soluble NiHCF, which is deposited on the glassy carbon electrode [140, 141]. The voltage sweep is stopped as the voltammogram becomes stable. The electrodeposited film obtained after 15 cycles was estimated to be 100 nm. The voltammogram exhibited peaks which has been associated with the (de)insertion of K^+ in NiHCF film [141, 187]. The shouldered peak has been attributed to the reversible insertion of K^+ in the different phases of the electrodeposited NiHCF film [141]. It can also be attributed to interactions between redox sites and insertion sites as reported in [104]. The reversible insertion process is often described using the ideal solution approximation but this is often not the case as shown in electrochemical behaviour of nickel hexacyanoferrate nanoparticles in aqueous electrolytes of univalent cations [104].

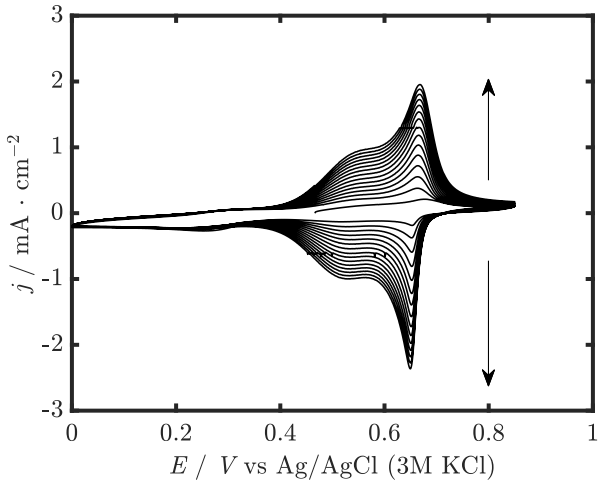

Figure 6.1: Cyclic voltammogram obtained during the electrodeposition of NiHCF in a freshly prepared solution of 2 mM $K_3Fe(CN)_6$, 2 mM $NiSO_4$ and 0.5 M K_2SO_4 using a scan rate of 25 mVs^{-1}.

6.3 SEM/EDX Analysis

The morphology of the electrodeposited film and the elemental composition was studied using scanning electron microscopy (SEM) and energy-dispersive X-ray spectroscopy(EDX).

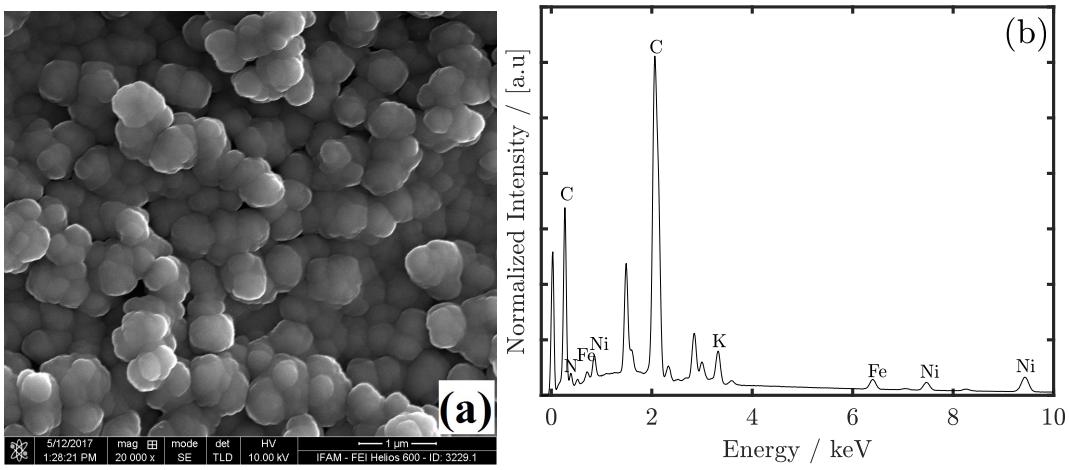

Figure 6.2: (a) SEM micrograph of the electrodeposited NiHCF (b) EDX pattern of the electrodeposited NiHCF film.

Fig. 6.2 shows the SEM micrograph of modified electrode, which suggests the deposited NiHCF film comprises of porous agglomerates and the NiHCF is not a compact film. The elements Fe, K and Ni in a ratio of 1:1:1.4 were obtained from the elemental composition of the NiHCF film suggesting $KNi_{1.42}[Fe(CN)_6]$ as the chemical formula of the electrodeposited NiHCF [140]. This is in agreement with what has been reported in literature as the insoluble form of the Prussian blue analogue [187, 203].

6.4 Electrochemical Analysis

Due to the instability of the NiHCF film made by cathodic electrodeposition, the stability of the reduced and oxidized forms of the NiHCF films were studied in order to ascertain the potential which the NiHCF can be held before polarization with the combined dc and multi-sine wave. The result obtained indicates that reduced form of the NiHCF is more stable than the oxidized form as seen in Fig 6.3.

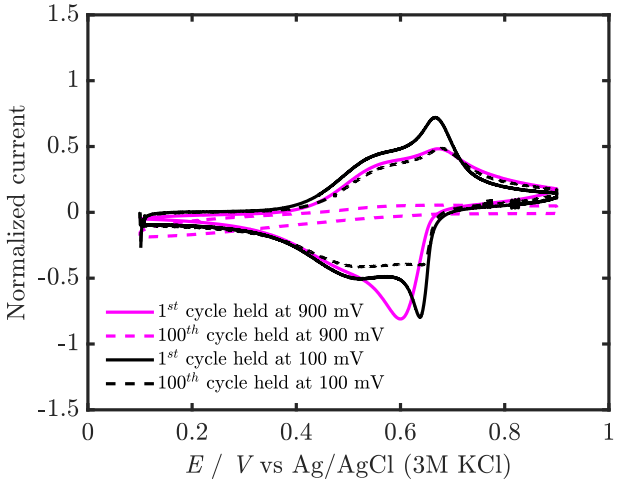

Figure 6.3: Cyclic voltammogram of NiHCF thin films in 0.5 M K_2SO_4 held at 100 mV and 900 mV for 5 minutes after every 5^{th} cycle.

Fig. 6.4 shows the voltammetric response of the NiHCF film in 0.5 M solutions of Na_2SO_4 and K_2SO_4 from the application of the quasi-triangular wave with a frequency of 125 mHz corresponding to a scan rate of 200 mVs^{-1}.

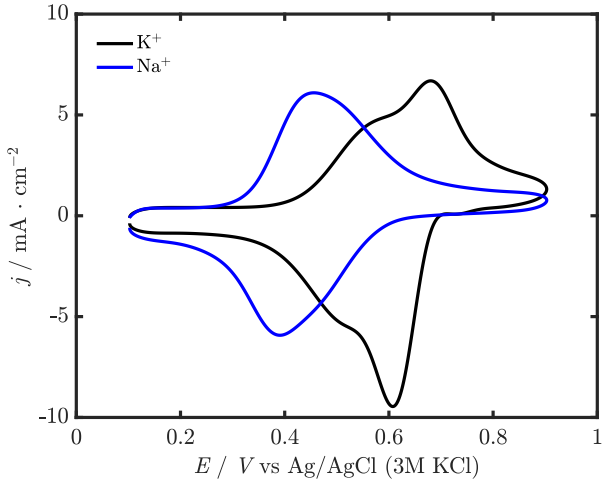

Figure 6.4: Cyclic voltammogram of NiHCF modified GCE electrode in 0.5 M Na_2SO_4 and K_2SO_4 using a scan rate of 200 mVs^{-1}.

Well defined peaks attributed to the reversible insertion of both cations were observed in the voltammogram, with Na^+ having a single peak in contrast to the shouldered peak observed in K^+. The (de)insertion potential ($\bar{E}$), which is the average of the cathodic and anodic peak potential was observed to increase with decreasing hydration radii. This has been attributed to the fact that the removal of the solvation shell has been reported as the major contribution of the Gibbs free energy of insertion ($\Delta G^0 = -nF\bar{E}$) [88, 89, 104]. Na^+ with an Stokes radius of 1.83 Å had a reversible insertion potential of 0.42 V compared to 0.64 V for K^+ with Stokes radius of 1.25 Å [88, 89, 204]. The cathodic and anodic peak separation (ΔE_p) for Na^+ and K^+ was estimated to be 60 mV and 80 mV at 200 mVs^{-1} indicating a fast charge transfer process.

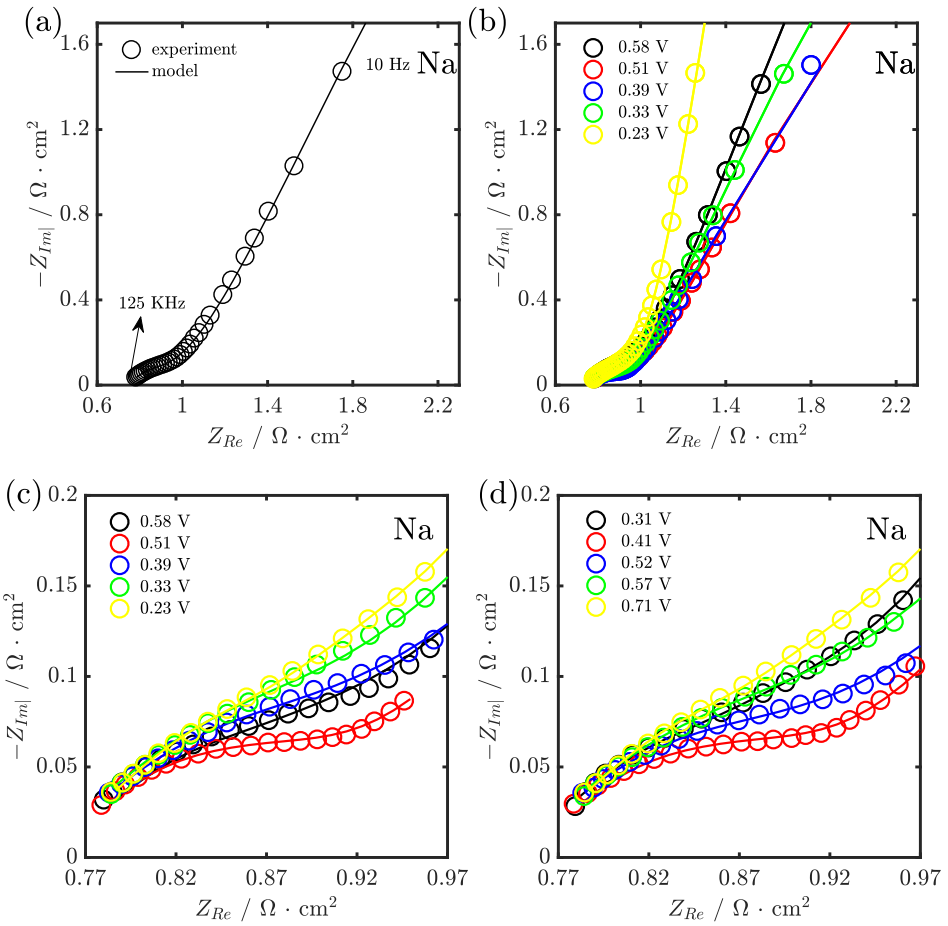

Figure 6.5: Nyquist plot of NiHCF film in 0.5 M Na_2SO_4 within the frequency range of 10 Hz to 125 KHz at (a) 0.38 V during cathodic scan (b) at different potential during cathodic scan (c) High-frequency region of the impedance spectra obtained at different potentials during the cathodic scan (d) High-frequency region of the impedance spectra obtained at different potentials during the anodic scan. ◯ represents the experimental data, while — represents the data from the model.

Fig 6.5 and Fig 6.6 show typical Nyquist plots of the impedance spectra obtained in 0.5 M Na_2SO_4 and K_2SO_4 at various electrode potentials during the cathodic and anodic voltage sweep. The impedance spectra consist of a semi-circle at the high frequency region terminated by a

straight line occurring at an angle of less than 90° which can been attributed to the mass transport of cations in porous electrodes [10, 205].

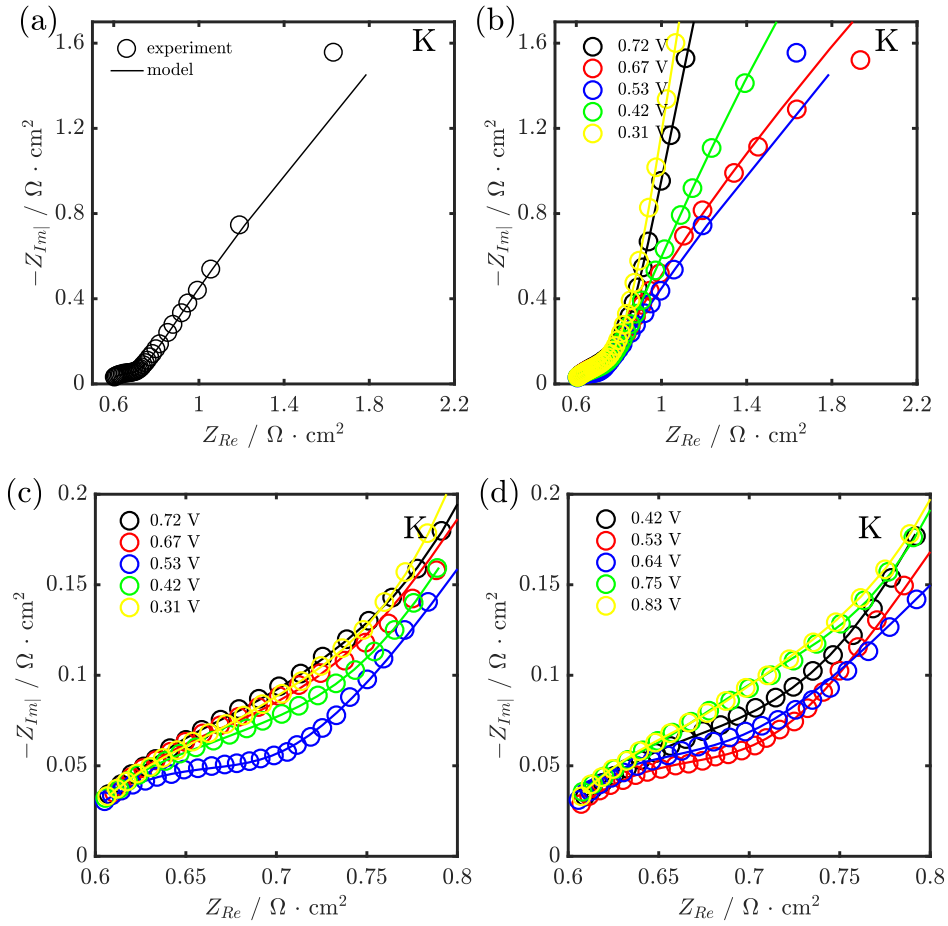

Figure 6.6: Nyquist plot of NiHCF film in 0.5 M K_2SO_4 within the frequency range of 10 Hz to 125 KHz at (a) 0.51 V during cathodic scan (b) at different potential during cathodic scan (c)High-frequency region of the impedance spectra obtained at different potentials during the cathodic scan (d) High-frequency region of the impedance spectra obtained at different potentials during the anodic scan. ◯ represents the experimental data, while — represents the data from the model.

The high frequency semi-circle was observed to be potential dependent as seen in the plot of the high frequency region of measured impedance (Fig 6.5c and 6.5d and Fig 6.6c and 6.5d). The impedance spectra obtained in this study are in contrast with those reported by Bandarenka and co-workers, who observed a low frequency inductive loop for NiHCF films and other Prussian blue analogues in aqueous and non-aqueous solvents within the frequency range of 50 kHz to 100 mHz [200–202]. The inductive loop observed by Bandarenka and co-workers could be as result of the instability of the NiHCF film or artefacts from the electrochemical set-up as discussed in section 6.1. The result obtained herein highlights the advantages of DMFA coupled with an optimized cell for studying the kinetics of unstable electrochemical systems over static electrochemical impedance spectroscopy. The result suggests that the reversible insertion process is a

two-step process with a (de)solvation step as the first step followed by (de)insertion step:

$$A_{\varepsilon}^{+} \rightleftharpoons A_{i}^{+} \tag{6.1}$$

$$A_{i}^{+} + ANi[Fe^{III}CN_6] + e^{-} \rightleftharpoons A_2Ni[Fe^{II}CN_6] \tag{6.2}$$

where the phases of the cations is represented as ε and i which corresponds to the electrolyte phase and the inner Helmholtz plane. The measured impedance spectra were fitted using the equivalent circuit obtained from modelling the reversible insertion process as a two-step process inserted in TLM, as shown in Fig. 4.2. The decision to use the TLM is supported by the shape of the high frequency part of the impedance spectra and the SEM image (Fig. 6.2a), which suggests that the electrodeposited film is porous. The fitting algorithm described in section 2.9 was used for fitting two hundred impedance per cation (one hundred for cathodic polarization and one hundred for anodic polarization). The results indicates that the model satisfactorily described the experimental data as the standard deviation (χ^2) was in the range of $1.3{\cdot}10^{-5}$ to $6.0{\cdot}10^{-6}$ suggesting a good agreement between the model and the experimental data.

6.5 Statistical Analysis

Despite the low χ^2 value obtained from fitting the measured impedance with the model, a t-test was done for each of the parameter in the equivalent circuit to avoid over-parameterization as explained in section 3.11. Fig. 6.8 shows the result obtained for the t-test for the equivalent circuit in Fig. 4.2, which indicates that the parameters C_{ad}, γ, R_{ct}, σ_{ad}, σ_{ct} and τ were below the 95 % confidence level for both cations as seen in Fig. 6.8a and Fig. 6.8b. C_{ad} which had the least t-value was removed from the equivalent circuit under the assumption that C_{ad} is higher than the capacitance in the IHP, which allows C_{ad} to be treated as a short circuit. Physically this implies that there is a large amount of adsorbed ion on the interface. This assumption results in the equivalent circuit shown in Fig. 6.7 and fitting the measured impedance with this equivalent circuit (Fig 6.7) did not compromise the goodness of fit, as χ^2 remained fairly constant. The t-test of the parameters obtained from fitting the data with the equivalent circuit (Fig. 6.7) still had parameters below the confidence level as seen in Fig. 6.8c and Fig. 6.8d. Subsequently, R_{ct} which had the least t-value was removed from the equivalent circuit under the assumption that charge transfer process occurs fast enough to be negligible i.e. the further desolvation of the ad-ion and the transfer of this desolvated cation across the electrode/electrolyte interface is very fast.

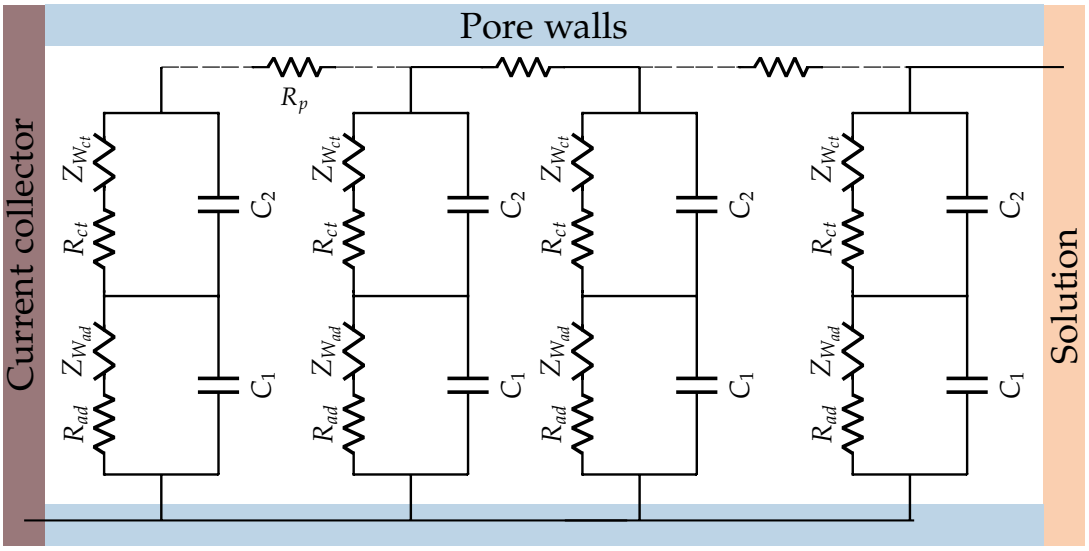

Figure 6.7: Equivalent circuit of the porous electrode including the equivalent circuit obtained from modelling the reversible insertion as two step process treating the capacitance of adsorption (C_{ad}) as a short circuit.

The cations are inserted/extracted through the channels connecting the A sites in NiHCF which has been reported to be 1.6 Å [87, 206]. On the other hand, the Stokes radii of Na^+ and K^+ has been reported as 1.83 Å and 1.25 Å respectively [87, 204]. Thus, the partial desolvated cations can be (de)inserted through the channels connecting the A sites of the NiHCF and this can result in charge transfer process occurring fast enough to be negligible. χ^2 in the order of 10^{-5} was obtained from fitting the measured impedance with the equivalent circuit in Fig. 6.9 and the t-value of the parameters (Fig. 6.8e and Fig. 6.8f) indicates τ is below the confidence level for both cations. The mass transport in the solid is described using the finite Warburg impedance diffusion with reflective boundary [127, 148]:

$$Z_{Wct} = \sigma_{ct}\sqrt{\tau} \cdot \left[\frac{1}{\sqrt{j\tilde{\omega}}} coth(\sqrt{j\tilde{\omega}})\right] \tag{6.3}$$

with $\tilde{\omega}$ is the characteristic diffusion frequency which is described as $\tilde{\omega} = \omega\tau$. For $\tilde{\omega} \gg 1$, equation 6.3 can be described as semi-infinite diffusion [148]. This assumption is used in this study due to the shape of the impedance spectra which does not exhibit a switch from 45° to 90° associated with the change from semi-finite diffusion to finite diffusion which occurs when $\tilde{\omega} \sim 1$.

$$Z_{Wct} = \frac{\sigma_{ct}}{\sqrt{j\omega}} \tag{6.4}$$

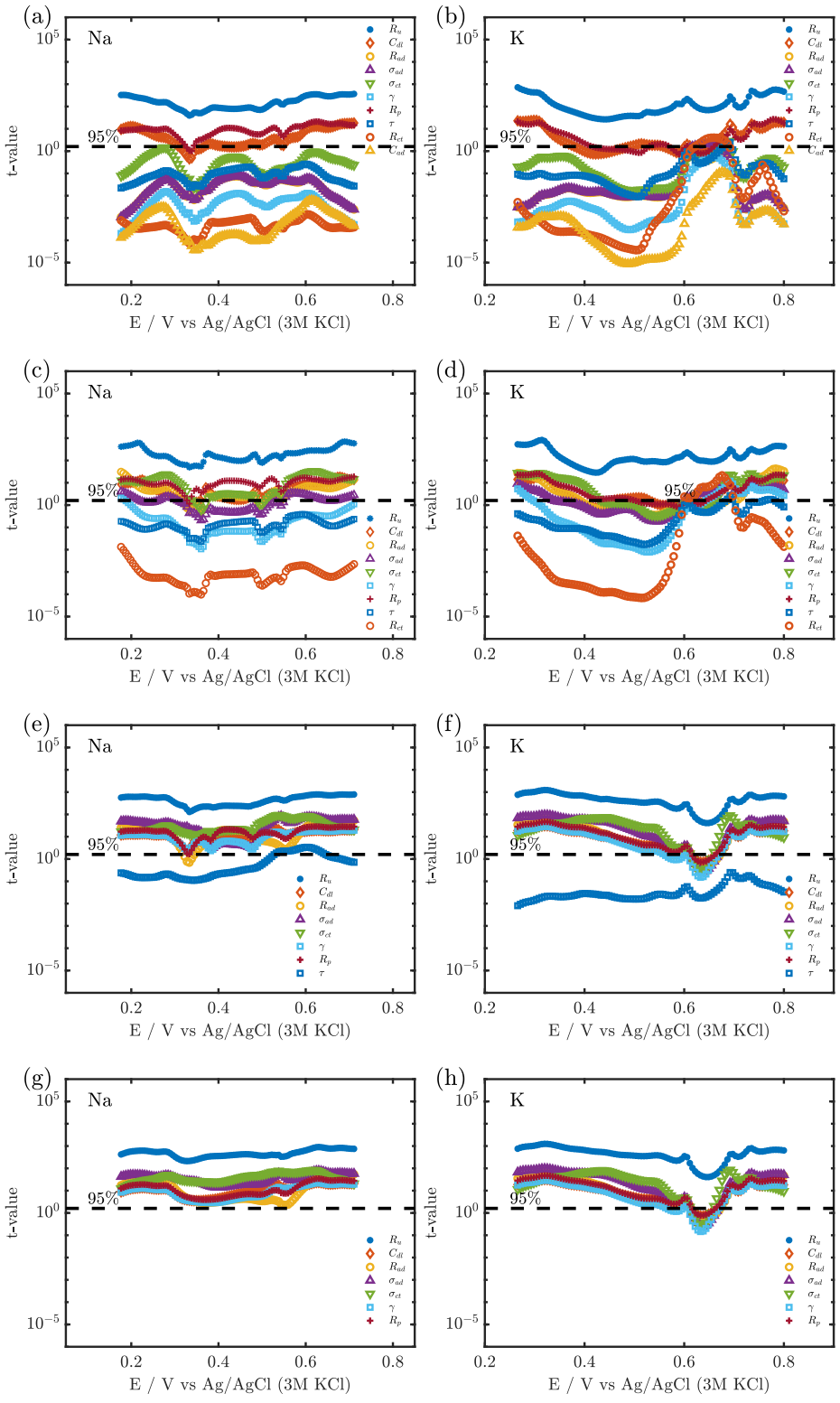

Figure 6.8: Results obtained from the t-test for the parameters obtained from fitting the measured impedance using (a) and (b) equivalent circuit obtained from the model (Fig. 4.2), (c) and (d) equivalent circuit obtained from the model treating C_{ad} as a short circuit (Fig. 6.7) (e) and (f) equivalent circuit obtained from the model treating C_{ad} as a short circuit and assuming the charge transfer process is fast enough to be negligible (Fig. 6.7) (g) and (h) equivalent circuit shown in Fig. 6.9 assuming a semi-infinite diffusion for the mass transport in the solid.

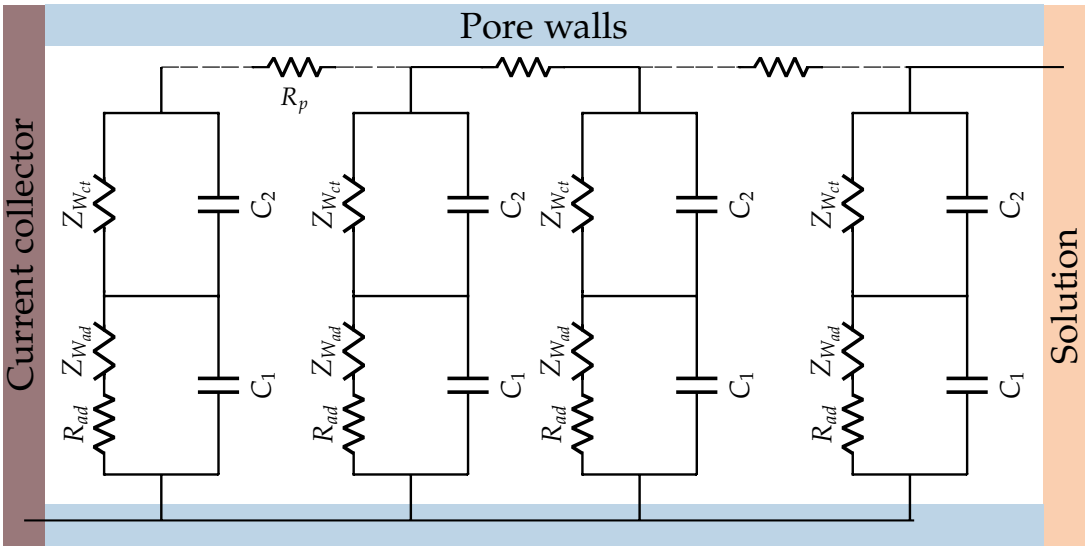

Figure 6.9: Equivalent circuit of the porous electrode including the equivalent circuit obtained from modelling the reversible insertion as two step process treating the capacitance of adsorption (C_{ad}) as a short circuit and the charge transfer resistance is fast enough to be negligible.

A good fit (— in Fig. 6.5 and Fig. 6.6) with χ^2 in the range of $1.3 \cdot 10^{-5}$ to $6.0 \cdot 10^{-5}$ for both cations with parameters above the confidence level(Fig. 6.8g and Fig. 6.8h) was observed when the mass transport was described using semi-infinite diffusion. For K^+, the parameters were above the confidence level with exception to parameters in the potential region where the shouldered peak occurs (0.61 V to 0.67 V) indicating that the model does not described properly the (de)insertion process of K^+ in this potential region.

6.6 Variation of Kinetic Parameters on Electrode Potential

The dependence on the kinetic parameters as a function of the electrode potential during the voltage sweep was investigated in this section. Fig. 6.10 shows the R_{ad} extracted from the fit of the reversible insertion of both cations. The result indicates that R_{ad} exhibited a compositional dependence with minimum which occurs around the standard potential of the (de)inserted cation. The variation of R_{ad} on potential obtained from the fit was observed to be similar to the variation of estimated R_{ad} on potential (Fig. 6.10b) obtained using the equation describing R_{ad} from the model (see chapter 4 for details) for (de)insertion process in host structure:

$$R_{ad} = \frac{RT}{F^2 k_1^0 \left[\frac{C_{A_\varepsilon}}{C_0}\right]^{1-\alpha_1} [1-\beta]^{1-\alpha_1} \beta^{\alpha_1}} \tag{6.5}$$

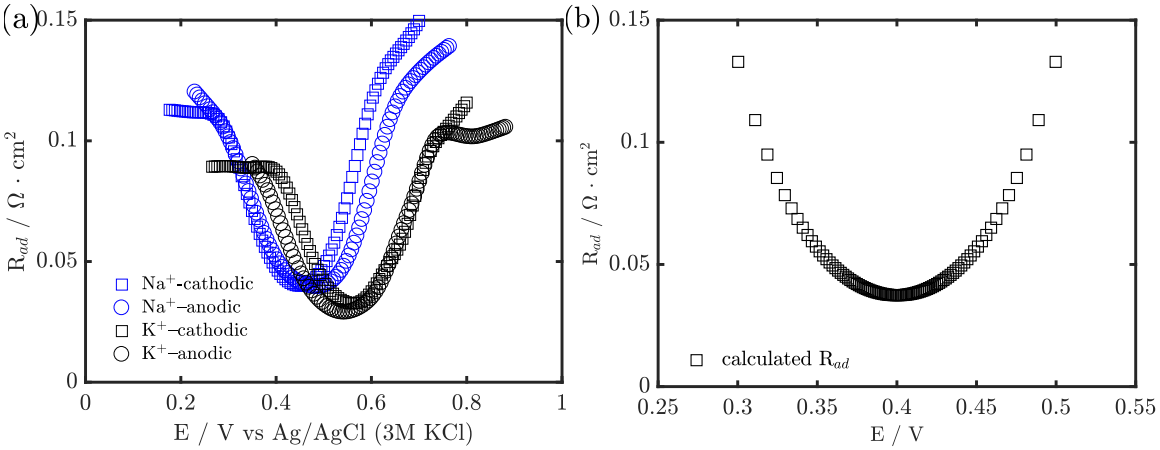

Figure 6.10: (a) Dependence of the extracted adsorption resistance (R_{ad}) on the potential during the cathodic and anodic voltage sweep. (b) Dependence of the calculated adsorption resistance (R_{ad}) using eq. 6.5 on the potential.

This indicates a good agreement between the model prediction and experimental data. The adsorption resistance for both cations was observed to be in the same order of magnitude and this can be attributed to similarity in the Stokes radii of the cations in aqueous media (Na^+ = 1.83 Å and K^+ = 1.25 Å). The Warburg coefficient of the cations in liquid (σ_{ad}) was observed to be independent on the electrode potential as suggested by eq. 4.71 which describes the mass transport in the liquid. σ_{ad} for both cations were in the same order of magnitude (K^+ = 7.89 Ω cm^2 s$^{-0.5}$ and Na^+ = 8.3 Ω cm^2 s$^{-0.5}$) which can be attributed to the fact the diffusion coefficient of both cations in aqueous media is in same order of magnitude ($Na^+ = 1.33 \cdot 10^{-5}$ cm^2 s^{-1} and $K^+ = 1.96 \cdot 10^{-5}$ cm^2 s^{-1}) [207]. On the other hand, the mass transport of the cations in the solid which is described with σ_{ct} was observed to exhibit compositional dependence as shown in Fig. 6.11a.

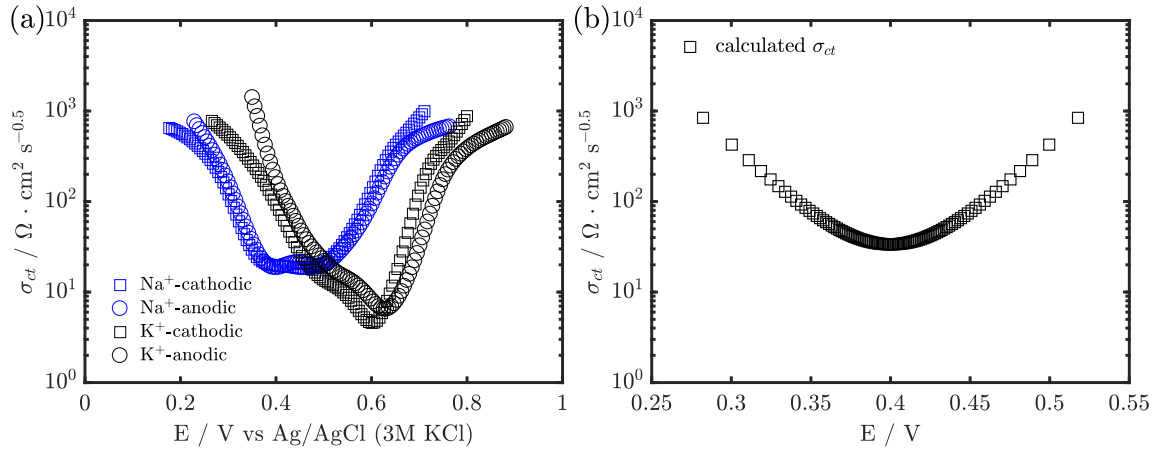

Figure 6.11: (a) Variation of the extracted Warburg coefficient in the solid (σ_{ct}) on the electrode potential. (b) Variation of the calculated Warburg coefficient in the solid (σ_{ct}) (eq. 6.6) using $D_\theta = 1 \cdot 10^{-7}$ cm^2 s^{-1} on the electrode potential.

This can be attributed to the term $([1-\theta]\cdot\theta)$ in the equation describing σ_{ct} from the model:

$$\sigma_{ct} = \frac{RT}{F^2}\frac{1}{\sqrt{D_\theta}}\frac{1}{C_T}\frac{1}{(1-\theta)\cdot\theta} \tag{6.6}$$

6.7 Conclusion

The results obtained in this study indicates that the kinetics of unstable electrochemical system such as NiHCF films made by cathodic electrodeposition can be studied using DMFA coupled with an optimized electrochemical cell set-up. Such unstable systems are difficult to study using the classic electrochemical impedance due to drift during the acquisition of low frequency impedance data point. The results obtained in this study differs from the results reported by Bandareka and co-workers, who observed an inductive loop in the impedance spectra of NiHCF film in aqueous and non-aqueous media [200–202]. This inductive loop could be as a result of drift of the system due to the instability of the NiHCF film and/or artefacts from the electrochemical cell used. The results shown in this chapter highlights the advantage of studying unstable electrochemical system using DMFA coupled with an optimized electrochemical cell. A good fit was obtained from fitting the impedance data with an equivalent circuit obtained from modelling the reversible insertion process as a two-step (de)insertion process: (de)solvation and (de)insertion. The mass transport in the liquid was independent on the electrode potential as predicted by the model. The adsorption resistance (R_{ad}) and the Warburg coefficient (σ_{ct}) extracted kinetic parameters were observed to exhibit compositional dependence with their minimum close to the standard potential of the (de)insertion of the cation.

Chapter 7

Kinetic Investigation of Reversible Insertion of Univalent Cations in Nickel Hexacyanoferrate Nanoparticles

Nickel hexacyanoferrate nanoparticles has been reported as a promising cathode material for aqueous rechargeable alkali-ion batteries and for ion pumping techniques as its output voltage is within the stability window of aqueous electrolytes [50]. In this chapter, a detailed kinetic study of the (de)insertion process is presented. The aim of this kinetic study is to elucidate the (de)insertion mechanism, extract kinetic constants as a function of state of charge under dynamic conditions, investigate the rate determining processes and estimate the activation energies of the various steps in the (de)insertion of univalent cations (Na^+ and K^+).

7.1 Introduction

Aqueous rechargeable alkali-ion batteries (ARABs) have attracted a lot of attention in stationary energy storage systems. These batteries are alternatives to current LIBs as they resolve some of the challenges associated with the usage of LIBs which include but are not limited to cost, environmental concerns and safety [16, 208, 209]. Transition metal hexacyanoferrate (MHCFs) have been reported as promising cathode materials in aqueous systems due to their cost effectiveness, relatively safety and good electrochemical performance [50, 82, 87–89, 210, 211]. The general formula of MHCFs is $A_xM_y[M'(CN)_6]_{Z'}$ where A is an alkali metal, M and M′ are transition metals [50, 87, 140]. MHCFs have open framework with large interstitial sites and channels for the insertion/extraction of the univalent, divalent and trivalent cations, making MHCFs suitable cathode materials for various battery chemistry [88, 99]. Cui and co-workers reported outstanding cycling and rate capability for nickel hexacyanoferrate nanoparticles, which is an analogue MHCF in aqueous solution of sodium and potassium [50, 89]. The NiHCF nanoparticles demonstrated an outstanding electrochemical performance up to five thousand deep cycles while cycling at 8.3 C, with no fractional capacity loss [50]. Copper hexacyanoferrate which also belongs to the transition

metal hexacyanoferrate family has been reported as an inexpensive cathode material for aqueous media exhibiting long cycle life, high rate capability and high round trip efficiency [87, 212]. Subsequently, various analogues of the transition metal hexacyanoferrates have been reported as cathode/anode materials for univalent, divalent and trivalent ion battery chemistry in aqueous and non-aqueous media [213–216]

Among the MHCFs, nickel hexacyanoferrate is an interesting cathode material for aqueous systems as its electrochemical reaction occurs within the stability window of aqueous electrolytes [53, 88, 89]. In addition to this, nickel hexacyanoferrate has also been reported as a zero strain insertion electrode for alkali ions which means a negligible change ($< 1\%$) in lattice parameters occurring during reversible insertion of univalent cations [56]. Thus, it exhibits a coulombic efficiency of 99.99% and a good rate capability when used as cathode material in aqueous Na-ion batteries [56]. Despite the promising electrochemical performance of NiHCF nanoparticles and metal hexacyanoferrate analogues as cathode materials, the kinetic mechanism of the ion transport in the NiHCF nanoparticles and MHCFs is still not clearly understood. As explained earlier, the understanding of the mechanism is important in optimizing the electrochemical performance of nickel hexacyanoferrate as an electrode material for batteries/battery based applications and also modelling the performance of technologies utilizing NiHCF at different working conditions.

Research involving nickel hexacyanoferrate nanoparticles often focus on the cycling and rate capability [53, 88, 89]. In cases where an attempt has been made in studying the kinetics, it is limited in scope and often carried out in electrochemical cells that are not optimized for kinetic studies using the classic impedance spectroscopy. For example, Wessels and coworkers reported a charge transfer of 1 Ω for 1 cm^2 for copper hexacyanoferrate, an analogue of NiHCF [87]. Omarova et al. estimated the diffusion coefficient of Li^+ in NiHCF to be in the range of 10^{-9} to 10^{-8} cm^2s^{-1} using galvanostatic intermittent titration technique (GITT) [85]. A comparison of the activation energy of the interfacial charge transfer of cations in aqueous and non-aqueous electrolytes was studied by Mizuno et al., who reported that the activation energy of interfacial charge transfer was lower in aqueous systems than in non-aqueous systems [217]. The low interfacial charge transfer in aqueous solvent was attributed to the reduced coulombic repulsion in aqueous media as the insertion process may involve partial desolvated or solvated cations [217]. The result is consistent with the reports of reduced charge transfer resistance of calcium in potassium barium hexacyanoferrate upon addition of 17% water to the acetonitrile-based electrolyte reported by Padigi and co-workers [52]. Thus far, a comprehensive study is still missing despite the huge potential of NiHCF and the role of kinetics in optimizing the cathode material, optimizing the technologies which utilizes NiHCF nanoparticles and modelling the power-energy relation of ARABs using

NiHCF as cathode material.

In this chapter, a comprehensive study of the kinetics of the reversible insertion of univalent cations (Na^+ and K^+) in NiHCF nanoparticles will be done with the aim of providing answers to salient questions needed for the optimization of aqueous batteries based on NiHCF and other technologies utilizing ion transfer of univalent cations. These points include:

- mechanism of the reversible insertion of cation in NiHCF nanoparticles
- temporal evolution of kinetic parameters under dynamic conditions
- rate determining process
- transfer coefficient of the various steps in the (de)insertion process
- activation energies of the various steps in the (de)insertion process

To address these questions, the kinetics of the reversible insertion of univalent cations (Na^+ and K^+) in NiHCF nanoparticles in aqueous media was studied using DMFA, which allows for the investigation of electrochemical systems in-operando.

7.2 Structural Characterization

Fig 7.1a shows the XRD pattern of the NIHCF powder obtained from the synthetic procedure described in section 3.2.

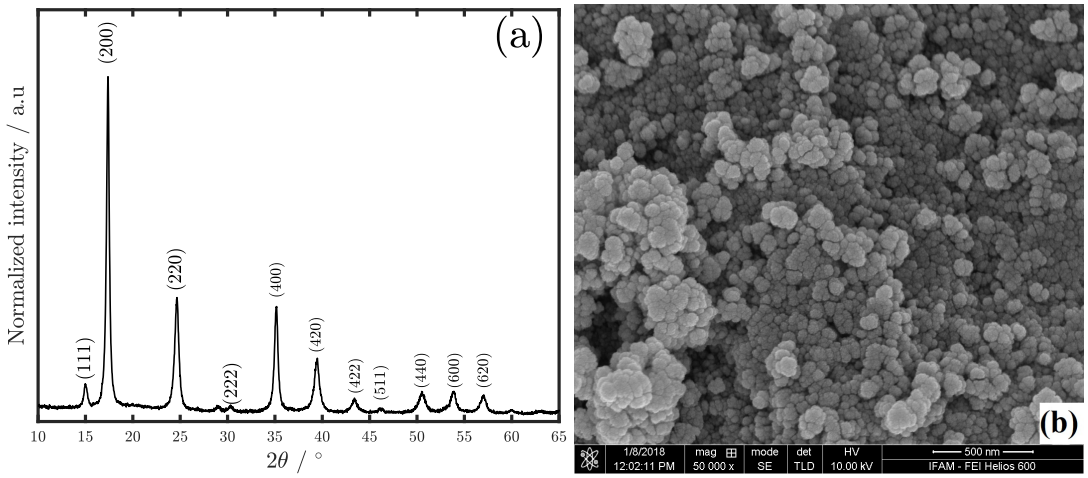

Figure 7.1: (a) XRD pattern (b) SEM image of nickel hexacyanoferrate nanoparticles synthesized using the co-precipitation method described in section 3.2.

The indexed XRD pattern indicates that the synthesized material has a Prussian blue crystal structure with the $Fm\bar{3}m$ space group and a lattice spacing of 10.23 nm [104]. The sharp well

defined peaks and high signal to noise ratio of the PXRD suggests that the synthesized material is highly crystalline. The SEM image (Fig. 7.1b) indicates that the synthesized NiHCF powder is made of porous agglomerated particles with individual particle size in the range of 20-70 nm.

7.3 Electrochemical Analysis

The voltammogram obtained from the application of the quasi triangular waveform in 0.5 M A_2SO_4 with A = Na and K at a scan rate of 8 mVs^{-1} within the potential range of 0 to 0.9 V vs Ag/AgCl is shown in Fig. 7.2. Well defined redox peaks associated with the reversible insertion of Na^+ and K^+ in NiHCF nanoparticles was observed in the voltammogram. The (de)insertion potential depended on the Stokes radius, as observed in the NiHCF film in chapter 6 and consistent with reports in literature [88, 89, 104]. This trend has been attributed to the fact that the reversible insertion potential ($\bar{E}$) can be described as $\bar{E} = -\Delta G^0/nF$ with ΔG^0 is the standard Gibbs free energy of insertion. The major contribution to ΔG^0 is the removal of the solvation shell [88, 89, 104]. As a result, $\bar{E}$ tends towards lower values as Stokes radius increases. Na^+ with a Stokes radius of 1.83 Å had a $\bar{E}$ of 0.4 V compared to 0.5 V for K^+ with Stokes radius of 1.25 Å. The voltammogram indicates that (de)insertion process is reversible and the absence of side reactions within the potential range of the voltammogram.

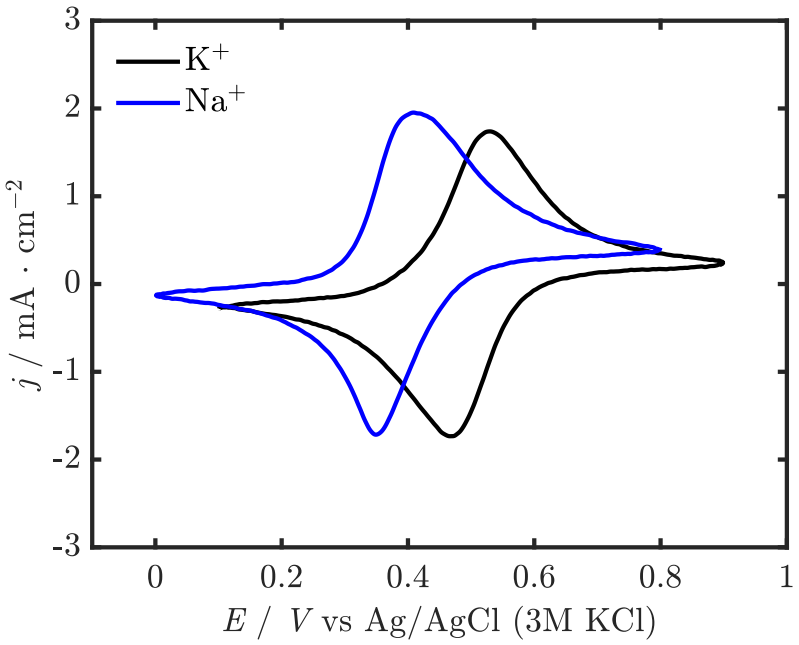

Figure 7.2: Voltammogram obtained from nickel hexacyanoferrate nanoparticles in 0.5 M A_2SO_4 with A = Na and K using a scan rate of 8 mVs^{-1}.

7.4 Dynamic Impedance Spectroscopy

The dynamic impedance obtained during the voltage sweep of the NiHCF electrode is shown in Fig. 7.3 and Fig. 7.4. The impedance spectra obtained at potential regions at the onset/offset of the (de-)insertion process exhibited a RC time constant at high frequency region (semi-circle 1) followed by a second RC time constant (semi-circle 2) terminated by a straight line at the low frequency region characteristic of mass transport. As the potential approaches the (de)insertion potential, the two RC time constants appear to merge and become indistinguishable, as seen in the Nyquist plot of the impedance spectra (Fig. 7.3 and Fig. 7.4).

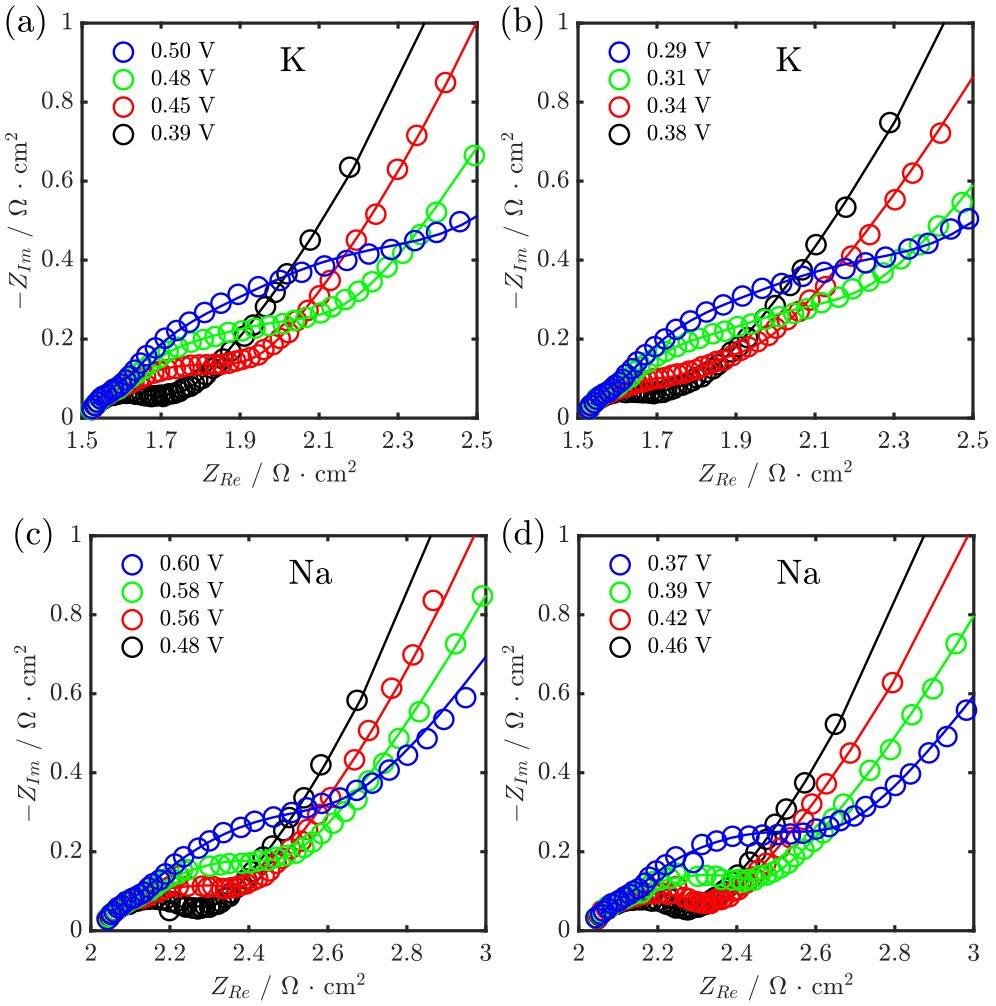

Figure 7.3: Nyquist plots of dynamic impedance spectra of nickel hexacyanoferrate nanoparticles in (a) and (b) 0.5 M K_2SO_4 (c) and (d) 0.5 M Na_2SO_4 during the cathodic scan. ◯ represents the experimental data, while — represents the data from the model.

The impedance spectra suggests that the reversible insertion step of univalent cations (Na^+ and K^+) follows the two step (de)insertion process proposed in chapter 4 and observed for NiHCF

thin film. The two-step involves a (de)solvation step as the first step and the second step is a (de)insertion step:

$$A_{\varepsilon}^{+} \rightleftharpoons A_{i}^{+} \tag{7.1}$$

$$A_{i}^{+} + ANi[Fe^{III}CN_6] + e^{-} \rightleftharpoons A_2Ni[Fe^{II}CN_6] \tag{7.2}$$

where A = Na^+ and K^+, while the IHP and electrolyte phase is denoted with i and ε respectively. The measured impedance was fitted using the modified non-linear least squares minimization objective function described in section 2.9 using the transmission line model modified with the equivalent circuit obtained from modelling the (de)insertion process as a two-step process (Fig. 4.2).

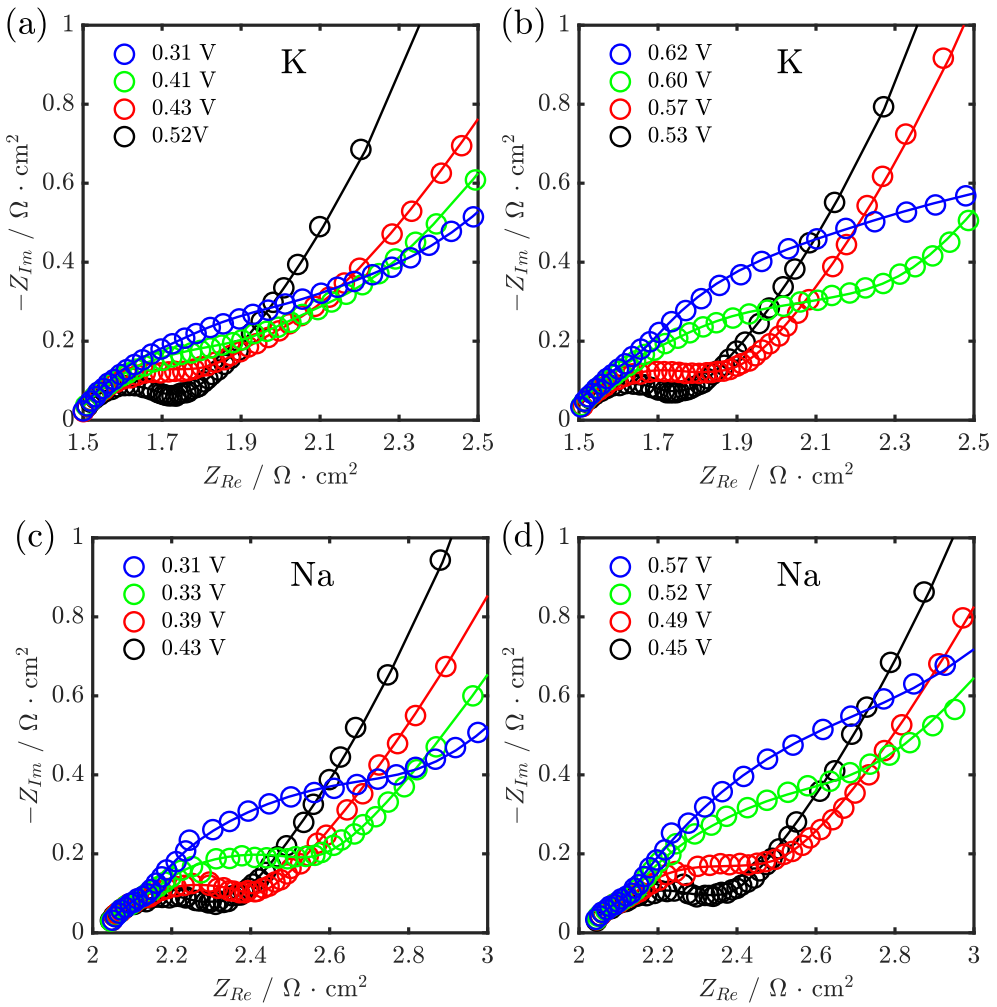

Figure 7.4: Nyquist plots of dynamic impedance spectra of nickel hexacyanoferrate nanoparticles in (a) and (b) 0.5 M K_2SO_4 (c) and (d) 0.5 M Na_2SO_4 during the anodic scan. ◯ represents the experimental data, while — represents the data from the model.

7.5 Statistical Analysis

The result obtained from fitting the experimental data with the TLM modified with equivalent circuit obtained from modelling the (de)insertion process as a two step process (Fig. 4.2) was subjected to statistical analysis, to eliminate parameters that are statistically insignificant using the method described in section 3.11.

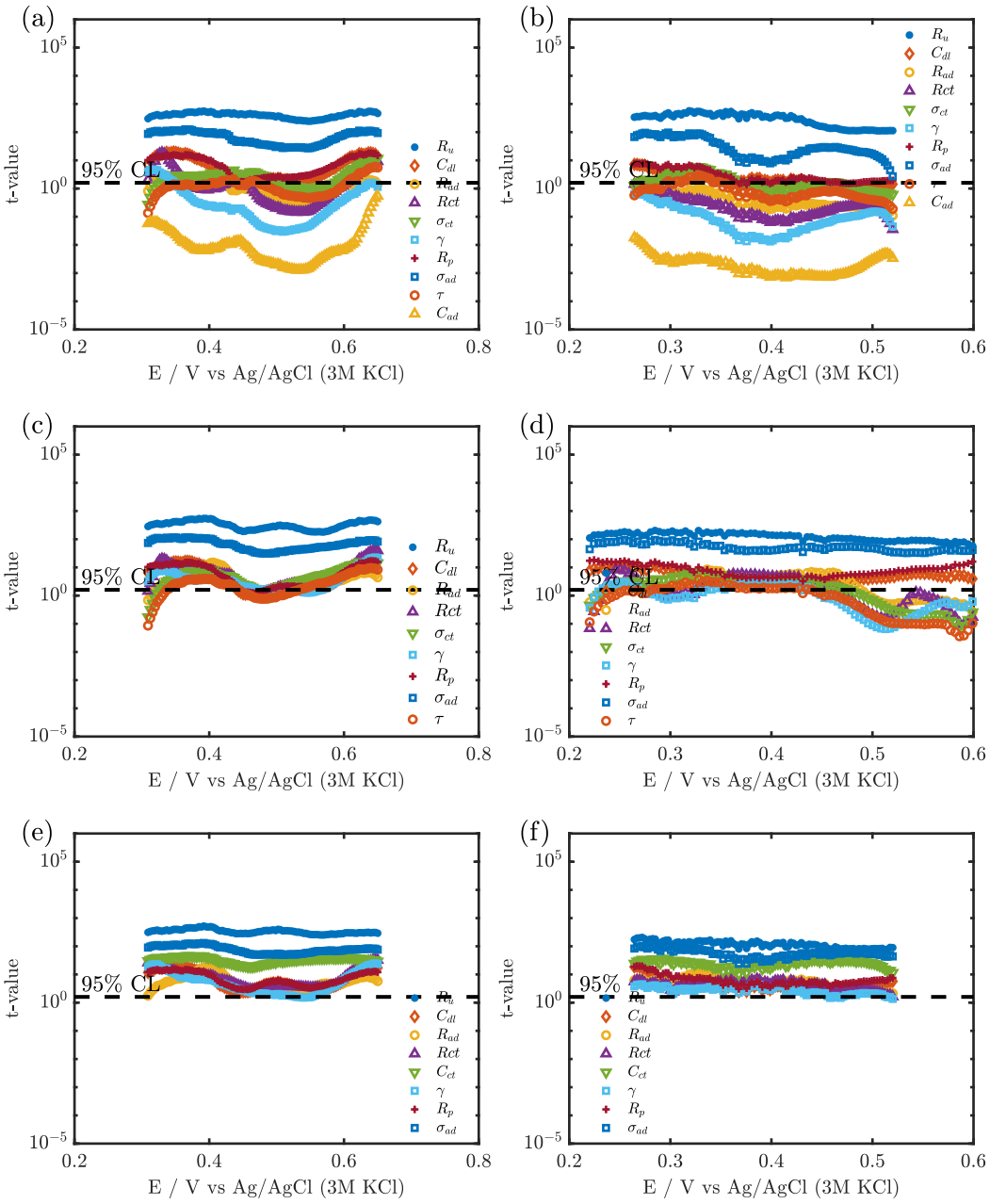

Figure 7.5: Results obtained from the t-test for the parameters obtained from fitting the measured impedance using (a) and (b) equivalent circuit obtained from the model (Fig. 4.2), (c) and (d) equivalent circuit obtained fro the model under treating C_{ad} as a short circuit (Fig. 6.7) (e) and (f) equivalent circuit obtained from the model treating C_{ad} as a short circuit and describing the mass transport in the solid with a capacitor (Fig. 7.6).

The result obtained indicates that most parameters in the circuit were below the 95% confidence level with C_{ad} having the least t-value. Thus, C_{ad} was treated as short circuit with the assumption that C_{ad} is higher than the capacitance in the IHP observed already for NiHCF films [140]. The assumption results in the equivalent circuit shown in Fig. 6.7 and was used for fitting the measured impedance. The fitting had χ^2 values in the range of $5{\cdot}10^{-5}$ to $6{\cdot}10^{-5}$ indicating the goodness of the fit was not compromised by treating C_{ad} as a short circuit. The *t*-values of the parameters extracted from this equivalent circuit indicates that τ was below the confidence level as shown in Fig. 7.5c and Fig. 7.5d. Thus far, the mass transport used in the model has been described using the finite Warburg element. For $\tilde{\omega} \ll 1$ finite Warburg element can be described as [127, 148]:

$$Z_{Wct} = \frac{\sigma_{ct}\sqrt{\tau}}{3} - j\frac{\sigma_{ct}}{\omega\sqrt{\tau}} \tag{7.3}$$

where the first term which corresponds to a resistive part of the Warburg impedance goes to a constant value at low frequency and the second term is the capacitive part of the Warburg impedance. Thus, the mass transport in the solid was described using a capacitor (C_{ct}) resulting in the circuit shown in Fig. 7.6. A good fit (— in Fig. 7.3 and Fig. 7.4) with χ^2 values of $5{\cdot}10^{-5}$ to $6{\cdot}10^{-5}$ with all parameters above the confidence level used in this work was observed from fitting the measured impedance with the equivalent circuit (Fig. 7.6).

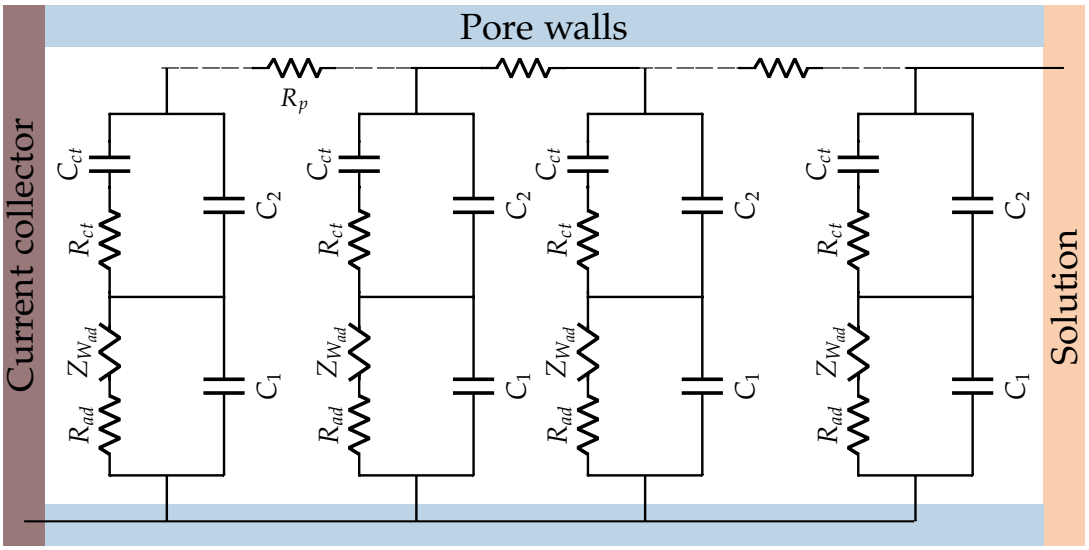

Figure 7.6: Equivalent circuit of the porous electrode including the equivalent circuit obtained from modelling the reversible insertion as two step process treating the capacitance of adsorption (C_{ad}) as a short circuit and describing the mass transport in the solid with a capacitor.

7.6 Kinetic Parameters

In this section, the extracted kinetic parameters as a function of the electrode potential under dynamic conditions is investigated as this provides more insight into the mechanism of (de)insertion.

7.6.1 Resistance

Fig 7.7 shows the adsorption resistance (R_{ad}) extracted from the fit for both cations (Na^+ and K^+). The result was observed to be in agreement with the prediction of the equation 4.56 describing R_{ad} which predicts a minimum in R_{ad} around the standard electrode potential of the reversible insertion process of the cations [140]. Like in NiHCF film, the magnitude of R_{ad} for Na^+ and K^+ was observed to be in same order of magnitude [140]. R_{ad} models the (de)solvation process and as such R_{ad} for cations with similar Stokes radius (Na^+ = 1.83 Å and K^+ = 1.25 Å) is expected to be in same order of magnitude [88, 89, 140, 204].

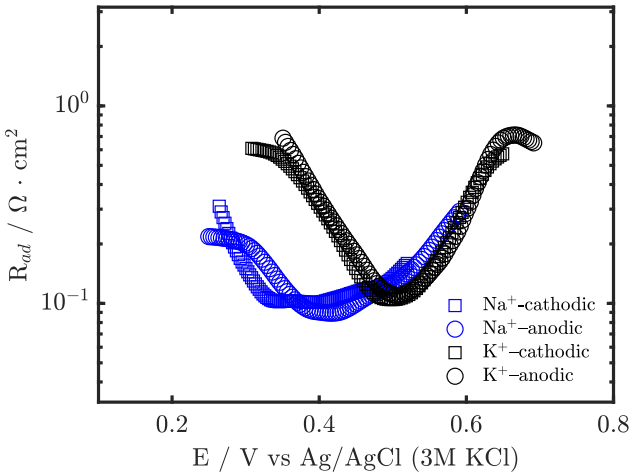

Figure 7.7: Variation of the adsorption resistance (R_{ad}) on the potential during the cathodic and anodic voltage sweep.

The charge transfer resistance (R_{ct}) extracted from the fit for both cations is shown in Fig. 7.7 and exhibited a similar dependence to R_{ad} on the electrode potential. Equation 7.4 predicts a compositional dependence for R_{ct} with a minimum occurrence in the standard electrode potential where the parameters $\theta = 0.5$ and $\beta = 0.5$ assuming a fractional coverage for β and $\alpha_2 = 0.5$ [140]. R_{ct} from reversible insertion of cations in the model can be described as [140]:

$$R_{ct} = \frac{RT}{F^2 k_2^0 C_T [1-\theta]^{1-\alpha_2} \beta^{1-\alpha_2} [1-\beta]^{\alpha_2} \theta^{\alpha_2}} \tag{7.4}$$

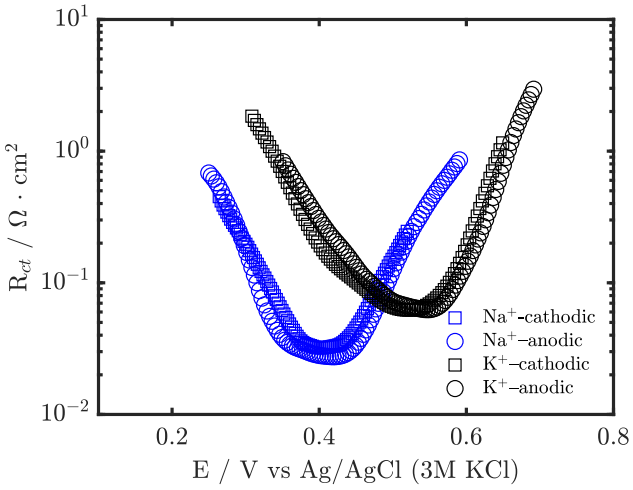

Figure 7.8: Variation of the charge transfer resistance (R_{ct}) on the potential during the cathodic and anodic voltage sweep.

The experimental result was observed to be in good agreement with the model prediction as shown in Fig 7.8.

7.6.2 Rate Determining Step

The rate determining step of the two consecutive steps in the reversible insertion of univalent cations was investigated. This was done by comparing the adsorption resistance to the charge transfer resistance. The result obtained suggests that the rate determining step depends on the state of charge and evolves during the charge/discharge process.

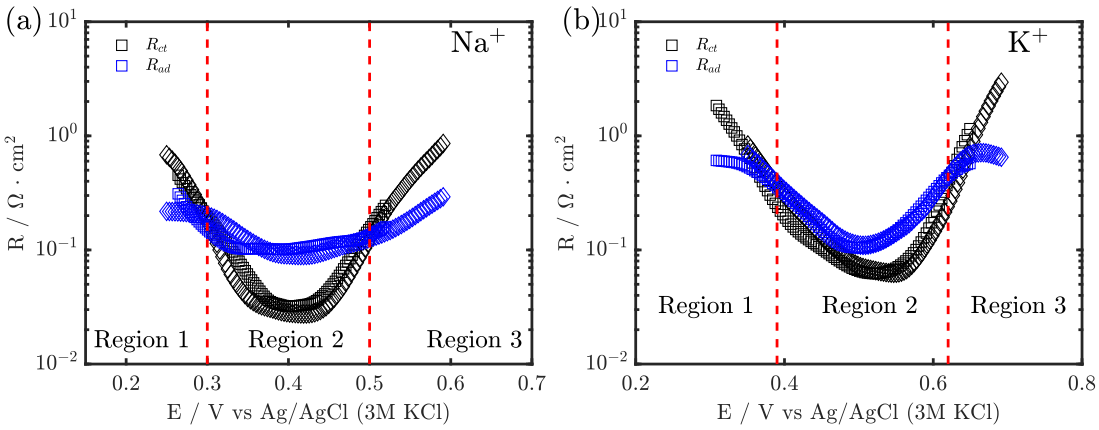

Figure 7.9: Comparison of the adsorption resistance (R_{ad}) and charge transfer resistance (R_{ct}) during the cathodic and anodic voltage sweep for the reversible insertion process of NiHCF nanoparticles in (a) 0.5 M Na_2SO_4 and (b) K_2SO_4.

At the onset/offset of the (de)insertion process i.e. region 1 and region 3 in Fig. 7.9a and Fig. 7.9b, the insertion process is the rate determining step as indicated by the result shown in Fig. 7.9 where R_{ct} is greater than the R_{ad} indicating that the (de)insertion process is the slow

step at this potential region. As the reversible insertion continues towards the standard electrode potential (region 2), R_{ct} is observed to decrease and becomes less than R_{ad} indicating a switch in the rate determining step. In this potential region, the result suggests that the slow step is the (de)solvation process thus it is the rate determining step at this potential region. As the rate determining step of the reversible insertion of cations in NiHCF has not been reported in literature prior to this work, there are no data for comparison. However, the result obtained is consistent with the trend observed for the reversible insertion of Li^+ in graphite and $LiNi_{1/3}Co_{1/3}Mn_{1/3}O_2$ in non-aqueous media where the desolvation step is reported as the rate limiting step [218, 219].

7.6.3 Mass Transport Resistance

Fig 7.10a shows the Warburg coefficient of the mass transport of the cations in the electrolyte (σ_{ad}) obtained during the voltage sweep.

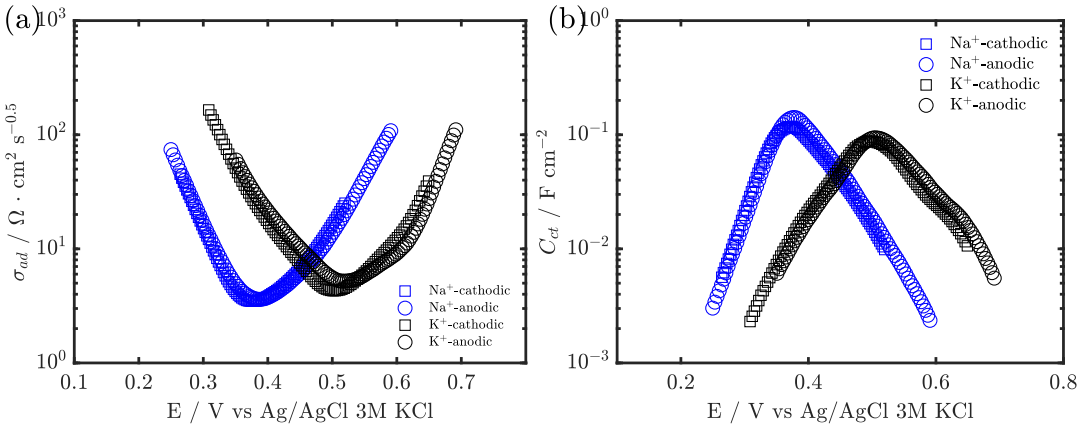

Figure 7.10: (a) Variation of the Warburg coefficient of the mass transport of the cations in the electrolyte (σ_{ad}) during the cathodic and anodic scan. (b) Variation of the pseudocapacitance (C_{ct}) during the cathodic and anodic scan.

The result indicates a dependence of σ_{ad} on electrode potential as observed in NiHCF thin film with a minimum occurrence at the standard electrode potential of the cations. This is contrary to the prediction of the model (eq. 4.71) which predicts that the mass transport resistance is independent on the electrode potential. Alternatives such as setting σ_{ad} to a fixed value, which was used for NiHCF thin films or assuming the mass transport in the liquid is negligible resulted in an increase in the χ^2 value by one order of magnitude. The dependence of σ_{ad} on electrode potential suggest that the model does not fully describe the mass transport in the liquid for the reversible insertion of univalent cations in NiHCF nanoparticles. Further investigation is needed to optimize the fitting and/or understand the reason behind this deviation. The mass transport resistance in the electrolyte was observed to be similar for both cations which has been attributed

to the similarity of their diffusion coefficient in aqueous systems where the diffusion coefficient for $Na^+ = 1.33 \cdot 10^{-5} cm^2 s^{-1}$ and $K^+ = 1.96 \cdot 10^{-5} cm^2 s^{-1}$) [207, 220].

The pseudocapacitance (C_{ct}) which describes the mass transport in the solid extracted from the fit is shown in Fig 7.10b exhibiting compositional dependence. This can be attributed to the term $[1-\theta] \cdot \theta$ in the description of C_{ct} (equation 7.5) which is obtained from substituting equation 4.79 into equation 7.3.

$$C_{ct}^{-1} = \frac{RT}{F^2} \frac{1}{C_T \, \theta \, (1-\theta) \, l} \tag{7.5}$$

7.7 Transfer coefficient

The transfer coefficient (α) which is a measure of the symmetry barrier was estimated for the (de)solvation and (de)insertion step.

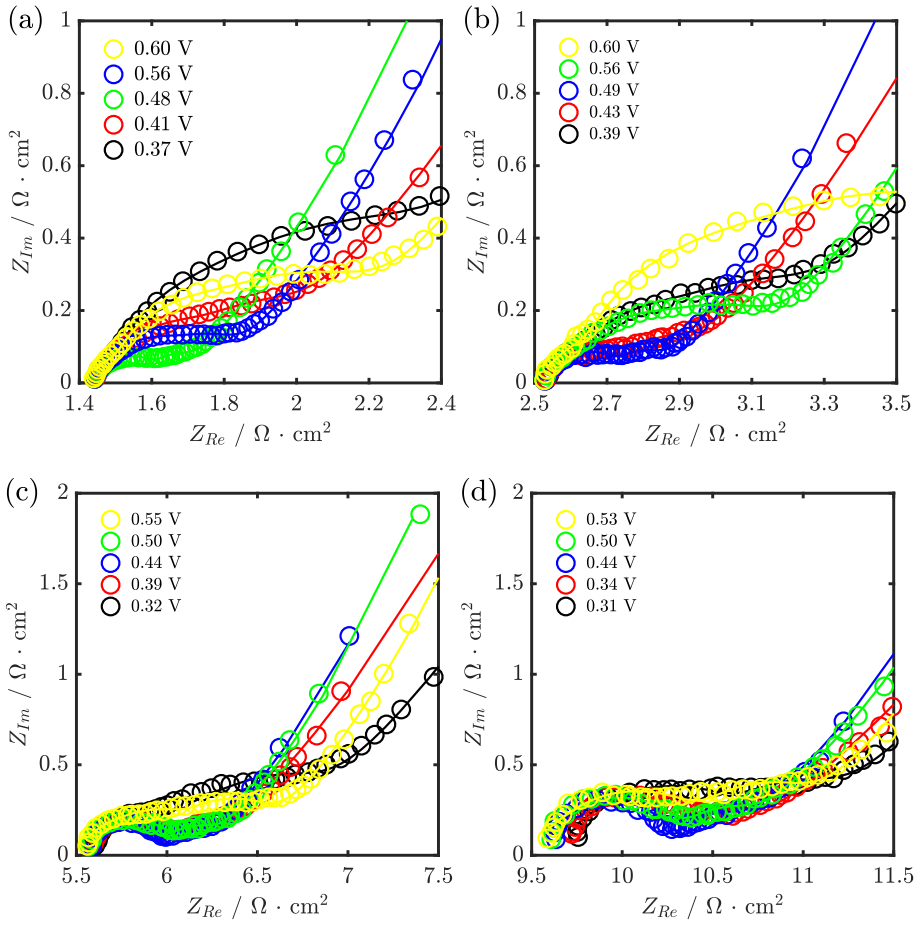

Figure 7.11: Nyquist plot of the measured impedance of Nickel hexacyanoferrate nanoparticles electrodes at different potential during the cathodic scan in (a) 500 mM (b) 250 mM (c) 100 mM and (d) 50 mM K_2SO_4.

The transfer coefficient (α) is an important kinetic parameter in batteries as it represents the fraction of electrostatic potential affecting the reaction rate in an electrochemical reaction [221]. To extract α, NiHCF nanoparticles were studied in 500 mM, 250 mM, 100 mM and 50 mM of A_2SO_4 with A = Na and K. Fig. 7.11 and Fig. 7.12 shows impedance spectra obtained at different potential during the cathodic scan in the different concentrations studied.

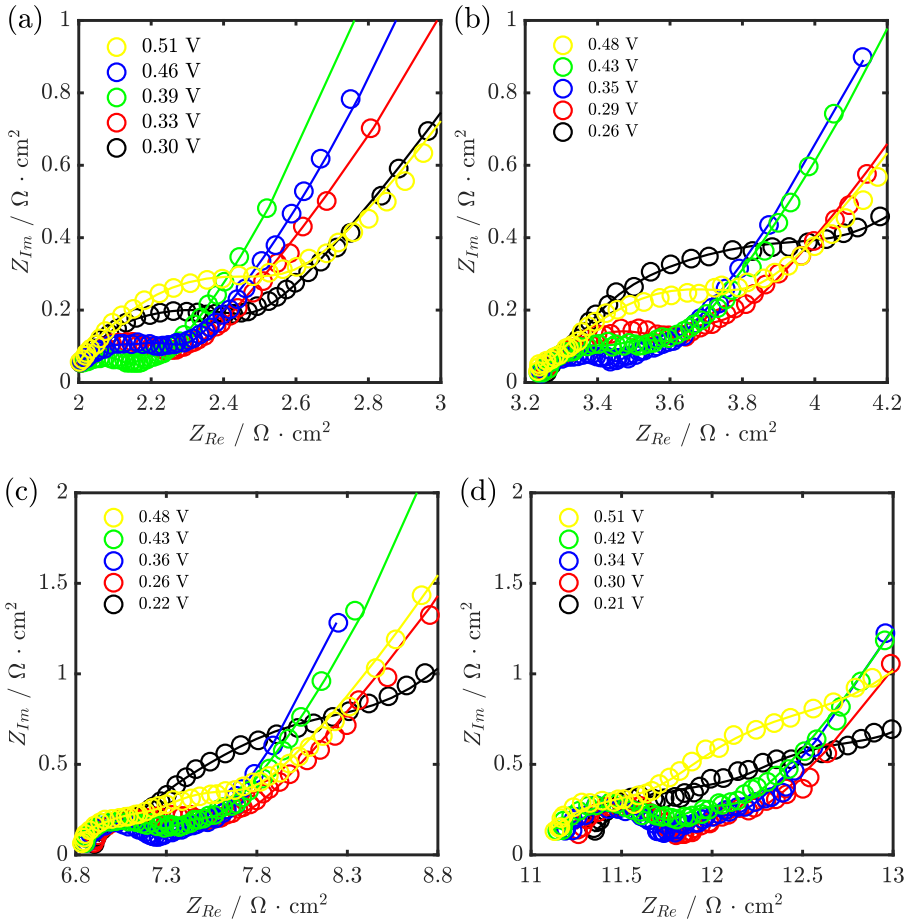

Figure 7.12: Nyquist plot of the measured impedance of Nickel hexacyanoferrate nanoparticles electrodes at different potential during the cathodic scan in (a) 500 mM (b) 250 mM (c) 100 mM and (d) 50 mM Na_2SO_4.

The spectra were observed to be similar in shape to those shown in Fig. 7.3 with two semi-circle at the onset/offset of the (de)insertion process which becomes indistinguishable as the reaction proceed. χ^2 in the range of $1 \cdot 10^{-5}$ to $5 \cdot 10^{-5}$ was obtained fitting the measured impedance with the equivalent circuit shown in Fig. 7.6. Fig. 7.13 shows the R_{ad}^{-1} extracted from the fit of the dynamic impedance acquired at the different concentration of the cations studied.

As predicted by the equation 4.56, which describes the adsorption resistance, R_{ad}^{-1} was observed to increase with increasing electrolyte concentration in potential regions away from the

onset/offset of the (de)insertion process. Using the linear form of equation 4.56 allows for the estimation of the transfer coefficient of the desolvation step (α_1) from the slope of the plot of log (R_{ad}^{-1}) versus log (C_{A_ε}) shown in Fig.7.14c. 0.72 and 0.80 was estimated as the transfer coefficient of the desolvation step for K^+ and Na^+ respectively. A transfer coefficient value of 0.5 indicates that the electrochemical process is symmetrical i.e. the amount of overpotential affecting the cathodic and anodic reaction rate is the same. The (de)solvation transfer coefficient value extracted in this work for both cations (Na^+ and K^+) indicates that the (de)solvation step is an asymmetrical process. The reason for this asymmetry is not clear at the moment and may require further studies. However, it may be speculated that the deviation of α_1 from 0.5 may be attributed to electrostatic interactions occurring during the reorganization of the double layer which occurs during the (de)solvation step.

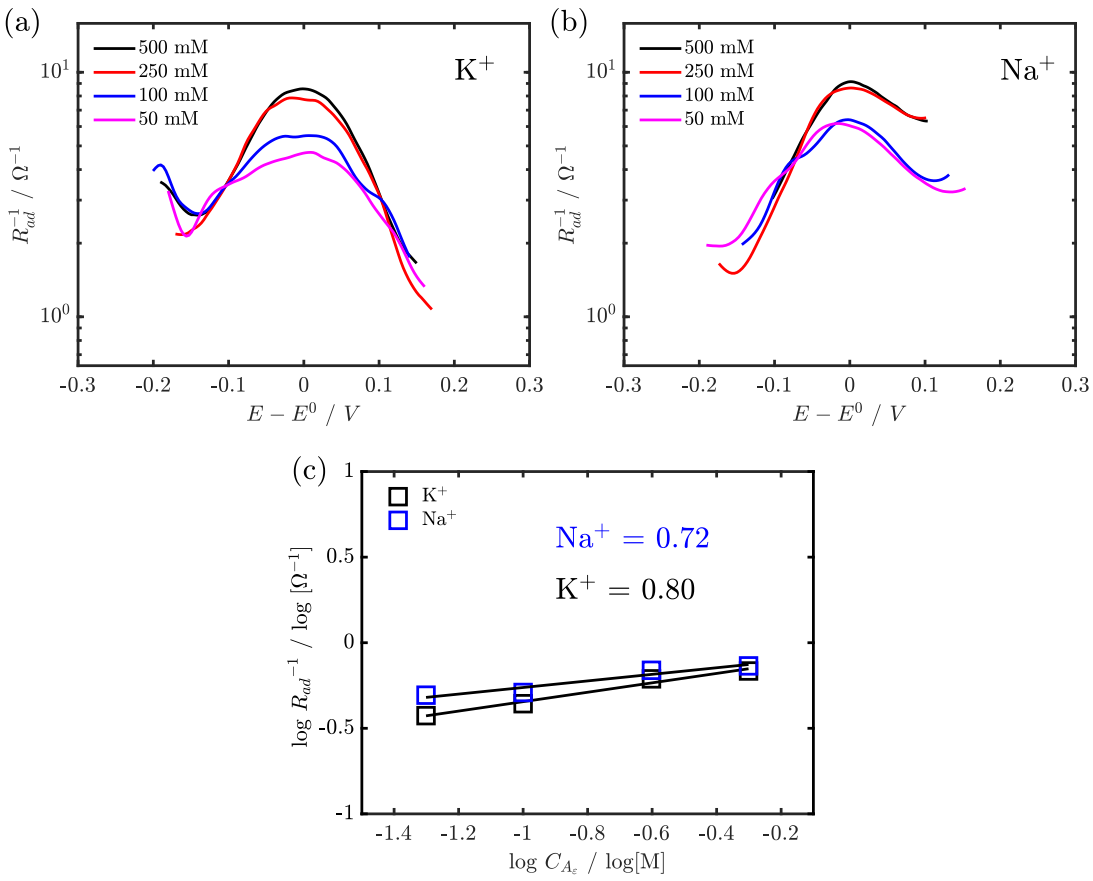

Figure 7.13: Plot of R_{ad}^{-1} versus electrode potential of nickel hexacyanoferrate nanoparticles at different concentration of (a) K_2SO_4 (b) Na_2SO_4 (c) Plot of $\log\left(R_{ad}^{-1}\right)$ against $\log(C_{A_\varepsilon})$ for nickel hexacyanoferrate nanoparticles.

The transfer coefficient of the (de)insertion step (α_2) was also estimated from the slope of plot of log (R_{ct}^{-1}) versus log (C_{A_ε}) shown in Fig.7.14c. While the linear form of the equation describing

R_{ct} predicts a dependence of R_{ct} on θ and β, close to equilibrium both θ and β depends on the electrolyte concentration as shown in equation 4.47, 4.48 and 4.49. Thus, α_2 can be extracted from the slope of log (R_{ct}^{-1}) versus log (C_{A_ε}). The transfer coefficient of the (de)insertion step was estimated to be 0.59 for Na^+ and 0.56 for K^+ from the slope of log (R_{ct}^{-1}) versus log (C_{A_ε}). It can be inferred from the values of α_2 for both cations, that the (de)insertion step is a symmetric process.

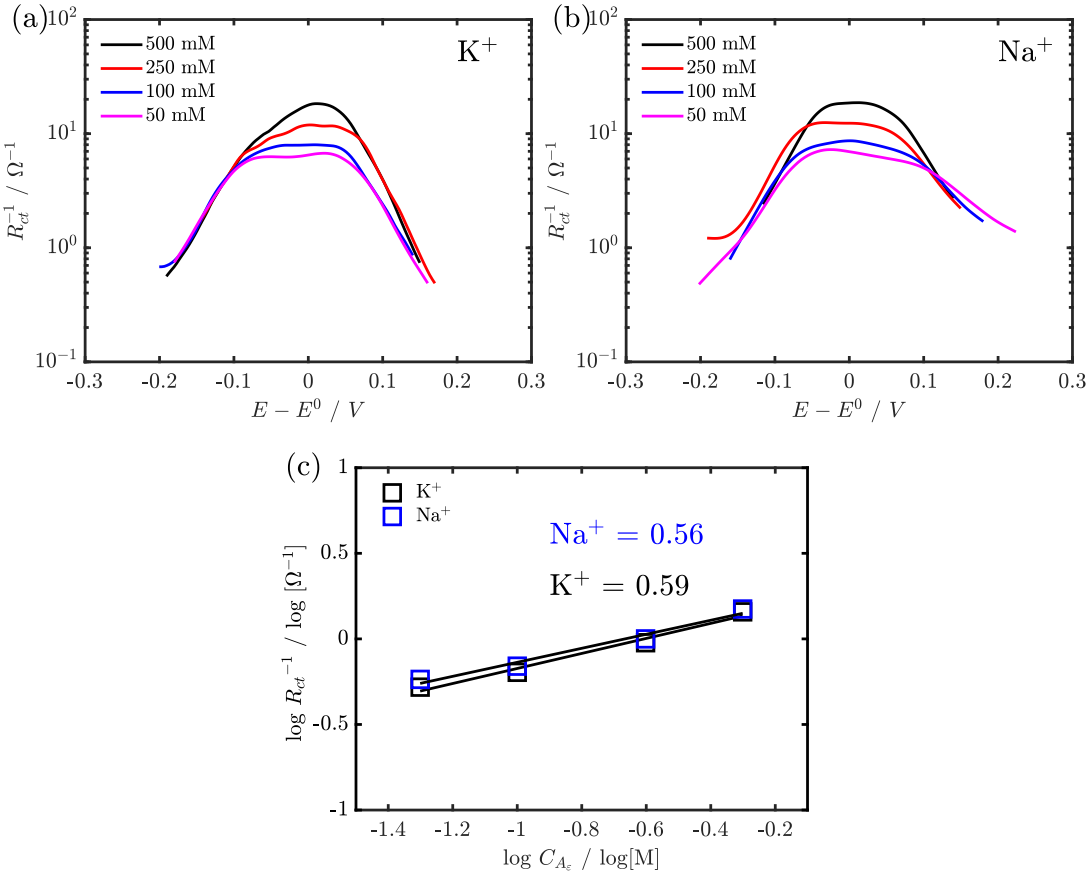

Figure 7.14: Plot of R_{ct}^{-1} versus electrode potential of nickel hexacyanoferrate nanoparticles at different concentration of (a) K_2SO_4 (b) Na_2SO_4 (c) Plot of $\log\left(R_{ct}^{-1}\right)$ against $\log(C_{A_\varepsilon})$ for nickel hexacyanoferrate nanoparticles.

7.8 Activation Energies of Various Physicochemical Processes

The result obtained thus far indicates that the reversible insertion involves various steps such as the (de)solvation, (de)insertion and mass transport both in the liquid and in the solid. In this section, the activation energies of the various steps in the (de)insertion process was estimated. The activation energy represents the barrier that must be surmounted for the various steps in the reversible insertion to occur, thus lower activation energy represents faster kinetics [217]. Dynamic

impedance of NiHCF in 0.5 M Na_2SO_4 and K_2SO_4 were acquired at different temperatures. The measured impedance spectra were fitted using the equivalent circuit shown in Fig. 7.6. The temperature dependence of R_{ad} for the NiHCF nanoparticles electrode in 0.5 M Na_2SO_4 and K_2SO_4 in the temperature range of 278.15 K to 298.15 K is shown in Fig. 7.15. The extracted R_{ad} increases as the temperature decreases exhibiting an Arrhenius type behaviour which is predicted by the equation describing the standard rate constant for the (de)solvation step (k_1^0):

$$k_1^0 = \frac{1}{R_{ad}} = A_{ad}\ \exp\left(\frac{-E_a^1}{RT}\right) \tag{7.6}$$

where A_{ad} is the frequency factor for the desolvation and E_a^1 is the activation energy of the (de)solvation step which represents the barrier for the cations have to overcome during the (de)solvation.

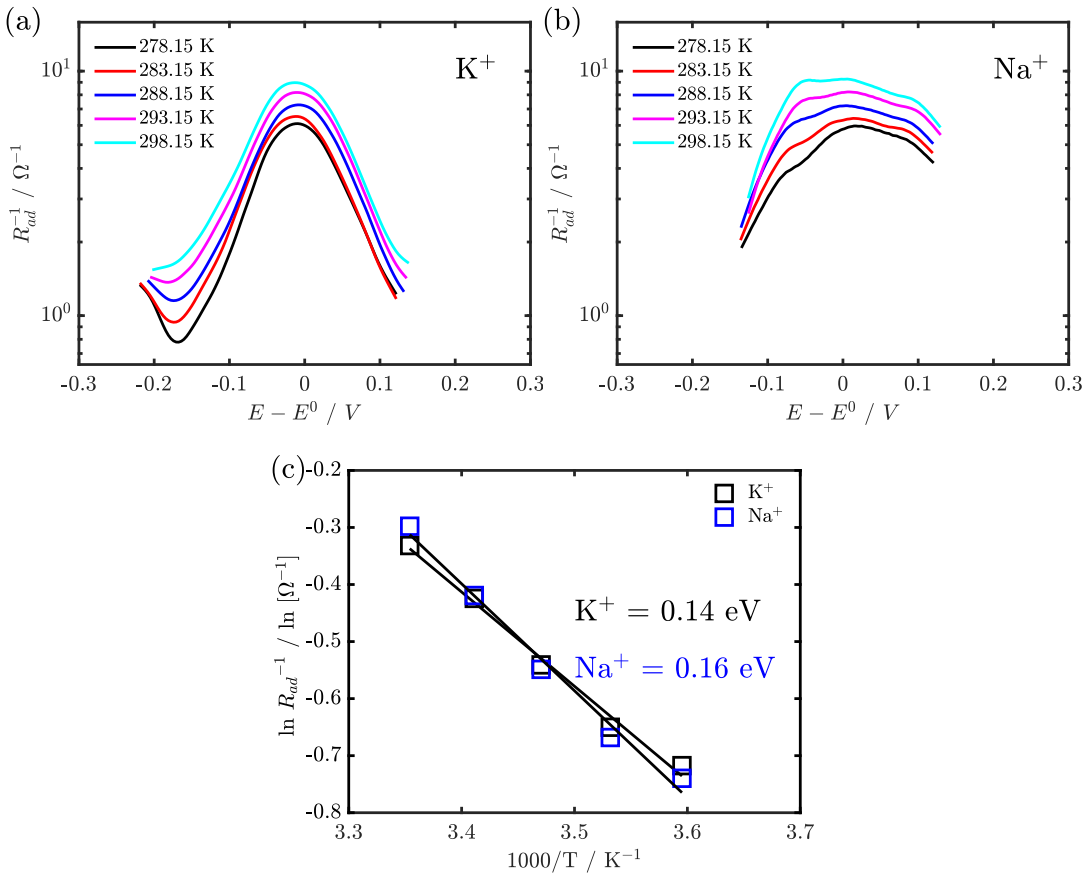

Figure 7.15: Plot of R_{ad}^{-1} versus electrode potential of nickel hexacyanoferrate nanoparticles in (a) 0.5 M K_2SO_4 (b) 0.5 M Na_2SO_4 (c) Plot of ln R_{ad}^{-1} against 1000/T for nickel hexacyanoferrate nanoparticles in 0.5 M K_2SO_4 and 0.5 M Na_2SO_4.

E_a^1 extracted from the slope of the plot of $\ln\left(R_{ad}^{-1}\right)$ at the standard electrode potential versus $1000/T$ was 0.16 eV for Na^+ and 0.14 eV for K^+. The similarity of E_a^1 for both cations suggests that the kinetic barrier surmounted by both cations during the (de)solvation process is similar. This can be attributed to similarity in Stokes radii of the cations since the (de)solvation step involves the removal/formation of the solvation sheath. The activation energy for the (de)insertion step was also estimated from the plot of $\ln\left(R_{ct}^{-1}\right)$ versus $1000/T$ which shows a linear behaviour with increasing R_{ct} as the temperature decreases. The thermal activation process for the (de)insertion step is postulated by the equation below:

$$k_2^0 = \frac{1}{R_{ct}} = A_{ct}\ \exp\left(\frac{-E_a^2}{RT}\right) \tag{7.7}$$

where k_2^0 is the standard rate constant of the (de)insertion step, A_{ct} is the frequency factor of the (de)insertion step and E_a^2 denotes the activation energy of the (de)insertion process. The E_a^2 for Na^+ was estimated to be 0.04 eV and 0.1 eV for K^+.

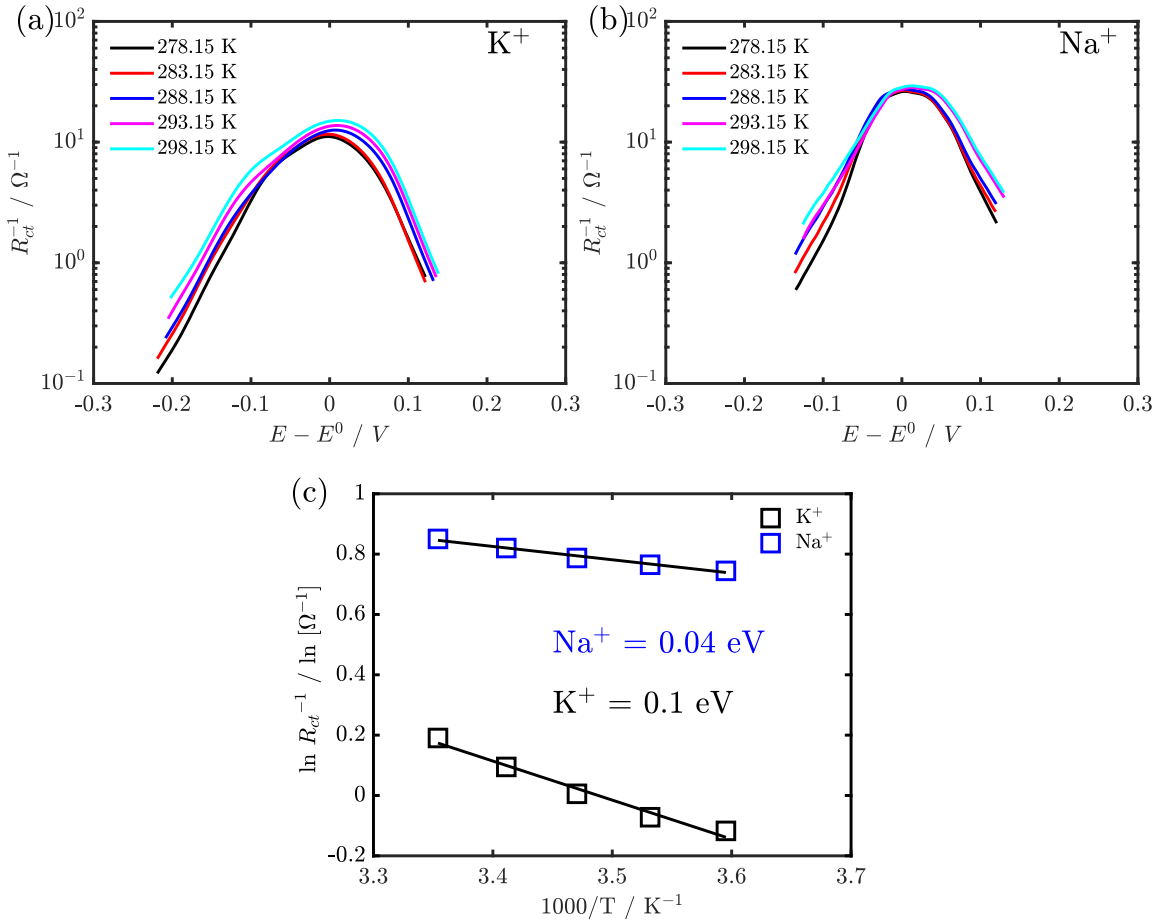

Figure 7.16: Plot of R_{ct}^{-1} versus electrode potential of nickel hexacyanoferrate nanoparticles in (a) 0.5 M K_2SO_4 (b) 0.5 M Na_2SO_4 (c) Plot of ln R_{ct}^{-1} against 1000/T for nickel hexacyanoferrate nanoparticles in 0.5 M K_2SO_4 and 0.5 M Na_2SO_4.

The result indicates that the activation energy for the (de)insertion of K^+ (0.1 eV) is higher than the activation energy of Na^+ (0.04 eV) despite having similar Stokes and ionic radii (Stokes radii Na^+ = 1.83 Å , K^+ = 1.25 Å, ionic radii = Na^+ = 1.00 Å, K^+ = 1.38 Å) [88, 89, 204]. This is in contrast to the result observed for the activation energy of the (de)solvation step, where a similar activation energy was observed for both cations. A plausible reason for the observed difference could be different coulombic repulsion at the electrode/electrolyte interface. To be certain about the origin of the observed difference, the reversible insertion process should be studied coupling DMFA with quartz crystal micro-balance (QCM). The use of QCM will provide information about the nature of the partial desolvated species, which is necessary to further understand the difference observed in E_a^2.

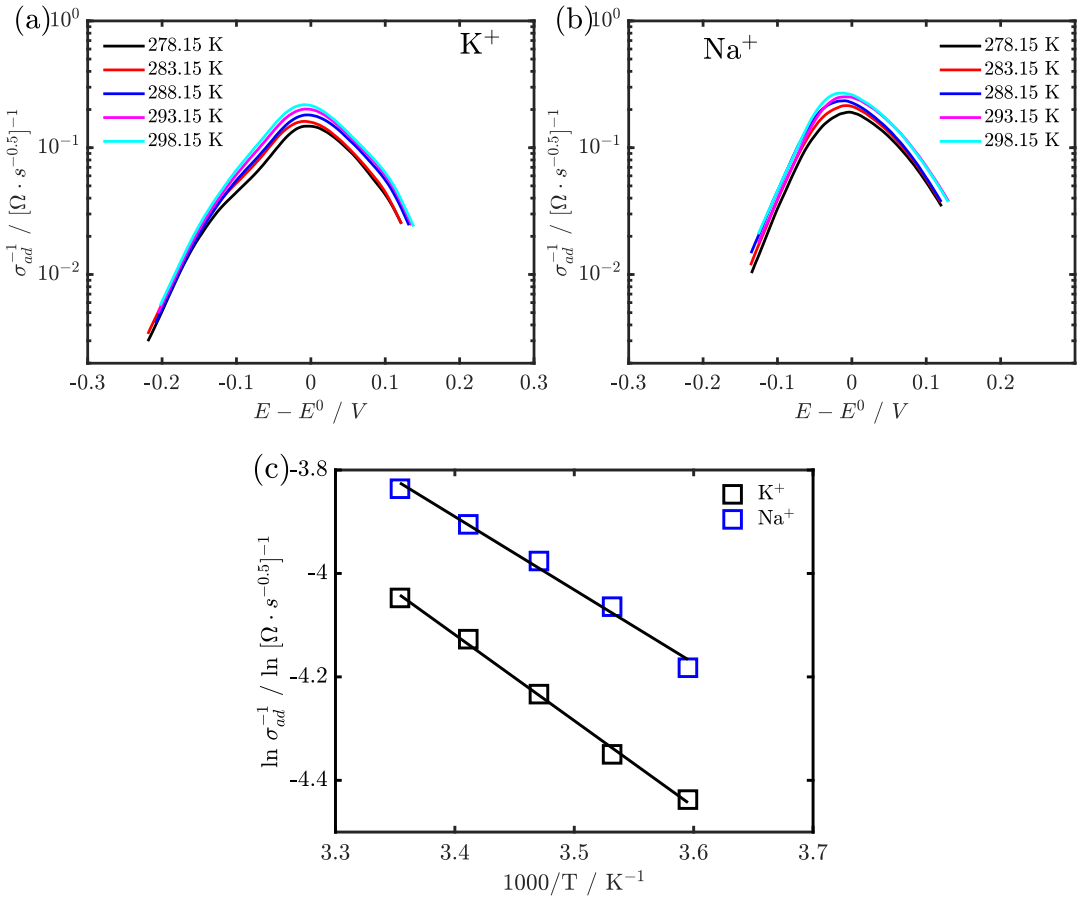

Figure 7.17: Plot of σ_{ad}^{-1} versus electrode potential of nickel hexacyanoferrate in (a) 0.5 M K_2SO_4 (b) 0.5 M Na_2SO_4 (c) Plot of ln σ_{ad}^{-1} against 1000/T for nickel hexacyanoferrate nanoparticles in 0.5 M K_2SO_4 and 0.5 M Na_2SO_4.

The diffusion coefficient of the cations in the electrolyte phase D_{A_ε} in the model is a temperature dependent parameter as suggested by equation 4.71 in chapter 4 and as such the activation

energy of the mass transport process can be estimated using an Arrhenius plot. Thus D_{A_ε} can be described as:

$$D_{A_\varepsilon} = \frac{1}{\sigma_{ad}} = A \ \exp\left(\frac{-E_a^3}{RT}\right) \tag{7.8}$$

where E_a^3 is the activation energy of the mass transport process in the electrolyte phase. Fig. 7.17 shows the plot of the extracted Warburg coefficient in the electrolyte (σ_{ad}) versus temperature for both cations. The result obtained indicates that σ_{ad}^{-1} increase with increasing temperature. The activation energy of the mass transport in the electrolyte estimated from the slope in Fig 7.17c was 0.14 eV for K^+ and 0.12 eV for Na^+. The observed similarity in activation energy can be attributed to similarity in the Stokes radii. The activation energy of the cations in the solid could not be determined in this study as the mass transport in the solid is described using a capacitance C_{ct} which is not dependent on the diffusion coefficient of the cations in the solid as shown in equation 7.5.

Thus far, it has been theorized that the desolvation step involves a partial desolvation of the cations followed by (de)insertion step which may involve further desolvation depending on the size of the channels connecting the (de)insertion site and the size of the cations. The rate determining step was observed to depend on the state of charge. At potential regions around the insertion potential of the charge/discharge process, the rate determining step was observed to be the (de)solvation step. This information can be used in optimizing electrode/electrolyte interface of battery or battery based application utilizing NiHCF. As the (de)solvation is the rate limiting step around the (de)insertion peak, strategies can be researched to increase the (de)solvation rate which may include the use of increased electrolyte concentration and the use of electrolytes additives. The transfer coefficient parameters extracted from this work also provides insight into the symmetry of the (de)solvation process and (de)insertion process and the results can be used in modelling of the reversible insertion process. The (de)insertion activation energy extracted in this study were observed to be in the same order of magnitude with the those reported by Mizuno et al. who reported 0.05 eV for the reversible insertion of Na^+ compared to 0.04 eV extracted in this study [217]. However, it is important to highlight that Mizuno et al. studied just the (de)insertion process as the static impedance used in their study were acquired from 50 kHz to 5 mHz, while the dynamic impedance acquired in this study was from 350 kHz to 2.8 Hz thus allowing for the desolvation process to be studied in this work.

7.9 Conclusion

In this chapter, the kinetics of the reversible insertion of univalent cations (Na^+ and K^+) in NiHCF nanoparticles in aqueous media were investigated. The result suggests a two step (de)insertion process: (de)solvation and (de)insertion. The rate determining step was observed to be dependent on the state of charge with the (de)solvation step as the rate determining step around the standard electrode potential. The desolvation process was observed to be asymmetric as suggested by the transfer coefficient for the (de)solvation step (0.80 for Na^+ and 0.72 for K^+) while the transfer coefficient of the (de)insertion process indicates a symmetric process (0.59 for Na^+ and 0.56 for K^+). The origin of the asymmetry in the (de)solvation step although not clear at the moment could originate from electrostatic interaction during the reorganization of the double layer which occurs during (de)solvation of cations. Activation energies of 0.16 eV and 0.14 eV was obtained for the (de)solvation of Na^+ and K^+ respectively while the activation energies for the (de)insertion process was estimated for Na^+ and K^+ were 0.04 eV and 0.1 eV respectively. As the rate determining process at the (de)insertion peak is the desolvation step, strategies to increase the rate of (de)solvation can be investigated. The qualitative and quantitative mechanistic information obtained in this chapter can be used in tailoring electrode/electrolyte interfaces as well as bulk NiHCF nanoparticles for improved electrochemical performance. The result also provides kinetic parameters that can be used for modelling the electrochemical process occurring in the electrode/electrolyte interface.

Chapter 8

Kinetic Investigation of Lithium Insertion in $LiMn_2O_4$ Thin Films Made by Multi-layer Pulse Laser Deposition

$LiMn_2O_4$ thin films made by multi-layer pulse lase deposition (PLD) has been reported as a promising cathode material for micro-batteries due to its cycling stability, high energy density, high power density, cost effectiveness and environmental friendliness [222, 223]. Increasing the energy density of $LiMn_2O_4$ films made by multi-layer pulse laser deposition (PLD) by increasing film thickness however results in a decrease in the power density [223]. In this chapter, the kinetics of the reversible insertion process in $LiMn_2O_4$ thin films made by multi-layer PLD was studied using DMFA.

8.1 Introduction

Due to the rapid growth in the usage of microelectronics, there has been an increase in the research and development of thin film cathode and anode materials with high energy density, high power density, good rate capability, cost effectiveness and environmental friendliness [224]. $LiMn_2O_4$ has been reported to meet these desired characteristic, making it a promising cathode material for the film batteries. Thin films of $LiMn_2O_4$ can be prepared using several methods ranging from chemical vapour deposition [225], sputtering [226], spray pyrolysis [227], and laser deposition [228]. By adapting the deposition parameters, such as temperature, background pressure target to substrate distance, the phase and microstructure of the $LiMn_2O_4$ thin films can be controlled [27, 229–234]. This allows for the electrochemical performance of the deposited films to be improved [27, 229–234].

Recently, $LiMn_2O_4$ thin films deposited on a silicon substrate with platinum as the current collector by multi-layer pulse laser deposition (PLD) were reported to have outstanding electrochemical performances in aqueous media, a coulombic efficiency of 99.999% while cycling at 348 C [222]. The films demonstrated a higher rate capability compared to films reported by Singh

et al. 99.986% per cycle for 1100 cycles at 18 C [232] and Tang et al. 99.981% per cycle for 500 cycles at 18 C [235]. Using zinc as an anode and $LiMn_2O_4$ thin films made by multi-layer PLD as a cathode, a dual ion aqueous battery with energy density similar to those of lithium-ion batteries was reported by Trócoli et al. [223]. The dual-ion battery had a specific power density of 3400 W kg^{-1} with a coloumbic efficiency of 99.94% over 300 cycles [223]. An increase in film thickness of $LiMn_2O_4$ thin films resulted in an increase in specific energy and a decrease in the power density [223]. Specific energy of 16 Wh kg^{-1} and 81 Wh kg^{-1} was reported for the 400 nm and 1000 nm $LiMn_2O_4$ films respectively while a power density of 3420 W kg^{-1} for the 400 nm thick film was obtained compared to 2640 W kg^{-1} for the 1000 nm film [223]. To understand this decrease in power density as the film thickness increases, the kinetics of the reversible insertion of lithium in $LiMn_2O_4$ thin films made by multi-layer PLD was studied in this work. Thus far, the kinetics of the reversible insertion of Li^+ in aqueous system has not been satisfactorily studied. This is in direct contrast to the kinetics of Li^+ in $LiMn_2O_4$ in non aqueous media where substantial amount of study has been done [232, 236–238]. In cases where an attempt has been made in studying the kinetics of reversible insertion of $LiMn_2O_4$ film in aqueous media, the aim was to explore the difference in kinetics in aqueous and non-aqueous media [237, 239]. Lee et al. reported that the reversible insertion of Li^+ in is more facile in aqueous systems than in non-aqueous systems due to the resistivity of solid electrolyte interphase (SEI) in non aqueous electrolyte and the reduced conductivity of the non-aqueous electrolyte [239]. Nakayama et al. reported an activation energy of 23—25 kJ/mol and 50 kJ/mol for interfacial lithium ion transfer in aqueous media and non aqueous media respectively, indicating a faster interfacial process in aqueous media [237].

In this chapter, the kinetics of the reversible insertion of Li^+ and the effect of film thickness on the kinetics in $LiMn_2O_4$ films made by multi-layer PLD was investigated using DMFA. The first part of the study focuses on studying the mechanism of the reversible insertion of lithium in $LiMn_2O_4$ in aqueous media and the effect of film thickness on the kinetics of the reversible insertion of lithium in $LiMn_2O_4$ films made by multi-layer PLD was investigated in the second part of the study.

8.1.1 Structural Characterization

Thin films made by multi-layer PLD used in this chapter were provided by collaborators from the Catalonia Institute for Energy Research (IREC) [223, 240, 241]. XRD pattern of the deposited 200 nm $LiMn_2O_4$ thin film on Si|TiN|Pt substrates is shown in Fig. 8.1. The (111) peak which is associated with $LiMn_2O_4$ at 18.6° was observed in the diffractogram indicating $LiMn_2O_4$ spinel (JCPDS 00-035-782) was obtained by the multi-layer PLD. The peaks observed at 33.1°, 39.2° and

61.8° are associated with the Si|TiN|Pt substrate. The presence of small amounts of Mn_3O_4 in the deposited $LiMn_2O_4$ layers is observed in the broad shoulder of the peak occurring at 18.6° which is consistent with reports in literature [223, 240].

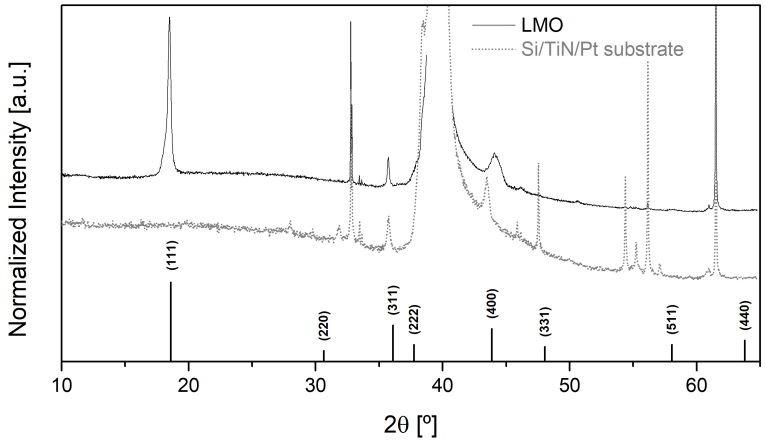

Figure 8.1: XRD diffractogram of the 200 nm thick multi-layer deposited thin film and the ascribed spinel phase $LiMn_2O_4$ (JCPDS 00-035-782) indicated in the plot with its corresponding (hkl) [242].

The top view and the cross-sectional SEM micrograph of the deposited $LiMn_2O_4$ film is shown in Fig 8.2. The SEM images indicates that the deposited film is a dense homogeneous film with randomly orientated grains. The thickness of the film estimated with FIB-SEM indicates the the deposited LMO film is ca. 200 nm thick [242]..

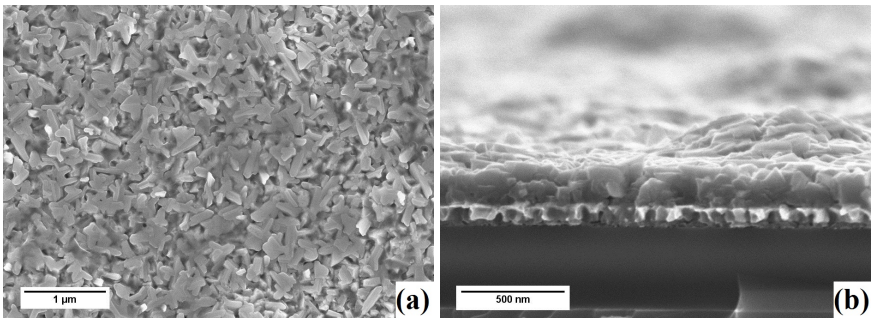

Figure 8.2: SEM images of the (a) top view and (b) cross-sectional view of the deposited 200 nm $LiMn_2O_4$ thin film [242].

8.1.2 Electrochemical Properties of $LiMn_2O_4$ Films made by Multi-layer PLD

The cyclic voltammogram obtained from the application of the quasi-triangular waveform to the 200 nm $LiMn_2O_4$ film in 1 M Li_2SO_4 is shown in Fig. 8.3. The voltammogram indicates two coupled peaks A/A' and B/B' occurring at 0.93 V/0.86 V and 0.79 V/0.74 V indicating a peak separation (ΔE_p) of 60 mV and 40 mV respectively. These peaks have been attributed to the

(de)insertion of Li^+ in the different solid solutions of the $LiMn_2O_4$ with different chemical potential of lithium (μ_{Li}) [160–162].

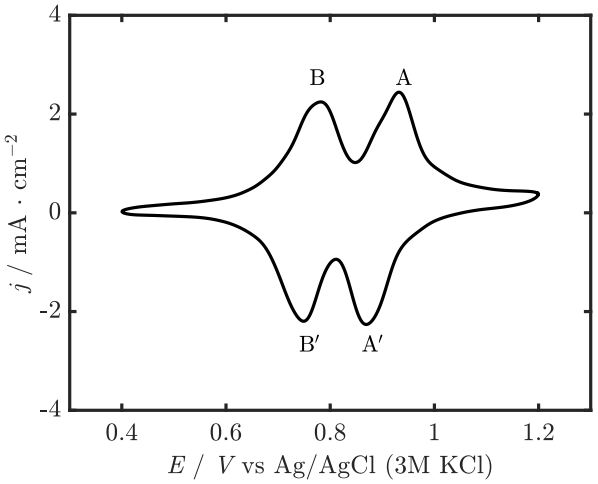

Figure 8.3: Voltammogram obtained from the quasi-triangular wave applied to 200 nm $LiMn_2O_4$ thin film in 1 M Li_2SO_4 solution at a scan rate of 16 mVs^{-1}.

The reversible insertion of Li^+ in $LiMn_2O_4$ has been reported to involve several steps [160–162]. At the beginning of the insertion process, Li^+ is inserted into a single phase which occurs within 0.0 to 0.10 of the total molar fraction of lithium in the $LiMn_2O_4$ (θ_T). The insertion process then proceeds in a way that it gives rise to the co-existence of two phases which has been named a lithium poor and lithium rich phases [161]. The ratio of the lithium rich phase increases as the insertion process continues resulting in a solely lithium rich phase at $\theta_T \approx 0.35$. Further intercalation into the lithium rich phase at $\theta_T \approx 0.4$ to 0.5 results in a decrease of the chemical potential of lithium (μ_{Li}) resulting in an increase in the lattice parameter [161]. The insertion continues after $\theta_T \approx 0.5$ into the other solid solution with a different μ_{Li} [161]. The voltammogram suggests that each solid solution with a different μ_{Li} contributes half of the total charge. The low polarization suggested by the relatively low ΔE_p for the peak pairs indicate a fast kinetics of the (de)insertion process [140, 243–245].

The Nyquist plot of the measured dynamic impedance is shown in Fig. 8.4. The results indicate that the impedance spectra comprises of a RC time constant (semi-circle 1) in the high frequency range followed by another RC time constant (semi-circle 2) in the medium frequency range and terminated by a straight line in the low frequency region, characteristics of a Warburg type impedance. The impedance spectra suggests a two-step intercalation process:

$$Li^+_\varepsilon \rightleftharpoons Li^+_i \tag{8.1}$$

$$Li_i^+ + \lambda - Mn_4O_8 + e^- \rightleftharpoons LiMn_4O_8 \tag{8.2}$$

$$Li_i^+ + LiMn_4O_8 + e^- \rightleftharpoons Li_2Mn_4O_8 \tag{8.3}$$

where ε and i represents the electrolyte phase and IHP respectively.

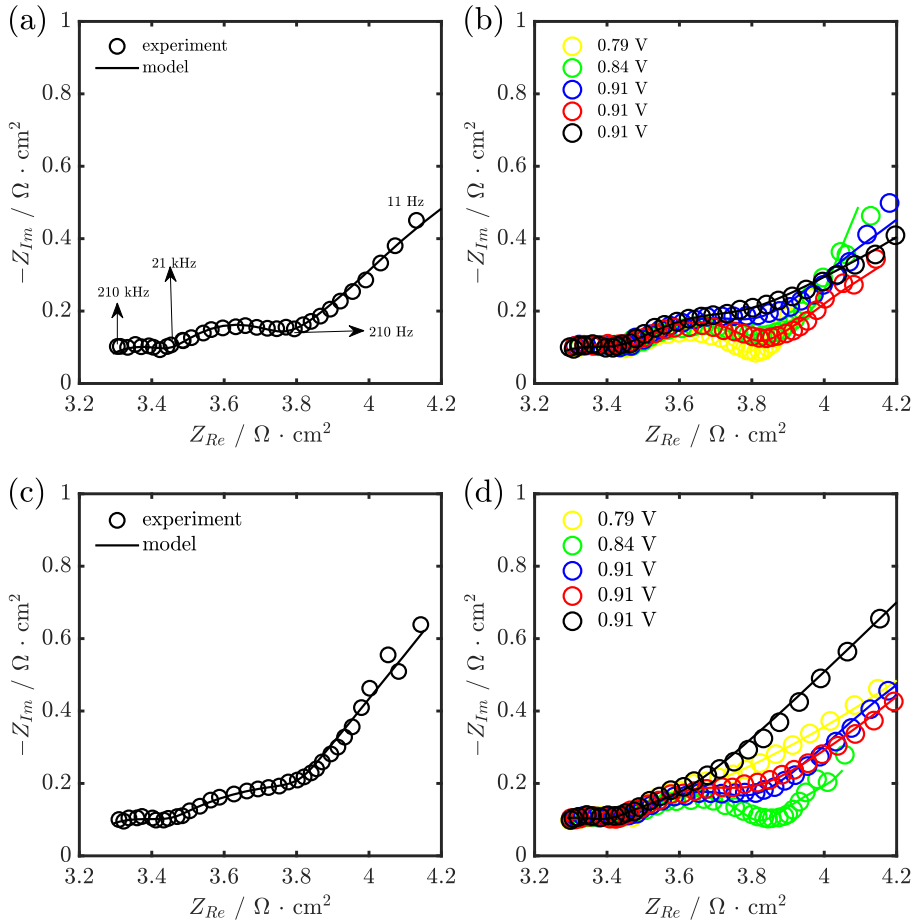

Figure 8.4: Nyquist plot of impedance spectra of $LiMn_2O_4$ films in 1 M Li_2SO_4 within the frequency range of 210 kHz to 11 Hz at different potentials during (a) and (b) cathodic scan (c) and (d) anodic scan. ◯ represents the experimental data, while — represents the data from the model.

The first semi-circle can be attributed to the (de)solvation step (equation 8.1) while the (de)insertion step of Li_i^+ into $LiMn_2O_4$ is the second step which is represented by the second RC time constant. For better illustration, the primitive cell of the LMO consisting of 14 atoms ($Li_2Mn_4O_8$) is used for depicting the (de)insertion step [246], where equation 8.2 and equation 8.3 denotes the reversible insertion step. The SEM image and shape of the impedance suggested a porous electrode and as such the equivalent (Fig. 4.2) described in section 4.1 for a two step intercalation process in a porous electrode was used in fitting the measured impedance.

8.1.3 Statistical Analysis

To avoid over-parameterization as explained before which occurs when negligible physicochemical process are represented in the equivalent circuit, t-test was done for the parameters obtained from fitting the measured impedance with the equivalent circuit shown in Fig. 4.2 as explained in section 3.11.

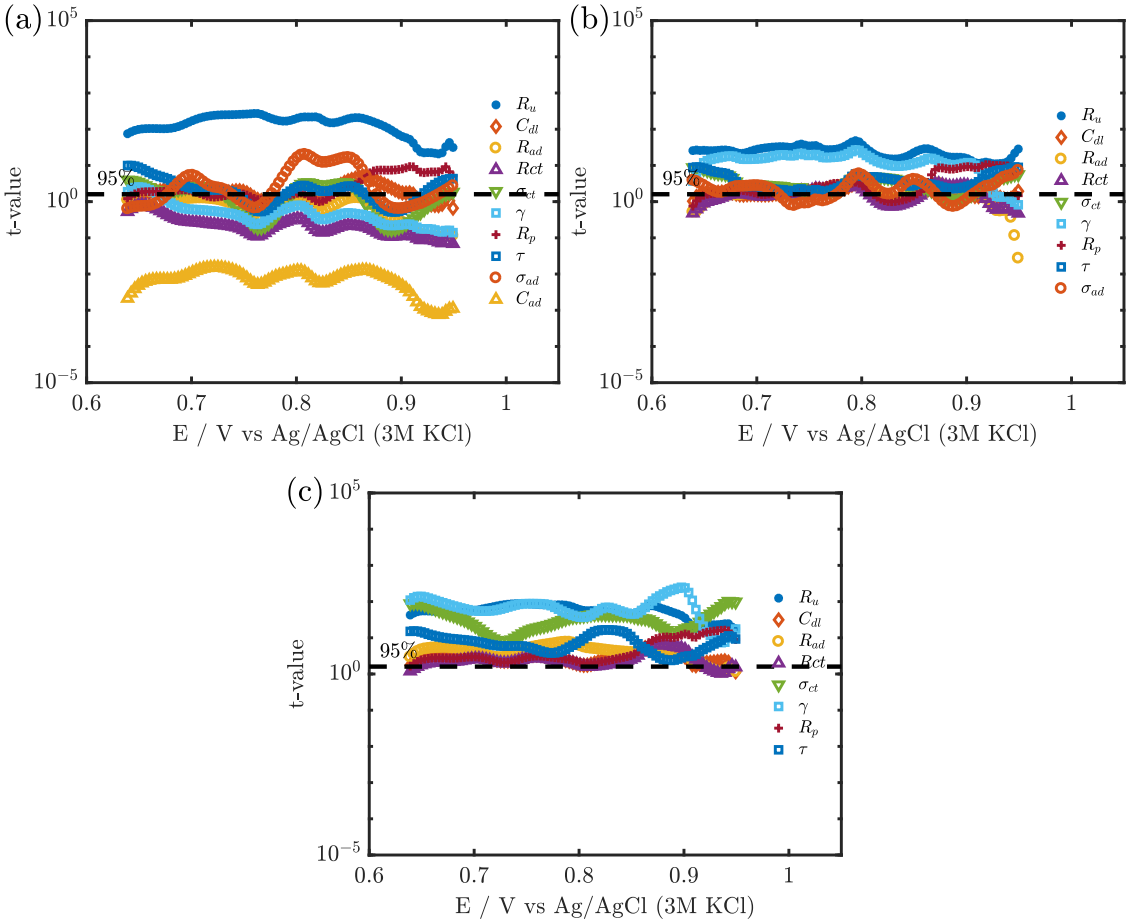

Figure 8.5: *t*-test for the parameters obtained from fitting the measured impedance using (a) equivalent circuit obtained from the model (Fig. in the main text), (b) equivalent circuit shown in Fig. 8.6a (c) equivalent circuit shown in Fig. 8.6b.

The result indicates that R_u was the only parameter above the confidence level despite the low χ^2 value ($3.2{\cdot}10^{-5}$). The parameter with the lowest t-value (C_{ad}) was removed from the equivalent circuit by treating C_{ad} as a short circuit similar to the assumption made for NiHCF film and nanoparticles [140, 242]. This assumption results in the equivalent circuit shown in Fig. 6.7 in section 6.5 which produced a good fit with χ^2 in the order of 10^{-5}. The equivalent circuit (Fig. 6.7) was observed to result in a good fit with most parameters still below the confidence level with σ_{ad} having the least *t*-value (Fig 8.5b). To remove the σ_{ad}, a negligible mass transport in the liquid

was assumed, which occurs when the mass transport in the liquid is fast. The equivalent circuit obtained using this assumption (Fig. 8.6) produced a good fit between the model(— in Fig. 8.4) and the measured impedance (◯ in Fig. 8.4) as indicated in the χ^2 value which was $3.4 \cdot 10^{-5}$. In addition to this low χ^2 value, all parameters in the equivalent circuit were above the confidence level as seen in Fig. 8.5c.

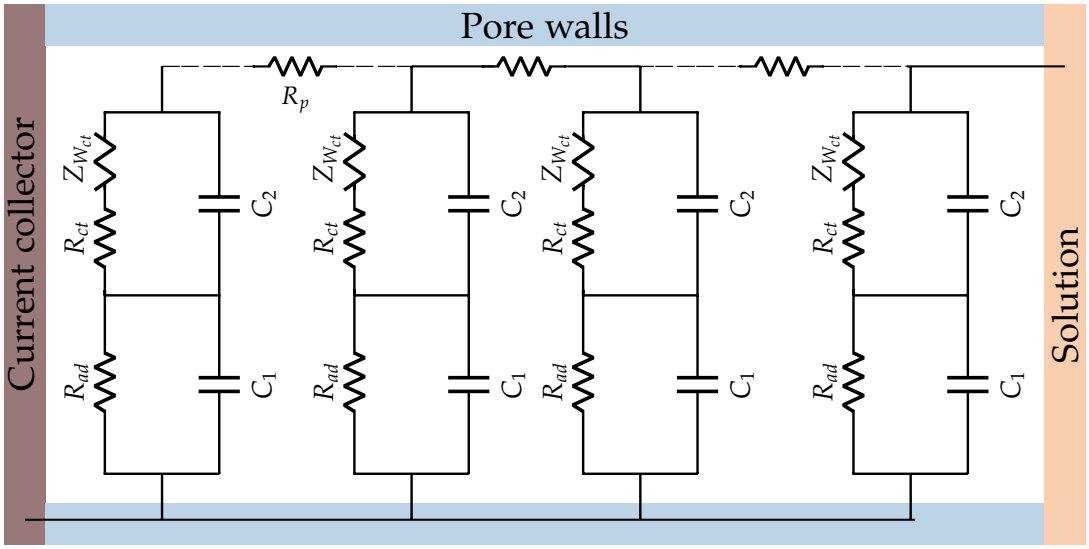

Figure 8.6: Equivalent circuit of the porous electrode including the equivalent circuit obtained from modelling the reversible insertion as two step process treating the capacitance of adsorption (C_{ad}) as a short circuit and the mass transport in the liquid is assumed to be negligible [242].

8.1.4 Compositional Dependence of Kinetic Parameters

The compositional dependence of the extracted kinetic parameters which is important for understanding the intercalation mechanism was also investigated. Fig 8.7 shows R_{ad} extracted from the fit as a function of θ_T estimated from the charge in the voltammogram. The result indicates that resistance of adsorption exhibits compositional dependence with a minimum in each of the solid solution with different μ_{Li}. R_{ad} in the two-step intercalation mechanism in host structure with two solid solution presented in chapter 4 is described as [242]:

$$R_{ad} = \frac{RT}{F^2 k_1^0 \left[\frac{C_{Li_\varepsilon^+}}{C_0}\right]^{1-\alpha_1} [1-\beta_i]^{1-\alpha_1} \beta_i^{\alpha_1}} \tag{8.4}$$

The dependence of R_{ad} in each solid solution is then predicted by the term $[1-\beta_i]^{1-\alpha_1}\beta_i^{\alpha_1}$ in equation 8.4 with a minimum occurring when β_i is half filled in each of the solid solution assuming α_1 = 0.5. Fig. 8.7b shows the estimated R_{ad} using equation 8.4 with two minima each in the

different solid solution of the $LiMn_2O_4$.

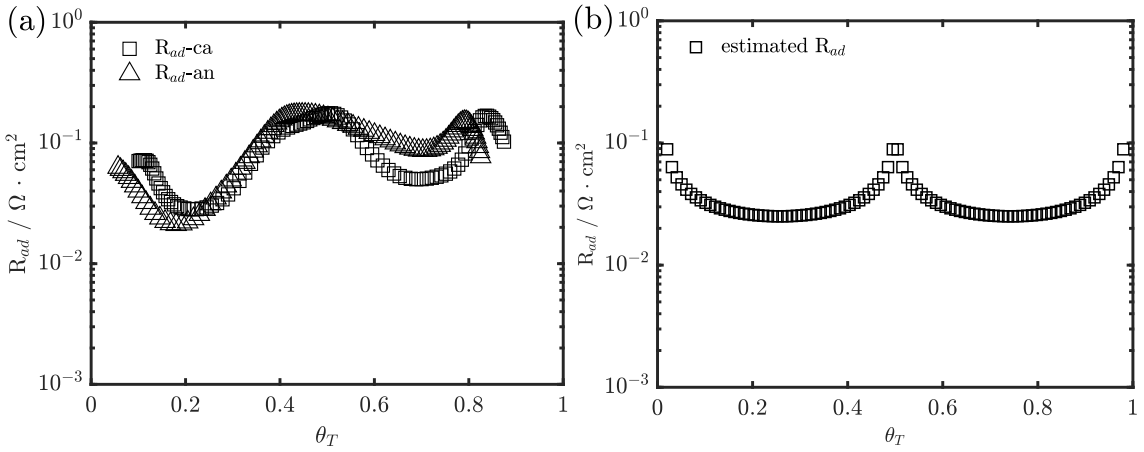

Figure 8.7: (a) Dependence of (a) the resistance of adsorption (R_{ad}) extracted from the fit against the molar fraction (θ) of Li^+ in LMO film (b) R_{ad} estimated from equation 8.4 with with $k_1^0 = 3{\cdot}10^{-5}$ cm s^{-1} and $\alpha_1 = 0.5$.

The model prediction was observed to be in good agreement with the extracted R_{ad} providing a validation for the the given description. The extracted R_{ct} from the fit was observed to also show compositional dependence and was in the same order of magnitude as R_{ad} as seen in Fig. 8.8. The charge transfer resistance in a host structure like $LiMn_2O_4$ treated as two solid solution can be described as [242]:

$$R_{ct} = \frac{RT}{F^2 C_T k_2^0 [1-\theta_i]^{1-\alpha_2} \beta_i^{1-\alpha_2} [1-\beta_i]^{\alpha_2} \theta_i^{\alpha_2}} \tag{8.5}$$

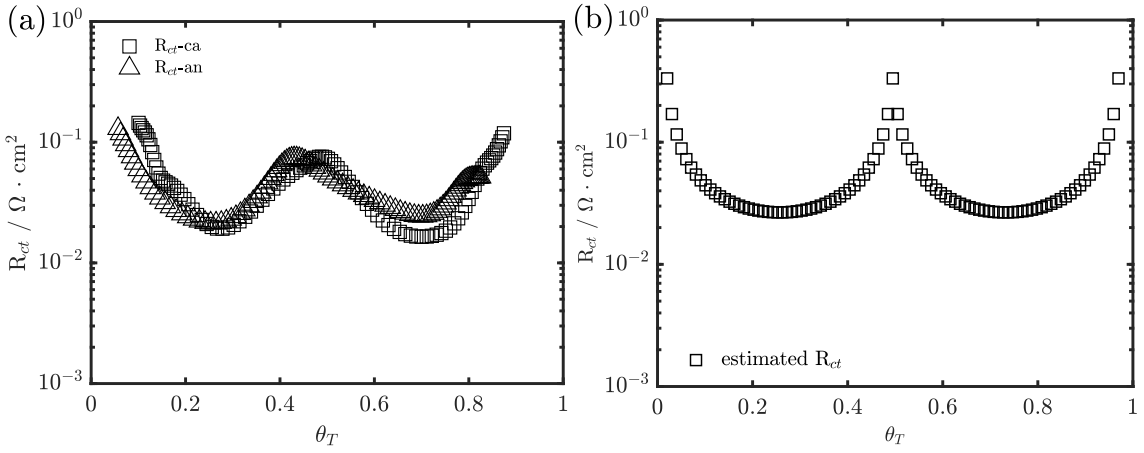

Figure 8.8: Compositional dependence of (a) charge transfer resistance (R_{ct}) extracted from fitting experimental data with model (b) Estimated R_{ct} obtained from equation 8.5 with $k_2^0 = 4 \cdot 10^{-5}$ cm s^{-1} and α_2=0.5.

The estimated R_{ct} using equation 8.5 for the different solid solution (equation 8.2 and equa-

tion 8.3) as a function of the total molar fraction of Li^+ in the LMO (θ_T) is shown in Fig. 8.8b with a minimum in the different solid solution. The curve is similar in shape to the curve of the extracted R_{ct} obtained from fitting the experimental data with the model indicating a good agreement between the model and the experimental data. The compositional dependence of R_{ct} observed in this work is consistent with reports by Marchini et al. for the (de)insertion of Li^+ in $LiMn_2O_4$ [160]. Fig 8.7a and Fig 8.8a indicates an hysteresis in the extracted R_{ad} and R_{ct} respectively. This can be attributed to the fact that concentration of Li^+ on the electrode surface changes and the diffusion profile depending on the direction of the scan and/or scan rate [118, 247, 248]. As the rate of the reaction is a function of the concentration of the surface concentration of the Li^+, this changes in surface concentration results in difference in the rate of the reaction occurring on the electrode surface. Such hysteresis due to changes in concentration of cations on the electrode surface for dynamic impedance has been reported for other electrochemical systems [118, 247, 248].

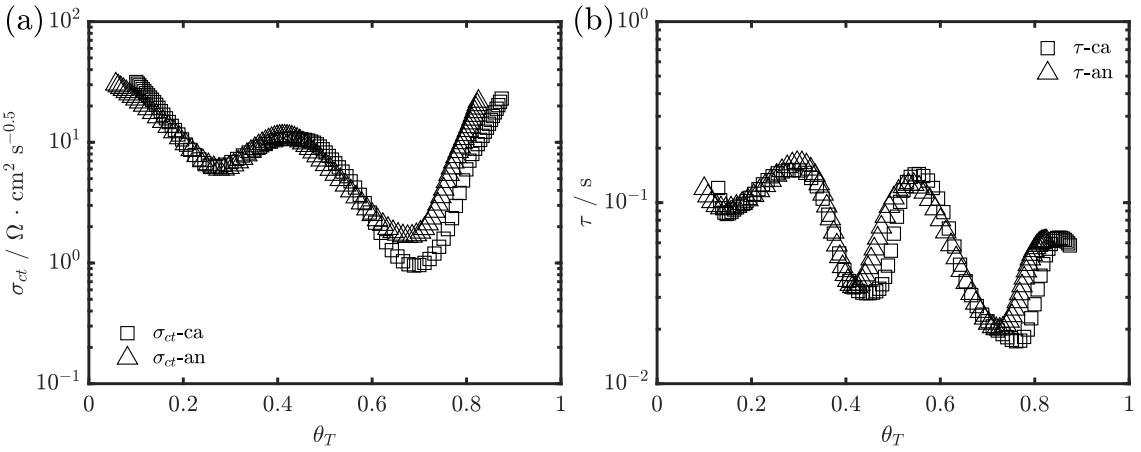

Figure 8.9: (a) Plot of the Warburg coefficient of Li^+ in LMO lattice (σ_{ct}) versus the total molar fraction of Li^+ in $LiMn_2O_4$ (θ_T) (b) Plot of diffusion time constant (τ) versus the total molar fraction of Li^+ in $LiMn_2O_4$ (θ_T).

The Warburg coefficient of Li^+ in $LiMn_2O_4$ (σ_{ct}) was observed to exhibit compositional dependence with a shape similar to the shape of the voltammogram as shown in Fig. 8.9. This dependence of (σ_{ct}) has been attributed to the term $([1-\theta]\cdot\theta)$ in the equation describing the Warburg coefficient in the model (equation 6.6). τ which represents the time taken from the Li^+ to diffuse from the surface to equilibrium in the solid shows compositional dependence which is consistent with literature [162, 249].

8.1.5 Conclusion

The result obtained in this study indicates that the reversible insertion in 200 nm $LiMn_2O_4$ film made by multi-layer PLD in aqueous media proceeds via a two step process: adsorption followed by the (de)insertion step. The equivalent circuit obtained from modelling and statistical analysis produced a good fit between the measured impedance and the model with all parameters above the 95% confidence level used in this work. The extracted resistances (R_{ad} and R_{ct}) were observed to be in good agreement with the prediction of the model having two minima, each occurring in the different solid solutions of the $LiMn_2O_4$. The extracted Warburg coefficient was also observed to depend on the lithium concentration in the $LiMn_2O_4$, and shows two minima each occurring around the standard electrode potential of the solid solutions in the $LiMn_2O_4$.

8.2 Effect of Film Thickness on the Kinetics of $LiMn_2O_4$ Films

The effect of the film thickness on the kinetics of the reversible insertion of Li^+ in $LiMn_2O_4$ films made by multi-layer PLD was investigated in this section.

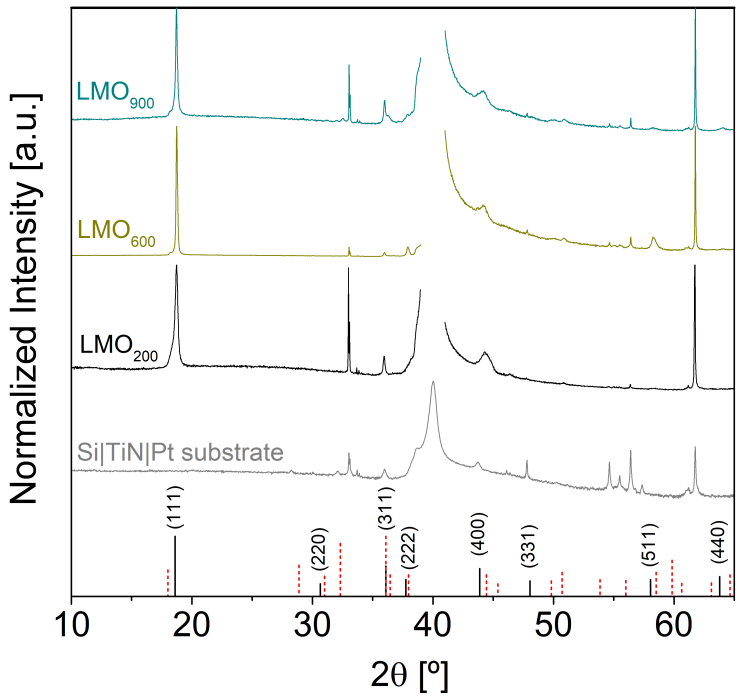

Figure 8.10: X-ray diffractogram of $LiMn_2O_4$ layers at different thicknesses (indicated by the lower indices in nm) in respect to the response from the Si|TiN|Pt substrate. Black lines correspond to spinel $LiMn_2O_4$ (JCPDS 00-035-0782) and red dashed lines indicate Mn_3O_4 (JCPDS 00-024-0734) as secondary phase.

The XRD pattern of the $LiMn_2O_4$ of different thickness made by multi-layer PLD is shown in

Fig. 8.10. The diffraction peaks associated with $LiMn_2O_4$ spinel (JCPDS 00-035-782) which occurs at 18.6° was observed in the films indicating that all films were $LiMn_2O_4$. Fig. 8.11 shows the SEM micrograph of top view and cross section of the $LiMn_2O_4$ films of different thickness obtained from multi-layer PLD. In all films, columnar grains randomly oriented was observed. The SEM image indicates a change in the microstructure of the film with increasing thickness with thicker films having a higher porosity than thinner films. Results from FIB-SEM indicates the layers had a thickness of 200 nm, 600 nm and 900 nm for the application of 30, 80 and 130 pulses on the Si|TiN|Pt substrates.

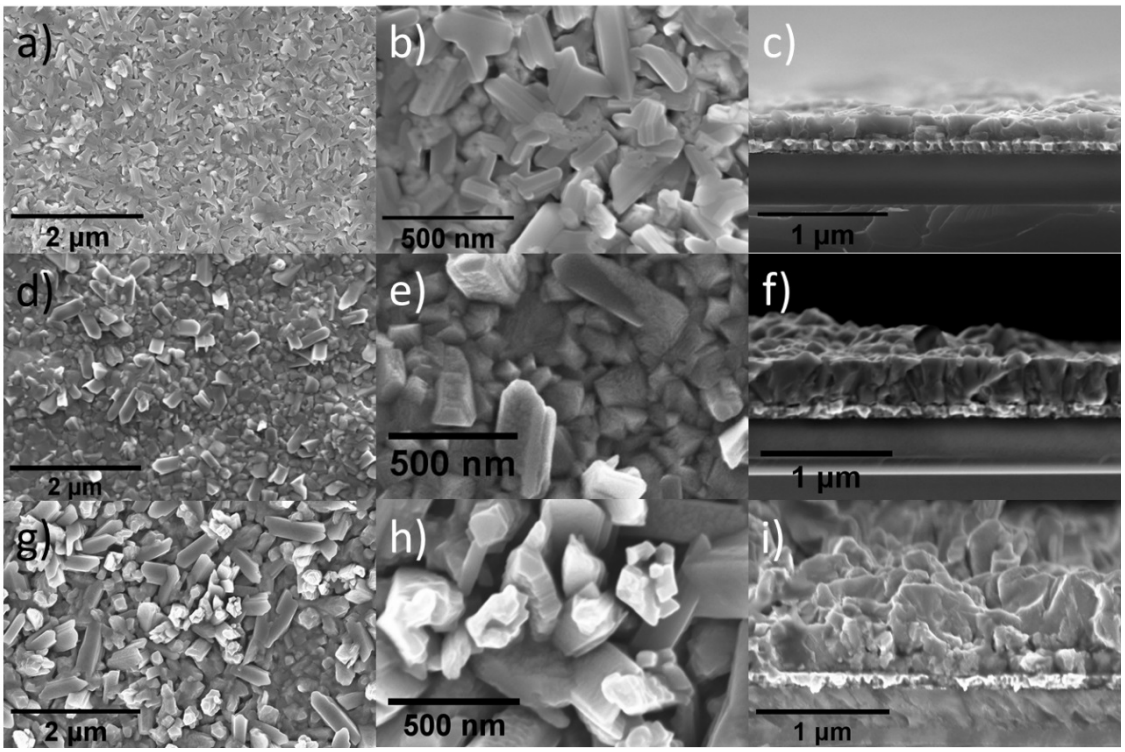

Figure 8.11: SEM micrographs of deposited $LiMn_2O_4$ layers with a-c) 200 nm, d-f) 600 nm and g-i) 900 nm, respectively.

8.2.1 Electrochemical analysis

The voltammogram obtained for the LMO layers in 1 M Li_2SO_4 is shown in Fig. 8.12. Well defined peak pairs was observed for all films with a voltage sweep of 16 mVs^{-1}. These peak pair have been attributed to the reversible insertion of Li^+ in two solid solutions with different chemical potential of lithium (μ_{Li}). The current in the voltammogram was observed to increase with increasing film thickness, which can be attributed to an increase in active material per unit area as the film thickness increases. The peak separation (ΔE_p) of the peak pairs was observed to increase with increasing film thickness as seen in table 8.1 with 200 nm having the least ΔE_p while 900 nm film

had the highest ΔE_p. This increase in ΔE_p suggests a decrease in the lithium transport kinetics as the film thickness increases.

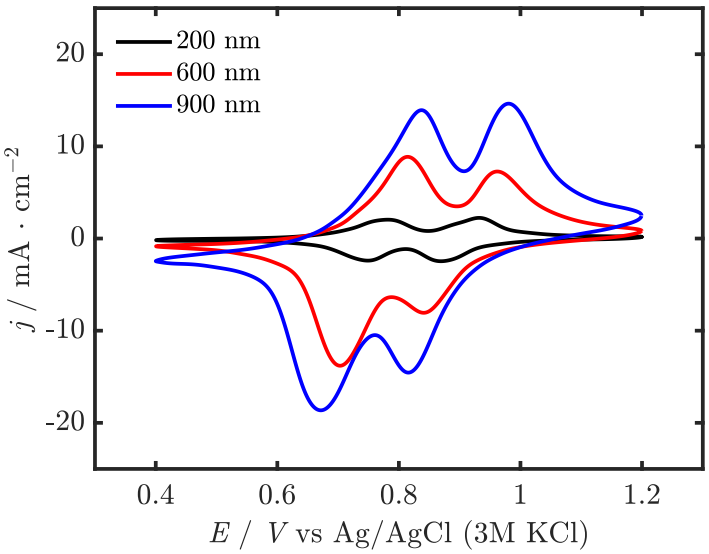

Figure 8.12: Voltammogram obtained from the quasi-triangular wave applied to 220 nm (black line), 600 nm (red line) and 900 nm (blue line) thick $LiMn_2O_4$ film in 1 M Li_2SO_4 solution at a scan rate of 16 mVs^{-1}.

Film thickness (nm)	ΔE_{p1} (mV)	ΔE_{p2} (mV)
200	38	68
600	120	105
900	160	165

Table 8.1: Peak separation (ΔE_p) for the peak pairs observed in the voltammogram of $LiMn_2O_4$ films of different thickness in 1 M Li_2SO_4 with a scan rate of 16 mVs^{-1}.

8.2.2 Dynamic impedance spectroscopy

The dynamic impedance spectra obtained from the perturbation of the electrochemical cell with $LiMn_2O_4$ films of different thickness with the combined quasi-triangular wave and multi-sine is shown in Fig. 8.13. The result indicates that the spectra obtained in the 200 nm, 600 nm and 900 nm comprises of the two RC time constants (semi-circle) in the high to low frequency region and terminated by a straight line which occurs at an angle of less than 90 attributed to solid state diffusion of Li^+ in LMO.

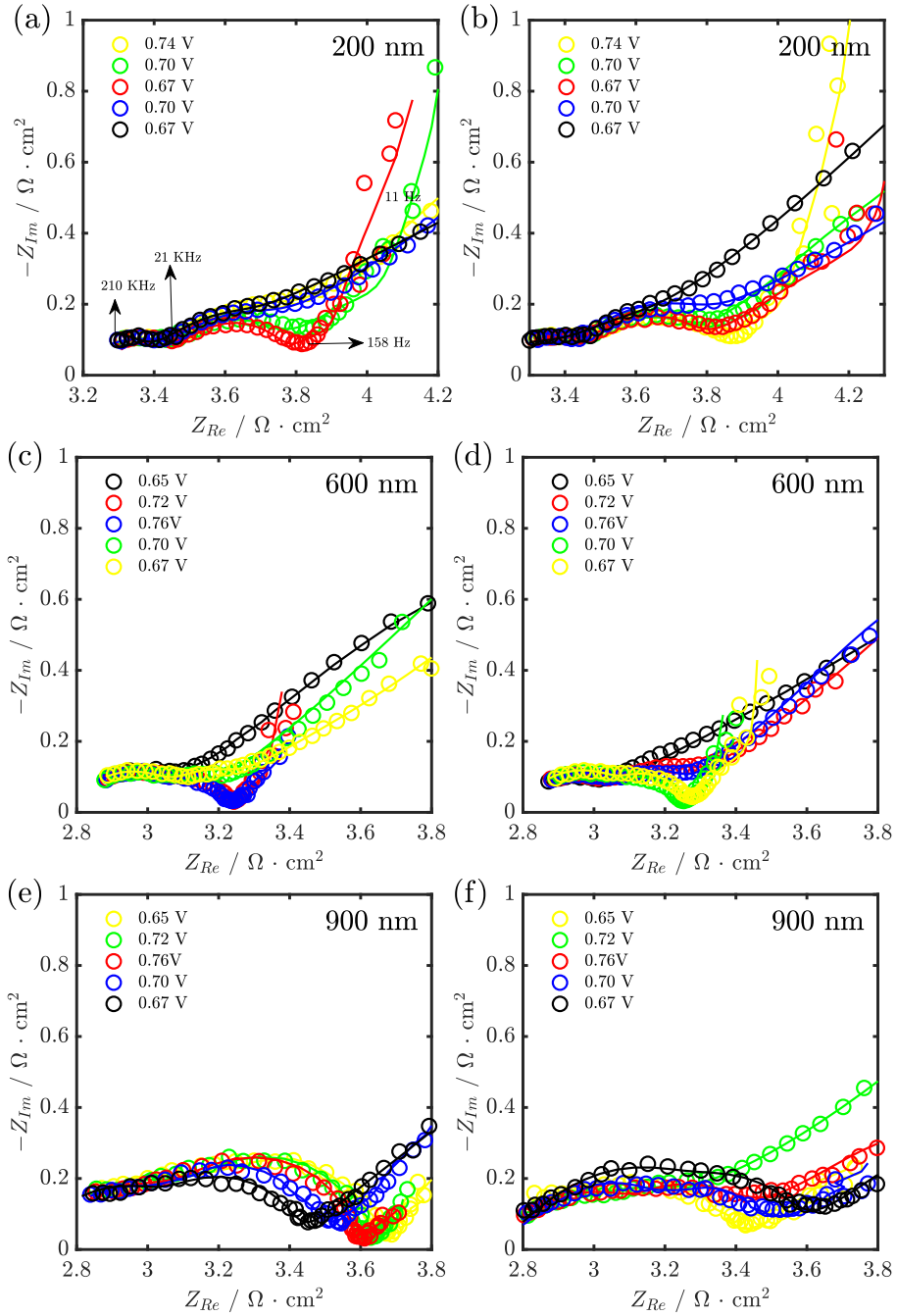

Figure 8.13: Nyquist plot of impedance spectra obtained in 1 M Li_2SO_4 within the frequency range of 210 KHz to 2.5 Hz at different potentials for $LiMn_2O_4$ films of different thickness (a) and (b) 200 nm (c) and (d) 600 nm (e) and (f) 900 nm. ◯ represents the experimental data, while — represents the data from the model.

The result obtained from fitting the data with the equivalent circuit shown in Fig. 8.6b indicates that the equivalent circuit could reproduce the measured data as indicated by the χ^2 value which was in the order of 10^{-4}. The parameters in the equivalent circuit were observed to be above the confidence level (95%) used in this work.

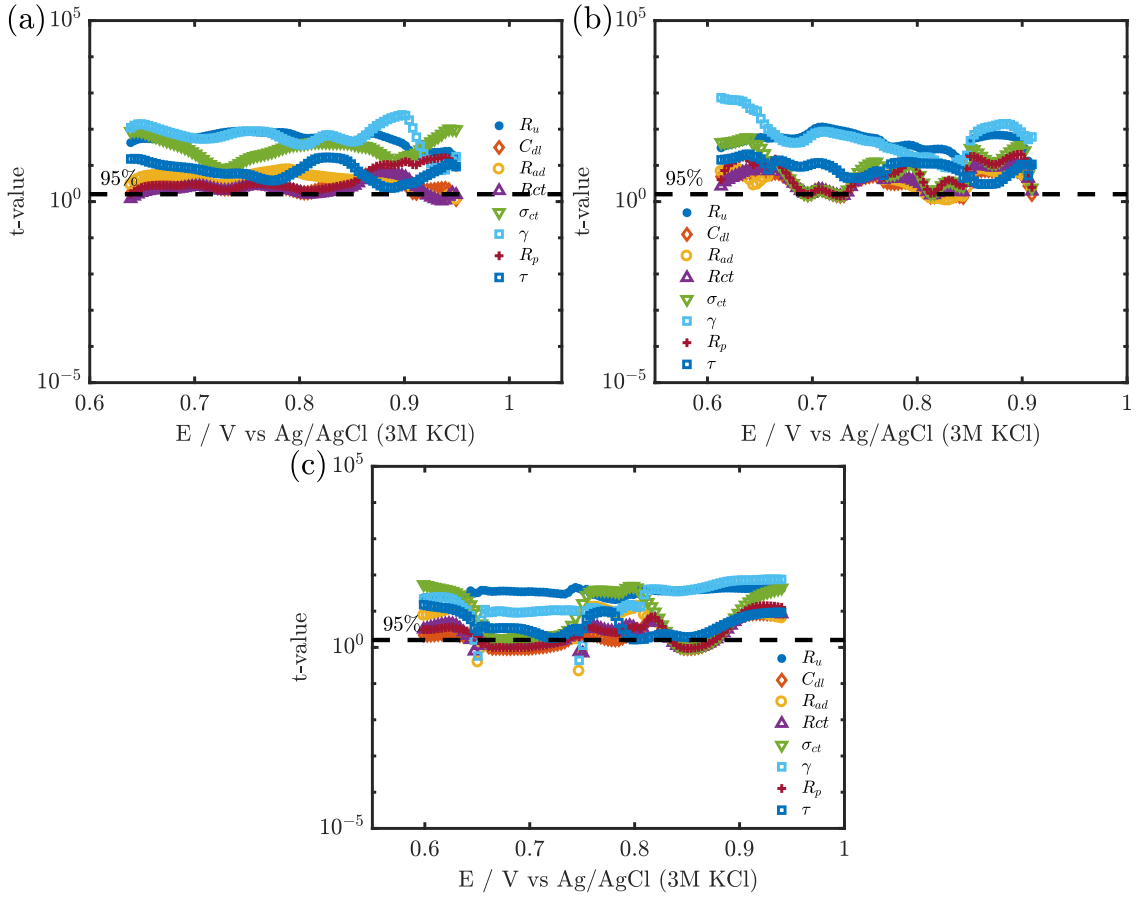

Figure 8.14: t-test for the parameters obtained from fitting the measured impedance using with the equivalent circuit shown in Fig. 8.6b for (a) 220 nm (b) 600 nm and (c) 900 nm $LiMn_2O_4$ film.

8.2.3 Dependence of the Kinetic Parameters on the Thickness of $LiMn_2O_4$ Films

The dependence of the kinetic parameters on the film thickness was investigated to provide an insight into the role of the kinetic parameters in the reduced power density observed for thicker films. Fig. 8.15 shows the adsorption resistance (R_{ad}) as a function of the total molar fraction of Li^+ in the $LiMn_2O_4$ (θ_T). The result indicates that R_{ad} extracted from the fit for all films depended on the electrode composition having a minimum in each of the solid solutions of the $LiMn_2O_4$ as observed previously in the 200 nm $LiMn_2O_4$ film. This has been attributed to the fact that surface atomic arrangement, which is in equilibrium with the bulk and changes during the (de)insertion process [164, 165]. Thus, the adsorption sites in the two solid solution is described independently. The minimum R_{ad} in each of the solid solution was observed to be independent on the film thickness indicating that the (de)solvation process is independent on film thickness.

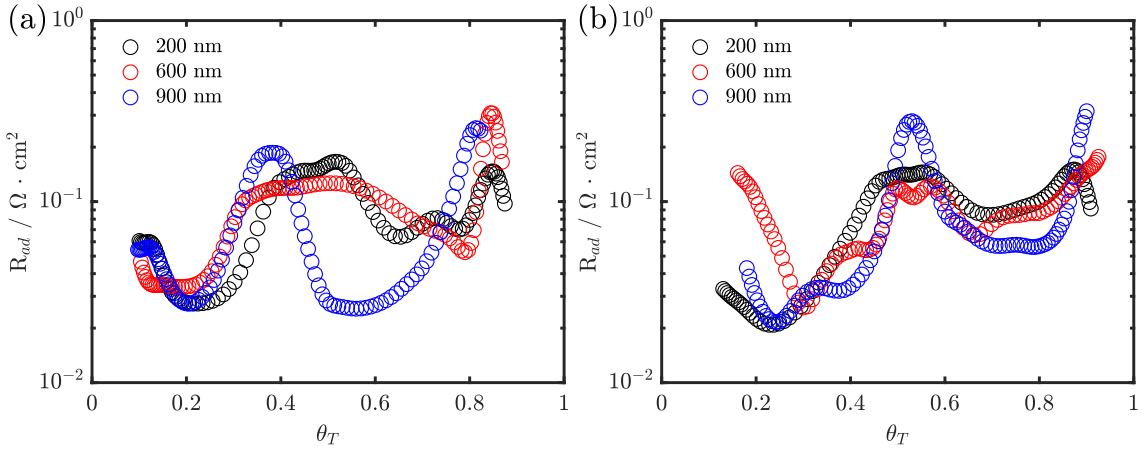

Figure 8.15: The variation of the adsorption resistance (R_{ad}) on the electrode composition for the $LiMn_2O_4$ films of different thickness during (a) cathodic voltage sweep (b) anodic voltage sweep.

The minimum R_{ad} in each solid solution was used for this comparison as the R_{ad} is expected to be independent on electrode composition at this point, hence providing a good basis for comparison. R_{ad} represents the kinetic barrier for the Li—O bond breaking/making and is dependent on the the standard rate constant of the (de)solvation process (k_1^0). In the simplified model used in this work, the (de)solvation step involves the bond breaking and making of the Li—O bond. As the bond energy is independent of the film thickness, R_{ad} is expected to be independent on the film thickness and microstructure as observed in the result obtained.

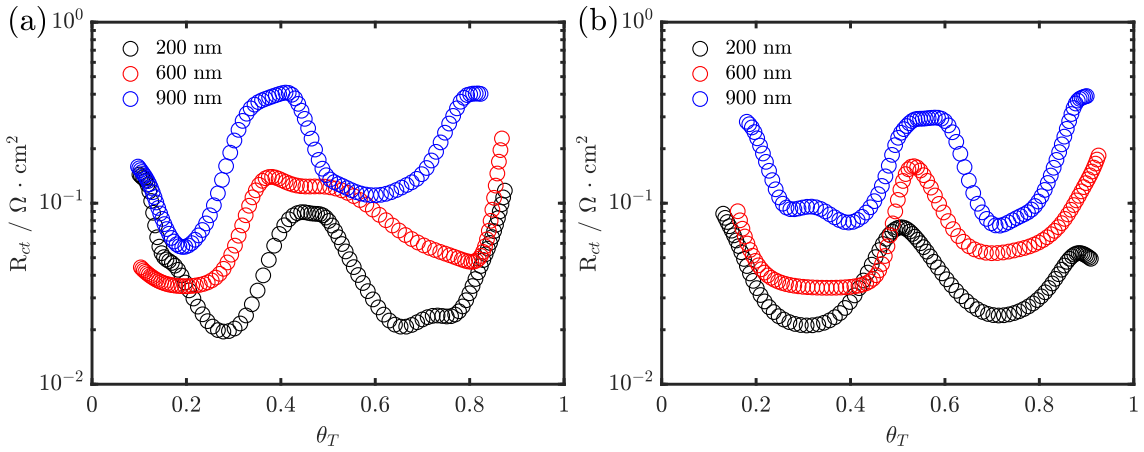

Figure 8.16: Dependence of the charge transfer resistance (R_{ct}) on the electrode composition during (a) cathodic voltage sweep (b) anodic voltage sweep.

The charge transfer resistance (R_{ct}) extracted from fitting the measured impedance and the equivalent circuit for the different LMO films was observed to show compositional dependence with a minimum in each solid solution of the $LiMn_2O_4$ for all films studied. This is in line with the result obtained for 200 nm $LiMn_2O_4$ films and the prediction of the model as shown in section 8.1.4. Using the minimum R_{ct} which occurs around standard electrode potential for each

solid solution for comparison, the result indicates that R_{ct} increases with increasing film thickness as seen in Fig. 8.17. The charge transfer resistance has an inverse relationship with the exchange current density which depends on surface area and the standard rate constants of the insertion step (k_2^0). Thus, the parameters that affect the minimum R_{ct} are surface area and k_2^0. Since the surface area does not show a clear trend as suggested by the double layer capacitance (Fig. A.2 in the appendix), a possible explanation for the trend observed in R_{ct}, is a change in k_2^0. This increase in the charge transfer resistance is consistent with the increase in peak separation (ΔE_p) observed in the voltammogram for increasing film thickness shown in table 8.1.

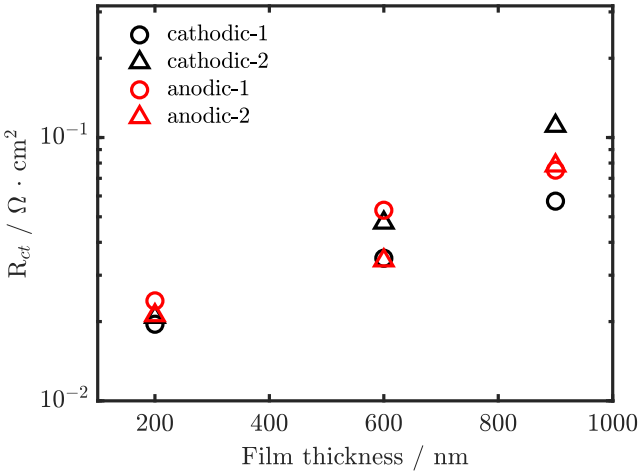

Figure 8.17: Plot of the minimum charge transfer resistance (R_{ct}) vs film thickness of the $LiMn_2O_4$.

The effect of the microstructure and film thickness on the mass transport of Li^+ in the $LiMn_2O_4$ was also investigated. The Warburg coefficient of Li^+ in $LiMn_2O_4$ (σ_{ct}) was observed to have a shape similar to the shape of the voltammogram which has been attributed to the term $([1-\theta]\cdot\theta)$ in the equation describing σ_{ct} (equation 6.6).

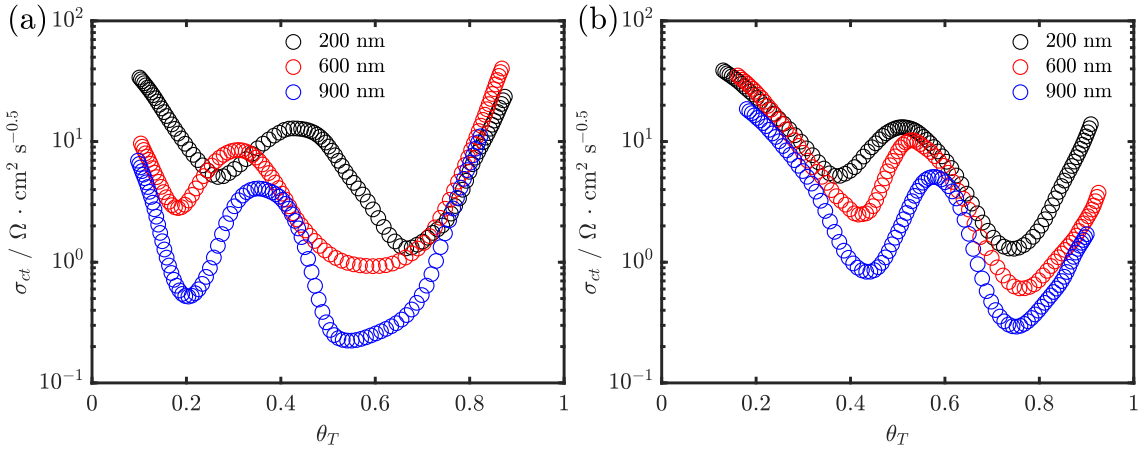

Figure 8.18: Variation of the Warburg coefficient of the Li^+ in the $LiMn_2O_4$ lattice (σ_{ct}) on the electrode composition during (a) cathodic voltage sweep (b) anodic voltage sweep.

Comparing the minima of the σ_{ct} of the films studied indicates that σ_{ct} tends to decrease with increasing film thickness with the 900 nm $LiMn_2O_4$ having the least σ_{ct} and the 200 nm had the highest σ_{ct} as seen in Fig 8.19. The SEM image obtained from the films (Fig 8.11) suggests that the microstructure of the $LiMn_2O_4$ film changes as the film thickness increases, with thicker films having better-grown crystal, resulting in higher diffusion coefficient [48, 250]. The result obtained indicates that the mass transport of Li^+ in LMO layers made by multi-layer PLD is enhanced by better-grown crystal obtained in thicker films.

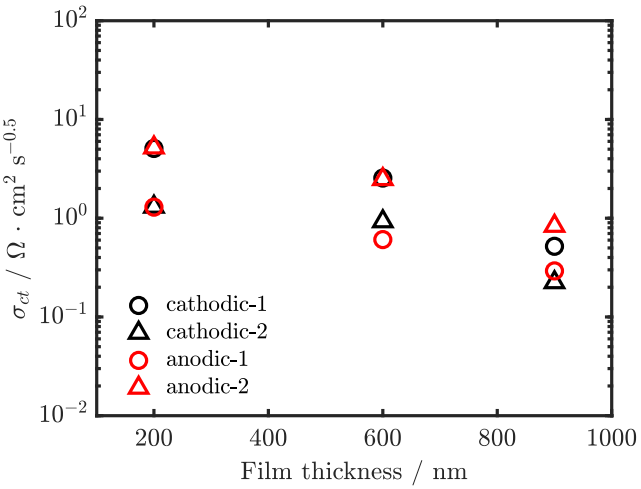

Figure 8.19: Plot of the minimum Warburg coefficient of the Li^+ in the $LiMn_2O_4$ lattice (σ_{ct}) as a function of film thickness.

The dependence of the diffusion time constant (τ) on the film thickness was also investigated. τ which is the time taken for Li^+ to diffuse from the surface to equilibrium in the solid host structure is important mass transport parameter.

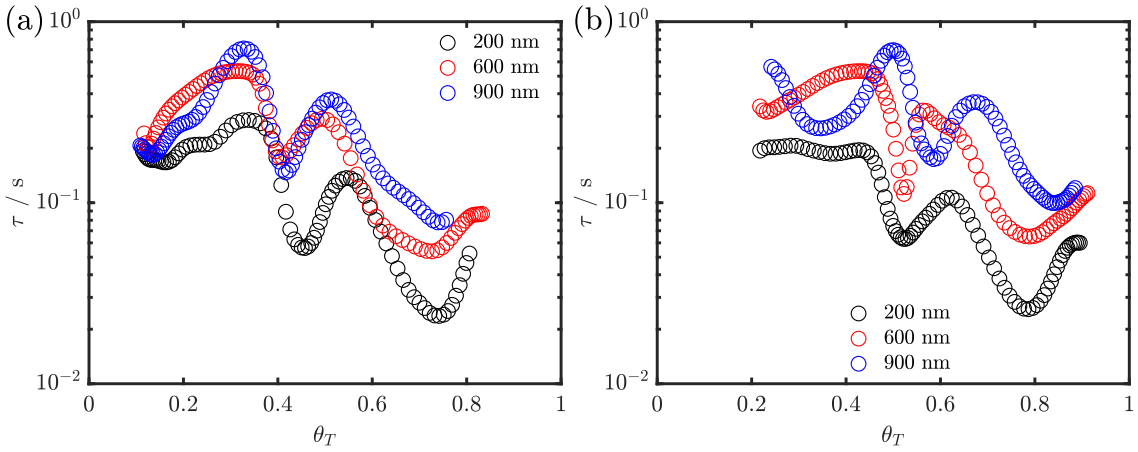

Figure 8.20: Dependence of the diffusion time constant (τ) on electrode composition during (a) cathodic voltage sweep (b) anodic voltage sweep.

τ around the standard electrode potential of the two solid solution in LMO was observed to

increases with increasing film thickness. The SEM image (Fig. 8.11) suggests that the particle size increases as the film thickness increases. This increased in particle size results in increased diffusion path length of Li^+ in the LMO layers and explains the increase in the diffusion time constant.

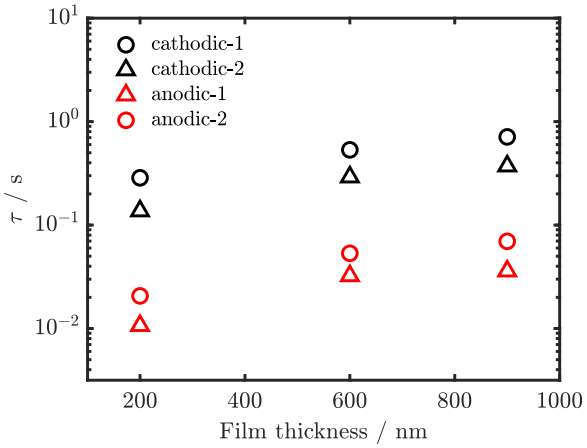

Figure 8.21: Plot of the diffusion time constant (τ) at the standard electrode potential vs film thickness.

8.2.4 Conclusion

The result in this study shows that the kinetics of the reversible insertion of Li^+ in $LiMn_2O_4$ films made by multi-layer PLD depends on the microstructure and thickness of the $LiMn_2O_4$ film. Kinetic parameters of surface phenomena such as adsorption resistance (R_{ad}) was observed to be independent on film thickness. R_{ad} represents the kinetic barrier in the bond breaking/bond making process in the Li—O bond during the (de)solvation process and as such does not show any dependence on film thickness. kinetics of the interfacial and bulk phenomena such as charge transfer resistance (R_{ct}), Warburg coefficient in the solid (σ_{ct}) and the diffusion time constant (τ) were observed to depend on the film thickness. The charge transfer resistance increases with increasing film thickness consistent with the increase in peak separation (ΔE_p) observed in the voltammogram as the film thickness increases. This was attributed to changes in the standard rate constants of the (de)insertion step as the electrochemical active surface area did not show a clear trend. The better-grown crystal observed in thicker films resulted in lower Warburg coefficient in the solid, indicating faster mass transport in thicker films. The diffusion time constant increased with increasing particle size which can be attributed to increase in diffusion path length of the LMO particles. The result obtained in this study provides valuable insights of the effect of the film thickness on the kinetics of the reversible insertion of Li^+ in $LiMn_2O_4$.

Chapter 9

Conclusions and Outlook

The aim of this thesis was to investigate the reversible insertion mechanism of cations in positive electrode materials in aqueous media. The understanding of the reversible insertion mechanism of cations is important in the optimization of aqueous rechargeable batteries by electrode engineering and tailoring of the electrode/electrolyte interface. This optimization is important in enhancing the electrochemical performance of aqueous battery systems, which are promising alternatives to lithium-ion batteries as energy storage systems for stationary applications. In literature, the kinetics of the reversible insertion mechanism is often studied using static electrochemical impedance spectroscopy (EIS). Due to the stationarity requirement of EIS, this technique is limited in studying the kinetics of unstable systems and electrochemical systems under non-stationary conditions. In this thesis, the kinetics of the reversible insertion of cations in various electrode materials under non-stationary conditions were studied with dynamic impedance spectroscopy acquired with dynamic multi-frequency analysis.

The extraction of reliable kinetic information from impedance spectra requires the acquisition of artefacts free impedance spectra over a wide range of frequency. However, the components of the instrumental setup used in acquisition of impedance deviates from ideal behaviour at high frequencies (operational amplifier and I/E converter), thereby introducing artefacts. This limits the upper frequency when acquiring impedance spectra. To avoid errors associated with artefacts in the high frequency region arising from instrumental setup, a method for the estimation and correction of instrumental artefacts was presented. The onset of artefacts was observed to occur at lower frequencies with increasing gain of the system. Using resistors at different current ranges, it was observed that impedance spectra can be acquired up to 1 MHz with a deviation of less than 1%. For μA current range, the result obtained from the study indicates that the upper frequency limit used for impedance acquisition can be extended using the correction method proposed. For the 10 μA current range, the upper frequency limit was extended by two orders of magnitude from 1 kHz to 100 kHz for a 500 kΩ resistor. Using a redox couple, the application of the pre-

sented correction method in the acquisition of artefact free impedance and high quality CV was also shown. In this case, the right current range (1 mA) needed to acquire high quality quasi cyclic voltammogram introduced an artefact (inductive behaviour) in the high frequency region of the dynamic impedance. Using the proposed method, it was possible to extract the true impedance free from the artefacts. The correction method was also applied to electrochemical systems (nickel hexacyanoferrate nanoparticles), where the errors may result in misleading quantification of the kinetic parameters. In general, the correction method presented in this work allows for the extension of the high frequency limit of the impedance to a certain limit. This is particularly of interest as the acquisition of artefacts free high frequency data points in impedance is important in understanding physicochemical processes such as ion-sorption, adsorption and charge transfer.

To extract qualitative and quantitative mechanistic information which are physically correlated to the electrochemical system being studied, measured impedance free from artefact will have to be fitted with a model based on the physicochemical process occurring in the electrochemical system. To this end, a model to describe the reversible insertion mechanism of cations in aqueous media was presented in this study. Statistical analysis was used to avoid the problem of over parametrization which may occur due to the inclusion of negligible physicochemical processes in the model and/or processes occurring outside the investigated frequency range. This approach allowed for narrowing the insertion mechanism from a general model to a more specific model for each electrode material.

Using nickel hexacyanoferrate thin films made by cathodic electrodeposition, which are unstable in their oxidized form, the advantages of using dynamic multi-frequency analysis coupled with an optimized electrochemical cell for investigating unstable electrochemical systems was shown in this thesis. High quality dynamic impedance were obtained, which were fitted using the transmission line model for porous electrode modified with the equivalent circuit from modelling the insertion as a two step process: partial desolvation of the cations and an insertion step. The impedance spectra obtained were different in shape from those obtained using static electrochemical impedance spectroscopy reported in literature, which exhibited low frequency loops [200–202]. The low frequency loop reported in literature can be attributed to instability of nickel hexacyanoferrate film and/or the cell configuration. The extracted kinetic parameters indicates that the (de)insertion rates depended on the nature of the cations (K^+ and Na^+) and the state of charge. The kinetic parameters extracted indicated that the kinetic rate of the various physicochemical processes in the reversible insertion of K^+ and Na^+ were in same order of magnitude. This can be attributed to similarity in their similar ionic radii (Na^+ = 1.00 Å, K^+ = 1.38 Å) and Stokes radii (Na^+ = 1.83 Å, K^+ = 1.25 Å) [88, 89, 140, 204, 217]. In a broader context, the result highlights

the possibility of employing DMFA in kinetic investigation of electrode materials for batteries, supercapacitors and ion pumping techniques under dynamic conditions.

The reversible insertion kinetics of univalent cations in nickel hexacyanoferrate nanoparticles, a promising cathode material for aqueous sodium and potassium battery was also investigated using DMFA. The result obtained indicates that the insertion process involves a partial desolvation and insertion step. The rate determining step was observed to depend on the state of charge. At the onset/offset of the (de)insertion process, the rate determining step was observed to be the (de)insertion step as the charge transfer resistance was higher than the resistance due to adsorption. Around the standard electrode potential, the adsorption resistance which models the kinetic barrier due to (de)solvation process, was observed to be higher than the charge transfer resistance indicating that the rate determining step is the (de)solvation process. The transfer coefficient of the charge transfer process extracted was 0.59 and 0.56 for Na^+ and K^+ respectively, indicating a symmetric process. In contrast to the charge transfer process, the desolvation process was observed to be asymmetric as the transfer coefficient of (de)solvation process was 0.80 and 0.72 for Na^+ and K^+ respectively. This asymmetry although not clear at this moment may arise from the electrostatic interactions occurring in the reorganization of the double layer during the (de)solvation process. The activation energy for the (de)insertion process of Na^+ and K^+ estimated from the study was 0.05 eV and 0.1 eV respectively while the activation energy of the (de)solvation step was 0.16 eV for Na^+ and 0.14 eV for K^+. The similarity in kinetic parameters and activation energy observed for both cations is related to their similarity in the Stokes radii and ionic radii of the cations. As the rate determining process around the standard electrode potential depends on the (de)solvation process, the electrode/electrolyte interface can be tailored by proper selection of electrolytes and concentration of electrolyte to reduce the adsorption resistance. The kinetic parameters extracted from this study can also be used in modelling the performance of technologies utilizing nickel hexacyanoferrate nanoparticles.

The kinetics of lithium (de)insertion in $LiMn_2O_4$ films made by multi-layer pulse laser deposition (PLD) and the effect of the film thickness on the kinetics was also investigated. The result obtained indicates the insertion process is a two-step process: (de)solvation process and insertion step. A minimum in the extracted kinetic parameters was observed around the peak potential in the voltammogram, which is in agreement with results from the modelling the reversible insertion of Li^+ in LMO. The adsorption resistance was observed to be independent on the film thickness. This can be attributed to the fact that the rate of the bond cleavage/bond formation in Li—O is independent on film thickness. Contrary to this, the charge transfer resistance was observed to depend on the film thickness, increasing with increase in film thickness. A plausible reason for

this, is change in the standard rate constant of the (de)insertion step. The mass transport resistance was observed to decrease with increasing film thickness. The diffusion time constant increased with increasing particle size which was attributed to increase in transport path length. The result obtained in this study provides an insight into parameters that can be optimized in the pulse laser deposition process to improve the electrochemical performance of LMO films made by multi-layer PLD.

Currently, the non-linear component of the response of the system is discarded in DMFA. Using carefully design waves, the second harmonic or intermodulation response of fundamental frequencies can be investigated. It will be possible to extract intermodulated differential admittance spectra alongside dynamic impedance spectra with this method using quadrature filters. This dynamic nonlinear analysis will allow for the symmetry of the various steps in the reversible insertion process to be measured during the voltage sweep. The result obtained in this PhD thesis indicates that the ion transfer at the electrode/electrolyte involves (de)solvation and (de)insertion. DMFA which utilizes the electrochemical response (current) of an electrochemical system to perturbation with a combined wave of multisine and quasi voltammetry, does not provide information about the identity of the electrochemical species at the interface. Thus, the (de)solvation process and (de)insertion process can not be uncoupled. The use of hyphenated technique in the form of coupling DMFA with fast response quartz crystal microbalance (QCM) will be needed in decoupling the ion sorption and charge transfer process. The coupling of DMFA with QCM will provide information about the mass changes of the reacting species in the frequency domain resulting in the separation of the (de)solvation process and (de)insertion process.

Thus far, the kinetics of the reversible insertion process was studied only in solution containing single cations. In some applications such as ion pumping techniques (ec-friendly lithium recovery) and dual ion batteries, solutions containing multiple cations are used. The effect of the presence of other cations in the solution on the kinetics of the reversible insertion process for both selective and non-selective electrodes should be investigated. Furthermore, the information obtained from this study can be used in optimizing technologies based on the reversible insertion of cations in aqueous systems such as aqueous batteries using nickel hexacyanoferrate nanoparticles as cathode materials, film batteries utilizing $LiMn_2O_4$ films, dual ion batteries and ion pumping techniques.

Appendix A

Appendix

A.1 Equivalence of C_{ad} and C_{int} at Equilibrium

C_{ad} and C_{int} from the model is given by:

$$C_{ad} = F\frac{\partial r_1}{\partial \phi_1}\left[\frac{\partial r_1}{\partial \beta}\right]^{-1} N_{ad} \tag{A.1}$$

$$C_{int} = -F\frac{\partial r_2}{\partial \phi_2}\left[\frac{\partial r_2}{\partial \beta}\right]^{-1} N_{ad} \tag{A.2}$$

The rate of the desolvation step (r_1) and insertion step (r_2) is:

$$r_1 = \frac{C_{A_\varepsilon}}{C_0}[1-\beta]k'_{f,1}\exp\left(\frac{-\alpha_1 F\phi_1}{RT}\right) - \beta k'_{b,1}\exp\left(\frac{(1-\alpha_1)F\phi_1}{RT}\right) \tag{A.3}$$

$$r_2 = [1-\theta]\beta k'_{f,2}\exp\left(\frac{-\alpha_2 F\phi_2}{RT}\right) - [1-\beta]\theta k'_{b,2}\exp\left(\frac{(1-\alpha_2)F\phi_2}{RT}\right) \tag{A.4}$$

The derivatives for the rate constant is given by:

$$-\frac{\partial r_1}{\partial \phi_1} = \frac{\alpha_1 F}{RT}\frac{C_{A_\varepsilon}}{C_0}[1-\beta]k'_{f,1}\exp\left(\frac{-\alpha_1 F\phi_1}{RT}\right) + \frac{(1-\alpha_1)F}{RT}\beta k'_{b,1}\exp\left(\frac{(1-\alpha_1)F\phi_1}{RT}\right) \tag{A.5}$$

$$-\frac{\partial r_1}{\partial \beta} = \frac{C_{A_\varepsilon}}{C_0}k'_{f,1}\exp\left(\frac{-\alpha_1 F\phi_1}{RT}\right) + k'_{b,1}\exp\left(\frac{(1-\alpha_1)F\phi_1}{RT}\right) \tag{A.6}$$

$$-\frac{\partial r_2}{\partial \phi_2} = \frac{\alpha_2 F}{RT}[1-\theta]\beta k'_{f,2}\exp\left(\frac{-\alpha_2 F\phi_2}{RT}\right) + \frac{(1-\alpha_2)F}{RT}[1-\beta]\theta k'_{b,2}\exp\left(\frac{(1-\alpha_2)F\phi_2}{RT}\right) \tag{A.7}$$

$$\frac{\partial r_2}{\partial \beta} = [1-\theta]k'_{f,2}\exp\left(\frac{-\alpha_2 F\phi_2}{RT}\right) + \theta k'_{b,2}\exp\left(\frac{(1-\alpha_2)F\phi_2}{RT}\right) \tag{A.8}$$

At equilibrium,

$$-\frac{\partial r_1}{\partial \beta} = \frac{1}{(1-\beta)}k'_{b,1}\exp\left(\frac{(1-\alpha_1)F\phi_1}{RT}\right) \tag{A.9}$$

$$\frac{\partial r_2}{\partial \beta} = \frac{1}{\beta}\theta k'_{b,2} \exp\left(\frac{(1-\alpha_2)F\phi_2}{RT}\right) \tag{A.10}$$

$$-\frac{\partial r_1}{\partial \phi_1} = \frac{F}{RT}\beta k'_{b,1} \exp\left(\frac{(1-\alpha_1)F\phi_1}{RT}\right) \tag{A.11}$$

$$-\frac{\partial r_2}{\partial \phi_2} = \frac{F}{RT}[1-\beta]\theta k'_{f,2} \exp\left(\frac{(1-\alpha_2)F\phi_2}{RT}\right) \tag{A.12}$$

$$C_{ad} \approx C_{int} = \frac{\frac{\partial r_2}{\partial \beta}}{-\frac{\partial r_1}{\partial \beta}} = \frac{-F\frac{\partial r_2}{\partial \phi_2}}{-F\frac{\partial r_1}{\partial \phi_1}} \tag{A.13}$$

$$\frac{\frac{\partial r_2}{\partial \beta}}{-\frac{\partial r_1}{\partial \beta}} = \frac{k'_{b,2}}{k'_{b,1}}\frac{1-\beta}{\beta}\theta \exp\left[\frac{(1-\alpha_2)F\phi_2 - (1-\alpha_1)F\phi_1}{RT}\right] \tag{A.14}$$

$$\frac{-\frac{\partial r_2}{\partial \phi_2}}{-\frac{\partial r_1}{\partial \phi_1}} = \frac{k'_{b,2}}{k'_{b,1}}\frac{1-\beta}{\beta}\theta \exp\left[\frac{(1-\alpha_2)F\phi_2 - (1-\alpha_1)F\phi_1}{RT}\right] \tag{A.15}$$

A.2 Capacitances

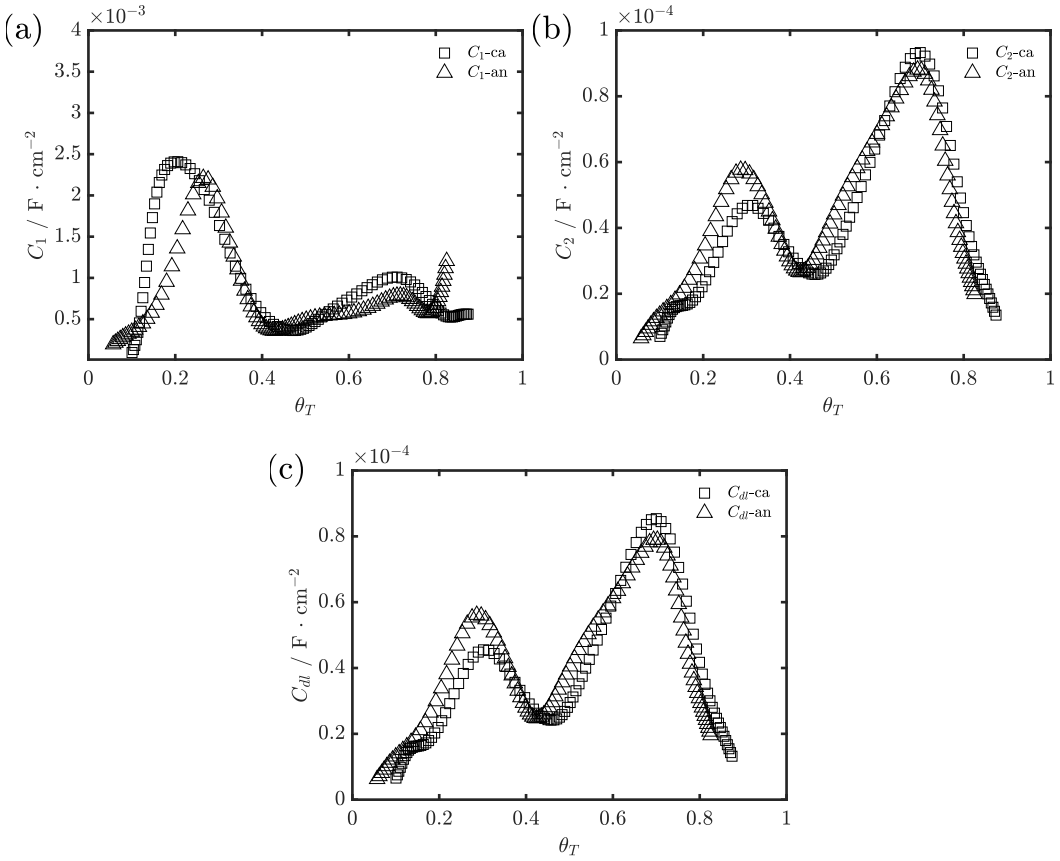

Figure A.1: (a) Capacitance in the outer Helmholtz plane (OHP) (C_1) (b) Capacitance in the inner Helmholtz plane (IHP) (C_2) and (c) Capacitance of the double layer (C_{dl}).

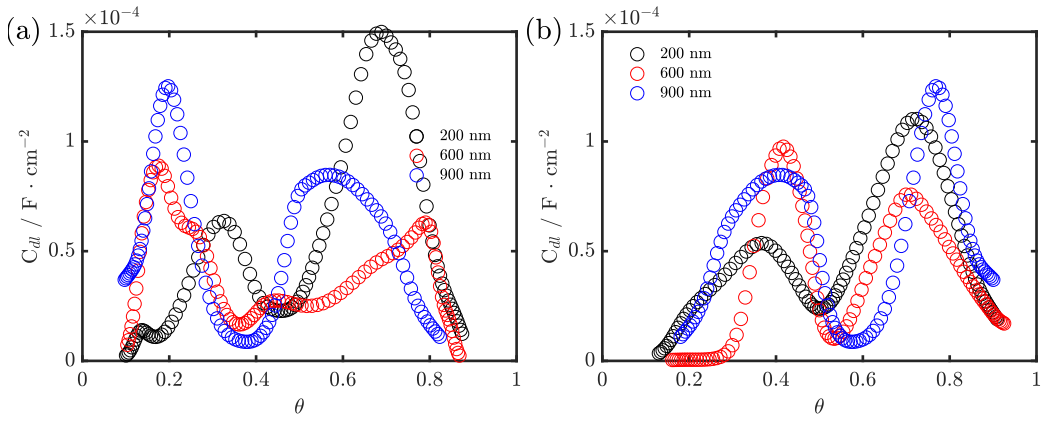

Figure A.2: (a) Double layer capacitance C_{dl} of $LiMn_2O_4$ films (a) during cathodic voltage sweep (b) during the anodic voltage sweep.

References

(1) Nadeem, F.; Hussain, S. M.; Tiwari, P. K.; Goswami, A. K.; Ustun, T. S. Comparative review of energy storage systems, their roles, and impacts on future power systems, 2019.

(2) Singh, M.; Khadkikar, V.; Chandra, A.; Varma, R. K. *IEEE Transactions on Power Delivery* **2011**, *26*, 307–315.

(3) Hannan, M. A.; Hoque, M. M.; Mohamed, A.; Ayob, A. Review of energy storage systems for electric vehicle applications: Issues and challenges, 2017.

(4) Cano, Z. P.; Banham, D.; Ye, S.; Hintennach, A.; Lu, J.; Fowler, M.; Chen, Z. Batteries and fuel cells for emerging electric vehicle markets, 2018.

(5) Manthiram, A. *The Journal of Physical Chemistry Letters* **2011**, *2*, 176–184.

(6) Goodenough, J. B. *Energy Environ. Sci.* **2014**, *7*, 14–18.

(7) Chen, H.; Cong, T. N.; Yang, W.; Tan, C.; Li, Y.; Ding, Y. *Progress in Natural Science* **2009**, *19*, 291–312.

(8) Yang, Z.; Zhang, J.; Kintner-Meyer, M. C. W.; Lu, X.; Choi, D.; Lemmon, J. P.; Liu, J. *Chemical Reviews* **2011**, *111*, 3577–3613.

(9) Hameer, S.; van Niekerk, J. L. *International Journal of Energy Research* **2015**, *39*, 1179–1195.

(10) Ibrahim, H.; Ilinca, A.; Perron, J. *Renewable and Sustainable Energy Reviews* **2008**, *12*, 1221–1250.

(11) Gür, T. M. *Energy & Environmental Science* **2018**, *11*, 2696–2767.

(12) Sarbu, I.; Sebarchievici, C., *Solar Heating and Cooling Systems : Fundamentals, Experiments and Applications*. Elsevier Science: 2016, p 442.

(13) Sarbu, I.; Sebarchievici, C.; Sarbu, I.; Sebarchievici, C. *Sustainability* **2018**, *10*, 191.

(14) Dinçer, İ.; Rosen, M. (A., *Thermal energy storage : systems and applications*; Wiley: 2011, p 599.

(15) Mukherjee, P.; Rao, V. V. *Journal of Modern Power Systems and Clean Energy* **2019**, *7*, 400–411.

(16) Kim, H.; Hong, J.; Park, K. Y.; Kim, H.; Kim, S. W.; Kang, K. Aqueous rechargeable Li and Na ion batteries, 2014.

(17) Krivik, P.; Baca, P. **2013**, DOI: 10.5772/52222.

(18) Choi, J. W.; Aurbach, D. Promise and reality of post-lithium-ion batteries with high energy densities, 2016.

(19) Kim, H.; Hong, J.; Park, K. Y.; Kim, H.; Kim, S. W.; Kang, K. Aqueous rechargeable Li and Na ion batteries, 2014.

(20) Rahman, M. A.; Wang, X.; Wenz, C. High energy density metal-air batteries: A review, 2013.

(21) Liu, C.; Neale, Z. G.; Cao, G. Understanding electrochemical potentials of cathode materials in rechargeable batteries, 2016.

(22) Bruce, P. G.; Scrosati, B.; Tarascon, J.-M.; Bruce, P. G. **2008**, 2930–2946.

(23) Armand, M. B. *NATO Conference Series, (Series) 6: Materials Science* **1980**, *2*, 145–161.

(24) Koksbang, R.; Barker, J.; Shi, H.; Saïdi, M. Y. Cathode materials for lithium rocking chair batteries, 1996.

(25) Jiang, Y.; Li, Y.; Zhou, P.; Lan, Z.; Lu, Y.; Wu, C.; Yan, M. *Advanced Materials* **2017**, *29*, DOI: 10.1002/adma.201606499.

(26) Yu, S.-H.; Feng, X.; Zhang, N.; Seok, J.; Héctor, H.; Abruñ, D. *Acc. Chem. Res* **2018**, *51*, 31.

(27) Yu, X.; Chen, X.; Buchholz, D. B.; Li, Q.; Wu, J.; Fenter, P. A.; Bedzyk, M. J.; Dravid, V. P.; Barnett, S. A. *ACS Applied Nano Materials* **2018**, *1*, 642–653.

(28) O'Mahony, D.; Lunney, J.; Dumont, T.; Canulescu, S.; Lippert, T.; Wokaun, A. *Applied Surface Science* **2007**, *254*, 811–815.

(29) Sandhya, C. P.; John, B.; Gouri, C. Lithium titanate as anode material for lithium-ion cells: A review, 2014.

(30) Wang, A.; Kadam, S.; Li, H.; Shi, S.; Qi, Y. Review on modeling of the anode solid electrolyte interphase (SEI) for lithium-ion batteries, 2018.

(31) Pinsona, M. B.; Bazant, M. Z. *Journal of the Electrochemical Society* **2013**, *160*, DOI: 10.1149/2.044302jes.

(32) Cho, Y.; Lee, S.; Lee, Y.; Hong, T.; Cho, J. *Advanced Energy Materials* **2011**, *1*, 821–828.

(33) Wu, F.; Li, N.; Su, Y.; Zhang, L.; Bao, L.; Wang, J.; Chen, L.; Zheng, Y.; Dai, L.; Peng, J.; Chen, S. *Nano Letters* **2014**, *14*, 3550–3555.

(34) Koo, B.; Kim, H.; Cho, Y.; Lee, K. T.; Choi, N. S.; Cho, J. *Angewandte Chemie - International Edition* **2012**, *51*, 8762–8767.

(35) Son, I. H.; Park, J. H.; Kwon, S.; Park, S.; Rümmeli, M. H.; Bachmatiuk, A.; Song, H. J.; Ku, J.; Choi, J. W.; Choi, J. M.; Doo, S. G.; Chang, H. *Nature Communications* **2015**, *6*, DOI: 10.1038/ncomms8393.

(36) Wang, Y.; Sahadeo, E.; Rubloff, G.; Lin, C. F.; Lee, S. B. High-capacity lithium sulfur battery and beyond: a review of metal anode protection layers and perspective of solid-state electrolytes, 2019.

(37) Cheng, X. B.; Zhang, R.; Zhao, C. Z.; Zhang, Q. Toward Safe Lithium Metal Anode in Rechargeable Batteries: A Review, 2017.

(38) Lin, Y.; Wen, Z.; Yang, C.; Zhang, P.; Zhao, J. *Electrochemistry Communications* **2019**, *108*, DOI: 10.1016/j.elecom.2019.106565.

(39) Li, O. **2012**, 6948–6950.

(40) Peng, Z.; Freunberger, S. A.; Chen, Y.; Bruce, P. G. *Science* **2012**, *337*, 563–566.

(41) Liebreich, M. *Bloomberg New Energy Finance Summit New York*; tech. rep.; 2017.

(42) Li, Y.; Dai, H. Recent advances in Zinc-air batteries, 2014.

(43) Li, Y.; Dai, H. Recent advances in Zinc-air batteries, 2014.

(44) Keily, T.; Sinclair, T. J. *Journal of Power Sources* **1981**, *6*, 47–62.

(45) Huot, J. Y. *Journal of Applied Electrochemistry* **1992**, *22*, 443–447.

(46) Vatsalarani, J.; Geetha, S.; Trivedi, D. C.; Warrier, P. C. *Journal of Power Sources* **2006**, *158*, 1484–1489.

(47) Simons, T. J.; Torriero, A. A. J.; Howlett, P. C.; MacFarlane, D. R.; Forsyth, M. *Electrochemistry Communications* **2012**, *18*, 119–122.

(48) Lee, J.-S.; Tai Kim, S.; Cao, R.; Choi, N.-S.; Liu, M.; Lee, K. T.; Cho, J. *Advanced Energy Materials* **2011**, *1*, 34–50.

(49) Wang, Y.; Chen, R.; Chen, T.; Lv, H.; Zhu, G.; Ma, L.; Wang, C.; Jin, Z.; Liu, J. Emerging non-lithium ion batteries, 2016.

(50) Wessells, C. D.; Peddada, S. V.; Huggins, R. A.; Cui, Y. *Nano Letters* **2011**, *11*, 5421–5425.

(51) Kundu, D.; Talaie, E.; Duffort, V.; Nazar, L. F. The emerging chemistry of sodium ion batteries for electrochemical energy storage, 2015.

(52) Padigi, P.; Goncher, G.; Evans, D.; Solanki, R. *Journal of Power Sources* **2015**, *273*, 460–464.

(53) Trócoli, R.; Battistel, A.; La Mantia, F. *ChemSusChem* **2015**, *8*, 2514–2519.

(54) Lin, M.-C.; Wang, D.-Y., DOI: 10.1038/nature14340.

(55) Xiang, X.; Zhang, K.; Chen, J. Recent advances and prospects of cathode materials for sodium-ion batteries, 2015.

(56) You, Y.; Wu, X.-L.; Yin, Y.-X.; Guo, Y.-G. *Journal of Materials Chemistry A* **2013**, *1*, 14061.

(57) Wu, X.; Deng, W.; Qian, J.; Cao, Y.; Ai, X.; Yang, H. *Journal of Materials Chemistry A* **2013**, *1*, 10130–10134.

(58) Wang, L.; Lu, Y.; Liu, J.; Xu, M.; Cheng, J.; Zhang, D.; Goodenough, J. B. *Angewandte Chemie - International Edition* **2013**, *52*, 1964–1967.

(59) Hwang, J. Y.; Myung, S. T.; Sun, Y. K. Sodium-ion batteries: Present and future, 2017.

(60) Fu, Y.; Wei, Q.; Zhang, G.; Sun, S. Advanced Phosphorus-Based Materials for Lithium/Sodium-Ion Batteries: Recent Developments and Future Perspectives, 2018.

(61) Zhang, C.; Xu, Y.; Zhou, M.; Liang, L.; Dong, H.; Wu, M.; Yang, Y.; Lei, Y. *Advanced Functional Materials* **2017**, *27*, DOI: 10.1002/adfm.201604307.

(62) Pramudita, J. C.; Sehrawat, D.; Goonetilleke, D.; Sharma, N. An Initial Review of the Status of Electrode Materials for Potassium-Ion Batteries, 2017.

(63) Jian, Z.; Luo, W.; Ji, X. *Journal of the American Chemical Society* **2015**, *137*, 11566–11569.

(64) Luo, X.; Wang, J.; Dooner, M.; Clarke, J. *Applied Energy* **2015**, *137*, 511–536.

(65) Ju, Z.; Zhang, S.; Xing, Z.; Zhuang, Q.; Qiang, Y.; Qian, Y. *ACS Applied Materials and Interfaces* **2016**, *8*, 20682–20690.

(66) Liu, Y.; Fan, F.; Wang, J.; Liu, Y.; Chen, H.; Jungjohann, K. L.; Xu, Y.; Zhu, Y.; Bigio, D.; Zhu, T.; Wang, C. *Nano Letters* **2014**, *14*, 3445–3452.

(67) Ponrouch, A.; Goñi, A. R.; Palacín, M. R. *Electrochemistry Communications* **2013**, *27*, 85–88.

(68) Komaba, S.; Murata, W.; Ishikawa, T.; Yabuuchi, N.; Ozeki, T.; Nakayama, T.; Ogata, A.; Gotoh, K.; Fujiwara, K. *Advanced Functional Materials* **2011**, *21*, 3859–3867.

(69) McCulloch, W. D.; Ren, X.; Yu, M.; Huang, Z.; Wu, Y. *ACS Applied Materials and Interfaces* **2015**, *7*, 26158–26166.

(70) Han, J.; Xu, M.; Niu, Y.; Li, G. N.; Wang, M.; Zhang, Y.; Jia, M.; Li, C. M. *Chemical Communications* **2016**, *52*, 11274–11276.

(71) Rollinson, H.; Adetunji, J. In, 2018, pp 738–743.

(72) Eftekhari, A. *Journal of Power Sources* **2004**, *126*, 221–228.

(73) Ponrouch, A.; Bitenc, J.; Dominko, R.; Lindahl, N.; Johansson, P.; Palacin, M. R. Multivalent rechargeable batteries, 2019.

(74) Lipson, A. L.; Pan, B.; Lapidus, S. H.; Liao, C.; Vaughey, J. T.; Ingram, B. J. *Chemistry of Materials* **2015**, *27*, 8442–8447.

(75) Xu, C.; Chen, Y.; Shi, S.; Li, J.; Kang, F.; Su, D. *Scientific Reports* **2015**, *5*, DOI: 10.1038/srep14120.

(76) Kravchyk, K. V.; Bhauriyal, P.; Piveteau, L.; Guntlin, C. P.; Pathak, B.; Kovalenko, M. V. *Nature Communications* **2018**, *9*, DOI: 10.1038/s41467-018-06923-6.

(77) Shakourian-Fard, M.; Kamath, G.; Taimoory, S. M.; Trant, J. F. *The Journal of Physical Chemistry C* **2019**, *123*, 15885–15896.

(78) Li, W.; Dahn, J. R.; Wainwright, D. S. *Science* **1994**, *264*, 1115–1118.

(79) Suo, L.; Borodin, O.; Gao, T.; Olguin, M.; Ho, J.; Fan, X.; Luo, C.; Wang, C.; Xu, K. *Science* **2015**, *350*, 938.

(80) Xu, K.; Wang, C. Batteries: Widening voltage windows, 2016.

(81) Yamada, Y.; Usui, K.; Sodeyama, K.; Ko, S.; Energy, Y. T. N.; undefined 2016 *nature.com*.

(82) Li, W.; Zhang, F.; Xiang, X.; Zhang, X. *ChemElectroChem* **2018**, *5*, 350–354.

(83) Su, D.; McDonagh, A.; Qiao, S.-Z.; Wang, G. *Advanced Materials* **2017**, *29*, 1604007.

(84) Ren, W.; Chen, X.; Zhao, C. *Advanced Energy Materials* **2018**, *8*, 1801413.

(85) Omarova, M.; Koishybay, A.; Yesibolati, N.; Mentbayeva, A.; Umirov, N.; Ismailov, K.; Adair, D.; Babaa, M. R.; Kurmanbayeva, I.; Bakenov, Z. *Electrochimica Acta* **2015**, *184*, 58–63.

(86) Kasiri, G.; Glenneberg, J.; Bani Hashemi, A.; Kun, R.; La Mantia, F. *Energy Storage Materials* **2019**, *19*, 360–369.

(87) Wessells, C. D.; Huggins, R. A.; Cui, Y. *Nature communications* **2011**, *2*, 550.

(88) Wessells, C. D.; Peddada, S. V.; McDowell, M. T.; Huggins, R. A.; Cui, Y. *Journal of the Electrochemical Society* **2012**, *159*, DOI: 10.1149/2.060202jes.

(89) Lee, H.-W.; Pasta, M.; Wang, R. Y.; Ruffo, R.; Cui, Y. *Faraday discussions* **2014**, *176*, 69–81.

(90) Luo, J. Y.; Xia, Y. Y. *Advanced Functional Materials* **2007**, *17*, 3877–3884.

(91) Luo, J. Y.; Liu, J. L.; He, P.; Xia, Y. Y. *Electrochimica Acta* **2008**, *53*, 8128–8133.

(92) Pasta, M.; Wessells, C. D.; Liu, N.; Nelson, J.; McDowell, M. T.; Huggins, R. A.; Toney, M. F.; Cui, Y. *Nature Communications* **2014**, *5*, DOI: 10.1038/ncomms4007.

(93) Sim, S. J.; Lee, S. H.; Jin, B. S.; Kim, H. S. *Scientific Reports* **2019**, *9*, DOI: 10.1038/s41598-019-45556-7.

(94) He, P.; Yu, H.; Li, D.; Zhou, H. *Journal of Materials Chemistry* **2012**, *22*, 3680–3695.

(95) Liu, C.; Neale, Z. G.; Cao, G. Understanding electrochemical potentials of cathode materials in rechargeable batteries, 2016.

(96) Thackeray, M. M. *Journal of the American Ceramic Society* **2004**, *82*, 3347–3354.

(97) Hong, J.; Society, S. O. J. o. t. K. E.; undefined 2003 *koreascience.or.kr*.

(98) Mosbah, A.; Verbaere, A.; Tournoux, M. *Materials Research Bulletin* **1983**, *18*, 1375–1381.

(99) Wang, R. Y.; Shyam, B.; Stone, K. H.; Weker, J. N.; Pasta, M.; Lee, H. W.; Toney, M. F.; Cui, Y. *Advanced Energy Materials* **2015**, *5*, DOI: 10.1002/aenm.201401869.

(100) Wang, B.; Han, Y.; Wang, X.; Bahlawane, N.; Pan, H.; Yan, M.; Jiang, Y. Prussian Blue Analogs for Rechargeable Batteries, 2018.

(101) José Piernas Muñoz, M.; Castillo Martínez, E. **2017**, DOI: 10.1007/978-3-319-91488-6_2.

(102) Itaya, K.; Shoji, N.; Uchida, I. *Journal of the American Chemical Society* **1984**, *106*, 3423–3429.

(103) Chapman, K. W.; Chupas, P. J.; Maxey, E. R.; Richardson, J. W. *Chemical Communications* **2006**, 4013–4015.

(104) Erinmwingbovo, C.; Palagonia, M. S.; Brogioli, D.; La Mantia, F. *ChemPhysChem* **2017**, *18*, 917–925.

(105) Ital., R. R. G. C.; undefined 1937.

(106) La Mantia, F., *Lecture notes in Methoden der modernen elektrischen Energiespeicherung*; Energiespeicher- und Energiewandlersysteme, Universität Bremen: Bremen, 2019.

(107) Bagotsky, V. S., *Fundamentals of Electrochemistry, 2nd Edition*; Wiley-Interscience: 2006, p 722.

(108) Bard, A. J.; Stratmann, M., *Encyclopedia of electrochemistry*; Wiley-VCH: 2001.

(109) Bandarenka, A. S. *The Analyst* **2013**, *138*, 5540–5554.

(110) Orazem, M. E.; Tribollet, B., *Electrochemical impedance spectroscopy. [electronic resource]*; The Electrochemical Society series; Hoboken, N.J. : Wiley, c2008.: 2008.

(111) Bond, A. M.; Schwall, R. J.; Smith, D. E. *Journal of Electroanalytical Chemistry* **1977**, *85*, 231–247.

(112) Stoynov, Z.; Savova-Stoynov, B.; Kossev, T. *Journal of Power Sources* **1990**, *30*, 275–285.

(113) Házì, J.; Elton, D. M.; Czerwinski, W. A.; Schiewe, J.; Vicente-Beckett, V. A.; Bond, A. M. *Journal of Electroanalytical Chemistry* **1997**, *437*, 1–15.

(114) Darowicki, K. *Journal of Electroanalytical Chemistry* **2000**, *486*, 101–105.

(115) Darowicki, K.; Ślepski, P. *Journal of Electroanalytical Chemistry* **2003**, *547*, 1–8.

(116) Sacci, R. L.; Harrington, D. A. In *ECS Transactions*, 2009; Vol. 19, pp 31–42.

(117) Battistel, A.; La Mantia, F. *Electrochimica Acta* **2019**, *304*, 513–520.

(118) Battistel, A.; Du, G.; La Mantia, F. *Electroanalysis* **2016**, *28*, 2346–2353.

(119) Koster, D.; Du, G.; Battistel, A.; La Mantia, F. *Electrochimica Acta* **2017**, *246*, 553–563.

(120) Koster, D.; Patzauer, M.; Salman, M. M.; Battistel, A.; Krischer, K.; La Mantia, F. *ChemElectroChem* **2018**, *5*, 1548–1551.

(121) Koster, D.; Zeradjanin, A. R.; Battistel, A.; La Mantia, F. *Electrochimica Acta* **2019**, DOI: 10.1016/J.ELECTACTA.2019.04.013.

(122) Bard, A. J.; Faulkner, L. R., *Electrochemical methods: Fundamentals and applications / Allen J. Bard, Larry R. Faulkner*, 2nd ed.; John Wiley: New York and Chichester, 2001.

(123) Newman, J. S.; Thomas-Alyea, K. E., *Electrochemical systems*; J. Wiley: 2004, p 647.

(124) Srinivasan, S. In *Fuel Cells*; Springer US: 2006, pp 27–92.

(125) Seeber, R.; Zanardi, C.; Inzelt, G. *ChemTexts* **2015**, *1*, 1–16.

(126) Chan, C. K.; Tüysüz, H.; Braun, A.; Ranjan, C.; La Mantia, F.; Miller, B. K.; Zhang, L.; Crozier, P. A.; Haber, J. A.; Gregoire, J. M.; Park, H. S.; Batchellor, A. S.; Trotochaud, L.; Boettcher, S. W. In *Topics in Current Chemistry*; Springer Verlag: 2016; Vol. 371, pp 253–324.

(127) Lasia, A., *Electrochemical impedance spectroscopy and its applications*; Springer: New York, 2014.

(128) La Mantia, F. **2008**, DOI: 10.3929/ETHZ-A-005707088.

(129) Battistel, A.; Fan, M.; Stojadinović, J.; La Mantia, F. *Electrochimica Acta* **2014**, *135*, 133–138.

(130) Victoria, S. N.; Ramanathan, S. *Electrochimica Acta* **2011**, *56*, 2606–2615.

(131) Sadkowski, A.; Dolata, M.; Diard, J. P. *Journal of the Electrochemical Society* **2004**, *151*, DOI: 10.1149/1.1633270.

(132) Creason, S. C.; Smith, D. E. *Journal of Electroanalytical Chemistry* **1972**, *36*, DOI: 10.1016/S0022-0728(72)80466-2.

(133) Blanc, G.; Epelboin, I.; Gabrielli, C.; Keddam, M. *Electrochimica Acta* **1975**, *20*, 599–601.

(134) Ragoisha, G. A.; Bondarenko, A. S. In *Electrochimica Acta*, 2005; Vol. 50, pp 1553–1563.

(135) Van Gheem, E.; Pintelon, R.; Vereecken, J.; Schoukens, J.; Hubin, A.; Verboven, P.; Blajiev, O. *Electrochimica Acta* **2004**, *49*, 4753–4762.

(136) Van Gheem, E.; Pintelon, R.; Hubin, A.; Schoukens, J.; Verboven, P.; Blajiev, O.; Vereecken, J. In *Electrochimica Acta*, 2006; Vol. 51, pp 1443–1452.

(137) Breugelmans, T.; Lataire, J.; Muselle, T.; Tourwé, E.; Pintelon, R.; Hubin, A. *Electrochimica Acta* **2012**, *76*, 375–382.

(138) Darowicki, K.; Orlikowski, J.; Lentka, G. *Journal of Electroanalytical Chemistry* **2000**, *486*, 106–110.

(139) Riley, K. F.; Hobson, M. P.; Bence, S. J. *Mathematical Methods for Physics and Engineering - 3rd Edition, by K. F. Riley, M. P. Hobson and S. J. Bence, pp. 1362. Cambridge University Press, March 2006. ISBN-10: 0521861535. ISBN-13: 9780521861533* **2006**, 1362.

(140) Erinmwingbovo, C.; Koster, D.; Brogioli, D.; La Mantia, F. *ChemElectroChem* **2019**, celc.201900805.

(141) Bácskai, J.; Martinusz, K.; Czirók, E.; Inzelt, G.; Kulesza, P. J.; Malik, M. A. *Journal of Electroanalytical Chemistry* **1995**, *385*, 241–248.

(142) Bunaciu, A. A.; gabriela Udriştioiu, E.; Aboul-Enein, H. Y. *Critical Reviews in Analytical Chemistry* **2015**, *45*, 289–299.

(143) Jensen, E. Mechanism of Scanning electron microscopy — TikZ example.

(144) Inkson, B. *Materials Characterization Using Nondestructive Evaluation (NDE) Methods* **2016**, 17–43.

(145) Goodhew, P. J.; Beanland, R.; Humphreys, F. J., *Electron microscopy and analysis*; Taylor & Francis: 2001, p 251.

(146) Carter, C. B.; Williams, D. B. (B., *Transmission electron microscopy : diffraction, imaging, and spectrometry*, p 518.

(147) Knudsen, K. B. Alkali Metal-O2 Batteries. Performance and Lifetime Limiting Effects, 2015.

(148) Song, J.; Bazant, M. Z. *Journal of The Electrochemical Society* **2013**, *160*, A15–A24.

(149) Li, W.; Zhang, F.; Xiang, X.; Zhang, X. *ChemElectroChem* **2017**, *4*, 2870–2876.

(150) Prosini, P. P.; Lisi, M.; Zane, D.; Pasquali, M. *Solid State Ionics* **2002**, *148*, 45–51.

(151) Gao, F.; Tang, Z. *Electrochimica Acta* **2008**, *53*, 5071–5075.

(152) Ju, H.; Wu, J.; Xu, Y. *Journal of Chemical Sciences* **2013**, *125*, 687–693.

(153) Mellgren, N.; Brown, S.; Vynnycky, M.; Lindbergh, G. *Journal of The Electrochemical Society* **2008**, *155*, A304.

(154) Vetter, J.; Novák, P.; Wagner, M.; Veit, C.; Möller, K.-C.; Besenhard, J.; Winter, M.; Wohlfahrt-Mehrens, M.; Vogler, C.; Hammouche, A. *Journal of Power Sources* **2005**, *147*, 269–281.

(155) Waag, W.; Käbitz, S.; Sauer, D. U. *Applied Energy* **2013**, *102*, 885–897.

(156) Orazem, M. E.; Tribollet, B., *Electrochemical impedance spectroscopy*, Second edi; The ECS series of texts and monographs; Wiley Blackwell: Hoboken, NJ, 2017.

(157) La Mantia, F.; Vetter, J.; Novák, P. *Electrochimica Acta* **2008**, *53*, 4109–4121.

(158) Bruce, P.; Saidi, M. *Solid State Ionics* **1992**, *51*, 187–190.

(159) Vassiliev, S. Y.; Sentyurin, V. V.; Levin, E. E.; Nikitina, V. A. *Electrochimica Acta* **2019**, *302*, 316–326.

(160) Marchini, F.; Williams, F. J.; Calvo, E. J. *Journal of Electroanalytical Chemistry* **2018**, *819*, 428–434.

(161) Liu, W. *Journal of The Electrochemical Society* **1998**, *145*, 459.

(162) Aurbach, D.; Levi, M. D.; Gamulski, K.; Markovsky, B.; Salitra, G.; Levi, E.; Heider, U.; Heider, L.; Oesten, R. *Journal of Power Sources* **1999**, *81-82*, 472–479.

(163) Kim, S.-W.; Lee, S.-B.; Pyun, S.-I. In *Solid State Electrochemistry I*; Wiley-VCH Verlag GmbH & Co. KGaA: Weinheim, Germany, pp 133–177.

(164) Amos, C. D.; Roldan, M. A.; Varela, M.; Goodenough, J. B.; Ferreira, P. J. *Nano Letters* **2016**, *16*, 2899–2906.

(165) Tang, D.; Sun, Y.; Yang, Z.; Ben, L.; Gu, L.; Huang, X. *Chemistry of Materials* **2014**, *26*, 3535–3543.

(166) Fafilek, G.; Breiter, M. *Journal of Electroanalytical Chemistry* **1997**, *430*, 269–278.

(167) Davis, J. E.; Toren, E. C. *Analytical Chemistry* **1974**, *46*, 647–650.

(168) Balabajew, M.; Roling, B. *Electrochimica Acta* **2015**, *176*, 907–918.

(169) Fan, M.; Stojadinović, J.; Battistel, A.; La Mantia, F. *ChemElectroChem* **2015**, *2*, 970–975.

(170) Fletcher, S. *Electrochemistry Communications* **2001**, *3*, 692–696.

(171) Khandpur, R. S., *Handbook of analytical instruments*; McGraw-Hill: 2007, p 770.

(172) Sadkowski, A.; Diard, J.-P. *Electrochimica Acta* **2010**, *55*, 1907–1911.

(173) Hsieh, G.; Ford, S.; Mason, T.; Pederson, L. *Solid State Ionics* **1996**, *91*, 191–201.

(174) Mansfeld, F. *Journal of The Electrochemical Society* **1988**, *135*, 906.

(175) Tran, A. T.; Huet, F.; Ngo, K.; Rousseau, P. In *Electrochimica Acta*, 2011; Vol. 56, pp 8034–8039.

(176) Stojadinović, J.; Fan, M.; Battistel, A.; La Mantia, F. *ChemElectroChem* **2015**, *2*, 1031–1035.

(177) Battistel, A. **2014**.

(178) Unwin, P. R. In *Encyclopedia of Electrochemistry*, 2007.

(179) Petrescu, B.; J.Diard, *Equivalent model of an electrochemical cell including the reference electrode impedance and the potentiostat parasitics*, Claix, FRANCE, 2013.

(180) Marzak, P.; Yun, J.; Dorsel, A.; Kriele, A.; Gilles, R.; Schneider, O.; Bandarenka, A. S. *Journal of Physical Chemistry C* **2018**, *122*, 8760–8768.

(181) Hao, X.; Schwartz, D. T. *Chemistry of Materials* **2005**, *17*, 5831–5836.

(182) Hao, X.; Li, Y.; Pritzker, M. *Separation and Purification Technology* **2008**, *63*, 407–414.

(183) Joseph, J.; Gomathi, H.; Prabhakara Rao, G. *Electrochimica Acta* **1991**, *36*, 1537–1541.

(184) Jeerage, K. M.; Steen, W. A.; Schwartz, D. T. *Chemistry of Materials* **2002**, *14*, 530–535.

(185) Coon, D. R.; Amos, L. J.; Bocarsly, A. B.; Fitzgerald Bocarsly, P. A. *Analytical Chemistry* **1998**, *70*, 3137–3145.

(186) Amos, L. J.; Duggal, A.; Mirsky, E. J.; Ragonesi, P.; Bocarsly, A. B.; Fitzgerald-Bocarsly, P. A. *Analytical Chemistry* **1988**, *60*, 245–249.

(187) Jeerage, K. M.; Steen, W. A.; Schwartz, D. T. *Chemistry of Materials* **2002**, *14*, 530–535.

(188) Siperko, L. M.; Kuwana, T. *Electrochimica Acta* **1987**, *32*, 765–771.

(189) Liu, C.; Wang, Y.; Zhu, G.; Dong, S. *Electrochimica Acta* **1997**, *42*, 1795–1800.

(190) Omarova, M.; Koishybay, A.; Yesibolati, N.; Mentbayeva, A.; Umirov, N.; Ismailov, K.; Adair, D.; Babaa, M.-R.; Kurmanbayeva, I.; Bakenov, Z. *Electrochimica Acta* **2015**, *184*, 58–63.

(191) Schneemeyer, L. F.; Spengler, S. E.; Murphy, D. W. *Inorganic Chemistry* **1985**, *24*, 3044–3046.

(192) Joseph, J.; Gomathi, H.; Prabhakara Rao, G. *Electrochimica Acta* **1991**, *36*, 1537–1541.

(193) Malik, M. A.; Miecznikowski, K.; Kulesza, P. J. *Electrochimica Acta* **2000**, *45*, 3777–3784.

(194) Chen, W.; Xia, X. H. *Advanced Functional Materials* **2007**, *17*, 2943–2948.

(195) Yu, Q.; Steen, W. A.; Jeerage, K. M.; Jiang, S.; Schwartz, D. T. *Journal of The Electrochemical Society* **2002**, *149*, E195.

(196) Trócoli, R.; Morata, A.; Fehse, M.; Stchakovsky, M.; Sepúlveda, A.; Tarancón, A. *ACS applied materials & interfaces* **2017**, *9*, 32713–32719.

(197) Bocarsly, A. B.; Sinha, S. *Journal of Electroanalytical Chemistry and Interfacial Electrochemistry* **1982**, *137*, 157–162.

(198) Rassat, S. D.; Sukamto, J. H.; Orth, R. J.; Lilga, M. A.; Hallen, R. T. *Separation and Purification Technology* **1999**, *15*, 207–222.

(199) Hao, X.; Yan, T.; Wang, Z.; Liu, S.; Liang, Z.; Shen, Y.; Pritzker, M. *Thin Solid Films* **2012**, *520*, 2438–2448.

(200) Ventosa, E.; Paulitsch, B.; Marzak, P.; Yun, J.; Schiegg, F.; Quast, T.; Bandarenka, A. S. *Advanced Science* **2016**, *3*, 1600211.

(201) Yun, J.; Pfisterer, J.; Bandarenka, A. S. *Energy & Environmental Science* **2016**, *9*, 955–961.

(202) Paulitsch, B.; Yun, J.; Bandarenka, A. S. *ACS Applied Materials & Interfaces* **2017**, *9*, 8107–8112.

(203) Steen, W. A.; Han, S.-W.; Yu, Q.; Gordon, R. A.; Cross, J. O.; Stern, E. A.; Seidler, G. T.; Jeerage, K. M.; Schwartz, D. T. *Langmuir* **2002**, *18*, 7714–7721.

(204) Pau, P. C. F.; Berg, J. O.; McMillan, W. G. *The Journal of Physical Chemistry* **1990**, *94*, 2671–2679.

(205) Gao, Z.; Bobacka, J.; Ivaska, A. *Electrochimica Acta* **1993**, *38*, 379–385.

(206) Humphrey, B. D.; Sinha, S.; Bocarsly, A. B. *The Journal of Physical Chemistry* **1987**, *91*, 586–593.

(207) Haynes, W. M., *CRC handbook of chemistry and physics*.

(208) Ovshinsky, S. R.; Fetcenko, M. A.; Ross, J. *Science* **1993**, *260*, 176–181.

(209) Tang, W.; Zhu, Y.; Hou, Y.; Liu, L.; Wu, Y.; Loh, K. P.; Zhang, H.; Zhu, K. Aqueous rechargeable lithium batteries as an energy storage system of superfast charging, 2013.

(210) Pasta, M.; Wessells, C. D.; Cui, Y.; La Mantia, F. *Nano Letters* **2012**, *12*, 839–843.

(211) You, Y.; Wu, X.-L.; Yin, Y.-X.; Guo, Y.-G. *Journal of Materials Chemistry A* **2013**, *1*, 14061.

(212) Pasta, M.; Wessells, C. D.; Huggins, R. A.; Cui, Y. *Nature communications* **2012**, *3*, 1149.

(213) Fernández-Ropero, A. J.; Piernas-Muñoz, M. J.; Castillo-Martínez, E.; Rojo, T.; Casas-Cabanas, M. *Electrochimica Acta* **2016**, *210*, 352–357.

(214) Deng, L.; Yang, Z.; Tan, L.; Zeng, L.; Zhu, Y.; Guo, L. *Advanced Materials* **2018**, *30*, DOI: 10.1002/adma.201802510.

(215) Tojo, T.; Sugiura, Y.; Inada, R.; Sakurai, Y. *Electrochimica Acta* **2016**, *207*, 22–27.

(216) Trócoli, R.; La Mantia, F. *ChemSusChem* **2015**, *8*, 481–485.

(217) Mizuno, Y.; Okubo, M.; Hosono, E.; Kudo, T.; Zhou, H.; Oh-Ishi, K. *Journal of Physical Chemistry C* **2013**, *117*, 10877–10882.

(218) Kasnatscheew, J.; Rodehorst, U.; Streipert, B.; Wiemers-Meyer, S.; Jakelski, R.; Wagner, R.; Laskovic, I. C.; Winter, M. *Journal of the Electrochemical Society* **2016**, *163*, A2943–A2950.

(219) Jow, T. R.; Delp, S. A.; Allen, J. L.; Jones, J. P.; Smart, M. C. *Journal of the Electrochemical Society* **2018**, *165*, A361–A367.

(220) Erinwingbovo, C.; Koster, D.; Brogioli, D.; La Mantia, F. *ChemElectroChem* **2019**, celc.201900805.

(221) Guidelli, R.; Compton, R. G.; Feliu, J. M.; Gileadi, E.; Lipkowski, J.; Schmickler, W.; Trasatti, S. **2014**, DOI: 10.1515/pac-2014-5026.

(222) Fehse, M.; Trócoli, R.; Ventosa, E.; Hernández, E.; Sepúlveda, A.; Morata, A.; Tarancón, A. *ACS Applied Materials & Interfaces* **2017**, *9*, 5295–5301.

(223) Trócoli, R.; Morata, A.; Fehse, M.; Stchakovsky, M.; Sepúlveda, A.; Tarancón, A. *ACS Applied Materials & Interfaces* **2017**, *9*, 32713–32719.

(224) Oudenhoven, J. F.; Baggetto, L.; Notten, P. H. All-solid-state lithium-ion microbatteries: A review of various three-dimensional concepts, 2011.

(225) Kim, K. W.; Lee, S. W.; Han, K. S.; Chung, H. J.; Woo, S. I. *Electrochimica Acta* **2003**, *48*, 4223–4231.

(226) Chiu, K. F.; Hsiao, H. H.; Chen, G. S.; Liu, H. L.; Her, J. L.; Lin, H. C. *Journal of the Electrochemical Society* **2004**, *151*, DOI: 10.1149/1.1644135.

(227) Subramania, A.; Karthick, S. N.; Angayarkanni, N. *Thin Solid Films* **2008**, *516*, 8295–8298.

(228) Striebel, K. A.; Deng, C. Z.; Wen, S. J.; Cairns, E. J. *Journal of the Electrochemical Society* **1996**, *143*, 1821–1827.

(229) Julien, C.; Haro-Poniatowski, E.; Camacho-Lopez, M.; Escobar-Alarcon, L.; Jimenez-Jarquin, J. *Materials Science and Engineering: B* **2000**, *72*, 36–46.

(230) O'Mahony, D.; Lunney, J.; Dumont, T.; Canulescu, S.; Lippert, T.; Wokaun, A. *Applied Surface Science* **2007**, *254*, 811–815.

(231) Zampardi, G.; Batchelor-McAuley, C.; Kätelhön, E.; Compton, R. G. *Angewandte Chemie International Edition* **2017**, *56*, 641–644.

(232) Singh, D.; Kim, W.-S.; Craciun, V.; Hofmann, H.; Singh, R. K. *Applied Surface Science* **2002**, *197-198*, 516–521.

(233) Morcrette, M. *Solid State Ionics* **2001**, *138*, 213–219.

(234) Morcrette, M. *Solid State Ionics* **1998**, *112*, 249–254.

(235) Tang, S. B.; Lai, M. O.; Lu, L.; Tripathy, S. *Journal of Solid State Chemistry* **2006**, *179*, 3831–3838.

(236) Dokko, K.; Mohamedi, M.; Umeda, M.; Uchida, I. *Journal of The Electrochemical Society* **2003**, *150*, A425.

(237) Nakayama, N.; Nozawa, T.; Iriyama, Y.; Abe, T.; Ogumi, Z.; Kikuchi, K. *Journal of Power Sources* **2007**, *174*, 695–700.

(238) Ma, J.; Wang, C.; Wroblewski, S. *Journal of Power Sources* **2007**, *164*, 849–856.

(239) Lee, J.-W.; Pyun, S.-I. *Electrochimica Acta* **2004**, *49*, 753–761.

(240) Fehse, M.; Trócoli, R.; Ventosa, E.; Hernández, E.; Sepúlveda, A.; Morata, A.; Tarancón, A. *ACS applied materials & interfaces* **2017**, *9*, 5295–5301.

(241) Fehse, M.; Trócoli, R.; Hernández, E.; Ventosa, E.; Sepúlveda, A.; Morata, A.; Tarancón, A. *Thin Solid Films* **2018**, *648*, 108–112.

(242) Erinmwingbovo, C.; Siller, V.; Nuñez, M.; Trócoli, R.; Brogioli, D.; Morata, A.; La Mantia, F. *Electrochimica Acta* **2019**, 135385.

(243) Che, G. *Journal of The Electrochemical Society* **2006**, DOI: 10.1149/1.1838181.

(244) Sofia Palagonia, M.; Erinmwingbovo, C.; Brogioli, D.; La Mantia, F. *Journal of Electroanalytical Chemistry* **2019**, DOI: 10.1016/j.jelechem.2019.05.052.

(245) Li, N.; Patrissi, C. J.; Che, G.; Martin, C. R. *Journal of The Electrochemical Society* **2002**, DOI: 10.1149/1.1393483.

(246) Kebede, M. A.; Phasha, M. J.; Kunjuzwa, N.; le Roux, L. J.; Mkhonto, D.; Ozoemena, K. I.; Mathe, M. K. *Sustainable Energy Technologies and Assessments* **2014**, *5*, 44–49.

(247) Itagaki, M.; Honda, K.; Hoshi, Y.; Shitanda, I. *Journal of Electroanalytical Chemistry* **2015**, *737*, 78–84.

(248) Pajkossy, T. *Electrochimica Acta* **2019**, *308*, 410–417.

(249) Aurbach, D. *Journal of The Electrochemical Society* **1998**, *145*, 3024.

(250) Feng, T.; Xu, W.; Liu, X.; Shao, M.; Guo, J.; Su, C. *Int. J. Electrochem. Sci* **2018**, *13*, 1027–1041.

List of Publications

[1] C. Erinmwingbovo, V. Siller, M. Nuñez, R. Trócoli, D. Brogioli, A. Morata, and F. La Mantia, "Dynamic impedance spectroscopy of LiMn2O4 thin films made by multi-layer pulsed laser deposition," *Electrochimica Acta*, p. 135 385, Nov. 2019, ISSN: 00134686. DOI: 10.1016/j.electacta.2019.135385. [Online]. Available: https://linkinghub.elsevier.com/retrieve/pii/S0013468619322571.

[2] C. Erinmwingbovo, D. Koster, D. Brogioli, and F. La Mantia, "Dynamic Impedance Spectroscopy of Nickel Hexacyanoferrate Thin Films," *ChemElectroChem*, celc.201900805, Aug. 2019, ISSN: 2196-0216. DOI: 10.1002/celc.201900805.

[3] M. S. Palagonia, C. Erinmwingbovo, D. Brogioli, and F. La Mantia, "Comparison between differential charge plots from galvanostatic cycling and cyclic voltammetry," *J. Electroanal. Chem.*, Jun. 2019, ISSN: 1572-6657. DOI: 10.1016/J.JELECHEM.2019.05.052. [Online]. Available: https://www.sciencedirect.com/science/article/pii/S1572665719304072.

[4] C. Erinmwingbovo, M. Palagonia, D. Brogioli, and F. La Mantia, "Intercalation into a Prussian Blue Derivative from Solutions Containing Two Species of Cations," *ChemPhysChem*, vol. 18, no. 8, 2017, ISSN: 14397641. DOI: 10.1002/cphc.201700020.

[5] R. Trócoli, C. Erinmwingbovo, and F. La Mantia, "Optimized Lithium Recovery from Brines by using an Electrochemical Ion-Pumping Process Based on λ-MnO and Nickel Hexacyanoferrate," *ChemElectroChem*, vol. 4, no. 1, 2017, ISSN: 21960216. DOI: 10.1002/celc.201600509.